



HAL
open science

Investigation of mm-wave imaging and radar systems

Armin Zeitler

► **To cite this version:**

Armin Zeitler. Investigation of mm-wave imaging and radar systems. Other. Université Nice Sophia Antipolis; Universität Ulm, 2013. English. NNT : 2013NICE4001 . tel-00832647

HAL Id: tel-00832647

<https://theses.hal.science/tel-00832647>

Submitted on 11 Jun 2013

HAL is a multi-disciplinary open access archive for the deposit and dissemination of scientific research documents, whether they are published or not. The documents may come from teaching and research institutions in France or abroad, or from public or private research centers.

L'archive ouverte pluridisciplinaire **HAL**, est destinée au dépôt et à la diffusion de documents scientifiques de niveau recherche, publiés ou non, émanant des établissements d'enseignement et de recherche français ou étrangers, des laboratoires publics ou privés.



UNIVERSITÉ NICE - SOPHIA ANTIPOLIS

Laboratoire d'Electronique, Antennes et
Télécommunications (LEAT)

Ecole Doctorale STIC, Information and Communication Sciences &
Technologies

ULM UNIVERSITY

Institute of Microwave Techniques (MWT)

Faculty of Engineering and Computer Science

P H D T H E S I S

Armin Zeitler

Investigation of mm-Wave Imaging and Radar Systems

defended on January 11, 2013

Supervisors LEAT: Prof. Dr. Claire MIGLIACCIO
Prof. Dr. Jean-Yves DAUVIGNAC

Supervisor MWT: Prof. Dr.-Ing. Wolfgang MENZEL

Jury:

Reviewers: MCF (HDR) Dr. Amélie LITMAN, Université Aix-Marseille
Prof. Dr. Alexander YAROVY, Delft University of Technology
Prof. Dr.-Ing. Wolfgang MENZEL, University of Ulm

President: Prof. Dr.-Ing. Hermann SCHUMACHER, University of Ulm

Examinators: Prof. Dr. Jean-Yves DAUVIGNAC, Université Nice-Sophia Antipolis
MCF Dr. Ioannis ALIFERIS, Université Nice-Sophia Antipolis
Prof. Dr. Claire MIGLIACCIO, Université Nice-Sophia Antipolis



Investigation of mm-Wave Imaging and Radar Systems by Armin Zeitler is
licensed under a
Creative Commons Attribution-NonCommercial-NoDerivs 3.0 Unported License.

Acknowledgment

This thesis has resulted from a cooperation between the University of Nice - Sophia Antipolis and the University of Ulm.

First of all, I thank my supervisor and mentor Prof. Dr. Claire Migliaccio: she guided me through my diploma thesis and found me a possibility to stay as research engineer for nine month at LEAT to present a valuable topic which has been financed by a French state scholarship. She supervised my the last five years towards the Ph.D. and has always been here to discuss technical as well as personal concerns. Furthermore, I highly acknowledge Prof. Dr. Jean-Yves Dauvignac, actual director of LEAT, for the supervision and support as well as for enabling me to work in his laboratory. At this point I also thank Dr. Pichot, former director of LEAT, for the numerous delightful discussions. Additionally, I am grateful to Dr. Ioannis Aliferis for providing me the spirit for valuable software engineering and its importance. Special thanks to Laurent Brochier and Franck Perret for the assistance in installing the measurement system.

I would like to express my very sincere and deep thanks to Prof. Dr.-Ing. Wolfgang Menzel who set the basis for this work as he accepted an external diploma thesis at LEAT in 2008. This would not be possible without the motivation of this idea of Dr.-Ing. Peter Feil and I owe him my thanks. Many thanks belong to Dr.-Ing. Frank Bögelsack who provided me with assistance in all questions concerning documentation and presentation of results.

For reviewing this manuscript and for their useful remarks and suggestions that helped to improve this manuscript I thank Dr. Amélie Litman and Prof. Dr. Alexander Yarovoy. I express my gratitude to Prof. Dr.-Ing. Hermann Schumacher for being the president of the jury.

I am deeply grateful to all my colleagues at LEAT for the great moments we shared together within but also beside the laboratory.

Also, I thank Savina, without her support, this work would not be possible to be accomplished. Finally, I would also like to thank my parents for their sacrifice, encouragement and support throughout my studies.

Munich, March 2013

Armin Zeitler

Contents

1	Introduction	1
2	Electromagnetic Modeling	5
2.1	Introduction of the Problem	5
2.2	Electromagnetic Modeling of the Direct Problem	9
2.2.1	Numerical Solution	9
2.2.2	Analytic Solution	16
2.2.3	Description of the Means of Simulation	17
2.3	Qualitative Imaging - Localization and Shaping	25
2.3.1	Back-propagation - Monochromatic Approach	25
2.3.2	Back-propagation - Multifrequency Approach	28
2.4	Quantitative Imaging - Reconstruction of the Complex Permittivity	30
2.4.1	Description of the Inversion Algorithm	30
2.4.2	Quantitative Imaging Performance for Metallic Objects	31
2.4.3	Quantitative Imaging Results	31
3	Scattered Field Measurement System for Imaging with mm-Waves	35
3.1	Comparison of Existing Systems	35
3.1.1	Two Dimensional Scattered Field Measurement Facilities	35
3.1.2	Measurement Systems Providing Three Dimensional Results	36
3.1.3	Compact Range Antenna Facilities	37
3.2	Description of the Measurement System	38
3.2.1	Introduction of Objectives	38
3.2.2	Description of Mechanical Modifications	38
3.2.3	Millimeter-Wave Antenna Measurement System	42
3.2.4	Investigated Measurement Area	42
3.3	Measurement Results	44
3.3.1	Measurement Parameters	44
3.3.2	First Measurement Results	44
3.4	Analysis and Error Correction	58
3.4.1	Characterization of Dielectric Targets	58
3.4.2	Precision of Setup Installation - Correction of Mechanical Errors	60
3.4.3	Match Experimental Setup with Simulation - Complex Normalization	66
3.4.4	Noise Sources - Filtering	67
3.5	Results over W-band and Discussion	79
3.5.1	Calibrated and Normalized Measured Scattered Fields	79
3.5.2	Overall Calibration Performance and Measurement Error	87
3.5.3	Mechanical Precision Versus Measurement Error	87
3.6	Conclusion	88

4	Qualitative and Quantitative Reconstruction	91
4.1	Qualitative Imaging	91
4.1.1	Localization of Targets	91
4.1.2	Reconstruction	94
4.2	Quantitative Imaging	98
4.2.1	Estimation of the Domain's Size	99
4.2.2	Expected Complex Permittivity Values	101
4.2.3	Inversion Results	101
4.3	Conclusion	106
5	FMCW-Radar Measurements	107
5.1	Introduction of Application	107
5.2	Theoretical Results - Simulation	109
5.3	Ideal Setup with Network Analyzer	112
5.3.1	Scene with Vertical Cylinders	112
5.3.2	Detection of Foreign Object Debris	116
5.4	FMCW-Radar System	120
5.4.1	Sensor Overview and Signal Processing	120
5.4.2	Measurement Results	122
5.5	Conclusion	127
6	Conclusion and Outlook	129
6.1	Conclusion	129
6.2	Outlook	129
7	Resume in German and French	131
7.1	Zusammenfassung und Ausblick auf Deutsch	131
7.2	Résumé en français	133
A	Approach of the Integration of the Green's Function	137
A.1	Self Element Case, $n = m$, Diagonal Matrix Elements	138
A.2	General Case, $n \neq m$, Non-diagonal Matrix Elements	140
B	Approach for the Integration over a Squared Disc with an Optimal Circular Disc	143
B.1	Demonstration	143
B.2	Numerical Integration	146
B.2.1	Approximate Integration	146
B.2.2	Approximate Double Integration	147
B.3	Chosen Approach versus Numerical Integration	147
B.3.1	Wavelength in the Order of Meters	147
B.3.2	Wavelength in the Order of Millimeters	149
C	Additional Scattered Field Measurements	151

Contents	vii
<hr/>	
Bibliography	167
Publications of the Author	179
Curriculum Vitae	181

List of Symbols and Abbreviations

Well known operators and functions are not stated here. The page numbers point to the first appearance of a symbol or abbreviation.

Symbols

ρ	Charge.....	6
\mathbf{J}	Current.....	6
$e^{j\omega t}$	Time dependency convention.....	6
\mathbf{r}	Vector to point of observation in space.....	7
$\mathbf{E}(\mathbf{r})$	Total field observed at \mathbf{r}	7
$\mathbf{E}^{(i)}(\mathbf{r})$	Incident field observed at \mathbf{r}	8
$\mathbf{E}^{(s)}(\mathbf{r})$	Scattered field observed at \mathbf{r}	8
$\Delta\phi$	Angle step size.....	21
λ_0	Free-space wavelength.....	21
$A_z^{(s)}$	Amplitude of scattered field in z -direction.....	62
$A_z^{(t)}$	Amplitude of total field in z -direction.....	62
$A_z^{(i)}$	Amplitude of incident field in z -direction.....	62
$\Phi^{(s)}$	Phase of scattered field.....	62
$\Phi^{(t)}$	Phase of total field.....	62
$\Phi^{(i)}$	Phase of incident field.....	62
$E_{\text{cal}}^{(s)}$	Calibrated measured scattered field.....	66
γ	Complex normalization factor.....	66
$E_{\text{cal, norm}}^{(s)}$	Measured scattered field calibrated and normalized.....	66
e	Measurement error.....	67
$E_{\text{exact}}^{(s)}$	Exact scattered field.....	67

Abbreviations

FOD	Foreign Object Debris	1
RCS	Radar Cross Section	2
TE	Transverse Electric	5
TM	Transverse Magnetic	5
EFIE	Electric Field Integral Equations	9
MoM	Method of Moments	11
PEC	Perfect Electric Conductor	20
SNR	Signal-to-Noise Ratio	23
FMCW	Frequency-Modulated Continuous Wave	28
SFCW	Stepped Frequency Continuous Wave	28
TUT	Target Under Test	30
AWGN	Additive White Gaussian Noise	31
SFMS	Scattered Field Measurement System	35
CATR	Compact Antenna Test Range	35
CAF	Complex Antenna Factor	45
PMMA	Polymethyl Methacrylate	58
CCD	Charge-Coupled Device	107
LIDAR	Light Detection and Ranging	107
LADAR	Laser Detection and Ranging	107
MMIC	Monolithic Microwave Integrated Circuit	107
FAA	Federal Aviation Administration	108
PLL	Phase Locked Loop	120
VCO	Voltage-Controlled Oscillator	120
LO	Local Oscillator	120
DDS	Direct Digital Synthesis	121
ADC	Analogue Digital Conversion	121

Introduction

In the last decade, microwave and millimeter-wave systems have gained importance in civil and security applications. Due to an increasing maturity and availability of circuits and components, these systems are getting more compact while being less expensive. Millimeter-wave systems—less affected by atmospheric conditions than those working in the infrared and visible spectrum—are currently being developed in a wide range of areas: their development is mainly driven by automotive applications at 24 GHz [1, 2] and 77 GHz [3]. Niche applications take advantage of this success, like power line detection at 77 GHz and 94 GHz [4–7] and Foreign Object Debris (FOD) detection at 77 GHz [8]. The choice for this frequencies is based on the short wavelength, providing a high resolution by itself, and the feasibility of directive antenna systems within compact platforms. All these applications can be classified under the terms of qualitative imaging and detection of objects and obstacles [1, 2, 4–13]. One is able to detect and localize objects but in order to classify them precisely these systems are pushed to identification nowadays that means an extension to more adequate imaging is needed. On one hand, this requires the improvement of the radar module itself to get a three dimensional image. On the other hand, the targets have to be reconstructed with qualitative and/or quantitative imaging algorithms.

Quantitative imaging has been conducted at lower frequencies [14–20] using computationally intensive inverse problem algorithms. Due to the ill-posed character of the inverse problem, these algorithms are, in general, very sensitive to noise: the key to their successful application to experimental data [21–25] is the precision of the measurement system. Only a few research teams investigate in imaging in the W-band or higher frequencies, where real-time back-propagation algorithms have been successfully applied [26–31].

The requirements for the presented work are developed based on former research activities of the two laboratories where this work is effected. In the past, measurements of radiation patterns of antennas in the W-band (75 - 110 GHz) have been successfully provided at LEAT [32], [113–118] in a laboratory environment, the anechoic chamber, on one hand. On the other hand, radar measurements have been done [33], [119, 120] in collaboration with the MWT [4, 8], [121]. Additionally, quantitative imaging algorithms have been developed at LEAT and successfully applied to measured data provided by academic partners, so far at lower frequencies [17, 19, 34, 35]. Therefore, this manuscript should demonstrate the

combination of these three mentioned competences: one would provide controlled measurements of scattered fields in the W-band, which can be used for quantitative imaging in order to develop further algorithms at this frequency band of interest. Furthermore, a first proposal should be developed in order to obtain “in-field” measurements with a radar system to get closer to applications of interest. To our best knowledge, there is no experimental system associated with a comparison of the scattered field of targets, in the amplitude and in the phase, with theoretical results in the W-band. In this manuscript such a system is presented, designed to provide scattered field data to quantitative reconstruction algorithms.

For qualitative imaging purposes, one can directly obtain scattered fields from the measurements and apply imaging algorithms. This has been done recently up to 18 GHz [10, 11], where imaging has been done with a time-reversal focusing algorithm. Back-propagation has been used for qualitative reconstruction in the W-band [29, 31], as well as for 310 GHz [26]. This work focuses firstly on the simulation of scattered fields—the calculation of the direct problem—before going into the measurements. Afterwards, reconstruction algorithms are studied on the simulated and the measured data. This has the following advantages:

- measurement configurations can be studied to get the optimal setup for the foreseen application (measurements of the Radar Cross Section (RCS), receivers arranged on a circle or on an equispaced line),
- error sources can be identified beforehand as one can compare simulated with measured data,
- these errors can be corrected with post-processing before doing the imaging,
- additionally, noise studies can be investigated on ideal scattered fields obtained by the simulation.

In order to validate the measurement system, one has to begin with simple objects. At mm-wave frequencies a great number of objects can be approximated in two dimensions due to the short wavelength, like power lines, which are a high risk for helicopters. Therefore, two metallic cylinders of different diameters and one dielectric cylinder have been chosen. In this case, presenting a symmetry of rotation, the multi-incident and the multi-view processes are simplified to mono-incident and multi-view ones. The measurements have been obtained with an inexpensive mechanical extension to an already existing installation, combined with a marginal rearrangement in the anechoic chamber. The objects are embedded in a homogeneous background and surrounded by a set of receivers. For each receiver, a set of data, representing the values of the scattered field in the amplitude and in the phase, is measured. The results are validated by comparisons with simulations, obtained with two different theoretical approaches. Additionally, first imaging proposals have been studied in order to provide adequate measurements with a radar system already at an early stage to answer to additional requirements asked

by “in-field” measurements.

This manuscript is divided into six chapters. In Chapter 2, the theory of the used methods to compute numerically the scattered fields of known objects is introduced. A 2D-TM Method of Moments with a regular square mesh, indice basis functions and pulse test functions are chosen. Two computer codes are developed and are presented to compare numerical and analytic solutions. Furthermore, qualitative imaging principles with back-propagation are summarized and an algorithm for quantitative imaging is explained. In Chapter 3, the investigated setup in the anechoic chamber, to measure scattered fields in the W-band of symmetrical scatterers, is shown. Additionally, the choice of the investigated targets and the used antennas is treated and preliminary measurement results are analyzed. Relying on the measurement results, the error sources are studied and solutions to improve the measurements via post-processing are proposed. The final results are used for the qualitative reconstruction of all three targets of interest and to image quantitatively the small cylinder. The reconstructed images are compared in detail in Chapter 4. In addition, close range imaging is investigated using a vector network analyzer measurement equipment and a radar system. This is described in Chapter 5, based on a future application, which is the detection of FOD on airport runways. The conclusion is addressed in Chapter 6 and some future investigations are discussed.

Electromagnetic Modeling

2.1 Introduction of the Problem

In this chapter, the theory, used in this manuscript to calculate scattered fields of known objects, is introduced. Simulations are also used as direct problem solver during the quantitative inversion process. Thus, they are compared to the analytic solution, which only exists for a limited number of cases, to evaluate the performance of the numerical simulation.

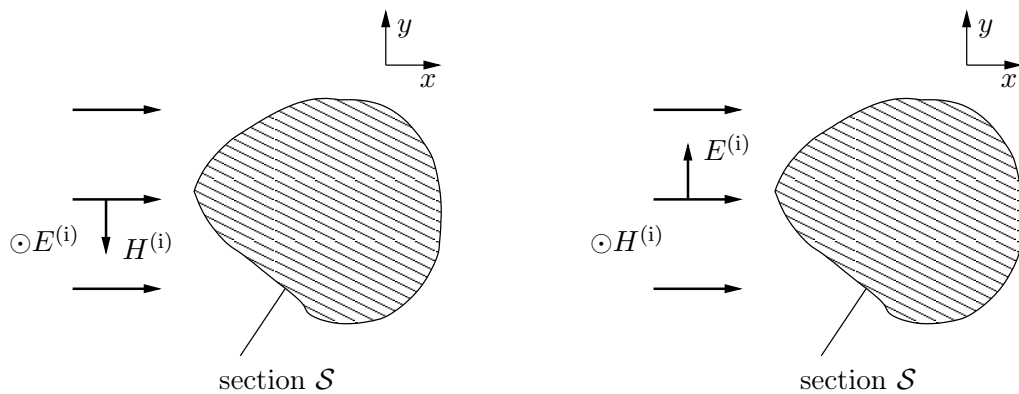


Fig. 2.1: Uniform plane wave incident on a cylindrical object. TM (left) and TE (right).

The problems described here are simplified to two-dimensional ones. Two-dimensional problems are those with invariance in the third dimension, such as an infinite cylindrical structure illuminated by a field that does not vary along the axis of the object. If the object axis lies along the z axis in a Cartesian coordinate system, it is convenient to separate the fields into Transverse Magnetic (TM) and Transverse Electric (TE) parts with respect to the variable z [38]. In practice, a problem can be considered as two dimensional if all parameters of the media are constant in z over several wavelengths. Many objects can be seen as 2D objects in a first approach for mm-wave applications due to the short wave-length (for example, power lines, pylons on the road etc). In general, objects are described as 3D objects in three dimensions with a volume \mathcal{V} . In the two-dimensional case, the object is described through its section \mathcal{S} . One can classify the object in two cases depending on the polarization of the incident field: 2D-TE and 2D-TM. The z -component of the electric field is absent in the TE case, while the z -component

of the magnetic field is absent in the TM case (see Fig. 2.1). In the latter case, namely 2D-TM, all electric fields have only one component, the one in z -direction. This case is studied in detail and presented in this manuscript.

Circular cylinders represent one of the most important classes of geometrical surfaces. The surface of many practical scatterers, for example the fuselage of airplanes and missiles, can often be represented by cylindrical structures in a first approach. For us, they are of particular interest as the measurement system, presented in the next chapter, deals with circular cylinders so far. For them, the scattered fields can be exactly calculated with the analytic solution. This special case of circular cylinders is used in order to validate the numerical solution as well as the measurement system.

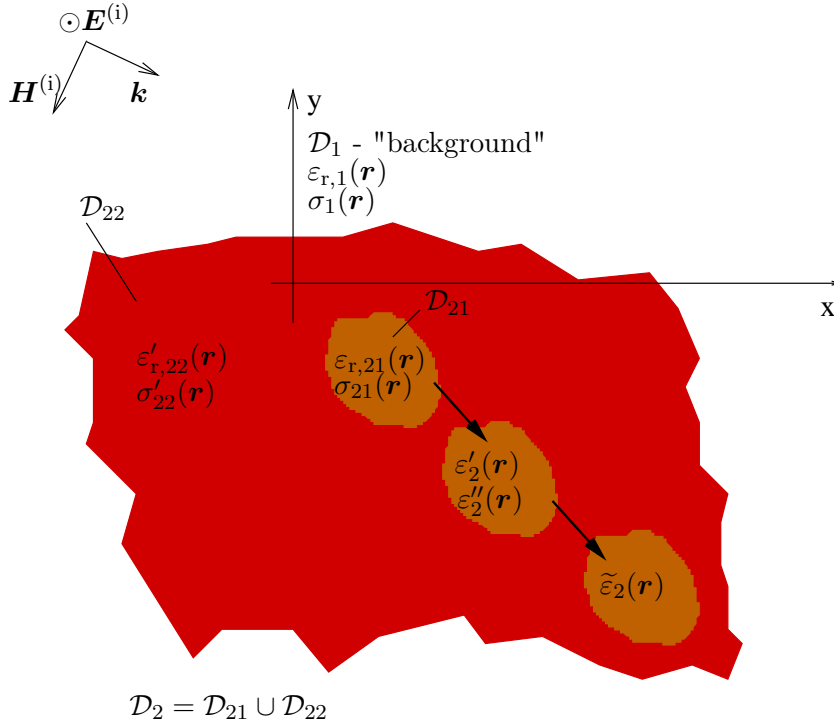


Fig. 2.2: Geometry of the problem.

The study of electromagnetics involves the application of Maxwell equations to a specific geometry. The most general case is discussed below. Considering a source-free region of space (no charges, $\rho = 0$, and no currents, $\mathbf{J} = 0$) containing an inhomogeneity characterized by a complex permittivity $\tilde{\epsilon}(\mathbf{r})$ and a complex permeability $\tilde{\mu}$ as shown in Fig. 2.2. If this region is illuminated by an electromagnetic field having the time dependence $e^{j\omega t}$, the fields in the vicinity of the inhomogeneity

satisfy Maxwell equations:

$$\nabla \times \mathbf{E} + j\omega\tilde{\mu}\mathbf{H} = 0 \quad (2.1)$$

$$\nabla \times \mathbf{H} - j\omega\tilde{\varepsilon}(\mathbf{r})\mathbf{E} = 0 \quad (2.2)$$

$$\nabla \cdot (\tilde{\varepsilon}(\mathbf{r})\mathbf{E}) = 0 \quad (2.3)$$

$$\nabla \cdot (\tilde{\mu}\mathbf{H}) = 0 \quad (2.4)$$

where \mathbf{E} and \mathbf{H} are the electric and magnetic fields, respectively. \mathbf{E} and \mathbf{H} are complex-valued and represent the vector amplitude and phase angle of the time-harmonic fields. Here, \mathbf{r} represents the point of observation in space. Before solving numerically these equations, the definition of the complex permittivity and permeability should be closer discussed. Permittivity is a number related to the ability of a material to propagate electromagnetic fields [39]. It is a quantity used to describe dielectric properties that influence the reflection of electromagnetic waves at interfaces and the attenuation of wave energy within materials. In the frequency domain, the complex permittivity $\tilde{\varepsilon}(\mathbf{r})$ (2.5) is defined with respect to the one of free space ε_0 (in F/m). With the complex permittivity $\tilde{\varepsilon}(\mathbf{r})$, one can express the complex relative permittivity $\tilde{\varepsilon}_r(\mathbf{r})$, also called dielectric constant, and define the complex wave vector:

$$\begin{aligned} \tilde{\varepsilon}(\mathbf{r}) &= \varepsilon_0 \left(\varepsilon_r(\mathbf{r}) - j \frac{\sigma(\mathbf{r})}{\omega\varepsilon_0} \right) \\ &= \underbrace{\varepsilon'}_{\text{real part}} - j \underbrace{\varepsilon''}_{\text{imaginary part}} \end{aligned} \quad (2.5)$$

$$\tilde{\varepsilon}_r(\mathbf{r}) = \varepsilon_r(\mathbf{r}) - j \frac{\sigma(\mathbf{r})}{\omega\varepsilon_0} \quad (2.6)$$

$$k^2(\mathbf{r}) = \omega^2 \tilde{\varepsilon}(\mathbf{r}) \mu_0. \quad (2.7)$$

The permittivity can be either expressed as a function of ε_r and σ , ε' and ε'' or in the most general case as complex value: $\tilde{\varepsilon}$. ε' is defined as the real part of the dielectric permittivity. It is complex when there is a delay between \mathbf{E} and the polarization \mathbf{P} [40]. The imaginary part, ε'' , is proportional to the conductivity σ (in S/m). The angular frequency ω is equal to $2\pi f$. The real part ε' is a measure of how much energy from an external electric field can be stored in a material. The dielectric loss factor ε'' , which is the imaginary part, influences the energy absorption and the attenuation. One more important parameter used in electromagnetic theory is the tangent of loss angle:

$$\tan(\delta) = \frac{\varepsilon''}{\varepsilon'}. \quad (2.8)$$

One can also define the complex permeability $\tilde{\mu}$ which consists as well of a real part, that represents the energy storage and an imaginary part, that corresponds to the energy loss term [41]. The relative permeability $\tilde{\mu}_r$ is the absolute permeability $\tilde{\mu}$ relative to the permeability of free space μ_0 . Some materials such as iron (ferrites),

cobalt, nickel and their alloys have magnetic properties; however many materials are non-magnetic. On the other hand, all materials have dielectric properties. In the following, it is assumed that $\tilde{\mu} \sim \mu_0$. The values for a perfect conductor in the microwave domain can be approximated for computation purposes [42] by: $\varepsilon_r = 1$, $\sigma = \infty$.

The geometry of interest for the application of the Maxwell equations (2.1)-(2.4) is shown in Fig. 2.2. The values indexed with 1 describe the homogeneous background media \mathcal{D}_1 . The inhomogeneous scatterer \mathcal{D}_2 , here described by an ensemble of different homogeneous portions \mathcal{D}_{21} and \mathcal{D}_{22} exemplary, is completely submerged in the homogeneous background. In general, one can define the complex permittivity for the whole area of interest as:

$$\tilde{\varepsilon}(\mathbf{r}) = \begin{cases} \tilde{\varepsilon}_2(\mathbf{r}), & \text{if } \mathbf{r} \in \mathcal{D}_2 \\ \tilde{\varepsilon}_1, & \text{if } \mathbf{r} \notin \mathcal{D}_2. \end{cases}$$

Furthermore, one can define, with the complex relative permittivity (2.6), the contrast $C(\mathbf{r})$:

$$C(\mathbf{r}) = \begin{cases} \tilde{\varepsilon}_{r2}(\mathbf{r}) - \tilde{\varepsilon}_{r1}, & \text{if } \mathbf{r} \in \mathcal{D}_2 \\ 0, & \text{if } \mathbf{r} \notin \mathcal{D}_2. \end{cases} \quad (2.9)$$

A forward or direct scattering problem can be defined, in general, as the determination of the scattered fields $\mathbf{E}^{(s)}(\mathbf{r})$ everywhere, inside or outside the scatterer \mathcal{D}_2 , from known incident fields $\mathbf{E}^{(i)}(\mathbf{r})$, scatterer and background media [43]. The superposition of the incident and scattered fields yields the total field $\mathbf{E}(\mathbf{r})$ in the presence of the scatterer:

$$\mathbf{E} = \mathbf{E}^{(i)} + \mathbf{E}^{(s)}. \quad (2.10)$$

Its solution based on Maxwell equations is presented numerically in Section 2.2.1 and analytically in Section 2.2.2.

An inverse scattering problem can be defined, in general, as the problem of retrieving information about the scatterer from obtained scattered fields in a finite domain, exterior to the scatterer \mathcal{D}_2 , for known incident fields and background medium. The observation of the scattered fields might be carried out successively with different types of incident fields for different frequencies, different positions of the sources and different locations of the receivers. The information about the scatterer could be any parameter which may characterize the scatterer, e. g. the shape (see Section 2.3.1) or the complex permittivity profile with its contrast as demonstrated in Section 2.4.

2.2 Electromagnetic Modeling of the Direct Problem

2.2.1 Numerical Solution

The basis for the used methods, an integral representation of the electric field (EFIE) solved with a moment method solution, is briefly introduced in [44] and [45]. They have been continuously further developed for several different applications and configurations. Inverse problem algorithms have been investigated in combination with a circular arrangement of emitters and receivers in [46] to reconstruct the complex permittivity profile of unknown objects based on simulated and measured data. In [47], the polarimetric influence of scattered fields on the reconstruction of 2D buried objects has been studied. A boundary-oriented inverse scattering method, based on contour deformations by means of level sets for radar imaging, has been presented in [48]. Furthermore, investigations have been done in microwave tomography for buried objects in two dimensions in [49] and extended to three dimensions in [50] to mention only a few examples. The choice of the methods, due to its success in the past, is not explained in the presented work here, but its theory is summarized below.

Starting points are the Maxwell equations presented in (2.1)-(2.4). They are applied to the problem described through the geometry shown in Fig. 2.2. In the case of TM (E_z, H_x, H_y) the incident, the total and the scattered fields have only a component of the E-field in z -direction. The magnetic fields, however, have components in x - and y -directions which leads to:

$$\frac{\partial E_z}{\partial y} + j\omega\mu_0 H_x = 0 \quad (2.11)$$

$$-\frac{\partial E_z}{\partial x} + j\omega\mu_0 H_y = 0 \quad (2.12)$$

$$\frac{\partial H_y}{\partial x} - \frac{\partial H_x}{\partial y} - j\omega\tilde{\varepsilon}(x, y)E_z = 0 \quad (2.13)$$

$$\frac{\partial H_x}{\partial x} + \frac{\partial H_y}{\partial y} = 0. \quad (2.14)$$

Equations (2.11) and (2.12) are differentiated with respect to y and x respectively and merged. Finally, with (2.13) one obtains:

$$\frac{\partial^2 E_z}{\partial x^2} + \frac{\partial^2 E_z}{\partial y^2} + \omega^2\tilde{\varepsilon}(x, y)\mu_0 E_z = 0 \quad (2.15)$$

which is equivalent to

$$\begin{aligned} \frac{\partial^2 E_z}{\partial x^2} + \frac{\partial^2 E_z}{\partial y^2} + \omega^2\tilde{\varepsilon}_1\mu_0 E_z - \omega^2\tilde{\varepsilon}_1\mu_0 E_z + \omega^2\tilde{\varepsilon}(x, y)\mu_0 E_z &= 0 \\ \frac{\partial^2 E_z}{\partial x^2} + \frac{\partial^2 E_z}{\partial y^2} + \omega^2\tilde{\varepsilon}_1\mu_0 E_z &= -\omega^2(\tilde{\varepsilon}(x, y) - \tilde{\varepsilon}_1)\mu_0 E_z. \end{aligned} \quad (2.16)$$

Assuming this, one can derive the equation of propagation (scalar Helmholtz equation):

$$\begin{aligned}\Delta E_z + k_1^2 E_z &= - (k^2(x, y) - k_1^2) E_z & (2.17) \\ k_1 &= \omega \sqrt{\tilde{\varepsilon}_1 \mu_0} \\ k(x, y) &= \omega \sqrt{\tilde{\varepsilon}(x, y) \mu_0}.\end{aligned}$$

A particular solution of the equation of propagation is given by:

$$E_z = G (k^2(x, y) - k_1^2) E_z(x, y) \quad (2.18)$$

where G is the impulse response also known as the Green's function. The homogeneous Helmholtz equation, that means without a right-hand-side term (without the presence of an object), holds true for the incident fields. The general solution of the equation of propagation is:

$$E_z = E_z^{(i)} + G (k^2(x, y) - k_1^2) E_z. \quad (2.19)$$

For an object in an arbitrary section \mathcal{D}_2 this leads to the following integral equation:

$$\begin{aligned}E_z(x, y) &= E_z^{(i)}(x, y) \\ &+ \int_{\mathcal{D}_2} (k_2^2(x, y) - k_1^2) G(x - x', y - y') E_z(x', y') dx' dy' \\ \forall (x, y) &\in \mathbb{R}^2.\end{aligned} \quad (2.20)$$

One has to solve the following integral equation of the total field $E_z(x, y)$ in the section where $\mathbf{r} \in \mathcal{D}_2$:

$$\underbrace{E_z(x, y)}_{\text{unknown}} = \underbrace{E_z^{(i)}(x, y)}_{\text{known}} + \underbrace{\int \int_{\mathcal{D}_2} \underbrace{(k_2^2(x', y') - k_1^2)}_{\text{known}} \underbrace{E_z(x', y')}_{\text{unknown}} \underbrace{G(x - x', y - y')}_{\text{known}} dx' dy'}_{E_z^{(s)}(\mathbf{r}) \text{ scattered field}} \quad (2.21)$$

$$E_z(x, y) = E_z^{(i)}(x, y) + E_z^{(s)}(x, y). \quad (2.22)$$

The domain of interest is discretized with N cells having the size of $\Delta x \times \Delta y$ (see Fig. 2.3). The pixels are addressed by \mathbf{r}_m and \mathbf{r}_n which are the points at the center of the cell m and n respectively.

$$\begin{aligned}E_z(\mathbf{r}) &= E_z^{(i)}(\mathbf{r}) + \int \int_{\mathcal{D}_2} (k_2^2(\mathbf{r}') - k_1^2) E_z(\mathbf{r}') G(\mathbf{r}, \mathbf{r}') d\mathbf{r}' \\ E_z(\mathbf{r}_m) &= E_z^{(i)}(\mathbf{r}_m) + \underbrace{\sum_{n=1}^N \int \int_{C_n} (k_2^2(\mathbf{r}_n) - k_1^2) E_z(\mathbf{r}_n) G(\mathbf{r}_m - \mathbf{r}_n) d\mathbf{r}_n}_{\text{scattered field of the } n^{\text{th}} \text{ pixel calculated at the point } \mathbf{r}_m}.\end{aligned} \quad (2.23)$$

Finally, one can calculate the total field at one point which is the sum of the incident field and the integral, corresponding to the scattered field, at this point.

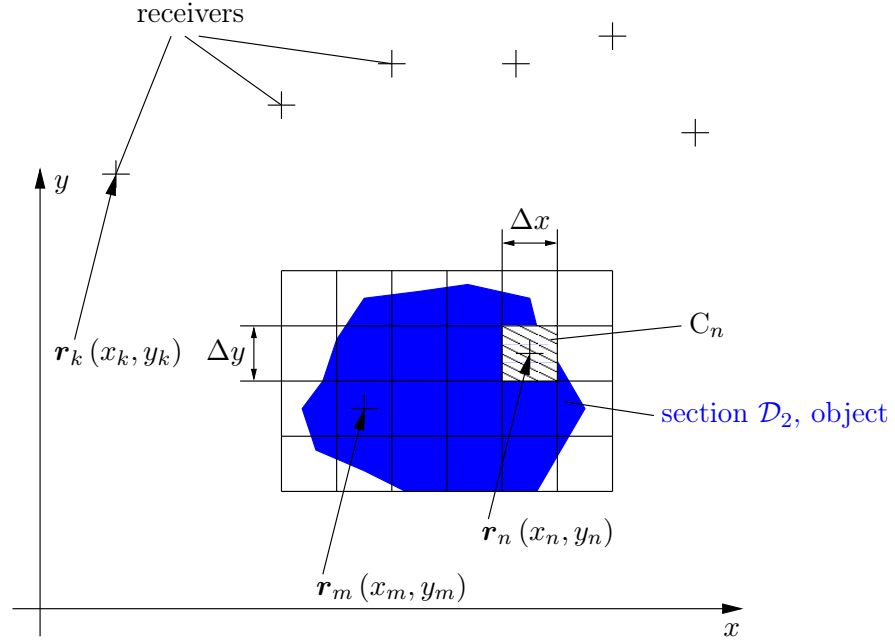


Fig. 2.3: Discretization for numerical modeling.

Method of Moments

Equation (2.21) presents a Fredholm integral equation of the second kind as the unknown $E_z(x, y)$ is inside and outside the integral. In this section, the Method of Moments (MoM) is introduced. It is a numerical technique used to convert an integral equation into a linear system that can be solved numerically [52–54]. Consider the general problem:

$$\mathcal{L}(f) = g \quad (2.24)$$

where \mathcal{L} is a linear operator, which is equal to $\mathcal{L} = \mathcal{I} - \mathcal{L}'$, with the identity \mathcal{I} . The function g is a known excitation source, also called forcing function, here the incident field, which corresponds to $E_z^{(i)}$. The unknown function f is the total electric field E_z .

$$\mathcal{L}' = \iint_{\mathcal{D}_2} (k_2^2(\mathbf{r}') - k_1^2) G(\mathbf{r}, \mathbf{r}') d\mathbf{r}' \quad (2.25)$$

$$\mathcal{L}(E_z) = E_z^{(i)}. \quad (2.26)$$

f is now expanded into a sum of N weighted basis functions,

$$E^N(\mathbf{r}) = \sum_{n=1}^N \alpha_n E_n(\mathbf{r}) \quad (2.27)$$

$$\sum_{n=1}^N \alpha_n \mathcal{L}(E_n(\mathbf{r})) \approx E^{(i)}(\mathbf{r}) \quad (2.28)$$

where α_n are unknown weighting coefficients. An inner product or moment between the basis function E_n and a testing or weighting function g_m is defined as:

$$\sum_{n=1}^N \alpha_n \langle \mathcal{L}(E_n(\mathbf{r})), g_m \rangle = \langle E^{(i)}(\mathbf{r}), g_m \rangle \quad (2.29)$$

$$m = 1, \dots, M.$$

The Dirac function $\delta(\mathbf{r} - \mathbf{r}_m)$ has been chosen as testing function g_m . This method is referred to as point matching or collocation method:

$$\delta(\mathbf{r} - \mathbf{r}_m) = \begin{cases} 1, & \text{if } \mathbf{r} = \mathbf{r}_m \\ 0, & \text{elsewhere.} \end{cases} \quad (2.30)$$

This collocation expresses an exact identity in the points \mathbf{r}_m .

$$\sum_{n=1}^N \alpha_n \mathcal{L}(E_n(\mathbf{r}_m)) = E^{(i)}(\mathbf{r}_m) \quad (2.31)$$

$$m = 1, \dots, M.$$

Furthermore, a set of pulse functions have been chosen as basis functions:

$$E_n(\mathbf{r}) = f_n(\mathbf{r}) \quad (2.32)$$

$$f_n(\mathbf{r}) = \begin{cases} 1, & \text{if } \mathbf{r} \in C_n \\ 0, & \text{if } \mathbf{r} \notin C_n \end{cases} \quad (2.33)$$

$$\alpha_n = E^N(\mathbf{r}_n) = E(\mathbf{r}_n). \quad (2.34)$$

It is assumed that $k_2(\mathbf{r})$ is constant inside one pixel, that means $k_2(\mathbf{r}) = k_2(\mathbf{r}_n)$ if \mathbf{r}_n is in C_n . Furthermore, one can express the integration over the Green's function by indexed elements G_{mn} which gives the following equations:

$$\sum_{n=1}^N \left(\delta_{nm} - (k_2^2(\mathbf{r}_n) - k_1^2) \iint_{C_n} G(\mathbf{r}_m, \mathbf{r}_n) d\mathbf{r}_n \right) E_z(\mathbf{r}_n) = E_z^{(i)}(\mathbf{r}_m) \quad (2.35)$$

$$\sum_{n=1}^N [E_z(\mathbf{r}_n) \delta_{mn} - (k_2^2(\mathbf{r}_n) - k_1^2) E_z(\mathbf{r}_n) G_{mn}] = E_z^{(i)}(\mathbf{r}_m).$$

With $k_0^2 = \omega^2 \varepsilon_0 \mu_0$ (k_0 is the propagation constant in free space) and $k^2 = k_0^2 \tilde{\varepsilon}_r$ one can introduce the contrast C defined in (2.9):

$$\sum_{n=1}^N [\delta_{mn} - k_0^2 C_n G_{mn}] E_n = E_m^{(i)} \text{ with } m = 1, \dots, N. \quad (2.36)$$

Finally, one can derive the matrix equation $\mathbf{A}\mathbf{x} = \mathbf{b}$ with

$$\begin{aligned}
 A_{mn} &= \delta_{mn} - k_0^2 C_n G_{mn} \\
 x &= E_n \\
 \mathbf{b} &= \begin{bmatrix} E_1^{(i)} \\ \vdots \\ E_N^{(i)} \end{bmatrix} \\
 \mathbf{A} &= \mathbf{I} - \mathbf{G}\mathbf{C} \text{ with } G = k_0^2 G_{mn} \\
 \mathbf{A} &= \begin{bmatrix} 1 - k_0^2 G_{11} C_1 & -k_0^2 G_{12} C_2 & \cdots & \\ -k_0^2 G_{21} C_1 & 1 - k_0^2 G_{22} C_2 & & \\ -k_0^2 G_{31} C_1 & \ddots & & \\ & & & 1 - k_0^2 G_{NN} C_N \end{bmatrix}. \quad (2.37)
 \end{aligned}$$

With the derived matrix equation one can calculate the total electric field inside the section with an operator which acts on an internal field to produce an internal field:

$$\mathbf{G}^{\text{O}} = k_0^2 G_{mn}^{\text{O}}. \quad (2.38)$$

This is called the coupling equation and gives \mathbf{E} . Then, the scattered field outside the section, captured by receivers in the background \mathcal{D}_1 , is calculated with $\mathbf{G}^{\text{R}}\mathbf{C}\mathbf{E} = \mathbf{E}^{(\text{s})}$. This equation is called the observation equation. The operator \mathbf{G}^{R} is defined as followed with respect to $r_k(x_k, y_k)$ (see Fig. 2.3):

$$\mathbf{G}^{\text{R}} = k_0^2 G_{kn}^{\text{R}}. \quad (2.39)$$

Integral over the Green's Functions

The integral over the Green's function of \mathbb{R}^2 space is generally defined as:

$$\begin{aligned}
 G_{mn} &= \int_{C_n} G(\mathbf{r}_m - \mathbf{r}_n) d\mathbf{r}_n \\
 &= -\frac{j}{4} \int_{C_n} H_0^{(2)}(k|\mathbf{r}_m - \mathbf{r}_n|) d\mathbf{r}_n \quad (2.40)
 \end{aligned}$$

with $H_0^{(2)}$ the Hankel function of the second kind. Here, $G(\mathbf{r}_m - \mathbf{r}_n)$ is the 2D free-space Green's function. Equation (2.40) has been calculated numerically on one hand. On the other hand, an approximation is presented, based on the common standard approach [55]. For the case of receivers, located in the far-field of the scatterer, a far-field approximation of the object-receiver integral has been developed.

Numerical Integration The object-object (G_{mn}) and object-receiver (G_{kn}) integrals over the Green's function can be calculated numerically. For the object-object case, one can distinguish the self element case ($m = n$) from the

general case ($m \neq n$). Indeed, self elements represent a singularity since $\mathbf{r}_m = \mathbf{r}_n$ (see Fig. 2.3) but this singularity is integrable.

$$\begin{aligned} G_{nn} &= \int_{C_n} G(x', y') dx' dy' \\ &= -\frac{j}{4} \int_{-\frac{\Delta}{2}}^{+\frac{\Delta}{2}} \int_{-\frac{\Delta}{2}}^{+\frac{\Delta}{2}} H_0^{(2)}(k_1 \sqrt{x'^2 + y'^2}) dx' dy' \end{aligned} \quad (2.41)$$

$$\begin{aligned} G_{mn} &= \int_{C_n} G(x_m - x', y_m - y') dx' dy' \\ &= -\frac{j}{4} \int_{x_n - \frac{\Delta}{2}}^{x_n + \frac{\Delta}{2}} \int_{y_n - \frac{\Delta}{2}}^{y_n + \frac{\Delta}{2}} H_0^{(2)}(k_1 \sqrt{(x_m - x')^2 + (y_m - y')^2}) dx' dy' \end{aligned} \quad (2.42)$$

$$\begin{aligned} G_{kn} &= \int_{C_n} G(x_k - x', y_k - y') dx' dy' \\ &= -\frac{j}{4} \int_{x_n - \frac{\Delta}{2}}^{x_n + \frac{\Delta}{2}} \int_{y_n - \frac{\Delta}{2}}^{y_n + \frac{\Delta}{2}} H_0^{(2)}(k_1 \sqrt{(x_k - x')^2 + (y_k - y')^2}) dx' dy'. \end{aligned} \quad (2.43)$$

Standard Approach This approach is based on [55, 56]. For the object–object integral over the Green’s function with $\mathbf{r}_m = \mathbf{r}_n$ one can write:

$$\underbrace{G_{mm}}_{\text{“self term”}} = -\frac{j\pi}{2} \frac{1}{k_1^2} \left[Rk_1 H_1^{(2)}(Rk_1) - \frac{2j}{\pi} \right]. \quad (2.44)$$

For the object–object or object–receiver integral respectively over the Green’s function with \mathbf{r}_m or $\mathbf{r}_k \neq \mathbf{r}_n$ one can write:

$$G_{mn} = -\frac{j\pi}{2} H_0^{(2)}(k_1 |\mathbf{r}_m - \mathbf{r}_n|) \frac{R}{k_1} J_1(Rk_1) \quad (2.45)$$

$$\text{with } R^2 = \frac{\Delta x \Delta y}{\pi} = \frac{\Delta^2}{\pi}. \quad (2.46)$$

The demonstration for (2.44) and (2.45) is shown in Appendix A.

Chosen Approximation Special care is taken for the calculation of the matrix self-elements [57, 58]. Following the standard approach, instead of integrating the singular Green’s function over a square cell, we use a circular disk of equal area. However, this integration has been performed in an exact way: it is easy to show that, for a polynomial of order three, the integral over the equivalent disk has to be corrected by a factor of $3/\pi$. One can further show that the integrands involved in the self-elements are polynomials of order three for ordinary cell sizes. For the object–object integral over the Green’s function with $\mathbf{r}_m = \mathbf{r}_n$ one can write:

$$\underbrace{G_{mm}}_{\text{“self term”}} = -\frac{3j\pi}{\pi} \frac{1}{2} \frac{1}{k_1^2} \left[Rk_1 H_1^{(2)}(Rk_1) - \frac{2j}{\pi} \right]. \quad (2.47)$$

For the object–object or object–receiver integral respectively over the Green’s function with \mathbf{r}_m or $\mathbf{r}_k \neq \mathbf{r}_n$ one can write:

$$G_{mn} = -\frac{3}{\pi} \frac{j\pi}{2} H_0^{(2)}(k_1 |\mathbf{r}_m - \mathbf{r}_n|) \frac{R}{k_1} J_1(Rk_1) \quad (2.48)$$

$$\text{with } R^2 = \frac{\Delta x \Delta y}{3}. \quad (2.49)$$

Far-Field Approximation The general case has already been shown and is presented in order to define clearly the coordinates.

$$E_z^s = \iint_{\mathcal{D}_2} G(\mathbf{r} - \mathbf{r}') C(\mathbf{r}') E_z(\mathbf{r}') d\mathbf{r}'$$

$$\text{with } G(\mathbf{r} - \mathbf{r}') = -\frac{j}{4} H_0^{(2)}(k_1 |\mathbf{r} - \mathbf{r}'|)$$

$$\mathbf{r}(x, y) \text{ and } d\mathbf{r} = dx dy$$

$$\mathbf{r}(r, \phi) \text{ and } d\mathbf{r} = r dr d\phi.$$

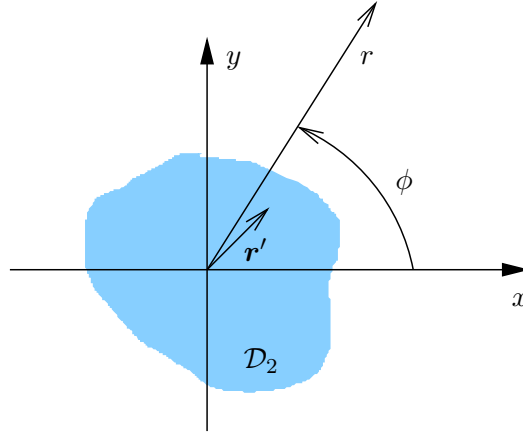


Fig. 2.4: Geometry of the far-field approximation.

$$H_0^{(2)}(k_1 |\mathbf{r} - \mathbf{r}'|) = H_0^{(2)}\left(k_1 \sqrt{r^2 + r'^2 - 2rr' \cos(\phi - \phi')}\right)$$

$$\text{where } H_0^{(2)}(\nu) \rightarrow \sqrt{\frac{2}{\pi\nu}} e^{-j(\nu - \frac{\pi}{4})} \text{ if } \nu \rightarrow \infty.$$

With $kr \gg 1$ and Taylor series [59], one can develop the Green’s function object–object:

$$G(\mathbf{r} - \mathbf{r}') \approx -\frac{j}{4} \sqrt{\frac{2}{\pi k_1 r}} e^{-j(k_1 r - \frac{\pi}{4})} e^{j k_1 (x' \cos(\phi) + y' \sin(\phi))}.$$

In the far-field, for $r \rightarrow \infty$, the scattered fields can be expressed by:

$$E_z^{(s)}(r, \phi) \approx \frac{e^{-jk_1 r}}{\sqrt{r}} F(\phi) \quad (2.50)$$

where the function $F(\phi)$ is called far-field pattern or scattered field pattern. It depends only on the angle ϕ . The radiation diagram and the presentation of $|F(\phi)|$ or $|F(\phi)|^2$ are generally expressed in dB. The center of the cells is taken as reference for the fields, the contrast and the Green's function. Doing so, one can finally obtain the function F :

$$F(\phi) = \sum_{n=1}^N E_n C_n \text{sinc} \left(k_1 \frac{\Delta x}{2} \cos(\phi) \right) \text{sinc} \left(k_1 \frac{\Delta y}{2} \sin(\phi) \right) \underbrace{\left(-\frac{j}{4} \sqrt{\frac{2}{\pi k_1}} e^{j\frac{\pi}{4}} \right) e^{jk_1(x_i \cos \phi + y_i \sin \phi)} \Delta x \Delta y}_{G} \quad (2.51)$$

2.2.2 Analytic Solution

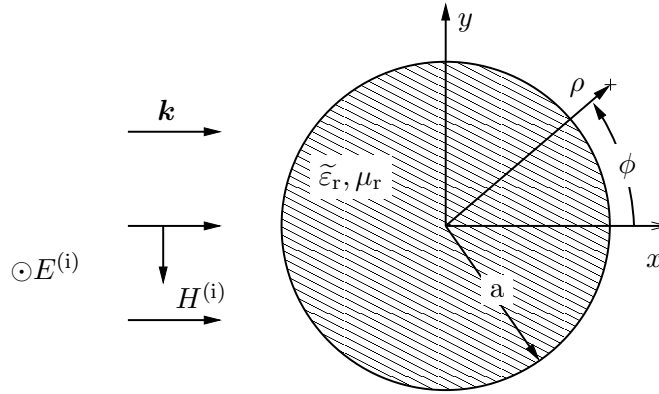


Fig. 2.5: Uniform plane wave incident on a conducting or dielectric circular cylinder.

With the described methods one can simulate the scattered fields of complex non-symmetric permittivity profiles. For certain electromagnetic scattering problems, one can obtain analytical solutions. In the cylindrical coordinates, the solutions are expressed in the series form of the products of Bessel and exponential functions. It serves to verify the implementations of the so far presented numerical methods to solve Maxwell equations in 2D. By comparison with the analytic solution, investigations have been done for simulations of different discretization. The size of the squared cells determines mainly the approximation of the contour of the targets of interest. Additionally, the discretization by itself introduces, due to a limited precision of the used machine, numerical noise. These effects have not

to be taken into consideration, at least much less significantly, by calculating the analytic solution. The solutions to these problems are explained in detail in [60]. The analytic solution is developed for the following cases:

- normal incidence plane wave scattering by conducting and dielectric circular cylinders,
- line source scattering by conducting and dielectric circular cylinders.

Here only the case of a plane wave scattered by a conducting cylinder and a dielectric cylinder is briefly introduced as it is used for comparison with the numerical simulations. The geometry is shown in Fig. 2.5 where a uniform plane wave is normally incident upon a circular cylinder of radius a . The Balanis' formula (e.g., chapter 11 in [60]) has been modified to take into account the complex permittivity $\tilde{\epsilon}_r$ of a lossy homogeneous dielectric cylinder. The scattered fields can be written as:

$$E_z^{(s)}(\rho, \phi) = E_0 \sum_{n=-\infty}^{+\infty} \alpha_n H_n^{(2)}(\beta_0 \rho) e^{jn\phi} \quad (2.52)$$

$$\alpha_n = j^{-n} \frac{J_n'(\beta_0 a) J_n(\tilde{\beta}_1 a) - \sqrt{\frac{\tilde{\epsilon}_r}{\mu_r}} J_n(\beta_0 a) J_n'(\tilde{\beta}_1 a)}{\sqrt{\frac{\tilde{\epsilon}_r}{\mu_r}} J_n'(\tilde{\beta}_1 a) H_n^{(2)}(\beta_0 a) - J_n(\tilde{\beta}_1 a) H_n^{(2)'}(\beta_0 a)}$$

with $\tilde{\beta}_1 = \omega \sqrt{\mu_r \tilde{\epsilon}_r}$
 $\mu_r = 1.$

2.2.3 Description of the Means of Simulation

Flexible Method of Moments Code (FLEXIMOM)

The first developed code is based on the Method of Moments. In its current form, this is a 2D-TM MoM, with a regular square mesh, pulse basis functions and point-matching. We have derived analytical expressions for the matrix elements (see Subsection 2.2.1) and have compared these formulas with the results of numerical integration, with no significant difference – except of course the computation time (see Tab. B.2). More detailed results are shown in the Annex B.3. The code, called FLEXIMOM, is written in FORTRAN 95/2003 [61]. Its architecture has been designed for flexibility, allowing easy maintenance and extension. The addition of features—e.g., various basis/test functions, mesh types, problem types (2D-TE, 3D), etc.—demands minor modifications of the code. We use UNDERSTAND [62], a static analysis tool, and LATTIX [63], an architecture analysis tool, to analyze and monitor the source code during development. The objectives are: the code structure must be divided into modules, possible since Fortran 95/2003, which gives the possibility for a future parallelization of the code. The applications of interest, the software has to be able to handle, are image reconstruction and detection through the wall on one hand. The so far presented theory of the direct problem solver is used to

calculate the scattered field for each iteration of an inverse problem algorithm presented in Section 2.4. The direct problem has been developed and implemented in collaboration with another Ph.D. student at the LEAT (A. Moynot) who added the inverse problem algorithm in FLEXIMOM. On the other hand, investigations should be done in the calculation of the RCS. The implemented version of FLEXIMOM answers already to the requested independence of the studied geometry (flexible meshing), the ability to provide multi frequency results and the flexible location of receivers: one can simulate the scattered fields on an equispaced line, on a circle around the scatterers or anywhere in the space as the receiver locations can be addressed by x - and y -coordinates. In the following, a short overview of the ac-

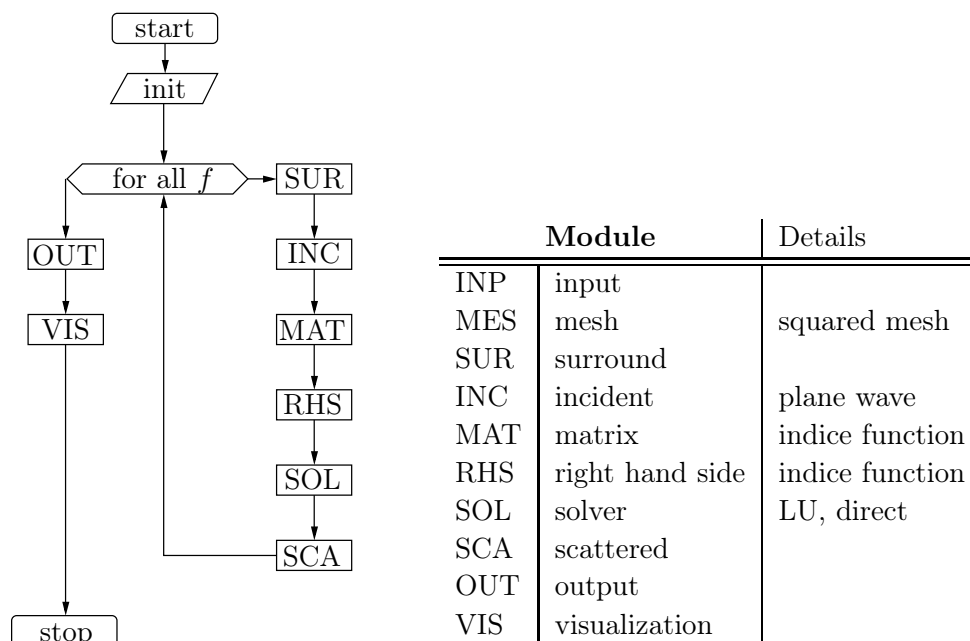


Fig. 2.6: Task-manager used by FLEXIMOM.

tual code structure of FLEXIMOM is given (see Fig. 2.6), and some perspectives, as it is supposed to be continuously upgraded in the future. The task-manager allocates all for the calculation needed matrices and calls the modules depending on the simulation problem of interest. Other task-managers can easily make use of the independent modules. In the module surround “SUR” the background \mathcal{D}_1 can be characterized with its complex permittivity $\tilde{\epsilon}_{r_1}$. In “MES” the meshing is done. So far a squared mesh is provided but other types are foreseen (triangular patches for example). In “INC” the incident fields are calculated in each pixel, so far plane waves have been considered (line sources, plane wave spectrum, spherical wave, spherical harmonics are supposably later). In the matrix module “MAT”, the “heart” of FLEXIMOM, all required matrices are calculated, namely the identity matrix, contrast matrix, Green’s matrix object–object and Green’s matrix object–receiver with the already presented numerical integration, the chosen approach and the far-field approximation. The solver “SOL” inverses directly the matrix \mathbf{A} with

a LU decomposition [64]. Iterative methods can be used in the future to speed up the calculation. A graphical visualization of the results after finishing the execution is provided by the visualization module with PLPLOT [65]. With FLEXIMOM the scattered field of a metallic circular cylinder has been simulated with the chosen approximation (2.48) and with the far-field approximation (2.50). The chosen parameters for the simulation are summarized in Tab. 2.1. The amplitudes of the simulated scattered fields are compared in Fig. 2.7. One can see that the simulation with the far-field approximation agrees perfectly with the simulation with the chosen approximation. Minor differences can be observed in the forward-scattered direction.

Frequency	f	1.0	GHz
Object: circular cylinder	radius	$0.45 = 1.5\lambda_0$	m
	position	$x = 0; y = 0; z = 0$	m
	ϵ_r	1.0	
	σ	100	MS/m
Domain of simulation	domain	$x = -1.5 \cdots 1.5$	m
		$y = -1.5 \cdots 1.5$	m
	Δx	$0.03 (\lambda_0/10)$	m
	Δy	$0.03 (\lambda_0/10)$	m
Receiver position on a circle	radius	$6.0 = 20\lambda_0$	m
	$\Delta\phi$	2.0	degrees

Tab. 2.1: Parameters of simulation to compare the scattered field for simulated, with the chosen approximation and with the far-field approximation, results.

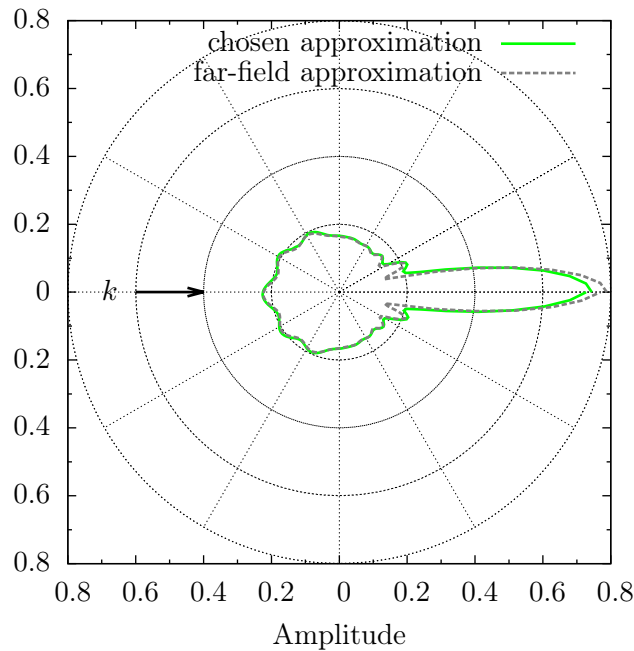


Fig. 2.7: Amplitude of the scattered field at points of receivers. Simulation of the scattered field with the chosen approximation (2.48) and with the far-field approximation (2.50).

Electromagnetic SCattering AnaLytic code (ESCALE)

The second code, ESCALE, is a set of GNU OCTAVE [66] scripts that provides a versatile interface to analytic solutions of scattering problems. It has been developed and implemented by a researcher at the LEAT (I. Aliferis).

In its current version, ESCALE calculates the electric scattered field by a Perfect Electric Conductor PEC or dielectric cylinder (ideal or with ohmic losses) under plane-wave or line-source illumination, based on analytic (closed-form) expressions as partly presented in Subsection 2.2.2. The infinite series are calculated term by term, till convergence to the numerical precision of the machine is achieved. More problem types will be added in the future.

Comparison with Numerical Results

As a preliminary step to the following chapter on measurements, we present here a comparison between numerical results obtained with the MoM and the analytic solution in the case of plane-wave scattering by two PEC cylinders and a dielectric cylinder at 92.5 GHz, the center frequency of the W-band. For simulations with FLEXIMOM, the area of the object of interest has to be discretized. The choice of the discretization is a trade off between calculation time and approach to the exact solution. As high the area of simulation is discretized, the longer the simulation takes

due to increasing number of elements of all mentioned matrices. The area which has to be taken into account for the simulation depends on the object of interest and limits therefore the minimal possible discretization. This has to be mentioned as the proposed direct problem is used in the later explained quantitative imaging process. The scattered field has been calculated on a circle, equispaced with $\Delta\phi = 0.2^\circ$, in a distance of 300 mm. The two conducting cylinders examined here, $D = 20$ mm, discretized at $\lambda_0/10$, see Fig. 2.8, and $D = 8$ mm, discretized at $\lambda_0/40$, presented in Fig. 2.9, correspond to the ones used in the experiments. Also a dielectric cylinder, $D = 15$ mm, discretized at $\lambda_0/\sqrt{\varepsilon_r}13.7$, see Fig. 2.10, is investigated. This cylinder has been characterized in the simulation with an $\varepsilon_r = 2.5$ and without losses which corresponds to acrylic as material. The cross-section of the dielectric cylinder has to be divided into sufficiently small cells so that the dielectric constant and the electric field intensity are essentially constant over each cell. For accurate results, the edge dimensions of each cell should not exceed $\lambda_0/(5\sqrt{\varepsilon_r})$ [55]. This is largely fulfilled with the chosen discretization for all three cylinders. For the simulations with FLEXIMOM the chosen approximation presented in Subsection 2.2.1 has been used.

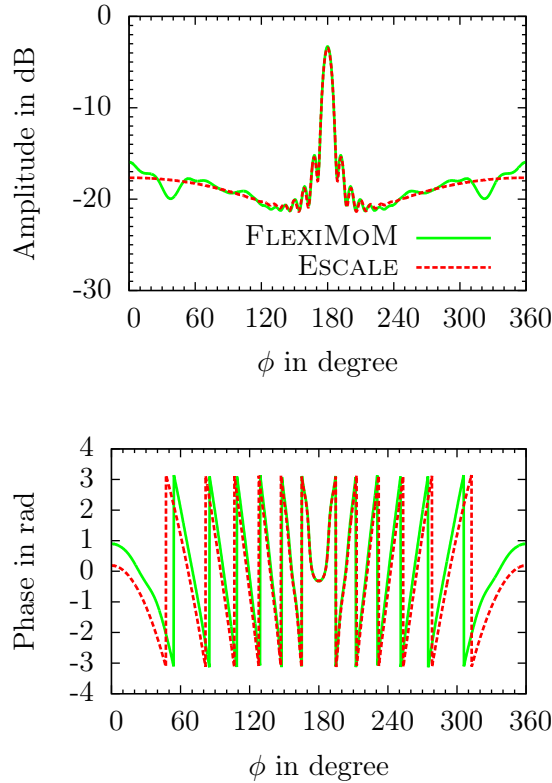


Fig. 2.8: Simulated scattered field of large cylinder, $D = 20$ mm ($\sim 6\lambda_0$), in amplitude (top) and phase (bottom).

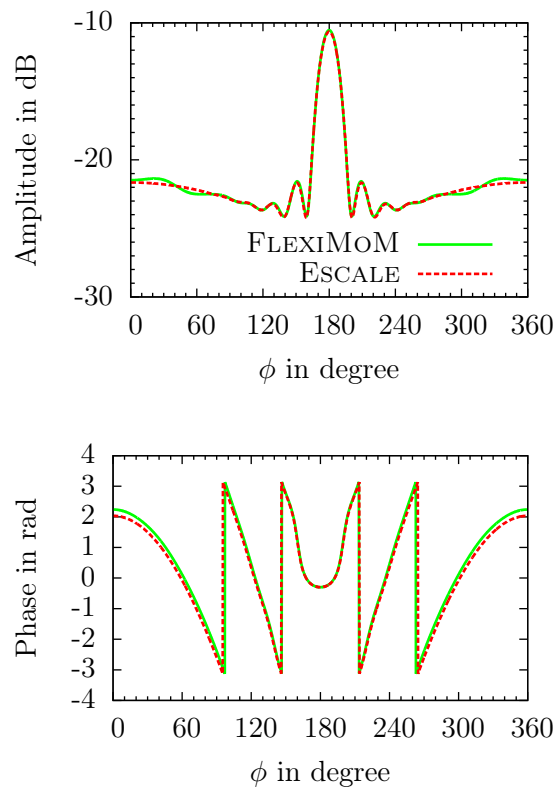


Fig. 2.9: Simulated scattered field of small cylinder, $D = 8 \text{ mm}$ ($\sim 2.5\lambda_0$), in amplitude (top) and phase (bottom).

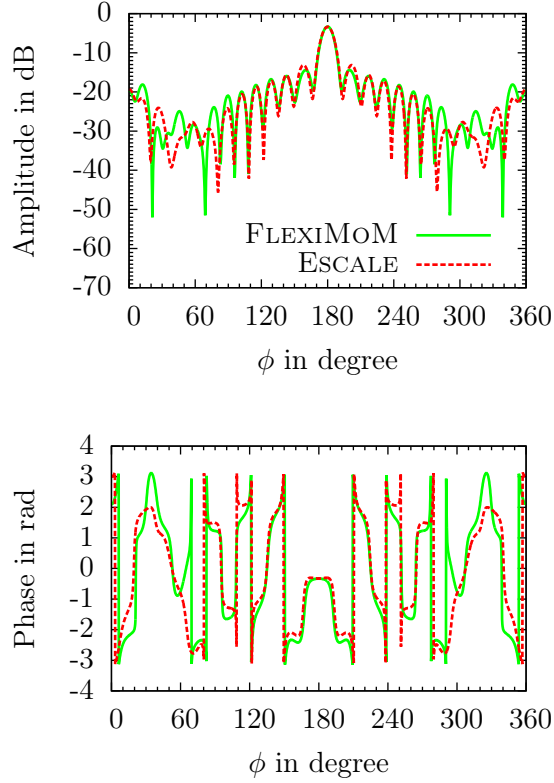


Fig. 2.10: Simulated scattered field of dielectric cylinder, $D = 15 \text{ mm}$ ($\sim 4.5\lambda_0$), in amplitude (top) and phase (bottom).

As seen in the results, FLEXIMOM fits well ESCALE, especially in the case of the small cylinder which is discretized at a higher precision. Some discrepancies in amplitude and in phase are present in the back-scattered region, due to the approximate (staircase) description of the cylinder's contour. This becomes more critical there for the comparison in phase of the dielectric cylinder.

Definition of the Signal-to-Noise Ratio

Before going further, the differences between the exact solution and the numerical simulation should be discussed more in detail. This difference can be estimated by using the same equation as for calculating the Signal-to-Noise Ratio (SNR) [67] based on the error e :

$$e = \frac{\langle E_{\text{sim.}}^{(s)} - E_{\text{exact}}^{(s)}, E_{\text{sim.}}^{(s)} - E_{\text{exact}}^{(s)} \rangle}{\langle E_{\text{exact}}^{(s)}, E_{\text{exact}}^{(s)} \rangle} \quad (2.53)$$

$$\text{SNR} \Big|_{\text{dB}} = -10 \log(e). \quad (2.54)$$

The reference signal is the analytic solution $E_{\text{exact}}^{(s)}$ from ESCALE. The error between the analytic solution and the numerical solution is the numerical noise introduced by the latter one. This difference depends on several choices made for the simulation, namely the size of the area taken into consideration for the simulation and the size of the cells (Δ). The discretization, that means the cell size, influences mainly the “error” of the numerical approach and results in a limited SNR. In the following, the SNR has been calculated for the three cylinders presented in this chapter and summarized in Tab. 2.2. The angular range $\phi \in [30 \cdots 330]$ has been taken into consideration in order to be in conditions imposed by the measurement system presented in Chapter 3.

	Δ	SNR in dB		
		75 GHz	92.5 GHz	110 GHz
Metallic cylinder				
$D = 20$ mm	$\lambda_{0,\text{min}}/9.1$	8.36	6.49 (Fig. 2.8)	5.03
$D = 8$ mm	$\lambda_{0,\text{min}}/34.1$	20.73	18.81 (Fig. 2.9)	17.23
	$\lambda_{0,\text{min}}/9.1$	8.65	6.83	5.36
Dielectric cylinder				
$D = 15$ mm	$\lambda_{0,\text{min}}/\sqrt{2.5}11.5$	7.78	13.88 (Fig. 2.10)	8.50

Tab. 2.2: SNR for 1501 points of the numerical simulation with FLEXIMOM.

One can see that the SNR depends mainly on the chosen discretization Δ . For the metal targets, the results show that the SNR decreases when the frequency increases for a constant discretization. This is not the case for the dielectric cylinder. The best SNR occurs at the center frequency but is worse for the lowest/highest frequency (7.78 dB/8.50 dB). In the future, further investigations are going to be done in studying the SNR for different dielectric targets as function of the pixel size Δ in the W-band.

2.3 Qualitative Imaging - Localization and Shaping

The term of qualitative imaging refers more or less to the representation of a parameter which cannot be related in a simple manner or quantitatively to a physical one or which is a non linear function of several physical parameters (as the electric current distribution inside the scatterer) but depends on the scatterer. Despite of this, the mapping of variations of the parameter can be of practical interest [43]. The localization and shaping of the targets is investigated and explained in detail in the following. This is done with the back-propagation of the scattered fields. Two cases have been studied: on one hand back-propagation of scattered fields in combination with incident plane wave sources as primary sources has been done. This is related to a circular configuration of several receivers pointed to the target of interest. On the other hand back-propagation is applied with scattered fields and the incident fields of only two emitters which act in the same time as receivers. Therefore, the primary source is assumed to be a line source.

2.3.1 Back-propagation - Monochromatic Approach

The scattered field $\mathbf{E}^{(s)}$ can be calculated with the matrix equation as shown in Section 2.2.1:

$$\mathbf{E}^{(s)} = \mathbf{G}^R \mathbf{C} \mathbf{E} \quad (2.55)$$

where \mathbf{G}^R is the matrix of the Green's function object-receiver, \mathbf{C} presents the contrast and \mathbf{E} the total fields inside the section.

The goal is to recalculate $\mathbf{C} \mathbf{E}$, also called the contrast source, based on simulated or measured scattered fields $\mathbf{E}^{(s)}$. One could think about $(\mathbf{G}^R)^{-1} \mathbf{E}^{(s)} = \mathbf{C} \mathbf{E}$, but the matrix $(\mathbf{G}^R)^{-1}$ cannot be calculated as it is not squared.

That's why in [19] a matrix $\mathbf{G}^{R*} = \overline{\mathbf{G}^{R^t}}$, which is the transposed conjugate of \mathbf{G}^R , has been used as initial guess for an inverse problem algorithm. With this matrix the scattered fields can be back propagated to get a field distribution $S(x, y)$ proportional to the polarization current in the target J_p :

$$\begin{aligned} S(x, y) &= \mathbf{G}^{R*} \mathbf{E}^{(s)} = \mathbf{G}^{R*} \mathbf{G}^R \mathbf{C} \mathbf{E} \\ &\simeq \gamma \mathbf{I} \mathbf{C} \mathbf{E} \end{aligned} \quad (2.56)$$

where $J_p = \mathbf{C} \mathbf{E}$. The matrix multiplication $\mathbf{G}^{R*} \mathbf{G}^R$ gives not exactly the identity matrix. Therefore, $\gamma \in \mathbb{R}$ is introduced as a scaling factor to obtain $\mathbf{G}^{R*} \mathbf{G}^R \simeq \gamma \mathbf{I}$. The elements of the matrix $\mathbf{C} \mathbf{E}$, which was used to simulate the scattered fields of the conducting cylinder of $D = 20$ mm in the Section 2.2.3, are visualized in Fig. 2.12. The results are compared with the image $S(x, y)$ obtained with the back-propagation via the matrix \mathbf{G}^{R*} . The configuration for the back-propagation is shown in Fig. 2.11.

The discrepancies are due to the matrix $\mathbf{G}^{\text{R}*}$ which is not a unitary matrix.

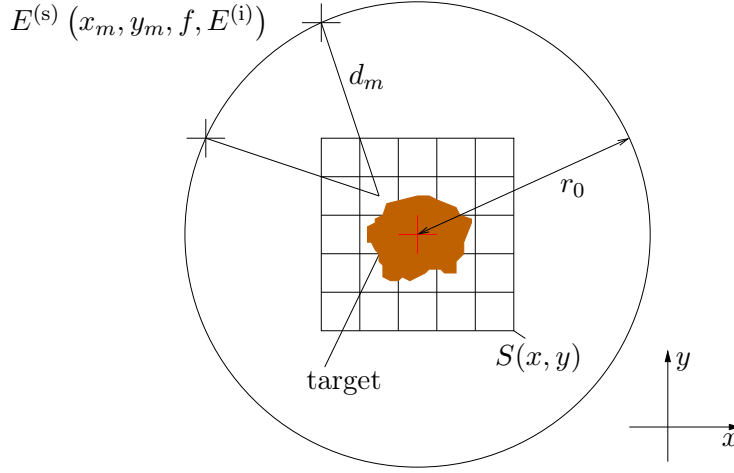


Fig. 2.11: Configuration assumed to back-propagate the scattered fields.

In the following the matrix product $\mathbf{G}^{\text{R}*} \mathbf{E}^{\text{s}}$ is approximated with the following incoherent sum over all receivers $m = 1, \dots, M$:

$$S(x, y) = \frac{1}{F} \frac{1}{L} \frac{1}{M} \sum_{f=1}^F \sum_{l=1}^L \left| \sum_{m=1}^M \sqrt{d_m} E^{(s)}(x_m, y_m, f, E_m^{(i)}) e^{j[\Phi(x, y, x_m, y_m, f)]} \right|. \quad (2.57)$$

The shift in phase $\Phi(x, y, x_m, y_m, f)$ depends on the geometry of the cells and the receiver positions and has to be calculated for each frequency and each emitter respectively. The emitter represents the primary source which can be replaced by the polarization currents in the objects (primary sources are replaced by secondary sources). A configuration with several emitters is taken into account by the incoherent sum in the presented approach. The images obtained for each emitter separately are summed up to retrieve the shape of the object. Therefore, the modules are separately summed up for all emitters $l = 1, \dots, L$ and frequencies $f = 1, \dots, F$. The derived sum is based on the similarity with the far-field approximation presented in 2.2.1. The general configuration is visualized in Fig. 2.11. The scattered field $E^{(s)}(x_m, y_m, f, E^{(i)})$ depends on the coordinates of the receiver and is calculated or simulated for each frequency and each emitter position respectively.

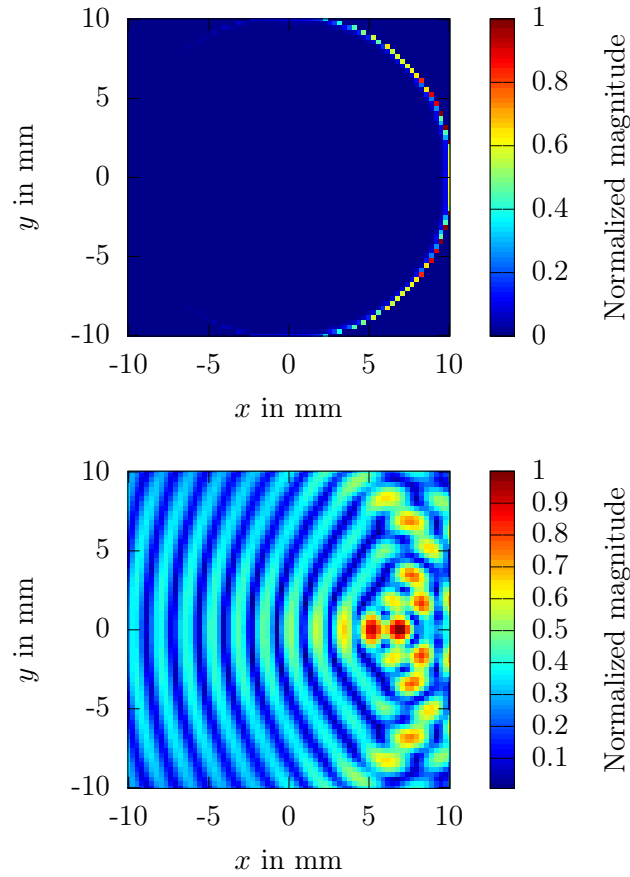


Fig. 2.12: Normalized magnitude of \mathbf{CE} used in the direct problem calculations (top) and the module of the product $S(x, y) = \mathbf{G}^{\mathbf{R}*} \mathbf{E}^{\mathbf{s}}$ after back-propagation (bottom) with $r_0 = 300$ mm.

2.3.2 Back-propagation - Multifrequency Approach

The following approach for qualitative imaging has been successfully used in combination with two stepped frequency radar sensors for close-range imaging for a bandwidth of 1 and 11 GHz [2, 68]. Similar approaches with more emitters and/or receivers have been documented in [69], for a system working at 24 GHz and in [70] for a system operating between 1 and 4 GHz. The mentioned systems work with Frequency-Modulated Continuous Wave (FMCW) or Stepped Frequency Continuous Wave (SFCW) sensors. On the contrary to the so far presented approaches, where several receiving and/or emitting sections are needed, this approximation aims for localization with measurements from only two different positions. The spacing between the antennas determines the area of measurement. For a single target, each antenna receives a mono-static and a bi-static response according to the respective distances. This leads to three independent sets of data for each target and is represented by two circles around each antenna and one ellipse with the antennas as focal points (Fig. 2.13). Based on this, one can again obtain an image

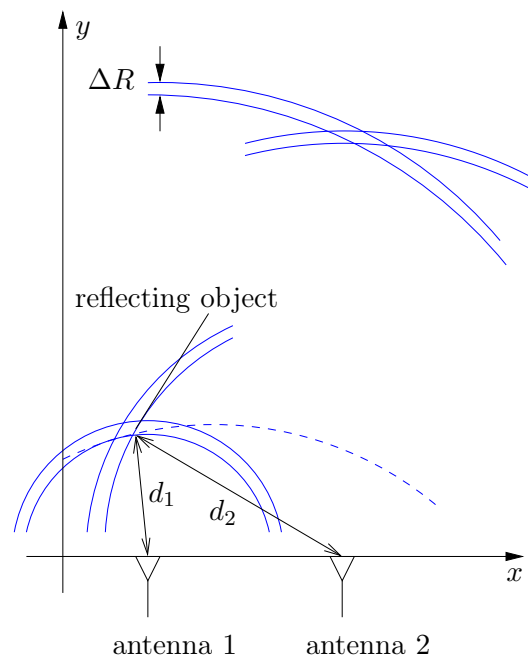


Fig. 2.13: Basic principle for the bi-static configuration.

$S(x, y)$:

$$\begin{aligned}
S(x, y) = & \left(d_1(x, y) \sum_{f=1}^F E_{1f}^{(s)} e^{j 2k_f d_1(x, y)} \right) \\
& \cdot \left(d_2(x, y) \sum_{f=1}^F E_{2f}^{(s)} e^{j 2k_f d_2(x, y)} \right) \\
& \cdot \left(\sqrt{d_1(x, y) d_2(x, y)} \sum_{f=1}^F E_{12f}^{(s)} e^{j k_f (d_1(x, y) + d_2(x, y))} \right) \quad (2.58)
\end{aligned}$$

where $S(x, y)$ is the amplitude from a possible target at the point (x, y) . The distance between one cell of the image and the first or second antenna is indicated with $d_1(x, y)$ and $d_2(x, y)$ respectively. The scattered field $E_{1f}^{(s)}$ is the mono-static response of the first and $E_{2f}^{(s)}$ the mono-static responses of the second antenna. The field $E_{12f}^{(s)}$ corresponds to the bi-static response which is reciprocal to $E_{21f}^{(s)}$. This leads to the circular and elliptical locus curves shown in Fig. 2.13. In the far-field of the antennas, one can suppose a two dimensional arrangement with an amplitude dependency of $1/\sqrt{r}$ (see (2.50)). That's why the range-dependent amplitude correction is done with the factor $d_1(x, y)$ and $d_2(x, y)$. Again, a summation over all frequencies for $f = 1, \dots, F$ is done. The longitudinal resolution can be specified as:

$$\Delta R = \frac{c_0}{2\Delta f} \quad (2.59)$$

where Δf corresponds to the frequency bandwidth of operation. The lateral resolution decreases with the distance to the both antennas as the intersections of the circles become larger.

2.4 Quantitative Imaging - Reconstruction of the Complex Permittivity

On the contrary to qualitative imaging, quantitative imaging retrieves a quantitative value of a physical parameter. In the following description, the reconstruction of the complex permittivity $\tilde{\epsilon}_r$ is investigated.

The following results have been obtained in collaboration with a Ph.D. student at the LEAT (A. Moynot). He is in charge of the development and implementation of the inverse problem. The goal has been to provide measurements which can be successfully used for quantitative imaging. Hereafter, the general principles of the used algorithm are briefly concluded.

2.4.1 Description of the Inversion Algorithm

The inverse scattering problem of reconstructing the complex permittivity profile of 2D or 3D metallic or dielectric objects is a well-known ill-posed and nonlinear problem, i.e. in the sense of Hadamard [71]. The existence, uniqueness and stability of the solution are not simultaneously ensured. Starting from an integral representation of the electric field (EFIE), as explained in detail in Section 2.2.3, an iterative algorithm has been developed based on a bi-conjugate gradient method for reconstructing the relative permittivity and conductivity (i.e. complex permittivity profile) of a Target Under Test (TUT). We assume that the two-dimensional object is contained in a bounded domain \mathcal{D}_1 (see Fig. 2.2) and irradiated successively by L different known incident fields. For each excitation $l = 1, \dots, L$, the scattered fields are measured by a set of receivers. Starting from the domain integral equation for the total fields inside \mathcal{D}_2 and from the integral representation of the scattered fields on the measurement points (2.36), the moment method yields the following nonlinear matrix system:

$$\mathbf{E}_l^{(s)} = \mathbf{G}^R \mathbf{C} (\mathbf{I} - \mathbf{G}^O \mathbf{C})^{-1} \mathbf{E}_l^{(i)} \quad (2.60)$$

where $\mathbf{E}_l^{(s)}$ represents the scattered field vector and $\mathbf{E}_l^{(i)}$ the incident field vector. We consider the real and imaginary part of the contrast \mathbf{C} as independent variables. The solution of the inverse scattering problem is given by minimizing the cost functional $J(\mathbf{C})$ representing the error matching the measured scattered fields $\mathbf{E}_{l,\text{meas.}}^{(s)}$ and the computed one $\mathbf{E}_{l,\text{comp.}}^{(s)}$ for a given contrast \mathbf{C} :

$$J(\mathbf{C}) = \sum_{l=1}^L \left\| \mathbf{E}_{l,\text{meas.}}^{(s)} - \mathbf{E}_{l,\text{comp.}}^{(s)} \right\|^2. \quad (2.61)$$

The inversion algorithm is based on a conjugate gradient method [19] for the real part and the imaginary part of the contrast \mathbf{C} and a Polak-Ribière conjugate

gradient direction. The gradient direction is determined by calculating the Fréchet derivative of the cost functional $J(\mathbf{C})$. The described method can be, in principle, applied to any kind of lossy dielectric objects with near-field as well as far-field data.

In the following, the inverse problem algorithm has been applied to simulated scattered fields. So far, no regularization has been investigated. In this manuscript only the quantitative reconstruction of metallic objects is of interest. For the inversion of scattered fields from dielectric objects a regularization scheme is necessary.

2.4.2 Quantitative Imaging Performance for Metallic Objects

For metallic objects one is not able to reconstruct the correct value of σ , which is in the order of MS/m . This is due to the small difference between the scattered fields from a PEC and a conductor having a finite value of σ . In order to demonstrate this, the scattered fields from the cylinder of 8 mm in diameter in a distance of 300 mm have been simulated with the analytic solution for PEC, on one hand. On the other hand, this has been done as function of σ as presented in Fig.2.14. The highest value for sigma in dielectric, which has been taken into account, is about $72\,300 \text{ S}/\text{m}$. Beyond this value, the Bessel functions give numerical errors. This corresponds to the numerical limit of the used code based on the exact solution and results for higher σ cannot be presented. In order to have an idea of the range of values of sigma that one can retrieve, the variation of the analytical scattered fields with respect to the conductivity from a cylinder corresponding to our configuration has been examined in detail. Using ESCALE, the SNR (2.54) as a function of σ has been calculated, where $E_{\text{sim}}^{(s)}$ is the analytical diffracted field of a finite-conductivity cylinder and $E_{\text{exact}}^{(s)}$ is the analytical diffracted field of a PEC cylinder. The graph of SNR(dB) versus $\log \sigma$, shown in Fig.2.15, is a straight line for $\sigma > 10\,000 \text{ S}/\text{m}$ (23 dB) with a slope of $\approx 10 \text{ dB}/\text{dec}$. The so calculated maximum of the SNR is 40.8 dB. This high value of SNR cannot be expected neither in simulation with FLEXIMOM nor in measurement. One can conclude that it is not possible to reconstruct the correct value of sigma for metallic objects and as consequence one can not predict the type of the metal. For these, the shape can be reconstructed, but the results cannot be used to determine if the target is only a metallic hollow body, a metallic solid body or a dielectric surrounded by metal.

2.4.3 Quantitative Imaging Results

For the inversion, the angular range $\phi \in [30^\circ \dots 330^\circ]$ has been taken into account which corresponds to the one provided by the later presented measurement system. The angular step has been chosen to be $\Delta\phi = 0.4^\circ$ which results in 751 points. The pixel size has been $270 \mu\text{m}$ which is less than a tenth of the wave-length. Results are shown in Fig. 2.16.

Afterwards to the ideal scattered field, an Additive White Gaussian Noise (AWGN)

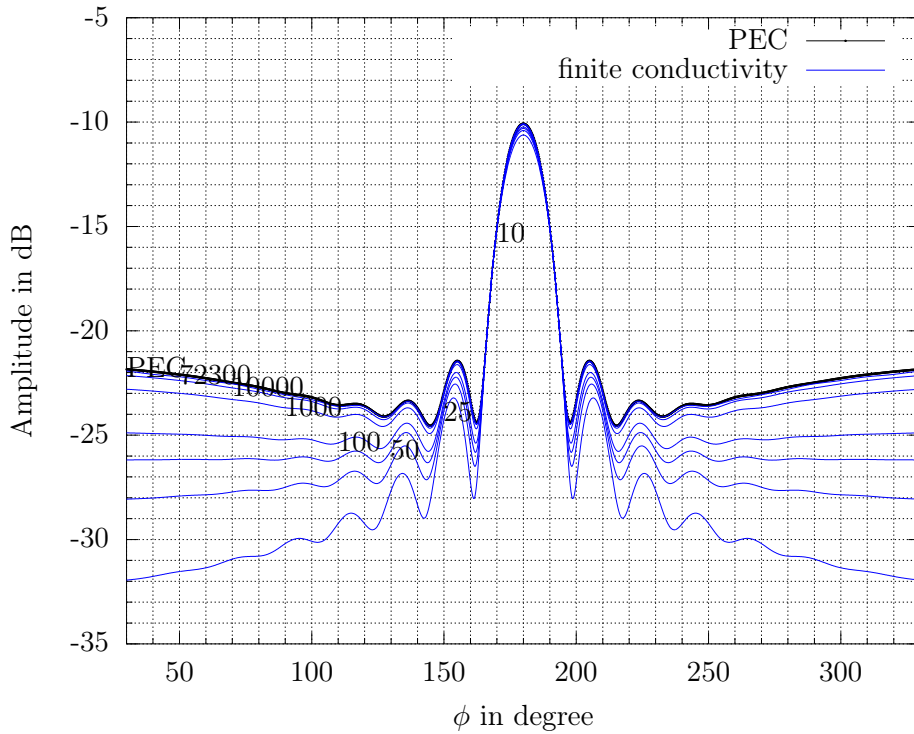


Fig. 2.14: Comparison of scattered fields from PEC and finite sigma conductor for a cylinder of 8 mm in diameter, simulated in a distance of 300 mm for $f = 110$ GHz.

has been added to obtain a SNR of 5 dB. The cost function, shown in Fig. 2.18, is higher for the noised case than for the ideal one. Anyway, the cylinder contour could be perfectly retrieved. Knowing this, one can apply the presented inverse problem algorithm to noised measurements as presented in Chapter 4.2.

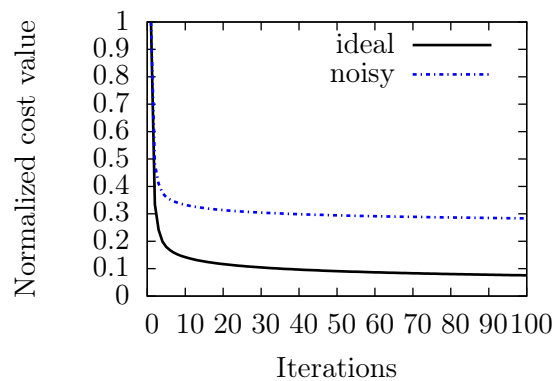


Fig. 2.18: Normalized cost values for each iteration obtained for 92.5 GHz. Scattered fields have been simulated with ESCALE ideal and with a SNR=5 dB.

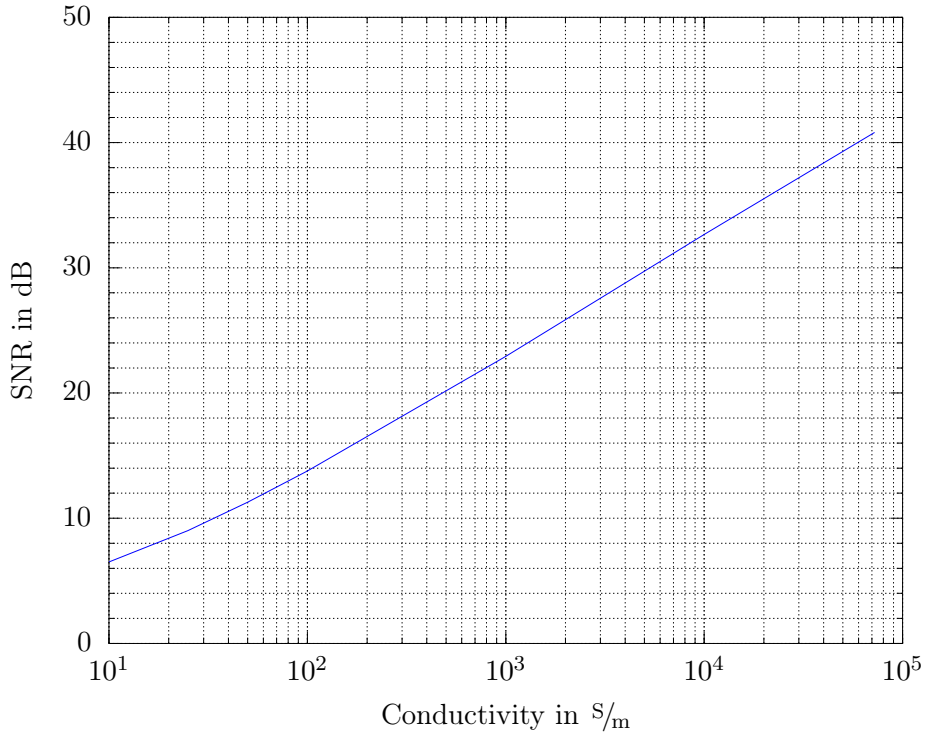


Fig. 2.15: Comparison of scattered field from a cylinder with $D = 8$ mm for a frequency of $f = 110$ GHz: sigma-PEC SNR versus finite sigma.

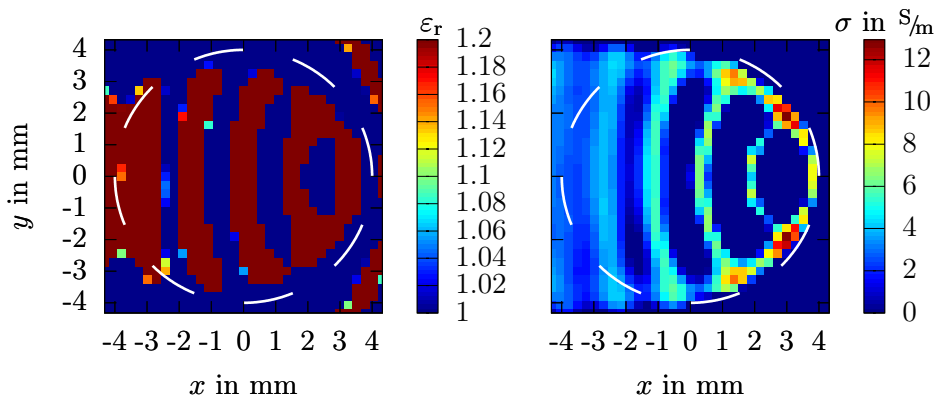


Fig. 2.16: The relative permittivity (left) and the conductivity (right) reconstructed with 100 iterations (751 receivers, 1 emitter, 92.5 GHz, discretization with $0.27 \text{ mm} \approx \lambda_{0,\text{min}}/10$). Scattered field of the cylinder, $D = 8$ mm, has been simulated with ESCALE for a distance of 300 mm.

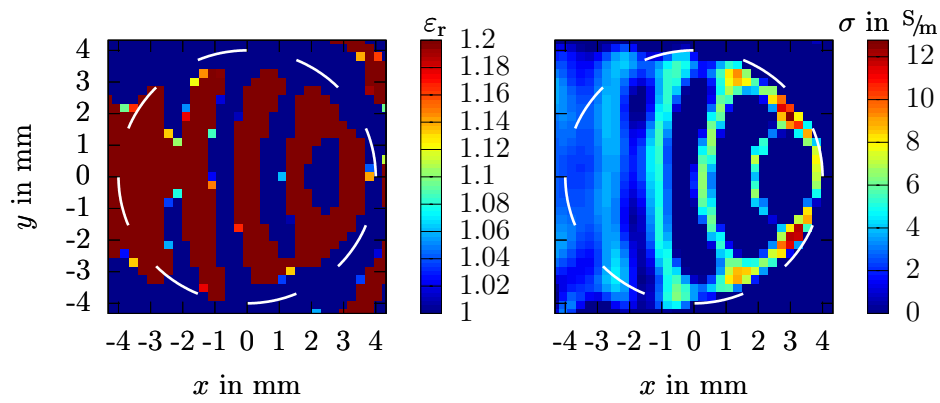


Fig. 2.17: The relative permittivity (left) and the conductivity (right) reconstructed with 100 iterations (751 receivers, 1 emitter, 92.5 GHz, discretization with $0.27 \text{ mm} \approx \lambda_{0,\text{min}}/10$). Scattered field of the cylinder, $D = 8 \text{ mm}$, has been simulated with ESCALE for a distance of 300 mm with a SNR=5 dB.

Scattered Field Measurement System for Imaging with mm-Waves

3.1 Comparison of Existing Systems

In this section a short description of the existing Scattered Field Measurement Systems (SFMS) is given. The references in [72] have been concluded and supplemented. Firstly, measurement facilities providing measurements in one plane are introduced. Secondly, systems operating on a sphere to obtain 3D field measurements are presented. These systems aim to provide accurate measurements to the inverse problem community. Also a last type of systems of an area becoming of increasing interest is going to be mentioned: Compact Antenna Test Ranges (CATR) that provide measurements of the radiation patterns of antennas in the W-band. They could be good candidates to be used as well for scattered field measurements, minor modifications and extensions assumed, as they aim to provide high precision and accuracy.

3.1.1 Two Dimensional Scattered Field Measurement Facilities

The following systems are developed to measure the amplitude of scattered fields to obtain the RCS of targets of interest. The systems described below provide measurements with a bi-static circular configuration:

- The automated swept-angle bi-static scattering measurement system of the ROME LABORATORY, NY, USA, [25] has been installed to obtain reliable measurements on canonical scatterers. The frequency of operation is in the S-, C- and X-bands (2 GHz to 12.4 GHz). Measurements, also known as IPSWICH DATA [73], have been successfully used for inversion and resulted in numerous publications like [17], [19] and [20] to mention only a few. The targets are mounted rotatable in the center of the system and the receive antenna sweeps to collect data as a direct function of the bi-static angle. The step size of the angle is 0.2° and the system is able to measure “on the fly” over an observation sector of 180° . The distance from the target to the aperture of the receive antenna is about 3.0 m and from the target to the emitting antenna is 3.7 m to measure in the far-field zone of the scatterers. Investigations have been done with 15.24 cm dish antennas in an anechoic chamber.

- The anechoic facility “BABI” of the Office National d’Etudes et de Recherche Aérospatiales (Onera), Châtillon, France, [74] provides bi-static RCS values of airborne targets. Measurements are possible in the L-, S-, C-, X- and Ku-bands (1 GHz to 18 GHz). The target is also fixed in the center of rotation where it can be turned on its own axis. Measurements are done over almost 160° in 0.5° steps. The distance between the center and the emitting and receiving modules are 5.5 m respectively. The used antennas are wide-band bi-polarized horn antennas.
- The measurement system “CACTUS”, of the CENTRE D’ETUDES SCIENTIFIQUE ET TECHNIQUES D’AQUITAINE (CESTA), Barp, France, [75] is closed in configuration to “BABI”. Measurements are investigated in stealth technology of military targets. The frequencies of interest are in the S-, C-, X- and Ku-bands (2 GHz to 18 GHz). Measurements can be done over 180° . The distance between the emitting section and the target is 5.6 m. The system is installed in an anechoic chamber.
- The UNIVERSITY OF FLORIDA’S LABORATORY FOR ASTROPHYSICS, FL, USA, [21] implemented a microwave scattering facility to test theoretical solutions to electromagnetic scattering problems of particles. The frequency of operation is in the W-band (75 GHz to 110 GHz). Measurements are provided, with a step size of 0.1° , from 0° to 168° where the latter corresponds to the forward scattering direction. The distance between the antennas and the center of the target is 1.35 m. Full band-width conical horn antennas in combination with Fresnel lenses are used to obtain far-field conditions. Mentionable is the given mechanical and thermal stability of $10 \mu\text{m}$. The facility is located in a chamber dedicated to this type of measurement.
- The INSTITUT FRESNEL, Marseille, France, [24] provides a database to the inverse problem community to test inversion algorithms against experimental data. These are obtained in the S-, C-, X- and Ku-bands (2 GHz to 18 GHz). Measurements in a two-dimensional configuration have been done on a circle from 60° to 300° with a step-size of 1.0° . The source-object center and object center-receiver distances are 1.67 m. The transmitting and receiving antennas are both wide-band ridged horn antennas. In order to provide measured fields in an electromagnetic free space configuration the whole system is installed in an anechoic chamber.

3.1.2 Measurement Systems Providing Three Dimensional Results

- The INSTITUT FRESNEL, Marseille, France, [24] has continued providing new measurement results also of three dimensional targets (see [23]). With the configuration presented in [76] the sources have been moved from -160° to 160° with a step of 40° in the azimuthal direction and from 30° to 160° with a step of 10° in the elevation direction. The receivers are restricted to the

equatorial plane and moving from -180° to 180° , with a step of 5° , and with an exclusion of 50° on both sides of the source meridian.

- The EUROPEAN MICROWAVE SIGNATURE LABORATORY, Ispra, Italy, [77] is a facility to conduct research in performing mono- and bi-static polarimetric radar measurements in a stable, controlled and reproducible way in an anechoic chamber of 20 m in diameter. The basic measurement system can be used in the L-, S-, C-, X-, Ku-, K- and Ka-bands (1 GHz to 40 GHz). The targets are rotatable of 360° . Two radar transmitters/receivers can be moved on a circle around the targets in a distance of 10 m from -115° to 115° with a precision of $\pm 0.005^\circ$.
- The UNIVERSITY OF MICHIGAN, MI, USA, [78] constructed a polarimetric bi-static radar facility to serve as a research tool for improved understanding of the nature of bi-static scattering for point and distributed targets. The system works at 10 GHz, 35 GHz and 94 GHz. The transmitter, a dish antenna, has two degrees of positional freedom, capable of moving in both the elevation plane (over 90°) and the azimuthal one (over 360°). The receiver, a horn antenna, can be positioned in the elevation plane (over 90°). The positional accuracy is given with $\pm 0.1^\circ$. The distances between the center and the aperture of the transmitter and the aperture of the emitter are 2.01 m and 3.26 m, respectively.

3.1.3 Compact Range Antenna Facilities

Systems facing the same challenges in point of view of mechanical limitations due to high frequencies are presented here. The increase in frequency adds additional requirements to the accuracy of the mechanical positioning devices required to move the probe and antenna under test.

- The MI TECHNOLOGIES, GA, USA, [79] has constructed a spherical near-field arch positioner with a 1.5 m radius to support measurements requiring accurate knowledge of the probe phase center within $64 \mu\text{m}$ throughout its range of travel.
- The EUROPEAN SPACE AGENCY, Noordwijk, Netherlands, [80] investigates in modeling the variation of atmospheric variables (humidity, temperature and pressure) on all the elements of a CATR facility used for mm-wave measurements.

3.2 Description of the Measurement System

3.2.1 Introduction of Objectives

A SFMS consists in placing the TUT at the center of one or two motorized circular rails or swivel arms, depending whether 2D or 3D measurements are performed. Horn antennas are generally used as illuminator and receiver. Most of time, installations are fixed in dedicated anechoic chambers as the mentioned examples have shown. The solution proposed in this manuscript is quite different. The SFMS has been developed with four main objectives:

1. being fully compatible with the actual antenna measurement system installed at the LEAT,
2. being low-cost,
3. reducing as much as possible the positioning errors due to the high frequency,
4. measuring 2D objects.

The first condition is very important for users whose anechoic chamber is mainly dedicated to antenna measurements. It implies that the system should be easy to remove. The second condition shall meet the requirement of an inexpensive mechanical extension to the already existing chamber (8.7 m × 4.3 m × 4.0 m) and its measurement devices [81]. The last condition drove our choice toward an overall small size system that is also coherent with the short wavelength value. The original measurement system is used to obtain the radiation pattern of antennas from 820 MHz to 50 GHz and from 75 to 110 GHz. The existing equipment meets all major requirements in already implemented soft- and hard-ware for the later mentioned purposes and has the advantage that interferences from the surroundings are suppressed by pyramidal absorbers (FPY205/310/470) [82]. One has to mention that the results which are presented in the following were obtained during one single series of measurements. This lasted only one week as the anechoic chamber had been booked by other researchers.

3.2.2 Description of Mechanical Modifications

The technical details are summarized in Tab. 3.1 and explained hereafter. In Fig. 3.1 the planned system with its additional installed parts and the following described modifications are shown. The emitting section is separated from the first tower and located in a distance of 400 mm between the antenna and the center of the second tower to ensure that the target is located in the far-field of the emitting antenna. The receiving part, displaced as well from its origin on the second turntower, is located on an additional swivel arm. The distance between the receiver and the center (300 mm) has been chosen to be as small as possible. At 110 GHz the $2D^2/\lambda_0$ far-field requirement limits the maximum target dimension to about 20 mm. Indeed,

the longer the receiver-tower distance, the higher is the torque on the step engine due to the additional weight of the support. This is enforced by longer stretches of the cables during one measurement cycle. One could combine the target and the emitter and turn the receiver separately from the target. In the proposed setup the target is fixed on the arm on the center of the tower and turns together with the receiver unit. This makes sure that the distance between the target and the receiver remains constant. The latter point is less critical, in terms of reproducibility and mechanical installation on the already existing tower. In order to confirm the feasibility of measurements with the chosen distances emitter-target and target-receiver a preliminary study had been investigated with AGILENT'S PNA-X microwave network analyzer in combination with mm-wave modules [83, 84].

Distance emitter - target	r_1	400	mm
Distance target - receiver	r_2	300	mm
Vertical distance target support - antenna	h	200	mm
Measurement zone	ϕ	30.0 : 330.0	degree
Step	$\Delta\phi$	0.2	degree

Tab. 3.1: Chosen parameters and dimensions of the measurement system.

The realized measurement system in the anechoic chamber is shown in Fig. 3.2. Some minor differences can be seen compared to Fig 3.1: the emitting section has been installed as well on the fixed part of the tower. This solution has been preferred because it does not require the removal of absorber material on the floor of the anechoic chamber. In order to prevent resonances from the turntable to the emitter it will be going to be installed independently in the future final installation. One can see that the harmonic mixer (HP 83550) is closed to the emitting antenna. As it is more bulky than the receiving section, it has been chosen to keep it fixed. The compact receiving section is rotating with the swivel arm (see Fig. 3.2).

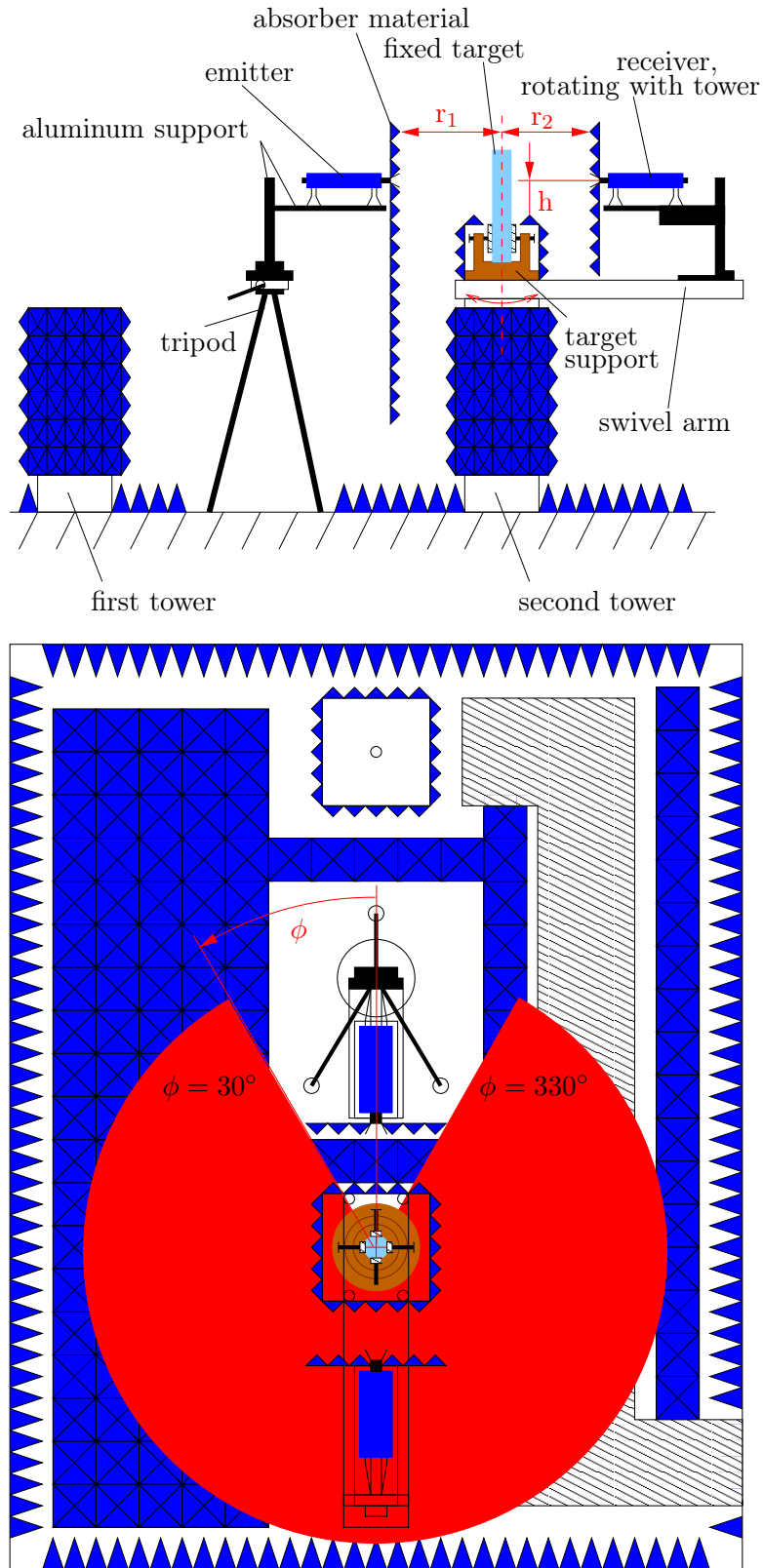


Fig. 3.1: Schematic of the extension setup in the anechoic chamber in side view (top) and top view (bottom). The zone in red indicates where measurements are done for $\phi \in [30^\circ \cdots 330^\circ]$.

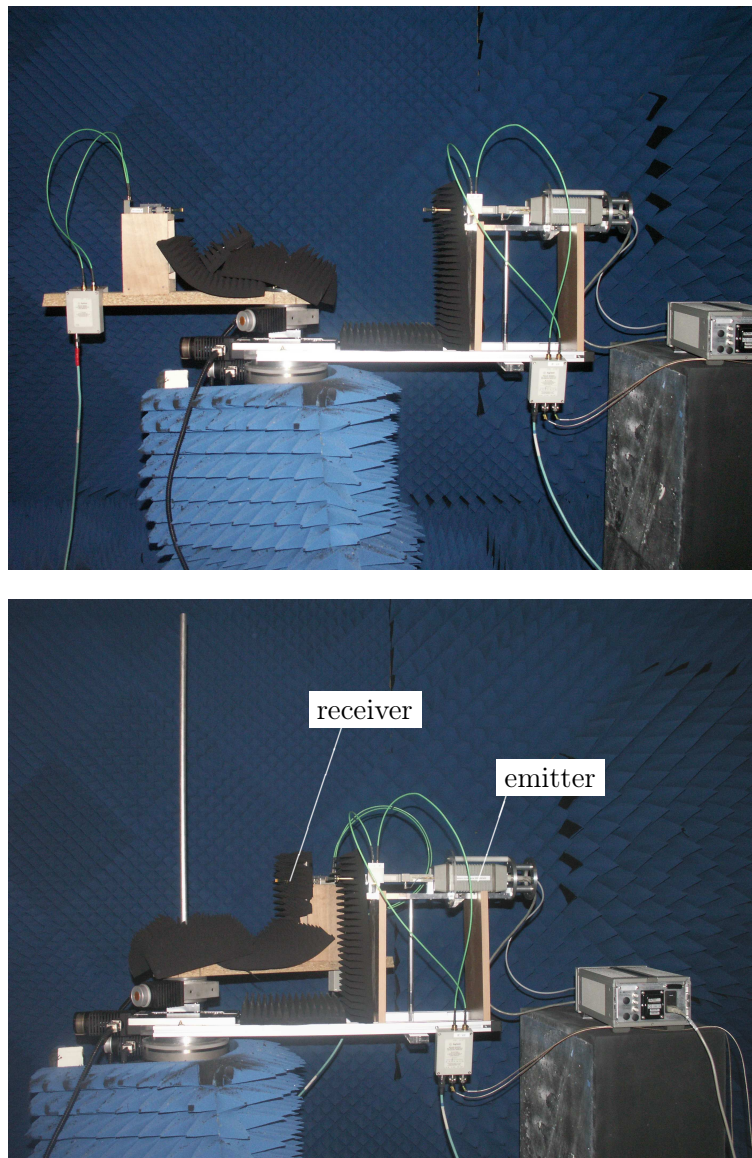


Fig. 3.2: Measurement set-up with receiver at 180° (top) and receiver in stop position at 330° (bottom). Metallic cylinder, $D = 20$ mm, is installed as TUT.

3.2.3 Millimeter-Wave Antenna Measurement System

The already installed equipment, used in general for antenna characterization, should be briefly explained (see Fig. 3.3). The measurements of the transmitting coefficient S_{21} are provided with a receiver (HP/Agilent 8510C) in combination with two external synthesizers (HP/Agilent 83650B and 83621B) and two external mixers (HP/Agilent 11970W).

The mm-wave antenna measurement system consists of transmitter and receiver sections. The transmitter is composed of a synthesized RF source, an amplifier, a mm-wave source module, that multiplies the RF frequency by a factor of six, and a transmit antenna. All these modules provide the transmitted incident field and the reference signal a_1 . The receiving antenna, the frequency converter, the mm-wave mixer modules, that transmit the test signal b_2 , and the receiver (HP/Agilent 8510 C) form the receiving section [81].

3.2.4 Investigated Measurement Area

The possible angular measuring range (ϕ) is between 30° and 330° as the receiver can not cover a whole circle due to the physical existence of the emitter (see Fig. 3.1). The step size of measurements has to be chosen with two main attentions: firstly, resonances are related to acceleration and deceleration of the swivel arm. Therefore, the angular step size has to be taken as small as possible to keep the time of acceleration and deceleration as short as possible as our system cannot measure “on the fly”. In order to overcome mechanical resonance problems, micro-steps are preferred to approach to the points of interest. Secondly, in order to take advantage of the maximum capacity of our rotating tower, the angular step has been chosen as small as possible. By this manner, one has more flexibility for applying post-processing techniques as well as for selecting the proper number of points in the perspective of inversion. This latter will be discussed in Chapter 4. Therefore, the angular step is chosen to 0.2° with a positioning precision of 0.05° that is also the best precision that is reachable with our rotating tower. The precision can be chosen by the controlling software of the rotating tower. The log-files of the measurements confirmed that this precision was reached for all investigated measurements. The chosen angular step results in a point-to-point distance (~ 1.047 mm for $r_2=300$ mm) less than $\lambda_0/2$ at the highest frequency of 110 GHz (1501 points from 30° to 330°). One scan over this area takes about 40 minutes.

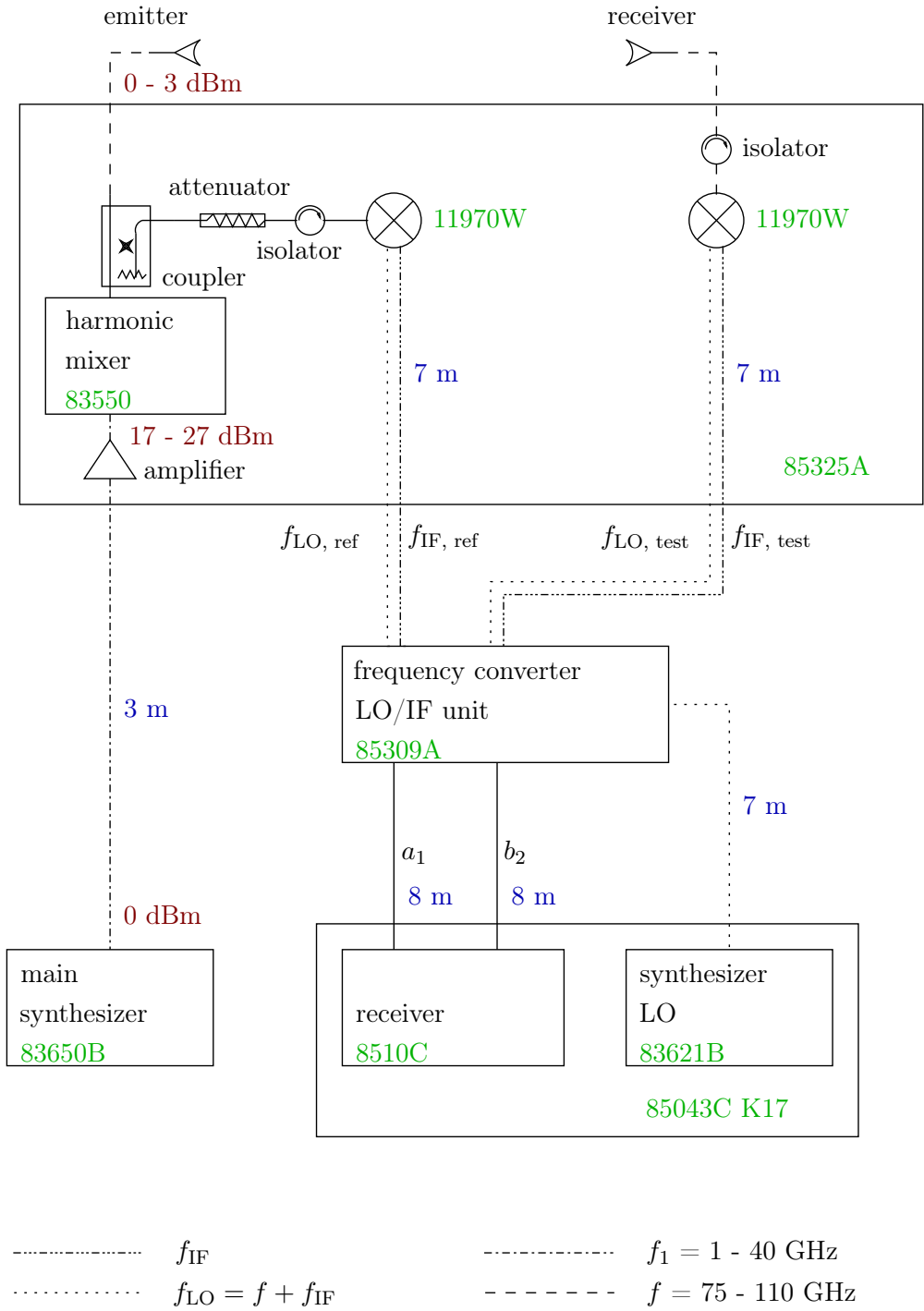


Fig. 3.3: Block diagram of the antenna measurement system.

3.3 Measurement Results

3.3.1 Measurement Parameters

The parameters used for the measurements are summarized in Tab. 3.2. The goal has been to prove the performance of scattered field measurements of TUT in the W-band. Therefore, a frequency in the center of the band of interest has been chosen as well as the two edge frequencies (75 and 110 GHz). Additionally the measurements must be done with a precision which is required to apply successfully the algorithm for quantitative imaging presented in Chapter 2.4.

The length of the measured cylinders is large, at least $125\lambda_0$ ($l = 500$ mm, $f = 75$ GHz), compared to the wavelength in the frequency band of interest to match the 2D-TM case used in the simulation. It also drastically reduces multiple reflections due to strong fields both at the upper corner of the target and the target support (surrounded by absorbers) [85].

Frequencies		f	75.0, 92.5 , 110.0	GHz
1. metal cylinder	diameter	D	20 ($\sim 5 - 7.5\lambda_0$)	mm
	length	l	1000	mm
2. metal cylinder	diameter	D	8 ($\sim 2 - 3\lambda_0$)	mm
	length	l	500	mm
3. dielectric cylinder	diameter	D	15 ($\sim 3.75 - 5.5\lambda_0$)	mm
	length	l	1000	mm

Tab. 3.2: Chosen targets with its dimensions.

3.3.2 First Measurement Results

On Calculation, Simulation and Measurement

In this manuscript, we compare the electric fields obtained by three different means: measurements, the analytic solution (i.e. the exact solution) and the simulation. Before proceeding, some more details on the exact nature of these three types of information are given. The analytic formulas (ESCALE) give the incident electric fields, the total fields and the scattered fields everywhere. On the other hand, the simulation software (FLEXIMOM) assumes plane-wave incidence and provides the incident fields and the total fields inside the computation domain and the scattered fields outside of the computation domain. Thus, comparison between ESCALE and FLEXIMOM for the scattered field is straightforward. However, the situation is more complicated regarding measurements. It is well-known that the electric field is not a physical observable [86]. What we really measure is the transmission S-parameter between the emitter and receiver antennas. In the far-field region, the

Complex Antenna Factor (CAF), [87] is defined as the ratio between the complex electric field incident on the antenna and the complex matched output voltage of the same antenna. In general, the CAF depends both on frequency and on angle of incidence. However, in our special case, the receiver “sees” the scatterer always under the same configuration, thus, the angle of incidence is constant and the CAF is only frequency-dependent. This remark permits us to easily obtain the electric fields from the measurement of the S-parameters. S-parameters can be measured with the receiver in linear magnitude and phase. S_{21} is proportional to the electrical field in the presented system through the effective length on the antennas [88] because we are working in the far-field area. The scattered field is extracted from the subtraction of the total field (the field in the presence of the target, $E_{\text{meas.}}^{(t)}$) and the incident field (the field measured without any target, $E_{\text{meas.}}^{(i)}$):

$$E^{(s)} = E_{\text{meas.}}^{(t)} - E_{\text{meas.}}^{(i)}. \quad (3.1)$$

This requires accurate amplitude and phase measurements. All the results in this manuscript are shown as a function of the measurement angle ϕ (see Fig. 3.1 (bottom)) with $\phi = 180^\circ$ corresponding to the forward scattering direction. As the targets of interest are axially symmetrical, the multi-incidence/single-view measurement configuration can be equivalently considered as a single-incidence/multi-view setup. This second approach is used to obtain simulated (FLEXIMOM) and analytical (ESCALE) data. In the theory described in Section 2.2, electric fields are calculated on independent points in free space, that means the receivers are modeled as ideal isotropic antennas. In an experimental environment this condition can not be fulfilled, as the results are influenced by the superposition of the radiation patterns of emitting and receiving antenna. For this reason the measured incident and total fields cannot be directly compared with numerical simulations. As a result, the amplitude of the incident field in the area close to the emitter (see Fig. 3.1) is below the noise-floor (see Fig. 3.4) for $\phi < 120^\circ$ and $\phi > 240^\circ$ here shown for the configuration with a standard gain horn as receiver and an open-ended waveguide as emitter. This limits the accuracy of the extracted scattered field because only the total field remains in this zone after the vectorial subtraction (see Fig. 3.5 and Fig. 3.6 (top)). Therefore, the total field must have a significant higher level than the measured incident field there, which is the case for the presented results (~ 20 dB above noise). With Fig. 3.4 one can estimate the dynamic of the measurements done with this configuration to 35 dB.

We obtain the measured scattered field after subtraction of the incident field from the total one. In order to compare measured and simulated scattered fields, we first normalize both of them with respect to their maximum amplitude (see Fig. 3.6).

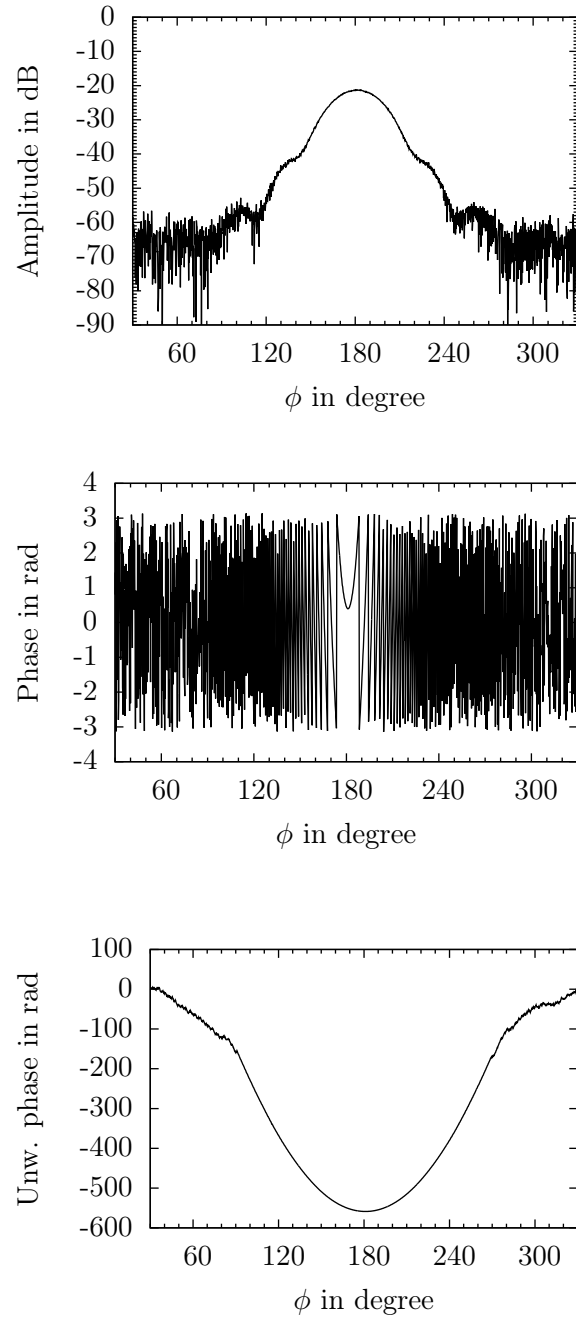


Fig. 3.4: Measured incident field (raw measurements) for $f = 92.5$ GHz in amplitude (top), phase (middle) and unwrapped phase (bottom).

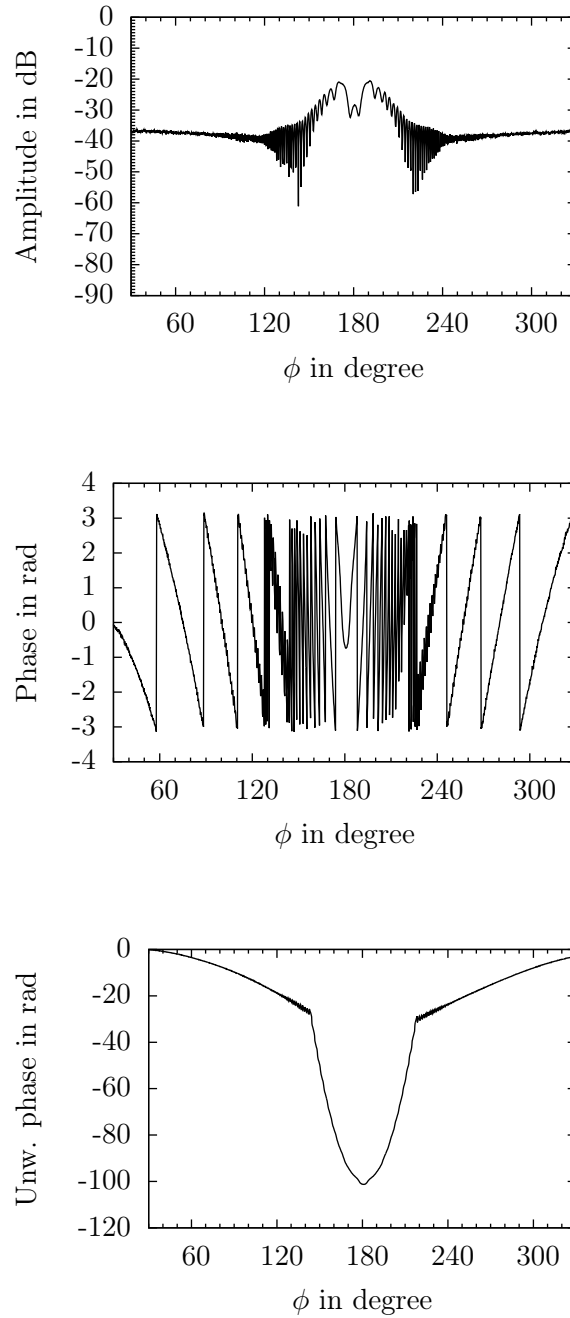


Fig. 3.5: Measured total field (raw measurements) with metallic cylinder, $D = 20$ mm, for $f = 92.5$ GHz in amplitude (top), phase (middle) and unwrapped phase (bottom).

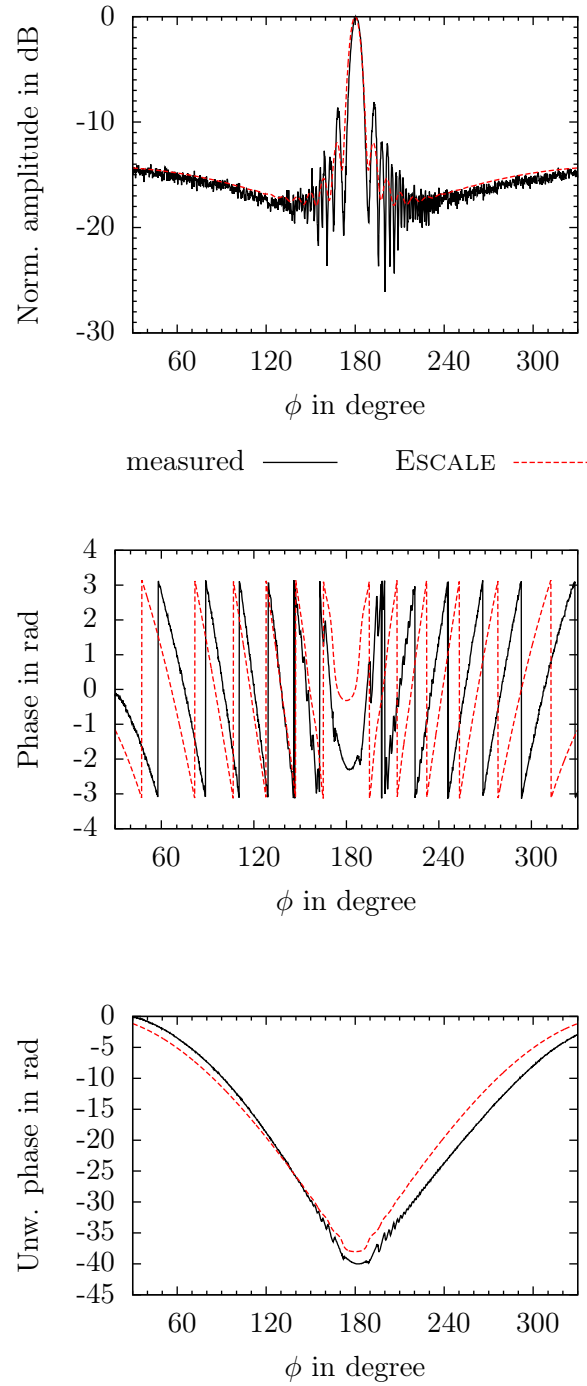


Fig. 3.6: Extracted scattered field (raw measurements) with metallic cylinder, $D = 20$ mm, for $f = 92.5$ GHz in normalized amplitude (top), phase (middle) and unwrapped phase (bottom).

Reproducibility of Measurements

In order to verify the reproducibility of measurements, the incident field has been measured twice and named with $E_1^{(i)}$ and $E_2^{(i)}$ respectively. The difference is obtained by subtracting the two measurements. This has been done with the standard-gain horn used as emitter and receiver. The magnitude of this difference is less than -34 dB (see Fig. 3.7 (top)). Additional, the relative error is calculated see (3.2). The maximal relative difference is 2% as shown in Fig. 3.7 (bottom). This demonstrates that the measurements with the installed system are repeatable.

$$\text{Relative difference} = \frac{|E_1^{(i)} - E_2^{(i)}|}{(|E_1^{(i)}| + |E_2^{(i)}|)/2} \quad (3.2)$$

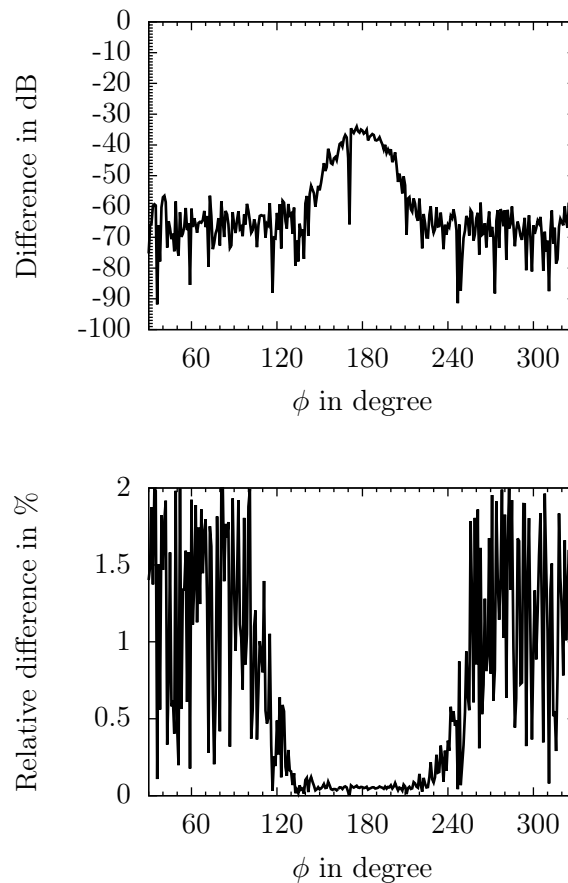


Fig. 3.7: Difference between measured incident fields (raw measurements) for $f = 92.5$ GHz (top) and relative difference (bottom). The configuration contains a standard-gain horn as emitter and as receiver.

Choice of Antennas

The choice of emitting and receiving antennas has to be made with respect to the SFMS constraints. Two open-ended waveguides and two standard gain horns with their four possible combinations as receiver and transmitter have been taken into consideration. The standard gain horn [89] has an aperture of 13 by 9 mm² and is 32.5 mm long. An open-ended waveguide as emitting antenna provides on one hand a less directive radiation pattern which ensures a constant illumination of the targets. As a result, a malpositioning of the cylinder out of the center is less critical (see Fig. 3.6 and 3.10). On the other hand, more points of measurement are closer to the noise floor of the receiver module (−70 dBm) and therefore more noised (see Fig. 3.4 (top)). This is enforced if the open-ended waveguide is also used as receiver as shown in Fig. 3.10. This can be avoided by the use of a standard gain horn. Then the received power level is enhanced because of the higher antenna gain (see Fig. 3.6). Its application as emitter in the same time provides a less constant illumination and increases the asymmetry due to an imprecision in positioning as presented in Fig. 3.9. This problem is discussed more in detail in the next section. Therefore, the best results have been obtained by using the open-ended waveguide as emitting antenna and the standard gain horn as receiver. This is a trade-off in having an acceptable noise level and to illuminate the target with an almost constant field strength in the target cross-section as plotted in Fig. 3.6. The open-ended waveguide is used as emitter in combination with the standard-gain horn as receiver for all measurements in the following. The three targets were fixed successively, and measurement cycles have been accomplished in the same manner for each frequency and each cylinder to achieve the total field including the influence of the cylinder. The results are shown in Fig. 3.11 and Fig. 3.13. Afterwards the scattered field has been extracted and is presented in Fig. 3.12 and Fig. 3.14 for the small metallic cylinder and the dielectric cylinder respectively.

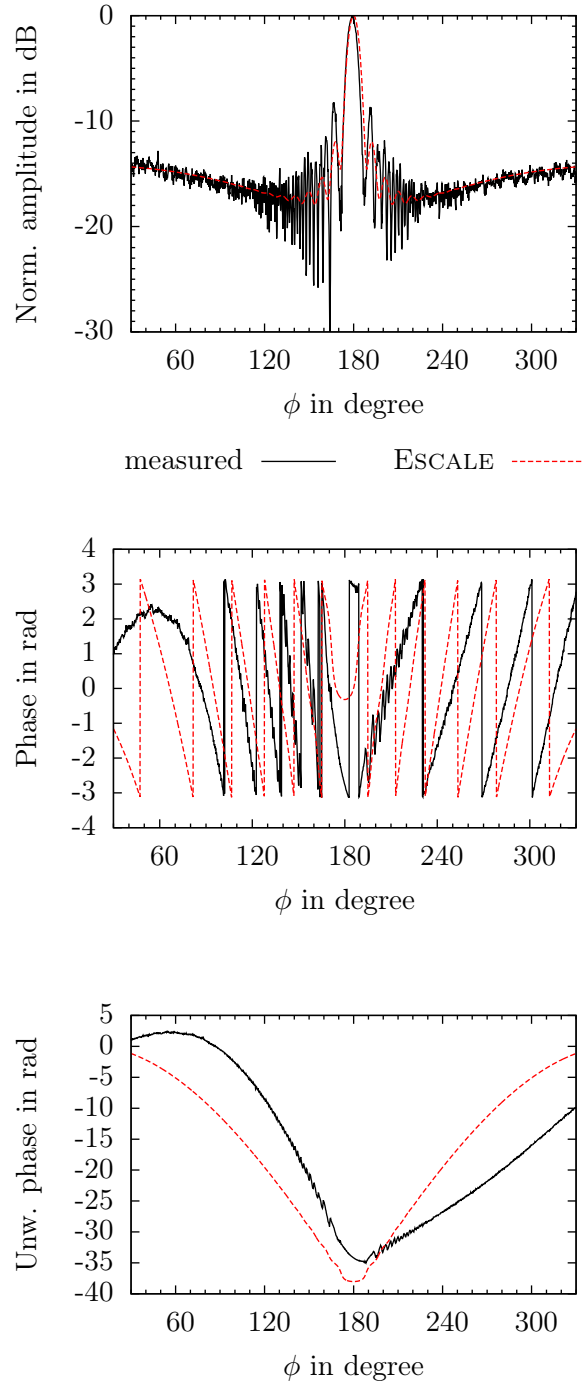


Fig. 3.8: Extracted scattered field (raw measurements) with metallic cylinder, $D = 20$ mm, for $f = 92.5$ GHz in normalized amplitude (top), phase (middle) and unwrapped phase (bottom). The configuration contains an open-ended waveguide as receiver and a standard-gain horn as emitter.

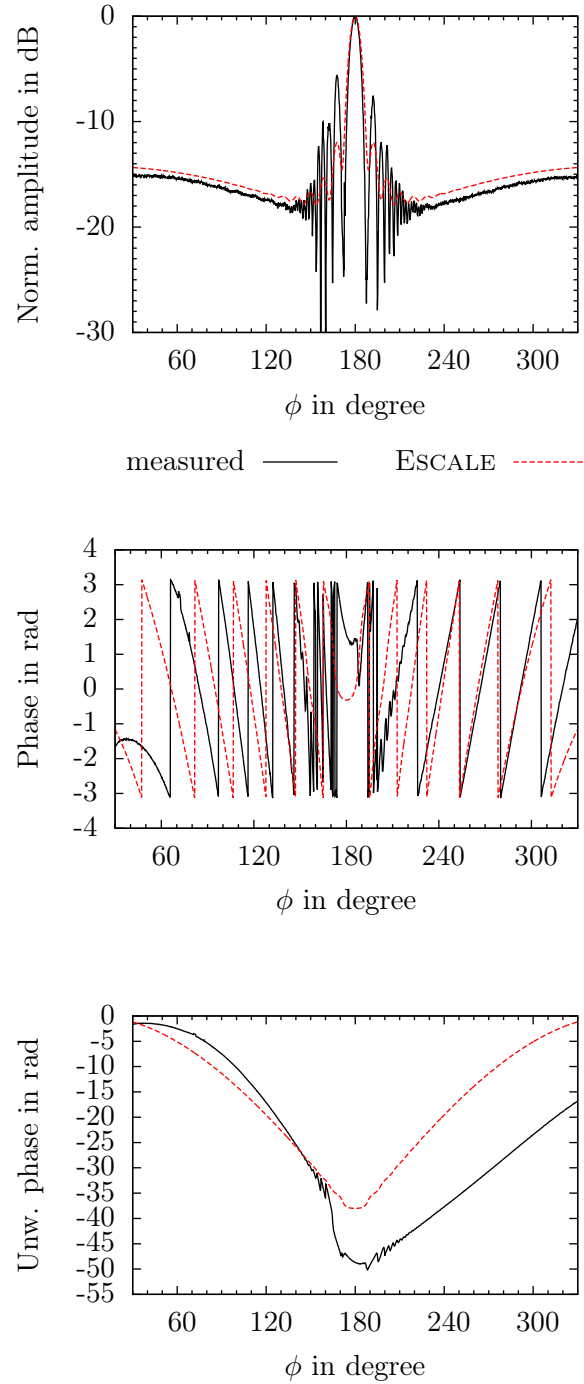


Fig. 3.9: Extracted scattered field (raw measurements) with metallic cylinder, $D = 20$ mm, for $f = 92.5$ GHz in normalized amplitude (top), phase (middle) and unwrapped phase (bottom). The configuration contains a standard-gain horn as receiver and as emitter.

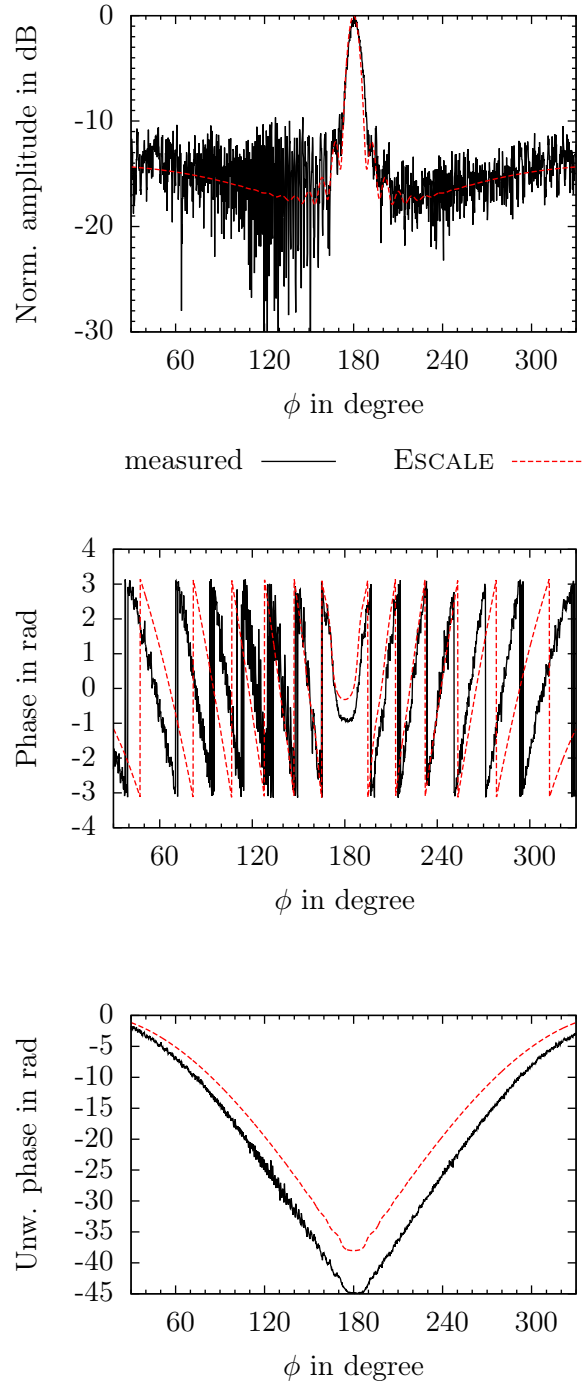


Fig. 3.10: Extracted scattered field (raw measurements) with metallic cylinder, $D = 20$ mm, for $f = 92.5$ GHz in normalized amplitude (top), phase (middle) and unwrapped phase (bottom). The configuration contains an open-ended waveguide as receiver and as emitter.

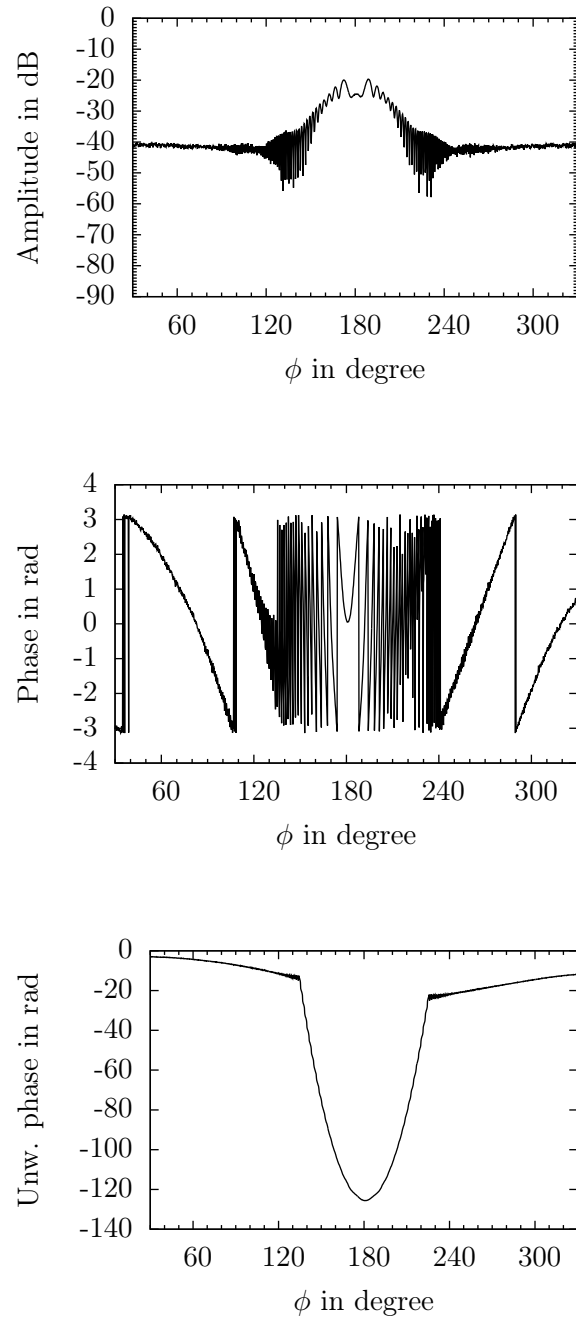


Fig. 3.11: Measured total field (raw measurements) with metallic cylinder, $D = 8$ mm, for $f = 92.5$ GHz in amplitude (top), phase (middle) and unwrapped phase (bottom).

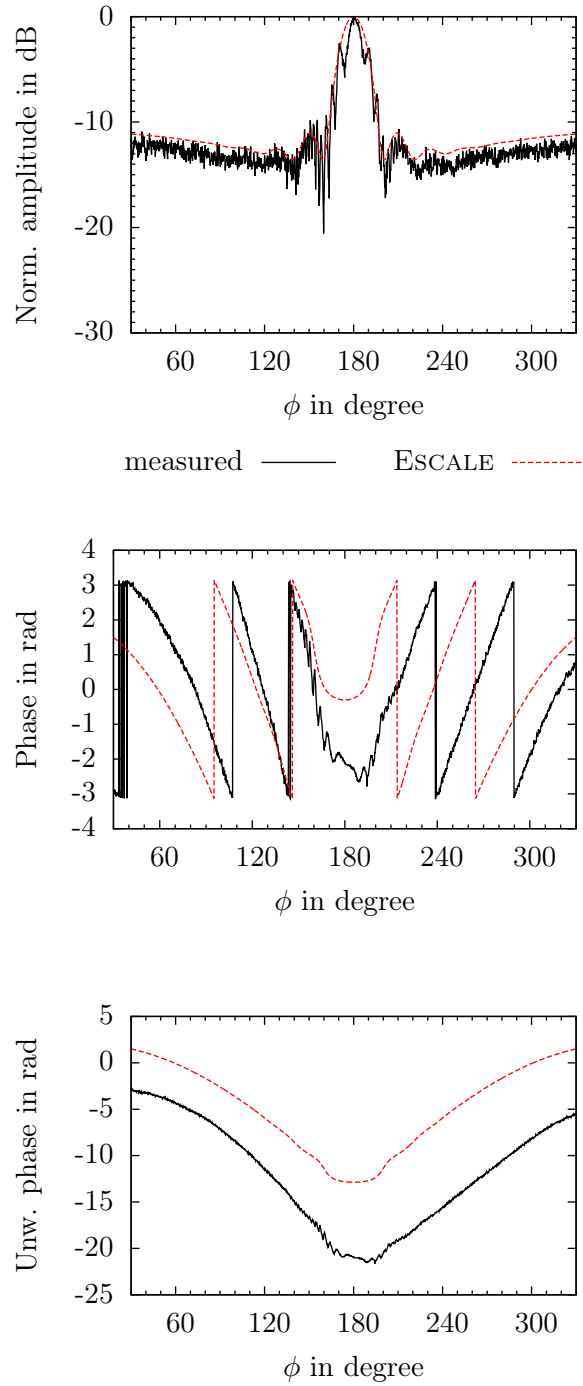


Fig. 3.12: Extracted scattered field (raw measurements) with metallic cylinder, $D = 8$ mm, for $f = 92.5$ GHz in normalized amplitude (top), phase (middle) and unwrapped phase (bottom).

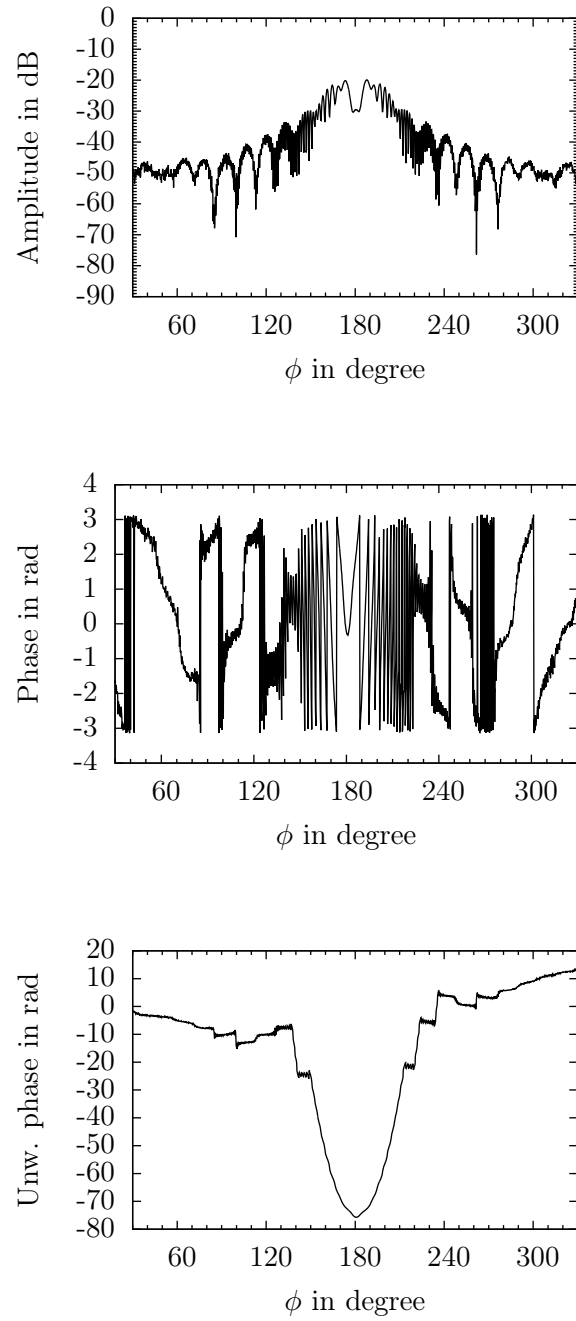


Fig. 3.13: Measured total field (raw measurements) with dielectric cylinder for $f = 92.5$ GHz in amplitude (top), phase (middle) and unwrapped phase (bottom).

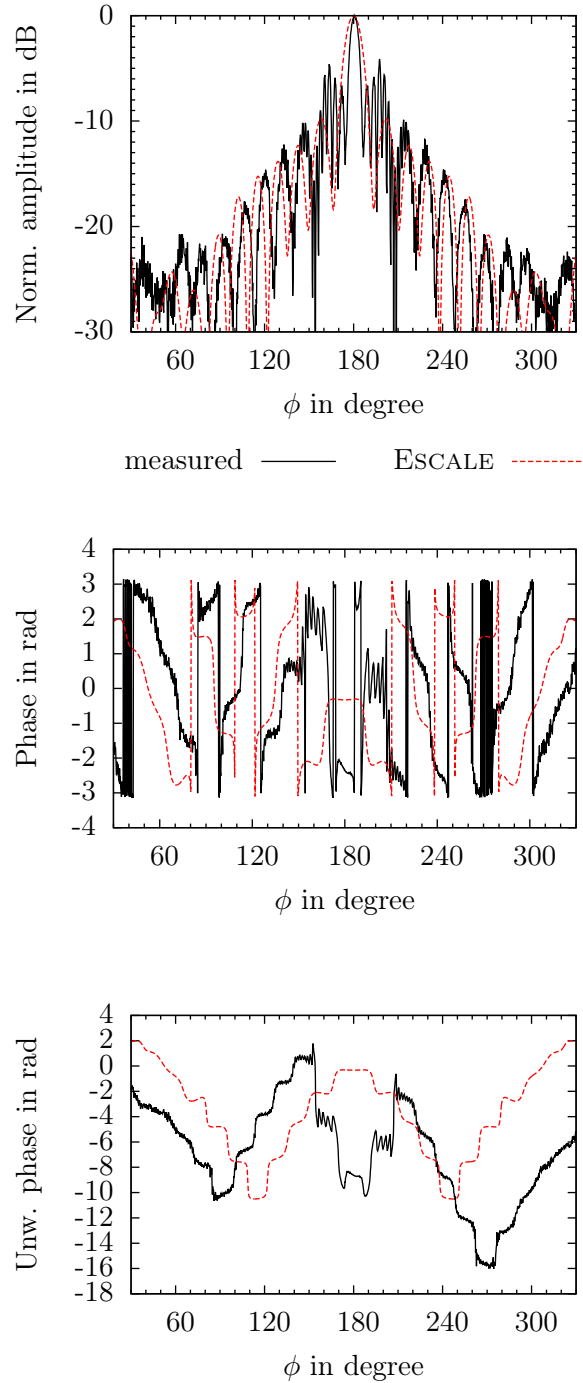


Fig. 3.14: Extracted scattered field (raw measurements) with dielectric cylinder for $f = 92.5$ GHz in normalized amplitude (top), phase (middle) and unwrapped phase (bottom). For the simulation with ESCALE a diameter of $D = 15$ mm and a relative permittivity of $\varepsilon_r = 2.5$ have been taken.

Results for 75 GHz and 110 GHz are presented in the Annex C. Although the simulated and measured scattered fields are close to each other, one can identify the following problems with respect to measurements:

- the amplitude calculated out of the measured values, apart from the main lobe, as well as the phase of the scattered field, are degraded by noise,
- the secondary lobes are drastically degraded by noise,
- the measured phase, observed on its own, is not symmetric,
- measurements need to be properly normalized in order to take into account the difference between the incident powers in measurement and simulation.

Possible reasons for this are explained in the following section, and proposals for reliable post-processing techniques in order to correct the measurements are disclosed and performed.

3.4 Analysis and Error Correction

As already mentioned in the previous section, the measured fields are degraded by noise as well as the extracted scattered field. In general, noise is introduced by the equipment itself and also by unavoidable reflections in the anechoic chamber. Moreover, additional noise, provoked by imprecision in the points of measurement, is going to be explained in detail and eliminated with digital filtering in the following. In addition, an asymmetry of the measured phase, caused by a mechanical misalignment, will be identified and corrected by post-processing. Furthermore, investigations are going to be done in the characterization of the complex relative permittivity of the dielectric cylinder as this is mandatory to compare its simulated and measured fields for the frequency of interest.

3.4.1 Characterization of Dielectric Targets

Before comparing measured scattered fields with simulated one, one must exactly characterize the TUT in order to provide comparable synthetic data. The used acrylic cylinder was supposed to provide the following characteristics: a diameter D of 15 mm (given by the manufacturer), an $\epsilon_r = 2.5$ with no losses (corresponding to acrylic). No reliable values have been found in the literature for the dielectric constant of the acrylic in the W-band. In the past, dielectric scatterers of Polymethyl Methacrylate (PMMA) have been often used as reference target because these plastics are remarkably consistent in their refractive index. Furthermore, there is indeed no measurable frequency dependence [90].

Differences in Diameter

The first studied parameter which influences the scattered fields is the diameter D . Its actual value has been measured to $D = 15.4$ mm. The previous taken value, provided by the manufacturer, has been $D = 15$ mm. The scattered fields have been simulated with ESCALE for both diameters and are compared in Fig. 3.15. The difference of $400 \mu\text{m}$ in diameter provokes minor discrepancies in amplitude in the backscattered region. On the contrary, not negligible differences occur in this region in phase (see Fig. 3.15 (right)).

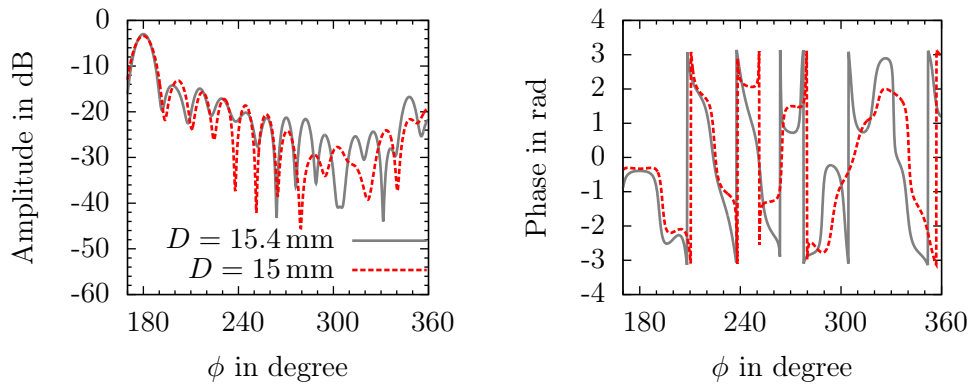


Fig. 3.15: Simulated scattered field (ESCALE) for different diameters for $f = 92.5$ GHz in amplitude (left) and phase (right).

Differences in the Complex Permittivity

In order to study the influence of different σ and ϵ_r of our target investigations have been done in simulation [122]. To estimate experimentally the actual permittivity and conductivity of a sample, made of the same acrylic as the measured cylinder, a characterization has been done with a quasi-optical measurement setup as used in [91]. The values of ϵ_r and $\tan \delta$ could be measured for two resonance frequencies as shown in Tab. 3.3. Simulations have been investigated with these parameters and are shown in Fig. 3.16. For both cases no notable changes can be seen for the amplitude. Minor differences in the phase occur.

Resonant frequency	ϵ_r	$\tan \delta$
69.13 GHz	2.44	0.0077
102.4 GHz	2.49	0.0082

Tab. 3.3: Measured values for characterized dielectric samples.

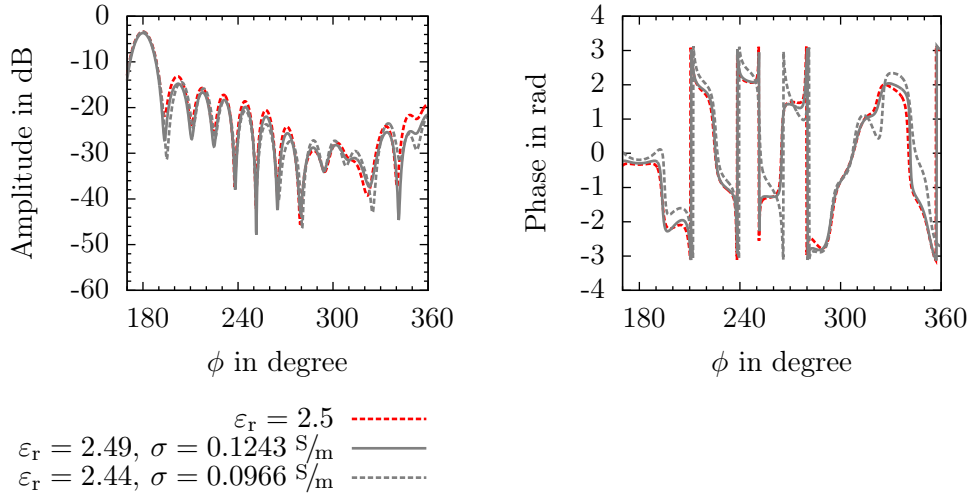


Fig. 3.16: Simulated scattered field (ESCALE) for different ε_r and σ for $f = 92.5$ GHz in amplitude (left) and phase (right) for a diameter D of 15 mm.

The parameters derived for the resonant frequency of 102.4 GHz have been used for further comparisons as this frequency is in the W-band in combination with the actual diameter of the cylinder which has been estimated to 15.4 mm.

3.4.2 Precision of Setup Installation - Correction of Mechanical Errors

The asymmetry in phase of the extracted scattered field is clearly pointed-out in its graphical unwrapped representation (see Fig. 3.6, Fig. 3.12 and Fig. 3.14 (bottom)). The measured phase is rotated with respect to the simulated one, which is the case for all three frequencies and targets in the same manner. It suggests a constant mechanical irregularity in the installation of the whole system. Its correction is demonstrated in the following. Several defaults in the installation can lead to an asymmetric measured field:

- the cylinder is inclined or shifted out of its foreseen center position. This influences only the measured total field, as the measurements without the target are not affected. The results have shown also an asymmetry of the incident field, even if less visible due to the bigger range of values of the phase than the one of the total field,
- a possible explanation (see Fig. 3.17) is that the swivel arm, with the centered target on top, is shifted out of its center position. This leads to an additional phase offset on the phase of the measured incident and total fields.

The additional swivel arm, with the receiver on the end and the fixing for the target on top, is assumed to be installed out of the center of the rotating tower. In order to calculate the resulting difference in phase only the x -direction is taken into

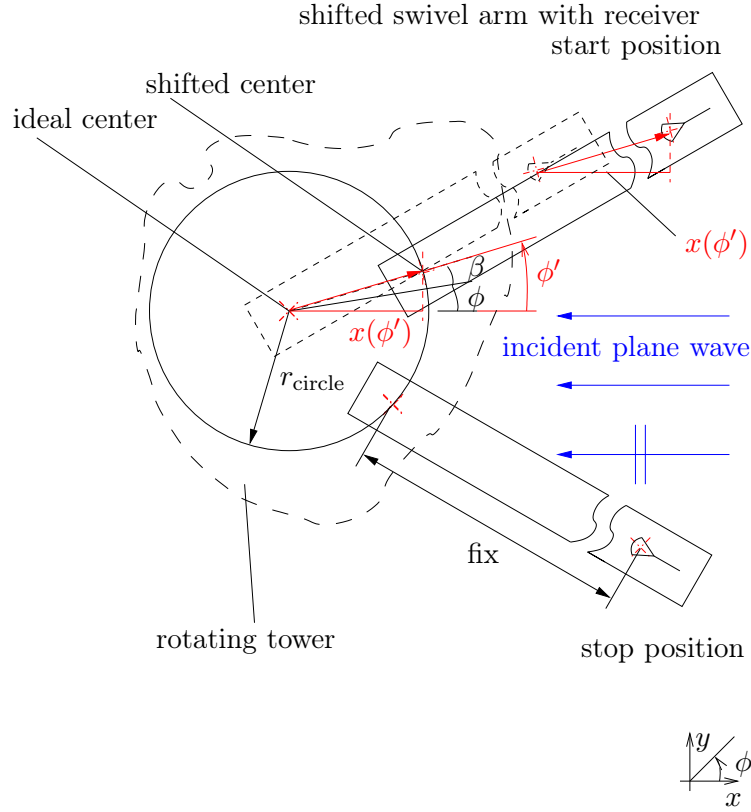


Fig. 3.17: Planned symmetric installation of the swivel arm with receiver and target on top and its shifted mounting.

account as it is parallel to the propagation direction of the incident plane wave. On one hand, this comes along with an additional unsymmetrical part in phase to the incident field, as the receiver does not turn on an ideal circle any more. On the other hand, an additional phase is added to the total field. This is also not symmetric as function of ϕ , as the movement of the target describes a circle instead of turning on its axis of symmetry (Fig. 3.17). The arm is shifted by r_{circle} from the center of the tower and by β with respect to ϕ , where ϕ describes the position of the rotating tower $\phi \in [30^\circ \dots 330^\circ]$. The actual accomplished position of the swivel arm is:

$$\phi' = \phi + \beta. \quad (3.3)$$

The additional length as function of ϕ can be calculated as following and is reduced by r_{circle} in order to obtain only the difference in length x' due to the mismatch:

$$x(\phi') = r_{\text{circle}} \cos(\phi') \quad (3.4)$$

$$x'(\phi') = x(\phi') - r_{\text{circle}} = r_{\text{circle}} [1 - \cos(\phi')]. \quad (3.5)$$

Finally, this error in distance can be expressed with the equivalent phase Φ :

$$\Phi(\phi) = -\frac{(2\pi x')}{\lambda_0}. \quad (3.6)$$

This influences the measured phase of the incident and the total fields and results in an extracted phase of the scattered field as shown in (3.7):

$$A_z^{(s)} e^{j(\Phi^{(s)} + \Phi)} = A_z^{(t)} e^{j(\Phi^{(t)} + \Phi)} - A_z^{(i)} e^{j(\Phi^{(i)} + \Phi)} \quad (3.7)$$

where $A_z^{(s)}$, $A_z^{(t)}$ and $A_z^{(i)}$ are the amplitudes of the scattered, total and incident fields, respectively, with their original phases $\Phi^{(s)}$, $\Phi^{(t)}$ and $\Phi^{(i)}$.

$\Phi(\phi)$ is a function of r_{circle} and β . The impact of β on the unwrapped phase of the scattered field for a fixed r_{circle} is shown in Fig. 3.18 (left). The influence of r_{circle} for $\beta = 45^\circ$ is demonstrated in Fig. 3.18 (right).

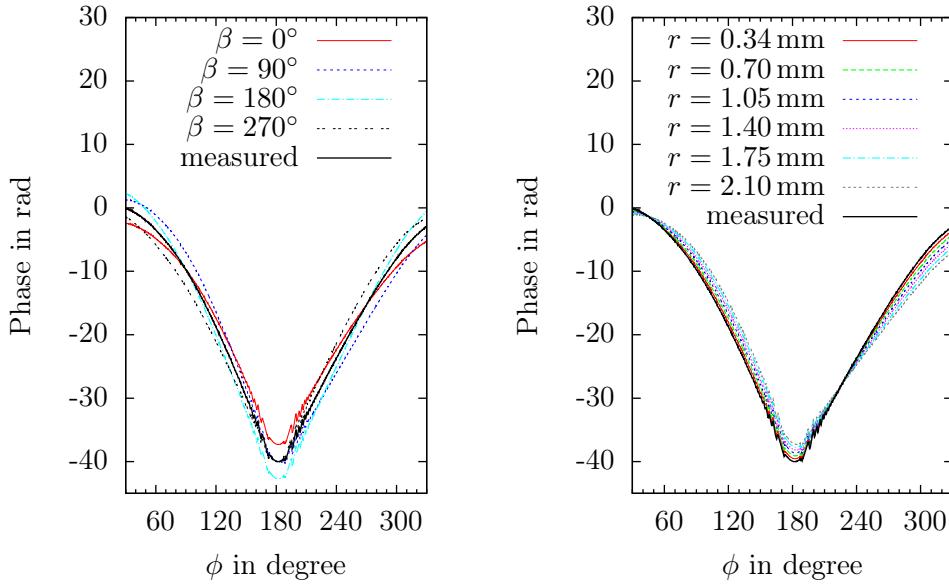


Fig. 3.18: Phase of extracted scattered field corrected by Φ for $r_{\text{circle}} = 1.4$ mm (left) and corrected by Φ for $\beta = 45^\circ$ (right).

Small misalignment errors expressed by r_{circle} and β result in a significant degradation, namely a provoked rotation, of the extracted phase. Its impact on the measured phase due to them is not linear as shown in Fig. 3.18. Therefore, a routine to estimate them precisely for all frequencies is expressed in the following.

The extracted phase is corrected by $\Phi(\phi, r_{\text{circle}} = 1.4 \text{ mm}, \beta = 280^\circ)$ and shown in Fig. 3.19 (left). At this state, r_{circle} and β have been chosen empirically. As the explained mechanical irregularity is a systematic error, the described correction allows to reconstruct results close to the simulated ones.

On the other hand, a phase offset has to be calculated in order to compare qualitatively simulations and measurements (see Fig. 3.19 (right)) as the phase centers of the antennas, which depend on the frequency, haven't been taken into account

yet in the simulation. The estimation of the real distance between the antennas and the target would still remain a challenging task and can be estimated only based on a more complex and more accurate installation than the actual one. Therefore, the difference between simulated and extracted phase of the scattered field is calculated as averaged offset in a zone at $\phi = 180^\circ \pm 5^\circ$ and subtracted from the latter one (3.8):

$$\text{averaged offset} = \sum_{\phi=175^\circ}^{\phi=185^\circ} \frac{\Phi_{\text{measured}}^{(s)}(\phi) - \Phi(\phi) - \Phi_{\text{simulated}}^{(s)}(\phi)}{\text{number of points}}. \quad (3.8)$$

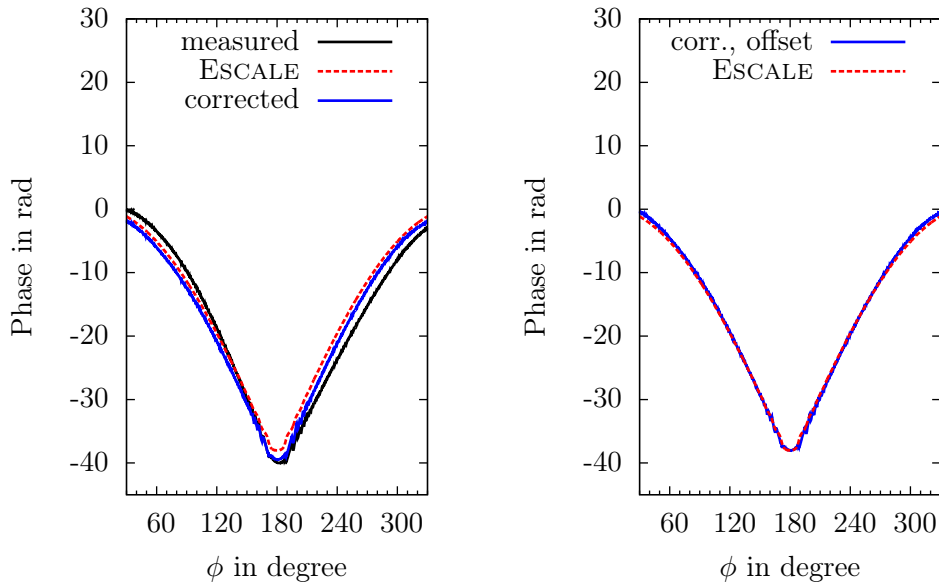


Fig. 3.19: Phase of extracted scattered field corrected by $\Phi(\phi, r_{\text{circle}} = 1.4 \text{ mm}, \beta = 280^\circ)$ (left) and phase of extracted scattered field corrected by $\Phi(\phi, r_{\text{circle}} = 1.4 \text{ mm}, \beta = 280^\circ, \text{offset} = -1.45 \text{ rad})$ (right).

After the phase correction, very good agreement is obtained between the simulation results and the measured ones.

The actual imprecision due to r_{circle} and β couldn't be measured because of two reasons:

- The measurements were done in a limited frame of time as the anechoic chamber is used by different research teams. As a consequence the system had been removed before the measurements were fully analyzed.
- The presented shift ($r_{\text{circle}} \sim 1.4 \text{ mm}$) is too small to be detected and surveyed with conventional tools with a sufficient precision. This magnitude of mechanical errors have been less critical for installations used at lower frequencies up to now in the laboratory.

Therefore, a process has been developed to improve the accuracy of r_{circle} and β , explained below: in order to identify the error, which corresponds most to the used setup, an optimization is conducted. For this purposes the built-in function of OCTAVE `fmins` has been used. The cost function is calculated as:

$$C = \frac{1}{N} \sum_{n=1}^N \left| \left(\Phi_{\text{measured}}^{(s)}(n) - \Phi(r_{\text{circle}}, \beta, n) - \text{GO} \right) - \Phi_{\text{simulation}}^{(s)}(n) \right|$$

where N is the number of measured points and $\Phi_{\text{measured}}^{(s)}(n)$ and $\Phi_{\text{simulation}}^{(s)}(n)$ are the extracted and simulated unwrapped phases of the measured and simulated scattered fields, respectively. The global offset (GO) is a scalar value. It is used as a simple phase normalization of the optimization process. As initial guess for the the optimization the averaged offset (3.8) is taken therefore. The optimization function finds the minimum of the cost function with the variables r_{circle} , β and GO. By default, the method used is the Nelder & Mead Simplex algorithm [92]. Investigations have been done in order to study the number of points of measurements taking into account for the optimization. Therefore, the metallic cylinder of $D = 20$ mm is taken as reference and future calibration target. The variables r_{circle} and β have been calculated with the described optimization routine as function of the number of points and the frequency. Thus, equispaced points have been chosen out of the 1501 available measured points (see Fig. 3.20).

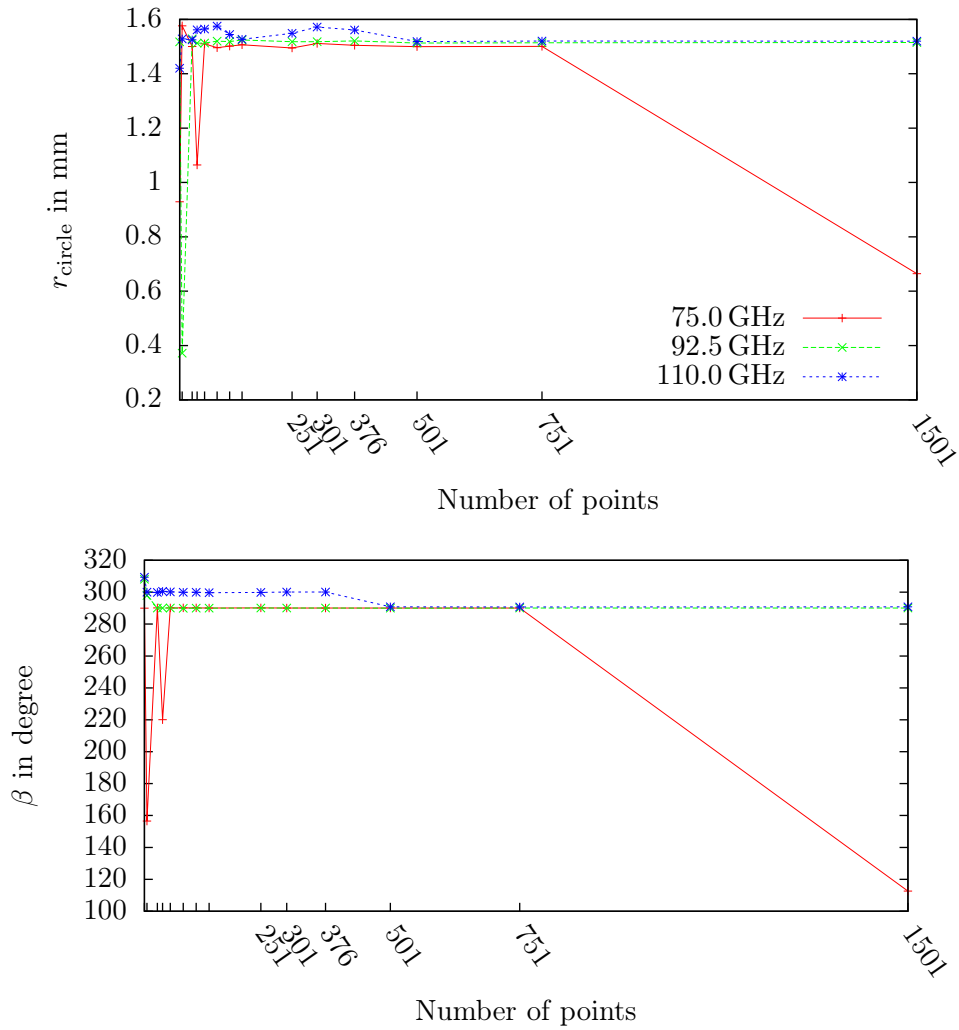


Fig. 3.20: Calculated coefficients after optimization; radius r_{circle} (top) and direction β (bottom).

The results show that almost constant calibration coefficients r_{circle} and β are found over the three frequencies and over the number of points. Results for 75 GHz and 1501 points have to be excluded as there is one point of the phase which degrades drastically the unwrapped phase. As the cost-function is less for 751 and 1501 points, these results have been averaged over the three frequencies. This lead to a $r_{\text{circle}} = 1.51$ mm and $\beta = 290.3^\circ$. These values have been supposed to estimate best the shift of the installed system and have been used as calibration coefficients in the following section to calibrate the measurement results. The obtained calibrated measured scattered field is called $E_{\text{cal.}}^{(s)}$.

3.4.3 Match Experimental Setup with Simulation - Complex Normalization

After the presented calibration a normalization [19] of the amplitude and the phase can be done. In order to match the experimental setup with the direct problem, a normalization on amplitude and phase has to be done on the data, by comparing them with synthetic (analytic solution) ones, matching more or less the targets. The complex normalization factor γ can be calculated, in case of known objects, as function of the measured scattered field and the simulated field [35] taking into account the receivers $m = 1, \dots, M$:

$$\gamma = \frac{\sum_{m=1}^M \langle (E_{\text{exact}}^{(s)})_m, (E_{\text{cal.}}^{(s)})_m \rangle}{\sum_{m=1}^M \left\| (E_{\text{cal.}}^{(s)})_m \right\|^2} \quad (3.9)$$

with the following definition of the discrete scalar product and the quadratic norm for vectors with complex entries:

$$\begin{aligned} \langle v_1, v_2 \rangle &= \sum_{m=1}^M v_{1m} \overline{v_{2m}} \\ \|v_1\|^2 &= \langle v_1, v_1 \rangle. \end{aligned}$$

Finally the measured scattered field calibrated and normalized $(E_{\text{cal.,norm.}}^{(s)})$ is obtained.

3.4.4 Noise Sources - Filtering

Per definition, the measured electric fields include systematic and random errors. The first one are repeatable, their origin can be identified and quantified, they are known as systematic errors. In other words they can be corrected by the calibration with the presented calibration coefficients (r_{circle} , β).

Signal-to-Noise Ratio Definition

As for any experimental study, defining a signal-to-noise ratio is an important step to analyze qualitatively the obtained results.

One can define the measurement error (e). The noise affecting the data is related to the mm-wave module and the receiver (noise floor, thermal drift), parasite reflections in the cables of the measurement system, unavoidable reflections in the anechoic chamber, misalignment errors (positioning of emitter, target and receiver) and random errors (deviation in measurement points shown in the following for example). After the calibration the remaining errors are due to random phenomena and one can define the SNR [93] based on the error e to evaluate the quality of the results at each frequency as following:

$$e = \frac{\langle E_{\text{cal.,norm.}}^{(s)} - E_{\text{exact}}^{(s)}, E_{\text{cal.,norm.}}^{(s)} - E_{\text{exact}}^{(s)} \rangle}{\langle E_{\text{exact}}^{(s)}, E_{\text{exact}}^{(s)} \rangle} \quad (3.10)$$

$$\text{SNR} \Big|_{\text{dB}} = -10 \log(e) \quad (3.11)$$

where $E_{\text{cal.,norm.}}^{(s)}$ are the scattered fields, calibrated and normalized, issued from measurements and $E_{\text{exact}}^{(s)}$ the exact fields. This reference signal is calculated with the analytic solution (ESCALE) because it is the exact solution as no numerical noise is introduced as it would be the case for the simulation with FLEXIMOM.

Two main sources of noise have been identified: on one hand, measurements are noisy due to the noise introduced by the equipment itself used for our measurements. On the other hand, the mechanical configuration comes into play: the scattered fields are obtained after subtraction of the incident and total fields. That means that two measurement cycles are mandatory to obtain one set of measurements corresponding to the scattered field. Additional noise occurs if the measurement points are not the same within these two measurement cycles.

Noise by Shift in Measurement Points

To perform the measurements, the highest precision possible for the positioning of the step engine, 0.05° has been chosen by software. The log files (see Tab. 3.4 for two measurements) show the actual deviation in approached and reached position, of the step motor for every cycle of measurements. In order to take into account this

Approached	Reached cycle 1	Reached cycle 2
ϕ in degree		
30	29.99	29.99
30.2	30.16	30.155
30.4	30.364	30.367
30.6	30.566	30.566
30.8	30.766	30.764
...
180.0	179.96	179.96
...
329.2	329.158	329.156
329.4	329.358	329.358
329.6	329.558	329.557
329.8	329.759	329.758
330.0	329.958	329.956

Tab. 3.4: Approached and actual reached positions of the receiver.

inevitable inaccuracy, the incident and the total fields have been simulated analytically (ESCALE) on exactly the same points where the measurements were realized for two different cycles, by using the saved positions in the log files. Afterwards, the scattered field has been obtained again by a vectorial subtraction (see Fig. 3.21).

The results in Fig. 3.21 show that the amplitude includes oscillations apart from the main and secondary lobes. In these regions, the phase is also degraded. This means, that even a perfect measured incident and a total field, here obtained in simulation, would result in a noisy scattered field due to the fact that with the installed system an inevitable imprecision in positioning has to be taken into account. The SNR of the noised scattered field which is shown in Fig. 3.21 has been calculated with (3.11) to 22 dB. This is far above the SNR that can be obtained after corrections, which is presented in the next section. This error is not the major contribution. Additionally, one can see that the noise caused by the step motor is mainly present out of the central region of the pattern. On the contrary, in the raw scattered field measured data, the noise is mainly concentrated in the central part of the pattern (see Fig. 3.6). This is even more critical on the small cylinder as shown in Fig. 3.12. Noise study has been further conducted while considering an additive white Gaussian noise model.

The previous study shows that even a noise-free incident and total field would

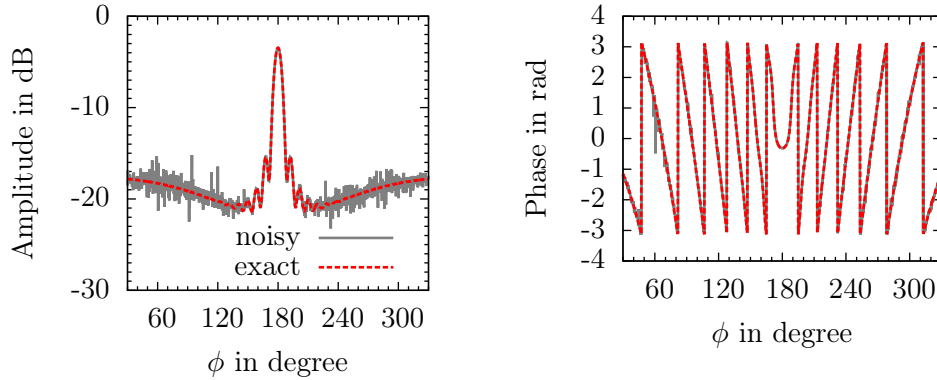


Fig. 3.21: Simulated scattered field (ESCALE) on points of the step motor, where measurements have been provided, $D = 2$ cm, $f = 92.5$ GHz, in amplitude (left) and phase (right).

result in a noised scattered field due to the fact that the measurements can't be performed on exactly the same points as foreseen. Even a marginal deviation in position of the receiver, where the measurements are effected, leads to a noisy scattered field. To overcome this problem, a filtering has been applied directly on the scattered fields.

Additional White Gaussian Noise

In order to model the noise behavior of the equipment by itself in general, an AWGN [67] has been added to the simulations. It might not be totally accurate for noise modeling of the measurement system but still provides a useful model for performance estimations. Fig. 3.22 shows the results of the large metallic cylinder for a SNR of 10 dB which corresponds to the value after calibration of the measured scattered field. As expected the AWGN shows a noise distribution that impacts all the radiation pattern over ϕ on the contrary to the noise introduced by the imprecision of positioning of the step motor. This model will be used for further investigations on the filtering.

Noise by Superposition of Fields

On one hand, the results have shown that the imprecision in the approach of the measuring points influences marginally the scattered field outside the main and the secondary lobes. It is not the main cause for the noise in the scattered fields. On the other hand, an AWGN degrades equally the whole pattern of the scattered field. The scattered fields extracted from measurements are locally more influenced by noise in the zone of the main and secondary lobes (see Fig. 3.6). The reason for this is demonstrated in Fig. 3.23 by super-positioning of the measured incident and total fields: in the region where the incident and the total fields are in the same order

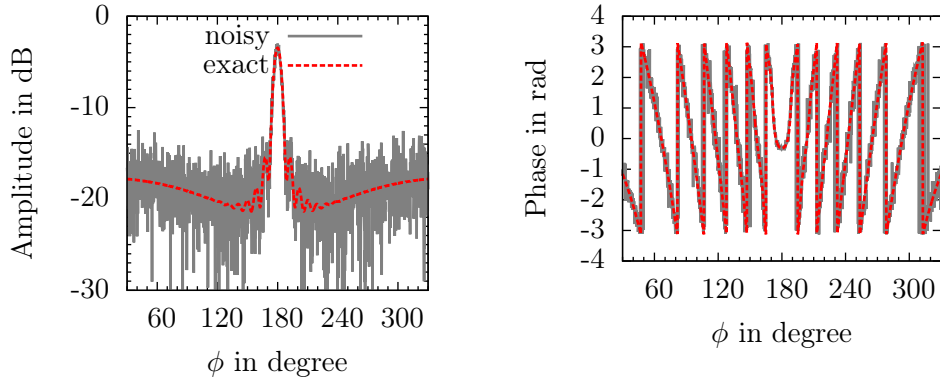


Fig. 3.22: Simulated extracted scattered field (ESCALE) with AWGN (SNR=10 dB), $D = 2$ cm, $f = 92.5$ GHz, in amplitude (left) and phase (right).

of magnitude the measurement errors are more contributing to the overall noise level of the extracted scattered field. One can retrieve that the noise distribution of the extracted scattered fields dominates in the regions where the total and the incident fields are close in values. For the metallic cylinders this zone of strong noise contribution influences the main and secondary lobes. The scattered field extracted from measurements of the dielectric cylinder shows that the zone also degrades more side lobes where the measured total field has the same magnitude as the incident field. For this reason, almost the whole measured area of the scattered field is degraded by noise. Further investigations on noise modeling are foreseen as following: to model precisely the actual noise distribution of the measurement system a comparison of the magnitudes of the incident and the total fields will be done. Depending whether the magnitudes of the two fields are in the same order, AWGN based on different given values for SNR is calculated and determines the additive noise to the simulated scattered fields.

The noise introduced by the step motor and by the equipment itself can be reduced by applying a low-pass filter on the extracted scattered fields. This is going to be explained in the next section.

Ideal Filtering Based on Measurements

In order to suppress noise, a filtering, that does not require a-priori knowledge of the target, has been developed. It is important, because the final application of interest is quantitative imaging with unknown targets under test. Therefore, the following filter process is applied: the scattered field as a function of the variable ϕ is transformed into the spectral domain with a Fourier transformation. Filtering is done with a multiplication by a rectangular window which has the width of the cut-off frequency (in $1/\text{degree}$) as demonstrated exemplary in Fig. 3.24.

In order to obtain the best SNR, which can be obtained with filtering, the fol-

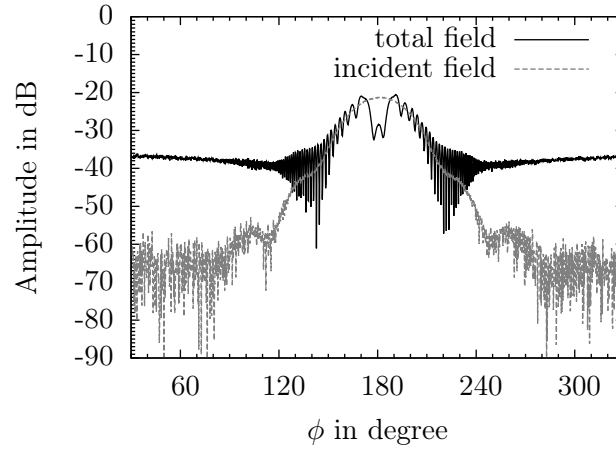


Fig. 3.23: Amplitude of the measured total and incident fields (raw measurements) for the metallic cylinder, $D = 2$ cm, $f = 92.5$ GHz.

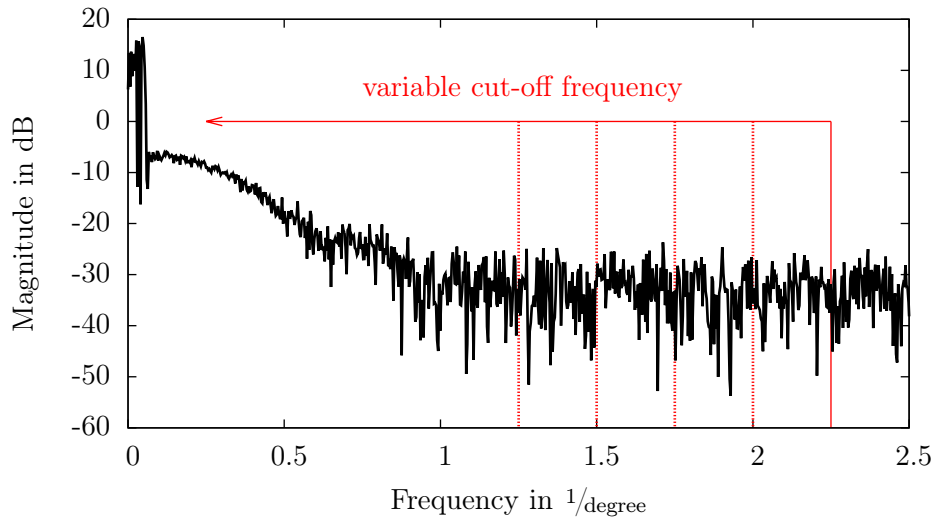


Fig. 3.24: The scattered field of the metallic cylinder with a diameter of $D = 20$ mm for $f = 92.5$ GHz as a function of the variable ϕ transformed into the spectral domain.

lowing investigations have been done: the filter frequency has been decreased progressively and the corresponding SNR value calculated; so far with the knowledge of the target, the two metallic cylinders. The SNR as function of the cut-off frequency is shown in Fig. 3.25 (left) for the large cylinder (top) and the small cylinder (bottom). The maximal SNR reachable by the explained filtering depends on the exact knowledge of the cut-off frequency which has to be chosen. This frequency depends on the TUT and the frequency of operation. For this cut-off frequency the maximum SNR is nearly constant over the measurement frequency, 15.81 dB for the large cylinder and 10.7 dB for the small cylinder. The results show that the best SNR as function over the frequency comes with different losses due to the filtering (see Fig. 3.25 (right)). The signal losses are defined as the difference between the power of the scattered field before and after filtering. Filtering relying on a criterion based on a constant value of losses for all frequencies would result in a final SNR far below the best SNR achievable by filtering depending on the frequency of operation and target. The best SNR due to filtering is shown in Tab. 3.5. The two cases for 751 and 1501 points of calibrated and normalized results have been calculated.

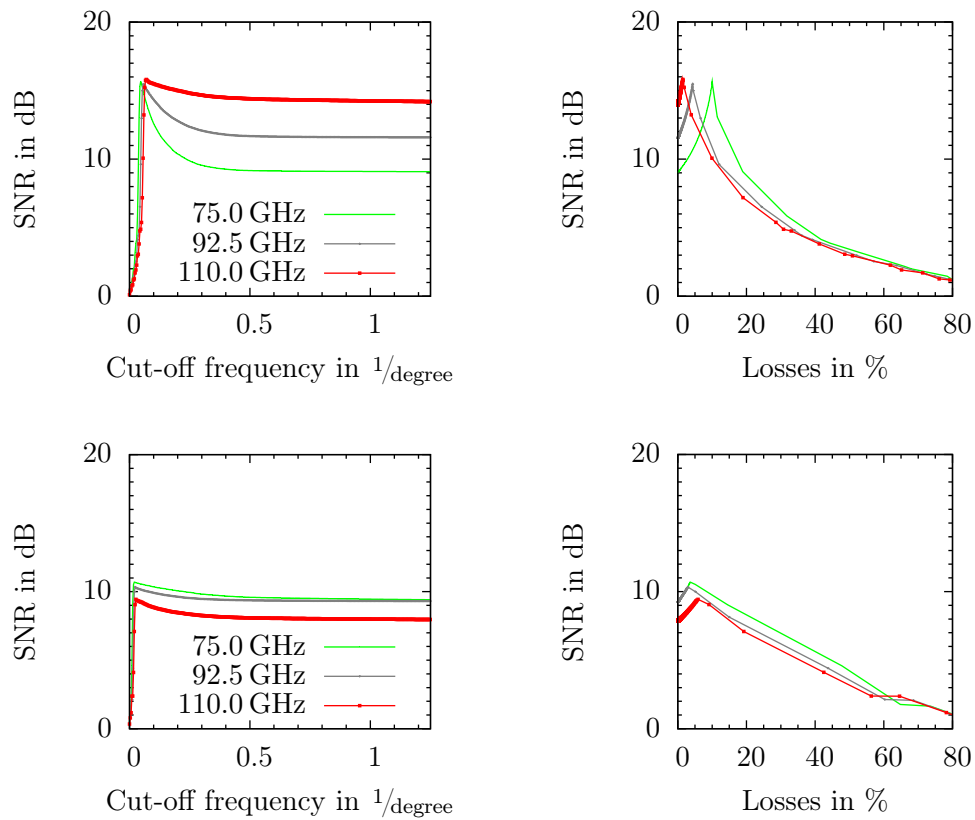


Fig. 3.25: SNR as function of the cut-off frequency and the frequency of operation, metallic cylinder, $D = 20$ mm (top left). SNR as function of the losses due to filtering and the frequency of operation, metallic cylinder, $D = 20$ mm (top right). SNR as function of the cut-off frequency and the frequency of operation, metallic cylinder, $D = 8$ mm (bottom left). SNR as function of the losses due to filtering and the frequency of operation, metallic cylinder, $D = 8$ mm (bottom right).

	f in GHz	751 points				1501 points			
		SNR - max		Slope detection		SNR - max		Slope detection	
		SNR in dB	f_c in 1/degree	f_c in 1/degree	SNR in dB	SNR in dB	f_c in 1/degree	f_c in 1/degree	SNR in dB
Metallic cylinder $D = 20$ mm	75.0	15.64	0.047	0.043	15.31	15.67	0.047	0.043	15.32
	92.5	15.46	0.057	0.053	14.97	15.46	0.057	0.053	15.00
	110.0	15.81	0.067	0.067	15.74	15.81	0.070	0.067	15.75
$D = 8$ mm	75.0	10.64	0.020	0.020	10.64	10.70	0.020	0.020	10.70
	92.5	10.36	0.023	0.023	10.36	10.34	0.023	0.023	10.34
	110.0	9.40	0.027	0.030	9.33	9.44	0.027	0.030	9.37
Dielectric cylinder $D = 15$ mm	75.0	5.65	0.033	0.037	5.55	5.67	0.033	0.037	5.56
	92.5	6.03	0.043	0.047	5.97	6.06	0.043	0.047	6.00
	110.0	5.54	0.057	0.053	5.54	5.53	0.057	0.053	5.53

Tab. 3.5: The maximal SNR achievable with filtering and its cut-off frequency compared with the cut-off frequency obtained by slope detection (100 percent degree) and its SNR for 751 and 1501 points of measurements.

The SNR based on (3.11) can only be calculated if the TUT is known, because so far the calibration and the SNR calculation have to be done with the synthetic data for the known target. Other calibration schemes could be used to overcome this problem by taking a known scattered field by a reference target for calibration [72]. Anyway the qualitative estimation of the SNR without synthetic data is a challenging task especially if this value depends on the TUT. In order to get the optimal cut-off frequency of the filter, only based on measured data, the following procedure has been used: the losses due to filtering as function of the cut-off frequency in the spectral domain have been calculated (see Fig. 3.26). For this, the cut-off frequency is decreased progressively in order to get the signal losses as function of the cut-off frequency. Indeed spectral domain of measurements has three regions:

- region 1: from 0 to a first value of the spectral variable (s_1) the slope is very high,
- region 2: from s_1 to s_2 : a smaller slope,
- region 3: above s_2 an almost flat curve.

The region 2 does not exist in the simulation as the results are free of noise. One can see that the value s_1 is the same in the simulation and the measurement for each frequency respectively.

Then the slope of this function can be directly calculated. Once the losses raise drastically the real spectrum of the scattered field itself is filtered. In this way, the optimal cut-off frequency of the filter can be found with a slope detection (frequency corresponding to s_1). In Fig. 3.27 the slope of the losses due to filtering based on the measurement and on the simulated scattered field noised with a white Gaussian noise (SNR=5 dB) are compared. This works well for the scattered field measurements of all targets and all frequencies (see Tab. 3.5). The only visible difference is one frequency step between the calculated cut-off frequency found with the maximal SNR and the presented approach with the slope detection. The frequency resolution in the spectral domain is $1/300^\circ$.

In order to prove the function of the presented approach in general, simulations have been investigated on asymmetric targets. Two objects of interest from mm-wave radar applications have been chosen. That is a thin metallic plate, used as target of interest in FOD detection and a power line section, used as target of interest in collision avoidance radar for helicopters. The ideal simulated scattered fields were noised with AWGN up to a SNR of 5 dB. Simulations were conducted with FLEXIMOM as no analytical model exists at least for the power line. Going back to the filtering and applying the presented method, we found out that it is still accurate for asymmetric objects under AWGN. The results are shown in Fig. 3.28 and Fig. 3.30.

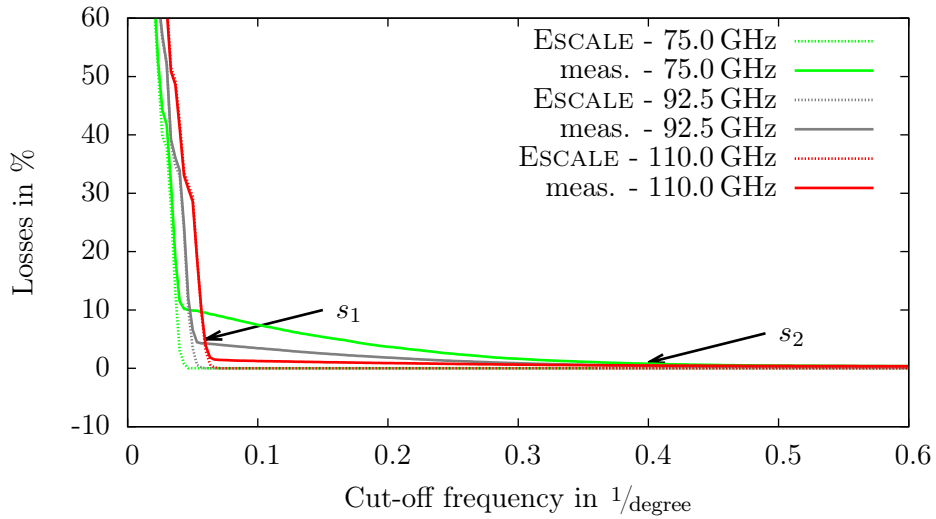


Fig. 3.26: Losses due to filtering as a function of the cut-off frequency, $D = 20$ mm.

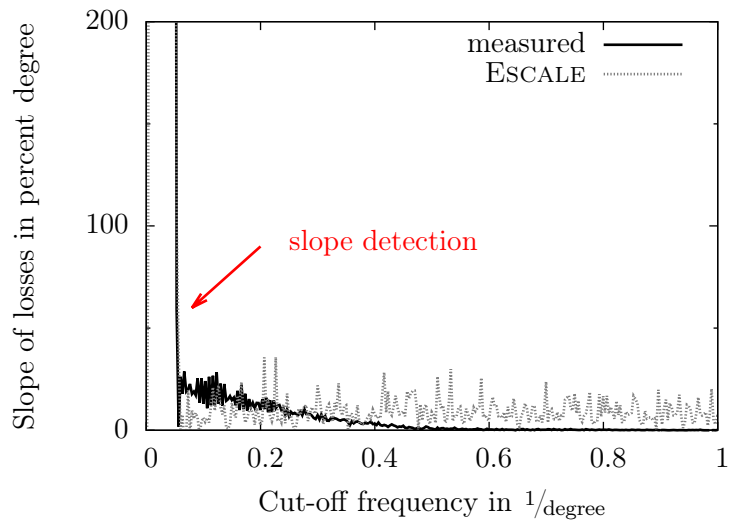


Fig. 3.27: Slope detection in order to find the cut-off frequency corresponding to the best signal to noise ratio obtained with filtering. Cylinder $D = 20$ mm, $f = 92.5$ GHz. Simulated scattered fields with a SNR=5 dB.

The presented approach has been verified on measured data for three different symmetric targets and three frequencies. The approach is verified with irregular objects as they are of particular interest for several applications which aim to detect objects like rectangular targets or targets with special cross sections as shown in the following.

Verification of Filtering - Metal Plate A metal plate ($100 \text{ mm} \times 5 \text{ mm}$), an object which is difficult to detect with actual radar systems on a runway of an airport, has been investigated. Its scattered fields have been calculated on 3600 equispaced points for a frequency of 100 GHz for an angle of incidence of 45° . The distance between the receivers and the center of the plate has been chosen to 300 mm. The plate is considered to be infinite in z -direction to fulfill the 2D-TM case for simulation purposes. An AWGN has been added to get a SNR of 5 dB to have an unfavorable case in measurement (see Fig. 3.28 (left)). The results have been filtered (see Fig. 3.28 (right)) with the presented approach which leads to a cut-off frequency of $0.256 \text{ } 1/\text{degree}$ with a final SNR of 15.42 dB. This is very close to the maximal SNR of 16.95 dB with its cut-off frequency of $0.294 \text{ } 1/\text{degree}$.

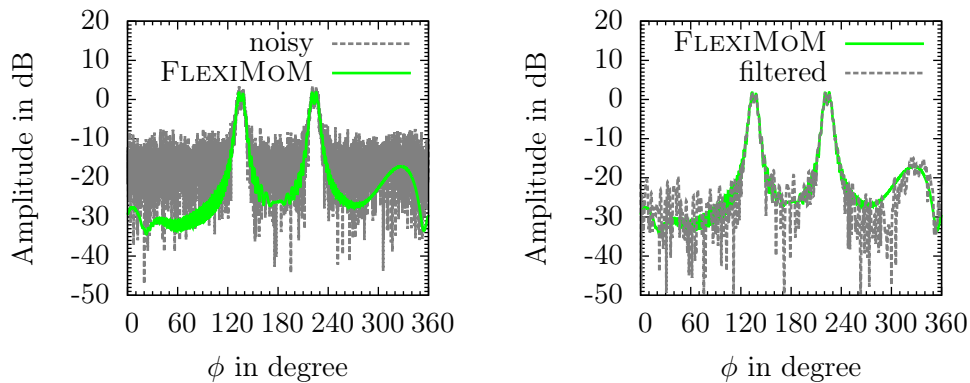


Fig. 3.28: The scattered field of the thin metallic plate under 45° incidence (size of the plate is $100 \text{ mm} \times 5 \text{ mm}$) before filtering (left) and after filtering (right).

Verification of Filtering - Cable Section A cable section (see description of dimensions in Fig. 3.29), has been simulated with $\rho_1 = 8.5 \text{ mm}$ and $\rho_2 = 5 \text{ mm}$. Its scattered fields have been calculated on 3600 equispaced points for a frequency of 100 GHz for an angle of incidence of 180° in a distance of 300 mm. An AWGN has been added to get a SNR of 5 dB to have an unfavorable case in measurement (see Fig. 3.30 (left)). The results have been filtered (see Fig. 3.30 (right)) with the presented approach which leads to a cut-off frequency of $0.108 \text{ } 1/\text{degree}$ with a final SNR of 20.87 dB. This is very close to the maximal SNR of 21.05 dB with its cut-off frequency of $0.094 \text{ } 1/\text{degree}$.

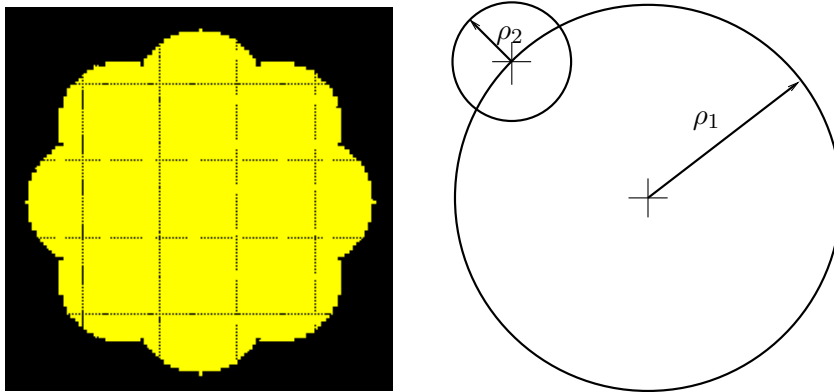


Fig. 3.29: Definition of the cross sections ρ_1 and ρ_2 of the simulated cable.

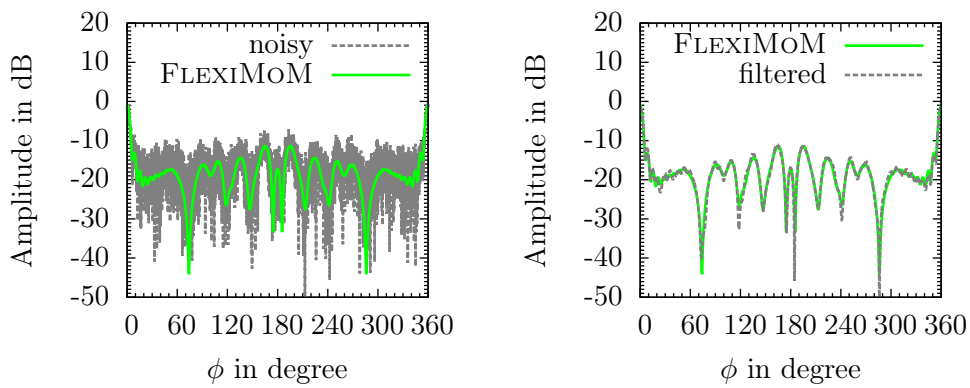


Fig. 3.30: The scattered field of the power cable section before filtering (left) and after filtering (right).

The presented results show that the presented approach is still accurate for asymmetric objects under AWGN.

3.5 Results over W-band and Discussion

The metallic cylinder with $D = 20$ mm has been taken as reference target and used to derivate the calibration coefficients r_{circle} and β . They are frequency independent except from a small variation of 1.5 % for r_{circle} . Therefore, an averaged value over the frequency is taken for the calibration, $r_{\text{circle}}=1.51$ mm. For the final comparison here all measured points 1501 have been taken into consideration. The calibration coefficients have been applied to the results of the extracted scattered fields of all measured targets. Then, an “optimal” filtering, based on the presented slope detection technique, has been done for each target and each frequency of operation respectively. An overall performance validation of the installed measurement system and the measured scattered fields is done: therefore the final results have been normalized by taking the exact solution as reference in order to compare them qualitatively to the latter one. Additionally the SNR has been calculated again by taking the analytic solution. In the following sections the results of the metallic cylinder, used as calibration target, are discussed as well as the metallic cylinder with $D = 8$ mm and the dielectric cylinder with $D = 15$ mm as TUT.

3.5.1 Calibrated and Normalized Measured Scattered Fields

In this section the final results of the corrected (calibrated and normalized) extracted scattered fields are compared with the corresponding exact solution.

Calibration Target

In Fig. 3.31 the final results of the corrected scattered field of the reference target are shown exemplarily for the center frequency of 92.5 GHz. The main as well as the secondary lobes have been perfectly retrieved. Also the level of the third and fourth side lobes corresponds to the one of the exact solution. Ripple leads to marginal discrepancies in the backscattered region. The phase is in perfect accordance over the whole angle range. As expected, as this cylinder has been used as reference target, this leads to an over the three frequencies averaged high SNR of 15.36 dB.

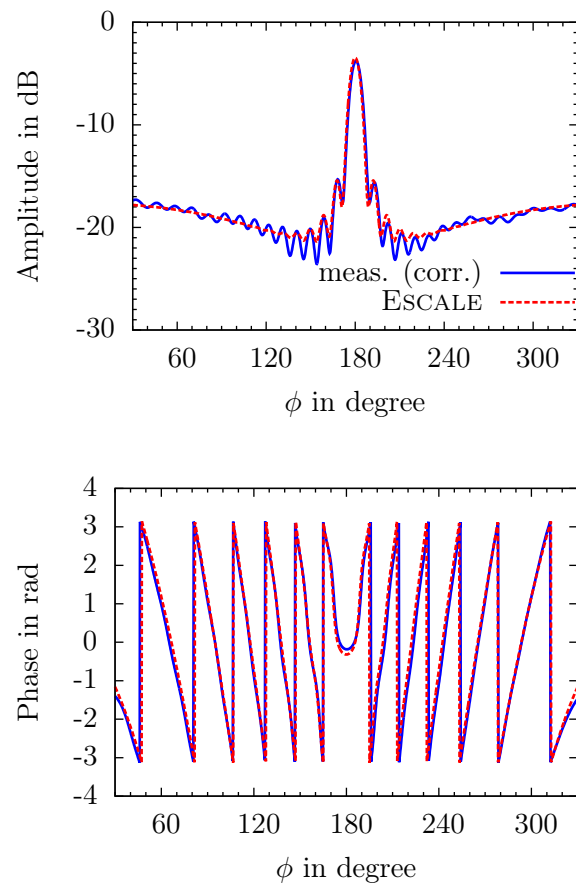


Fig. 3.31: Calibrated and normalized measured scattered field of metallic cylinder with $D = 20$ mm, $f = 92.5$ GHz, in amplitude (top) and phase (bottom).

Metallic Circular Cylinder

The first discussed TUT, measured and corrected with the already calculated calibration coefficients, is the metallic cylinder with a diameter of 8 mm. Results for 75 GHz in amplitude are shown in Fig. 3.32 (left). The main lobe between 150° and 210° matches perfectly the analytic solution. The secondary side lobes have marginal less energy but are still in good accordance with the exact solution. Small differences are visible between 260° and 330° on the phase curve (see Fig. 3.32 (right)). This is because the unwrapped phase is even after calibration slightly asymmetric. The presented results give of all three frequencies the best SNR of 10.7 dB for this target.

For 92.5 GHz (see Fig. 3.33) the main and secondary lobes as well as further side lobes have been measured in good matching with ESCALE. A marginal asymmetry in amplitude of the secondary lobes, 1.13 dB, is visible. The phase is again slightly unsymmetrical in the angular range above 260° .

A symmetric pattern in amplitude has been obtained for 110 GHz as shown in Fig. 3.34. This excludes an inclined installation as reason for the slight asymmetric patterns in amplitude for 75 and 92.5 GHz. The same minor discrepancies in phase as already discussed for the two lower measured frequencies are there.

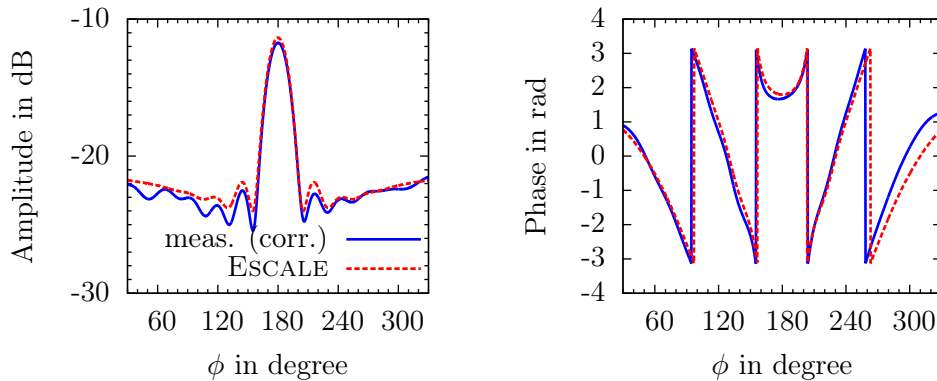


Fig. 3.32: Calibrated and normalized measured scattered field of metallic cylinder with $D = 8$ mm, $f = 75$ GHz, in amplitude (left) and phase (right).

Marginal discrepancies in phase due to a slight asymmetric phase of the corrected measured scattered field is visible. One could overcome this problem by calculating the calibration coefficients for this target and calibrate it with this specific values, which is for sure not possible for unknown targets and has not been done therefore. The results show very good agreement between the exact solution (ESCALE) and measurements for all three frequencies.

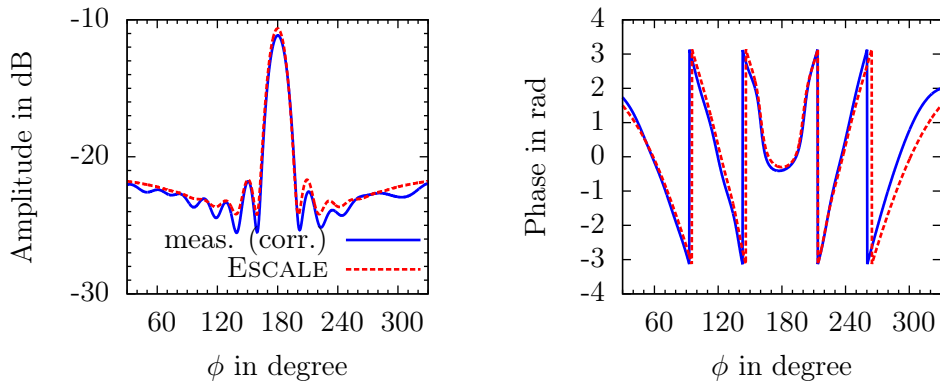


Fig. 3.33: Calibrated and normalized measured scattered field of metallic cylinder with $D = 8$ mm, $f = 92.5$ GHz, in amplitude (left) and phase (right).

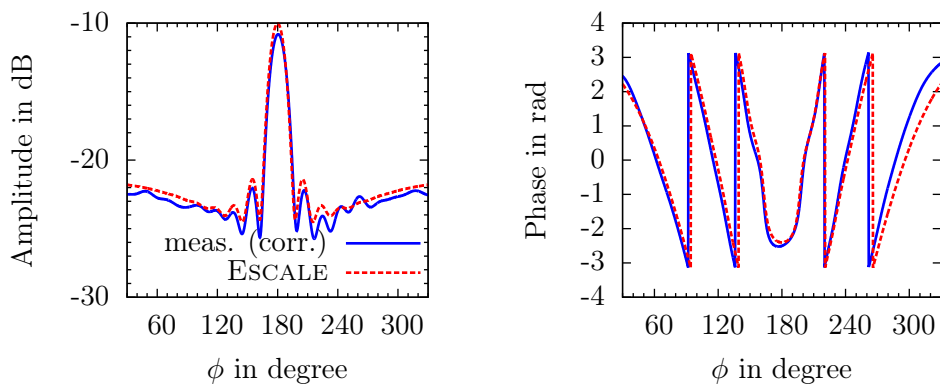


Fig. 3.34: Calibrated and normalized measured scattered field of metallic cylinder with $D = 8$ mm, $f = 110$ GHz, in amplitude (left) and phase (right).

Dielectric Circular Cylinder

The second discussed target is the dielectric cylinder. The material of the cylinder and its geometry have been characterized as explained in detail in Section 3.4.1. The retrieved values have been used for the simulation of the analytic solution for comparison purposes in the following.

The results for 75 GHz are shown in Fig. 3.35. There is a very good matching between the corrected extracted amplitude of the scattered field and the reference amplitude. The minima are on the same angular positions as foreseen by simulation. The second and third side lobes and the pattern in a zone for $\phi \in [30 \cdots 60^\circ]$ and for $\phi \in [270 \cdots 330^\circ]$ have less energy in measurement as predicted by the analytic solution. The phase is symmetric after its calibration. Small discrepancies in the phase response over the whole angular area are visible.

Good matching could be obtained in amplitude and in phase for 92.5 GHz as presented in Fig. 3.36. The secondary side lobes in the simulation have less energy, 4 dB. The measured phase corresponds well, even in the backscattered region, to the analytic solution. These results give the best SNR (6 dB) for this target.

For 110 GHz the number of side lobes in measurement correspond to the one of the analytic solution but the lobes have less energy over the whole angular range (see Fig. 3.37). The extracted phase of the measurements is very close, especially in the backscattered region, to simulations.

Also the results obtained with a dielectric scatterer correspond to the analytic solution for all three frequencies. Minor discrepancies occur in amplitude and in phase. This results from the inexact knowledge of the permittivity for certain frequencies (75, 92.5 and 110 GHz). Further investigations should be done in the characterization of the complex relative permittivity for the frequencies of interest in order to provide more reliable simulations.

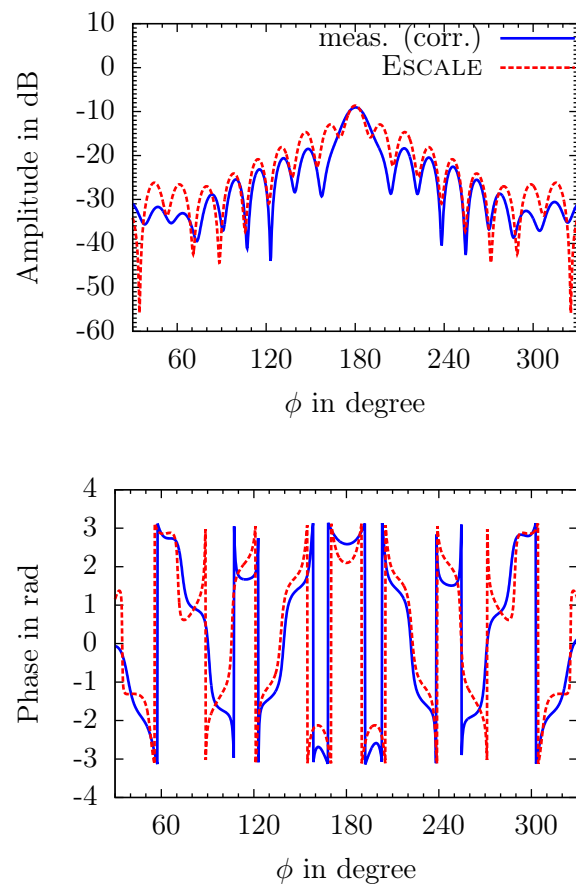


Fig. 3.35: Calibrated and normalized measured scattered field of dielectric cylinder, $f = 75$ GHz, in amplitude (top) and phase (bottom). In simulation with ESCALE a diameter of 15.4 mm, an $\epsilon_r = 2.49$ and a $\sigma = 0.1243$ S/m have been taken to characterize the dielectric cylinder.

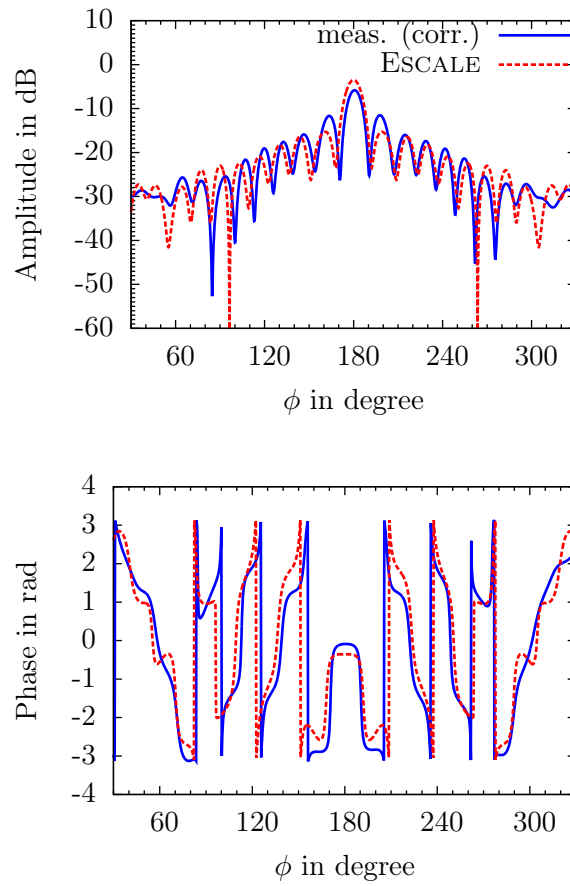


Fig. 3.36: Calibrated and normalized measured scattered field of dielectric cylinder, $f = 92.5$ GHz, in amplitude (top) and phase (bottom). In simulation with ESCALE a diameter of 15.4 mm, an $\epsilon_r = 2.49$ and a $\sigma = 0.1243$ S/m have been taken to characterize the dielectric cylinder.

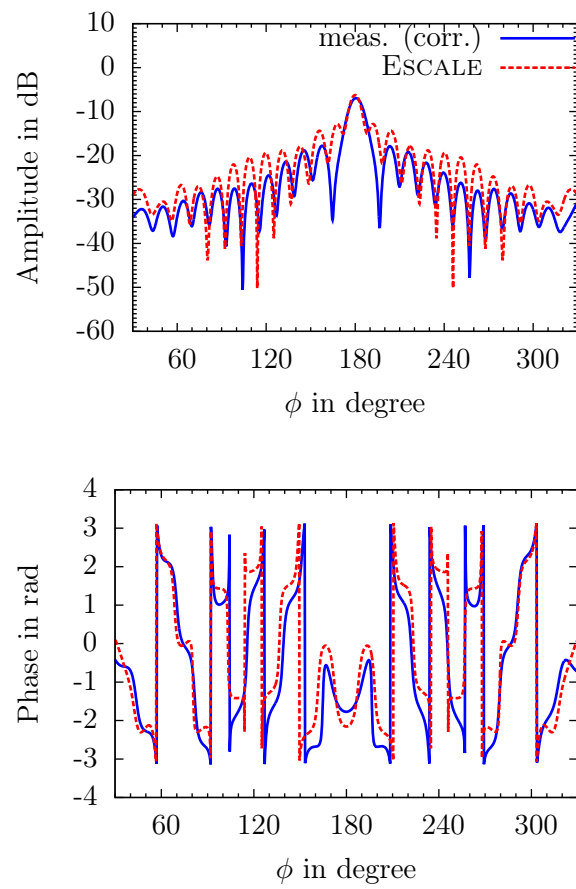


Fig. 3.37: Calibrated and normalized measured scattered field of dielectric cylinder, $f = 110$ GHz, in amplitude (top) and phase (bottom). In simulation with ESCALE a diameter of 15.4 mm, an $\epsilon_r = 2.49$ and a $\sigma = 0.1243$ S/m have been taken to characterize the dielectric cylinder.

3.5.2 Overall Calibration Performance and Measurement Error

The SNR for all three targets and frequencies is summarized in Tab. 3.6 before and after filtering. As expected, the highest values are obtained for the large cylinder

	f in GHz	SNR in dB	SNR in dB
		before filtering	after filtering
Metallic cylinder $D = 20$ mm	75	9.02	15.32
	92.5	11.54	15.0
	110	13.95	15.75
$D = 8$ mm	75	9.24	10.70
	92.5	9.26	10.34
	110	7.85	9.37
Dielectric cylinder $D = 15$ mm	75	3.59	5.56
	92.5	4.12	6.0
	110	4.79	5.53

Tab. 3.6: The SNR before and after filtering for 1501 points of measurement.

that has been used as reference target for calibration. Before the filtering was applied, values varied from 9 to 14 dB. The latter has been obtained for the highest frequency. After filtering, the SNR is almost constant above 15 dB for all frequencies. For the small cylinder the start SNR is between 7.85 dB for 110 GHz and 9.26 dB for 92.5 GHz. The final values for the SNR are less than for the large cylinder and vary from 9.37 dB at 110 GHz to 10.7 dB for 75 GHz. The dielectric cylinder comes with the worst SNR. After filtering, where the patterns match well the analytic solution, the best SNR for this target is 6 dB for 92.5 GHz.

3.5.3 Mechanical Precision Versus Measurement Error

As mentioned above, working at mm-waves emphasizes the effects of mechanical errors. Therefore, the impact of the swivel arm's shift has been evaluated versus the measurement error e (3.10). The latter has been calculated as function of r_{circle} . For this, simulations were conducted taking into account the swivel arm's shift. The resulting scattered fields are used as measured fields in the error formula. The measurement error versus r_{circle} for the large cylinder with $D = 20$ mm at 92.5 GHz is plotted in Fig. 3.38.

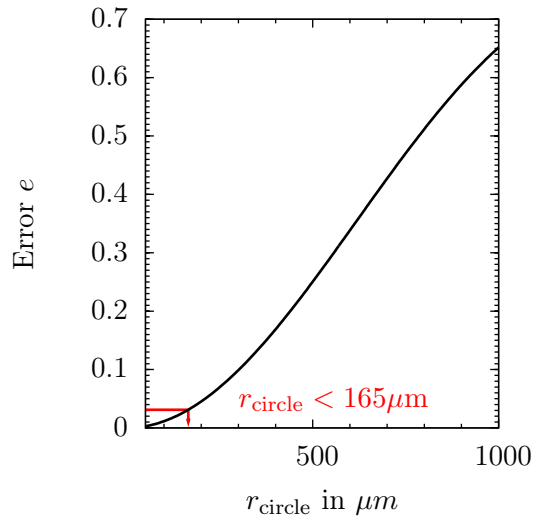


Fig. 3.38: Error e as function of shift r_{circle} out of the center position, cylinder $D = 20 \text{ mm}$, $f = 92.5 \text{ GHz}$.

Interesting is that a SNR of 15 dB ($e = 3.2\%$), that is our actual value after calibration and filtering with the presented slope detection, corresponds to a swivel arm positioning precision of $165\mu\text{m}$. This value is relevant since it roughly corresponds to a twentieth of the wavelength. Obtaining this precision is not straightforward even with an optical alignment system and is certainly not cost effective, on the contrary to the post-processing developed in the proposed correction scheme.

According to the good performance of the measurement system after calibration, measured data have been used for quantitative imaging as described in the next chapter.

3.6 Conclusion

In the presented chapter, the scattered field of two different metallic and one dielectric cylinders has been extracted for 75, 92.5 and 110 GHz to demonstrate the feasibility in W-band. For this purpose, a very compact extension to the already existing equipment in an anechoic chamber has been built: the antennas, which are small and not very directive, have been mounted very close to the targets. Additionally, the mixers have been located next to the emitting and receiving antennas. Thereby, the mm-wave part is clustered to minimize phase errors due to long transmitting distances at mm-wave frequencies. For this, we took advantage of the short wavelength value to build a small size system ($0.7 \text{ m} \times 0.6 \text{ m}$) and used post-processing to correct misalignment errors as well as to reduce the noise. An original filtering has been developed that does not require a-priori knowledge of the target. This is a key point in the perspective of inversion of unknown objects. It has been successfully applied to measured data and validated in simulations on irregular objects under AWGN. Finally the large metallic cylinder is used as

reference target for deriving the calibration coefficients. Averaged values of the signal to noise ratio over W-band are 15.4 dB, 10.1 dB and 5.7 dB for the large, the small metallic and the dielectric cylinders respectively. It has been shown that the proposed system is suitable for providing measurement results which can be successfully compared with the exact solution. Furthermore, it has been presented that an error in positioning of the target by 1.51 mm out of the center of rotation leads to a high degree of asymmetry in phase. This can be corrected by post-processing and points-out the benefit of having a symmetrical object in order to calibrate a more complete future system before measuring irregular objects.

Final comparisons obtained from corrected measured values give very good accuracy over the whole measured angular range.

Finally, the system sets the first basis for a more complex system capable to handle irregular objects. This extension requires an additional rotation of the emitting section, as this is not possible so far due to the limitation related to the mono-incidence.

Qualitative and Quantitative Reconstruction

The objective of this chapter is to validate the measurement system as well as the done post-processing, presented in the previous chapter, by use of the measurement results for qualitative and quantitative imaging.

4.1 Qualitative Imaging

In this section the goal is to obtain an image of a field distribution proportional to the polarization current J_p . Therefore, the complex scattered fields, measured by the receiver on different positions, have been back-propagated. This has been done for each frequency separately. This sum, presented in Subsection 2.3.1 (2.57), can be calculated directly with a matrix multiplication and allows a fast validation of the measurements and the applied corrections on one hand. On the other hand, as each field distribution is independently calculated from other cells, large areas can be taken into consideration as well with small pixels to obtain a resolution which corresponds to the physical one, the half of the wavelength. Afterwards, an incoherent sum over these images has been done (2.57) for each frequency and each emitter.

4.1.1 Localization of Targets

First of all, potential targets have to be detected in general in the whole measurement area. Therefore, it has been discretized by cells of $\lambda_{0,\min}/0.75$ and the measured complex scattered fields have been back-propagated (Fig. 4.1). The wavelength $\lambda_{0,\min}$ corresponds to the highest frequency which is 110 GHz. The extracted scattered field from measurements has been directly used. Only a normalization with respect to the maximum of measured amplitudes has been done in order to overcome differences in the received power levels introduced by the used measurement equipment over the frequency band of interest. Therefore, no a-priori knowledge of the scatterer is required, which is also advantageous for future investigations and drove our choice to this approach for a first validation of the measurements. The image indicates the position on a circle of the 1501 points of measurement (white circle) as well as the localization of the fixed emitter (red cross). The image is blurred in a zone between the maximum, which corresponds to

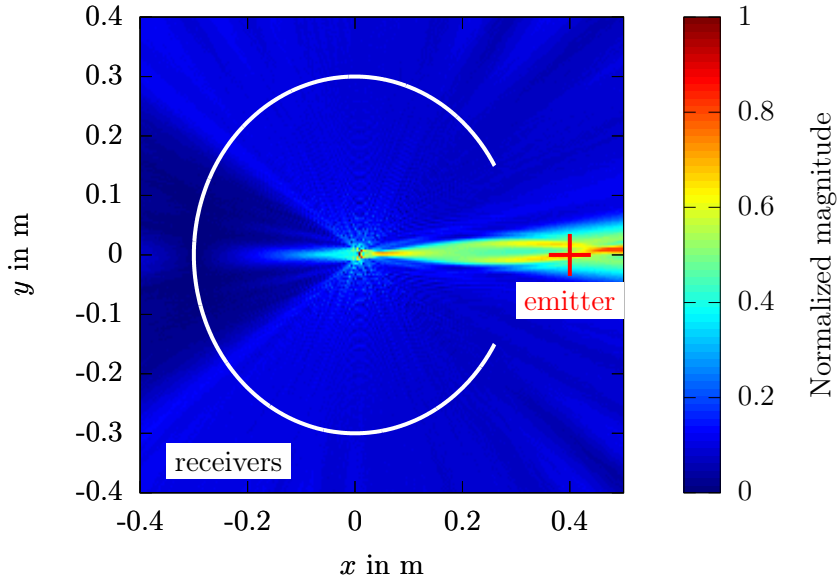


Fig. 4.1: Localization of potential objects in the measurement area. Image obtained with an incoherent sum over all frequencies (75, 92.5 and 110 GHz), 1501 receivers and 1 emitter. Discretization with $\lambda_{0,\min}/0.75 \approx 3.6$ mm.

the TUT and the emitter. This is also the case for scattered fields simulated over a complete circle of 360° . One could overcome this problem by using a coherent sum instead of the chosen incoherent one, that means (2.57) without $|\cdot|$. The drawback is that this only gives the position of a point scatterer and no information about the contour can be retrieved any more. Cells who contain high density are more visible after a zoom and show clearly the position of the scatterer, here the metallic cylinder with $D = 20$ mm (see Fig. 4.2 (top)). Finally, the domain for the reconstruction in this case can be drastically reduced.

The reduced domain as shown in Fig. 4.2 (bottom) has been higher discretized with $\lambda_{0,\min}/10$. One can directly see the good accordance with the image obtained with a back-propagation scheme using the adjoint operator $\mathbf{G}^{\text{R}*}$ presented in Section 2.3.1 (see Fig. 2.12 (bottom)). One would estimate the position of the contour of the TUT as indicated with the white circle. The misalignment, the shift between the actual position of the cylinder (black dashed cylinder) and the reconstructed contour (white cylinder), corresponds to the calculated calibration coefficients $r_{\text{circle}} = 1.51$ mm and $\beta = 290^\circ$. The results show that already with the measured raw data one can reconstruct the contour of the target under test closed to simulations. Additionally, the calibration coefficients found with the presented optimization in Section 3.4.2 are therefore validated.

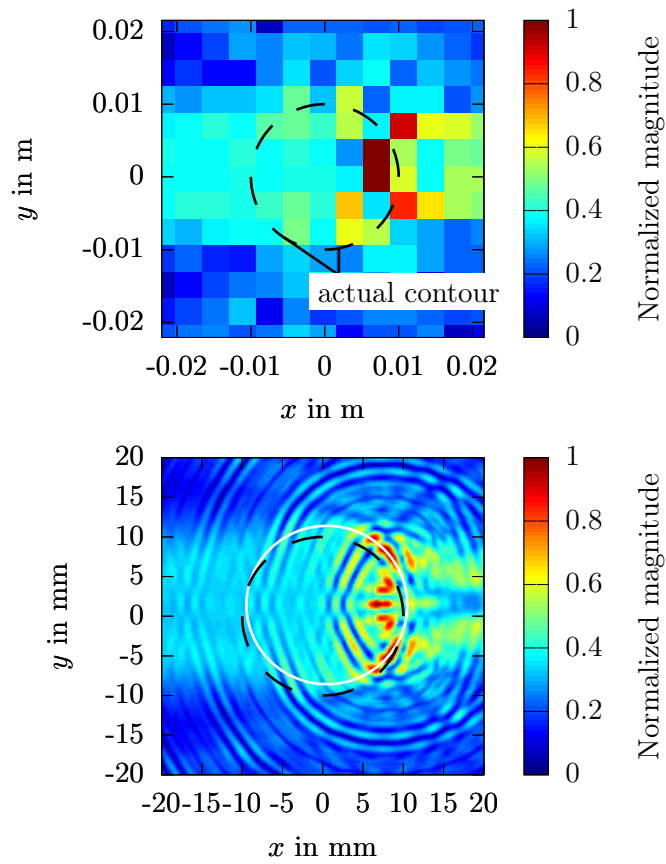


Fig. 4.2: Zoom in order to identify objects in the measurement area. Image obtained with an incoherent sum over all frequencies (75, 92.5 and 110 GHz), 1501 receivers and 1 emitter; discretized with $\lambda_{0,\min}/0.75 \approx 3.6$ mm (top) and discretized with $\lambda_{0,\min}/10 \approx 0.27$ mm (bottom).

4.1.2 Reconstruction

The extracted scattered fields have been calibrated and filtered. Again, only a normalization with respect to the maximum amplitude has been done as no a-priori information should be preconditioned. That means that for this studies the complex normalization, explained in Subsection 3.4.3, has not been applied here. The same normalization has been done with results obtained with the analytic solution for comparison purposes.

Calibration Target

Results obtained with the presented back-propagation algorithm are shown in Fig. 4.3 (left) and compared with simulations (Fig. 4.3 (right)) for the used calibration target. The results based on the calibrated and filtered measurements are in perfect accordance with the simulation. The actual measurement system has pro-

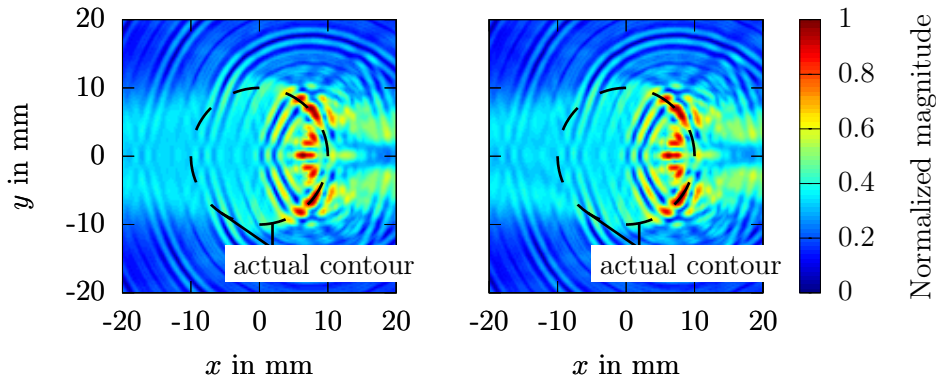


Fig. 4.3: Image obtained with an incoherent sum over all frequencies (75, 92.5 and 110 GHz), 1501 receivers and 1 emitter for a metallic cylinder of $D = 20$ mm. Discretization with $\lambda_{0,\min}/10 \approx 0.27$ mm. Results have been obtained in simulation with ESCALE (left) and in measurements (right).

vided measurements obtained with one incidence direction (single-incidence case) as the emitter has been fixed so far.

As the targets of interest have been axially symmetrical, the amplitude and the phase of the scattered fields are symmetrical as well. This is the case after the mentioned corrections. That's why one can expect exactly the same results for any other incidence direction. Consequently, multi-incidence/multi-view data can be obtained by rotation of the single-incidence/multi-view measurements provided by our setup. Therefore, the same measured and corrected scattered fields have been shifted 35 times by 10° in order to suppose over all 36 emitters. The scattered fields have been taken into account for 36 virtual emitters. It has been a trade-off between having a well described surface of the targets of interest and also an acceptable time for simulations. In order to improve the results some image-processing can be done: investigations in smoothing and methods to increase the contrast of images based on radar measurements have been done in [94]. The chosen approach makes use of

a-priori information on the object to be reconstructed as modeled with homogeneous areas separated by border-like discontinuities. This is the case for all three measured homogeneous targets. To enhance the contrast of the final image only pixels who are at least 3 dB over the averaged image energy have been taken into account. This approach has been already successfully applied to images obtained with a FMCW-radar in the W-band [33] and is here further investigated. Final results are presented

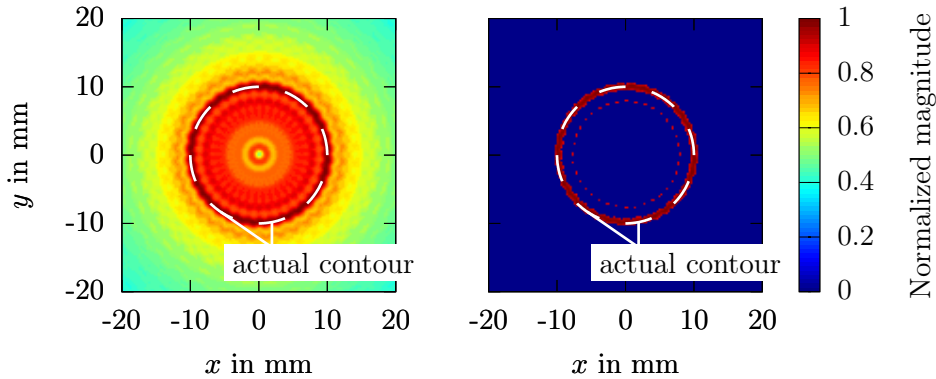


Fig. 4.4: Image obtained from measurements with an incoherent sum over all frequencies (75, 92.5 and 110 GHz), 1501 receivers and 36 assumed emitters for a metallic cylinder of $D = 20$ mm. Discretization with $\lambda_{0,\min}/10 \approx 0.27$ mm. The image $S(x, y)$ is presented without processing (left) and with cells having energy at least 3 dB more than the averaged energy of the image (right).

in Fig. 4.4 and show the main benefit of using millimeter waves. This is the high absolute resolution provided by the short wavelength. The results show that there is a perfect accordance between the actual contour of the TUT and the simulation.

Metallic Circular Cylinder

Results after back-propagation for the metallic cylinder of 8 mm in diameter, calibrated with the large cylinder, are compared with simulations in Fig. 4.5. Only minor differences are visible in the back-scattered region. The image obtained based on the calibrated measurements is perfectly symmetric which shows the validity of the applied post-processing with the presented calibration scheme. Final results are shown in Fig. 4.6. The reconstructed contour corresponds perfectly to the actual one. A zone of strong field distribution of three cells around the actual contour exists which corresponds to a half of the wavelength. The investigated area has been discretized with $\Delta = \lambda_{0,\min}/10$. Three cells are close to the half of the wavelength. That is the theoretical resolution. The maximum of the image corresponds perfectly to the actual contour.

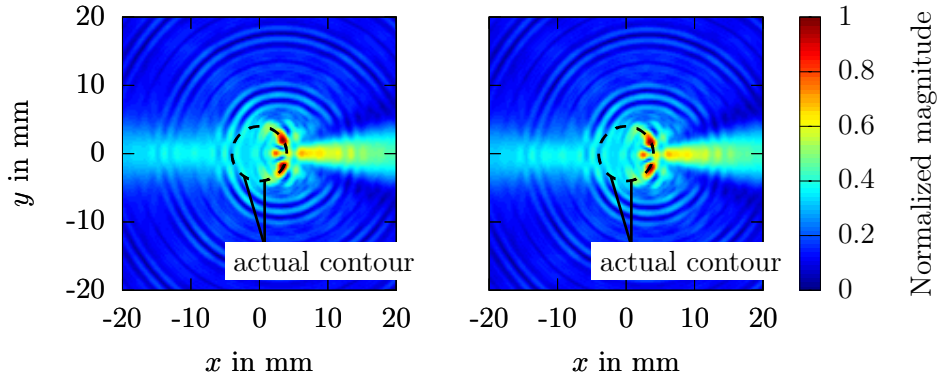


Fig. 4.5: Image obtained with an incoherent sum over all frequencies (75, 92.5 and 110 GHz), 1501 receivers and 1 emitter for a metallic cylinder of $D = 8$ mm. Discretization with $\lambda_{0,\min}/10 \approx 0.27$ mm. Results have been obtained in simulation with ESCALE (left) and in measurements (right).

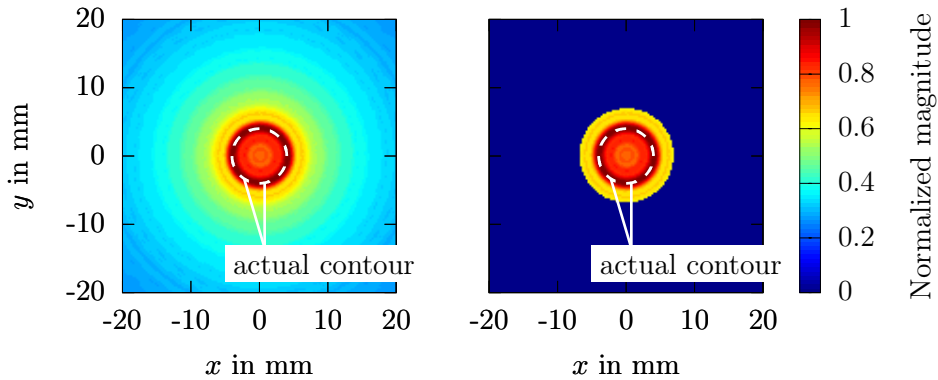


Fig. 4.6: Image obtained from measurements with an incoherent sum over all frequencies (75, 92.5 and 110 GHz), 1501 receivers and 36 assumed emitters for a metallic cylinder of $D = 8$ mm. Discretization with $\lambda_{0,\min}/10 \approx 0.27$ mm. The image $S(x, y)$ is presented without processing (left) and with cells having energy at least 3 dB more than the averaged energy of the image (right).

Dielectric Circular Cylinder

In Fig. 4.7 results are shown for the target with the worst SNR. Differences in the field distribution are visible. The zone where the maximum is located, on the opposite side from the emitter, is the same in the image obtained with measurements and the one based on simulation. These field distributions are typical for dielectric objects where strong fields occur due to the reflection at the surface between air and the dielectric medium [95].

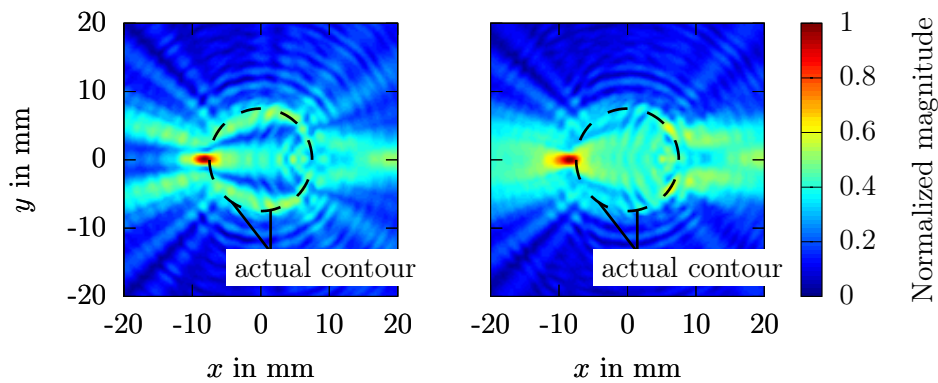


Fig. 4.7: Image obtained with an incoherent sum over all frequencies (75, 92.5 and 110 GHz), 1501 receivers and 1 emitter for a dielectric cylinder of $D = 15$ mm. Discretization with $\lambda_{0,\min}/10 \approx 0.27$ mm. Results have been obtained in simulation with ESCALE (left) and in measurements (right).

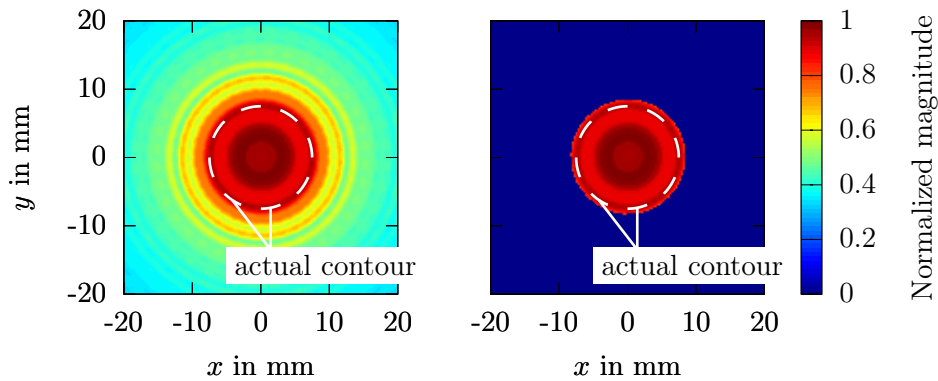


Fig. 4.8: Image obtained from measurements with an incoherent sum over all frequencies (75, 92.5 and 110 GHz), 1501 receivers and 36 assumed emitters for a dielectric cylinder of $D = 15$ mm. Discretization with $\lambda_{0,\min}/10 \approx 0.27$ mm. The image $S(x,y)$ is presented without processing (left) and with cells having energy at least 3 dB more than the averaged energy of the image (right).

Final results are shown in Fig. 4.8. The contour of the dielectric cylinder has been perfectly reconstructed. This has been possible even with an averaged SNR less than 6 dB.

The presented results have shown that the measured results and the applied post-processing are suitable for imaging in the W-band. The contour of two metallic and one dielectric cylinders has been perfectly reconstructed. The contour precision is about $\lambda_0/2$ which corresponds to the theoretical limit. Based on the knowledge of the area for simulation, which is required for reconstruction, a more intensive inverse problem algorithm has been investigated and results are shown in the next section.

4.2 Quantitative Imaging

In this chapter results obtained with quantitative imaging applied to the already measured scattered fields are presented.

The in the following presented results were obtained as already mentioned in cooperative work with A. Moynot, Ph.D. student at the LEAT, who investigates the inverse problem. As the measurement system should be validated we took advantage of the already developed inverse problem algorithms successfully applied to two dimensional objects at LEAT: starting from the direct problem solver that is an integral representation of the electric field (EFIE), and applying a moment method solution, as explained in detail in Subsection 2.2.1, an iterative algorithm is used based on a bi-conjugate gradient method for reconstructing the relative permittivity and conductivity (i.e. complex permittivity profile) of the objects under test. Details on the global procedure of the 2D-inversion have been explained in Section 2.4. The novelty here is to apply these algorithms in the mm-wave domain now.

The large metallic cylinder has not be taken for inversion as it had been the calibration target. As so far no regularization scheme has been investigated, the dielectric cylinder is not studied for inversion. Therefore, the small cylinder is used as object for quantitative reconstruction at the three test frequencies. It requires the smallest domain for reconstruction and results in the lowest number of variables to reconstruct of all three measured targets.

In the past, the quantitative reconstruction has been initialized with or without initial guess, i.e., the starting value is zero contrast. In order to start the iterative procedure of a conjugate-gradient method with an initial guess, a back-propagation scheme has been investigated [19, 34, 35, 46]. The iterative algorithm has been determined with the specification of the starting value \mathbf{C}_0 for the contrast. The convergence of the algorithm depends also on this initial guess. This has been calculated with a back-propagation method, using the adjoint operator $\mathbf{G}^{\text{R}*}$ (see Subsection 2.3.1). This allows to provide an estimate of the induced current J_p inside

the object. This approach comes with the associated cost of more computation time with the danger of becoming trapped in a local minimum [42]. That's why the quantitative inversion has been initialized with a contrast equal to zero. The results obtained with the back-propagation have been used to determine the area, which has to be discretized for reconstruction. This is an important point because the number of cells fixes the time for inversion first and the convergence of the inversion depends as well mainly on the number of cells.

Before going into the inversion of the results one has to discuss the number of measurement points to take for the inversion. In [96] it is demonstrated that for the single incidence case with M receivers placed on a circle, the number of points M required for the inversion should not exceed:

$$M = \lceil \beta D \rceil \quad (4.1)$$

D being the object diameter and β the propagation constant and $\lceil \cdot \rceil$ gives the first integer superior or equal to βD . The value M also represents the number of degrees of freedom for the inversion, therefore, increasing the number of receivers, will be time consuming but not more efficient. Of course, working with a single incidence is not enough for reconstructing the entire object and in [96] the multi-incidence criteria is also given. The upper limit for the degrees of freedom is stated with $M^2/2$. Considering that the number of receivers is M we can deduce the number of emitters as:

$$L = \left\lceil \frac{M^2}{2M} \right\rceil, \text{ that is } L = \left\lceil \frac{M}{2} \right\rceil. \quad (4.2)$$

In our case, having a diameter of 8 mm and considering the highest operating frequency value of 110 GHz one obtains $M = 19$ and $L = 10$. Therefore, the inversion should be implemented with 19 receivers and 10 emitters. Considering our measurement step of 0.2° the closest possible value for the emitters has been chosen that is 12. The number of receivers is 21 (slightly superior than the upper limit).

The 2D-domain for inversion has been discretized for all three frequencies with $\lambda_{0,\min}/10$ with $\lambda_{0,\min}$ being calculated for the highest frequency of interest which is 110 GHz. The already presented back-propagation algorithm has been first applied in order to estimate the size of the domain for inversion.

4.2.1 Estimation of the Domain's Size

The presented back-propagation has been applied to estimate the domain, which is further used for the quantitative inversion. Once again, one has to discuss the number of receivers M and emitters L which are needed for an accurate estimation of the domain's size. In our back-propagation algorithm we back-propagate plane waves. When the object is within a pixel this latter provides a higher signal than for pixels without object. The signal level also depends on the direction of the incidence:

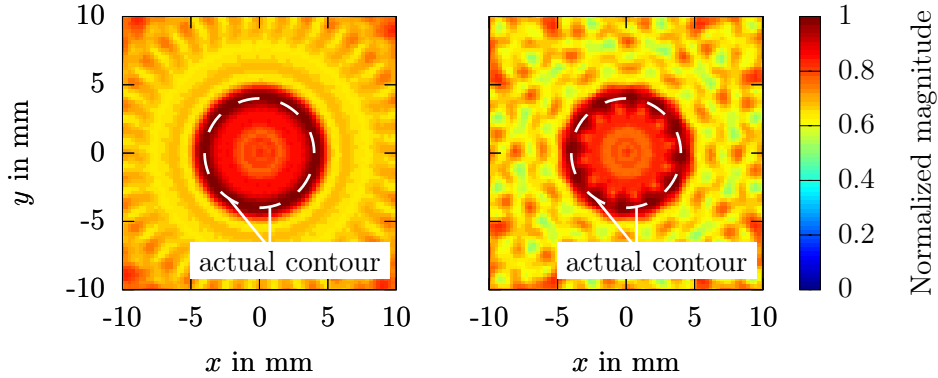


Fig. 4.9: Image obtained from measurements with an incoherent sum over all frequencies (75, 92.5 and 110 GHz), 21 receivers and 36 assumed emitters (left) and 21 receivers and 12 assumed emitters (right) for a metallic cylinder of $D = 8$ mm. Discretization with $\lambda_{0,\min}/10 = \sim 0.27$ mm.

it has been seen in Chapter 2 that with a single incidence one can get high signals (“hot spots”) on the cylinder contour only in front of the emitter (see Fig. 2.12). From this we conclude that working with multi-incidence will add more “hot spots” on the cylinder contour. In practice, one could count the number of incidences by counting these “hot spots”. For having a perfect shape reconstruction of the cylinder one has to increase the number of emitters until the different “hot spots” are superimposed and form a continuous contour. The influence of the number of receivers is quite different. By taking many receivers the wave-front is better discretized and grating lobes are avoided when the signal is back-propagated (typical when the distance between receivers is less than $\lambda_0/2$). This means that the contrast between pixels with and without object will be reinforced. For illustration purpose the Figures 4.6 and 4.9 show the influence of M and L . The ideal case with 36 emitters and 1501 receivers is considered and presented in Fig. 4.6. With this configuration, the distance between receivers is less than $\lambda_0/2$ at the highest frequency of 110 GHz. The contrast between the cylinder contour and outside is roughly 0.5 (3 dB). The object shape is continuous due to the high number of emitters. From this one can get the proper size of the domain that is going to be used for the inversion. If the number of receivers is reduced to 21, without changing the number of emitters, a continuous shape is obtained but the contrast is drastically decreased to 0.7 (1.5 dB). In this case, it becomes difficult to decide which domain has to be used for the inversion (see Fig. 4.9 (left)). Finally, applying the values of M and L from [96], these are 21 and 12, one has neither a high contrast nor a continuous shape (see Fig. 4.9 (right)). From this we conclude that for an accurate estimation of the size of the domain used in the inversion we need, in our case, 1501 receivers and at least 36 emitters. The results have shown (see Fig. 4.6) that the object of interest is located in a circle of ~ 8 mm diameter and therefore the square domain for reconstruction has been taken $8.910 \times 8.910 \text{ mm}^2$.

4.2.2 Expected Complex Permittivity Values

The next step is to apply the inverse problem algorithm. Before going into reconstruction results, one has to discuss about expected complex permittivity values. Metallic targets have been investigated in simulations with a relative permittivity of 1 and conductivity values usually up to several MS/m . Nevertheless, lower frequency reconstructions [19] have shown that conductivity values of 7 to 8 S/m were retrieved for metallic objects. The reasons that limit the actual sigma values is the lack of significant difference between scattered field results when sigma reaches a certain value. In the Subsection 2.4.2 expected sigma values as function of the SNR have been theoretically investigated. The shown results cannot be taken directly as reference for expected values obtained by the inversion. As shown in Fig. 2.15 one gets for an SNR of 10 dB, which can be obtained in measurements with the small metallic cylinder, a sigma between 25 S/m and 50 S/m . This shows the introduced SNR by approximation a PEC with a cylinder having a finite conductivity by taking the exact solution. One has also to take into account the influence of the used algorithm to calculate the direct problem, who introduces numerical noise due to the discretization of the domain. In order to estimate it, the SNR has been again computed versus sigma values. The reference signal, the exact solution, assumes an infinite conductivity whereas sigma values are varying for $E_{\text{sim.,norm.}}^{(s)}$ calculated with FLEXIMOM. SNR versus sigma has been computed at the central frequency of the W-band. The results presented in Fig. 4.10 show logically that the SNR increases with sigma but also that it saturates for values of sigma far below the physical order of magnitude of several MS/m .

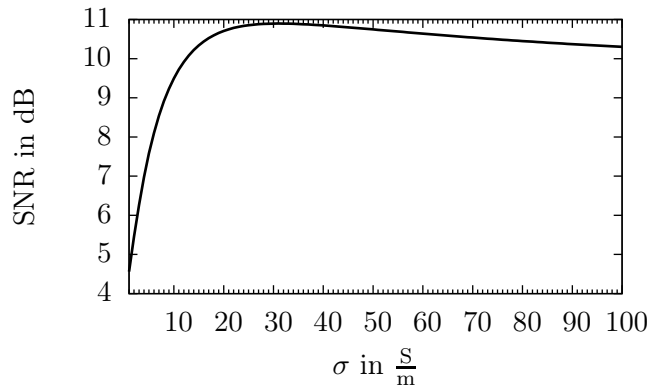


Fig. 4.10: SNR calculated as function of σ for 751 receivers, cylinder $D = 8$ mm, $f = 92.5$ GHz. The expected value of sigma after reconstruction is indicated based on the SNR of the calibrated and normalized measurements.

4.2.3 Inversion Results

In a first step results are presented for 751 receivers. The extracted scattered fields have been used for reconstruction after its calibration, filtering and normalization.

This has been done for 751 points of measurement that means every second point is taken from the 1501 available points in order to accelerate the process to obtain rapidly first results. Simulations with 1501 has been investigated but only marginal differences have been visible. A-priori information concerning the range of the searched values of the permittivity and conductivity profiles can be easily incorporated in the reconstruction algorithm. Therefore, a study on the influence of a-priori information (minimum and maximum values) of the complex permittivity is quite of interest. For the results presented hereafter, the minimum and maximum values for the permittivity and conductivity are, respectively, $\varepsilon_{r,\min} = 1.0$, $\varepsilon_{r,\max} = 1.2$; $\sigma_{\min} = 0 \text{ S/m}$, $\sigma_{\max} = 100 \text{ S/m}$. Results after 100 iterations are shown in Fig. 4.11.

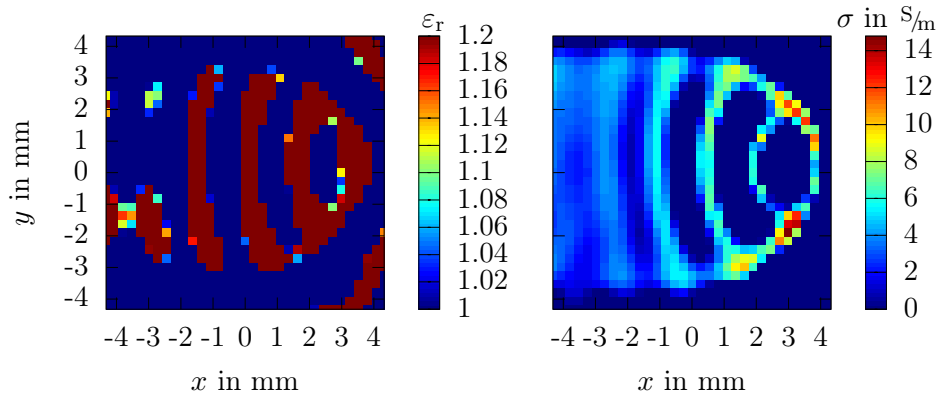


Fig. 4.11: The relative permittivity (left) and the conductivity (right) reconstructed with 100 iterations (751 receivers, 1 emitter, 92.5 GHz, discretization with $0.27 \text{ mm} \approx \lambda_{0,\min}/10$). Scattered fields of the cylinder, $D = 8 \text{ mm}$, have been measured in a distance of 300 mm.

As expected, for the one emitter configuration almost one half of the contour could be retrieved as it has been also the case with the back-propagation scheme. The maximum value for the conductivity is 14.79 S/m . Minor discrepancies in symmetry haven't been visible anymore in results obtained with the back-propagation. Here the asymmetry results in small deviations of the calculated values of ε_r and σ .

The symmetry of the results has been again taken into account as already done for the back-propagation scheme and has been explained in Subsection 4.1.2. Therefore, the number of illuminations symmetrizing the set of measurements has been increased in order to simulate different number of angles (8, 12, 15 and 18 angles of incidence). Results are presented in [123].

Results of reconstruction after 100 iterations for 75 GHz are shown in Fig. 4.12.

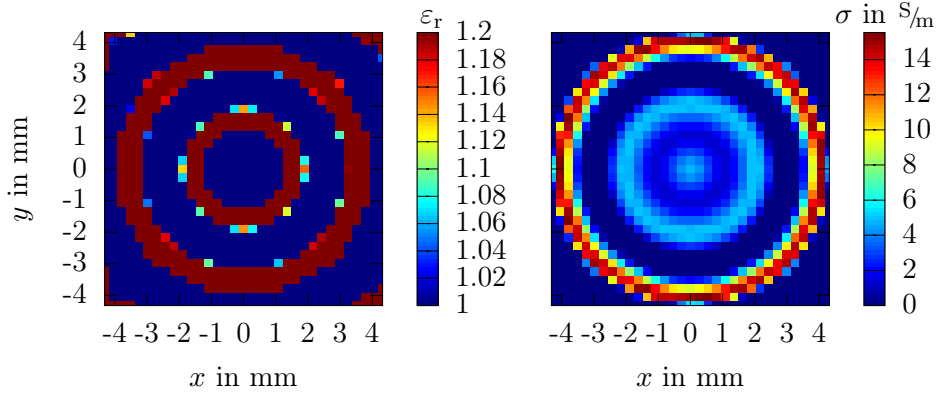


Fig. 4.12: The relative permittivity (left) and the conductivity (right) reconstructed with 100 iterations (751 receivers, 15 emitters, 75 GHz, discretization with $0.27 \text{ mm} \approx \lambda_{0,\min}/10$). Scattered fields of the cylinder, $D = 8 \text{ mm}$, have been measured in a distance of 300 mm.

At this frequency the best SNR for this target, 11.7 dB, has been provided. The results are in perfect accordance with the actual contour of the cylinder. The maximum sigma value on the reconstructed contour is 15.54 S/m .

For the center frequency, where a SNR of 10.34 dB has been obtained, the results are presented in Fig. 4.13.

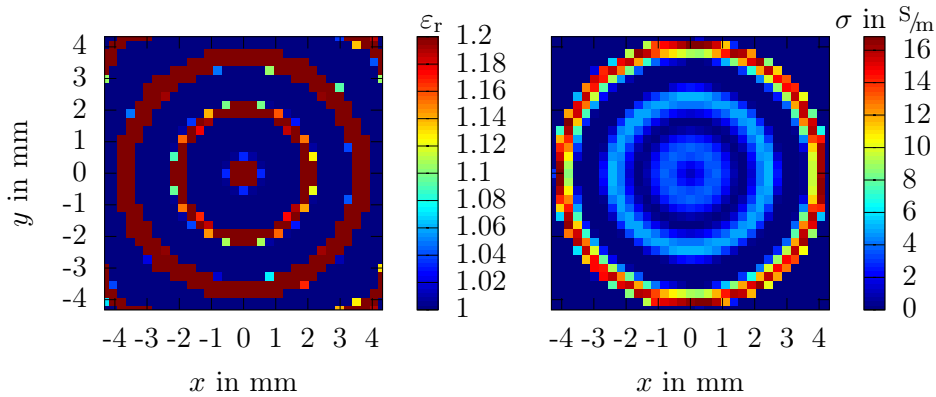


Fig. 4.13: The relative permittivity (left) and the conductivity (right) reconstructed with 100 iterations (751 receivers, 15 emitters, 92.5 GHz, discretization with $0.27 \text{ mm} \approx \lambda_{0,\min}/10$). Scattered fields of the cylinder, $D = 8 \text{ mm}$, have been measured in a distance of 300 mm.

Again, the contour of the cylinder could be perfectly reconstructed with a maximum value for sigma of 16.83 S/m .

For the highest frequency the results for the complex permittivity are shown in Fig. 4.14. This frequency corresponds to the worst case for the quality of the input data (i.e. measured scattered fields) with a SNR of 9.37 dB as well as for

the inversion algorithm because it is where the domain has the lowest discretization.

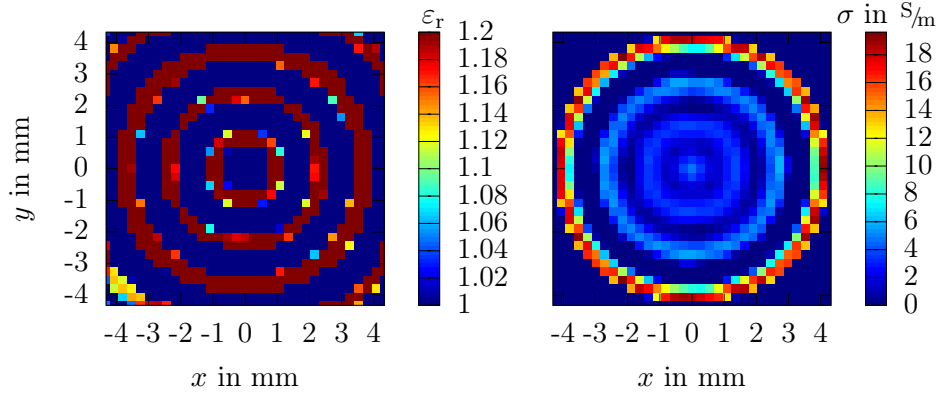


Fig. 4.14: The relative permittivity (left) and the conductivity (right) reconstructed with 100 iterations (751 receivers, 15 emitters, 110 GHz, discretization with $0.27 \text{ mm} \approx \lambda_{0,\text{min}}/10$). Scattered fields of the cylinder, $D = 8 \text{ mm}$, have been measured in a distance of 300 mm.

The Fig. 4.15 demonstrates that the presented results for 110 GHz have been obtained with the worst convergence of the cost function $J(\mathbf{C})$.

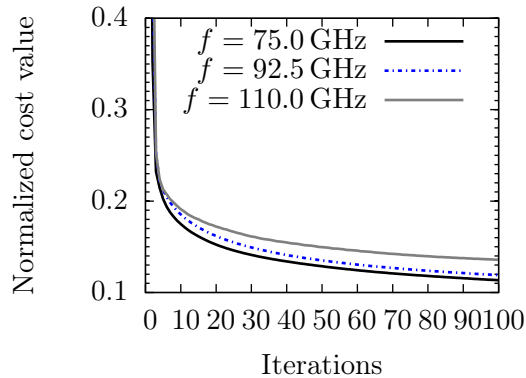


Fig. 4.15: Normalized cost values for each iteration obtained for 75, 92.5 and 110 GHz separately.

The contour of the cylinder has been retrieved with a sigma value of 19.62 S/m . This is almost three times higher than at lower frequencies (10 GHz, [19]). For the so far presented results one can conclude that with increasing frequency the obtained sigma value also increases.

In order to improve the former results (that is to retrieve higher values for sigma), the number of receivers and emitters is now chosen according to [96]. Because of the discretization of 0.2° of the measured field we cannot exactly match the 19 receivers and 10 emitters and have to chose 21 receivers and 12 emitters. Results are shown in Fig. 4.16, Fig. 4.17 and Fig. 4.18 for 75 GHz, 92.5 GHz and 110 GHz respectively.

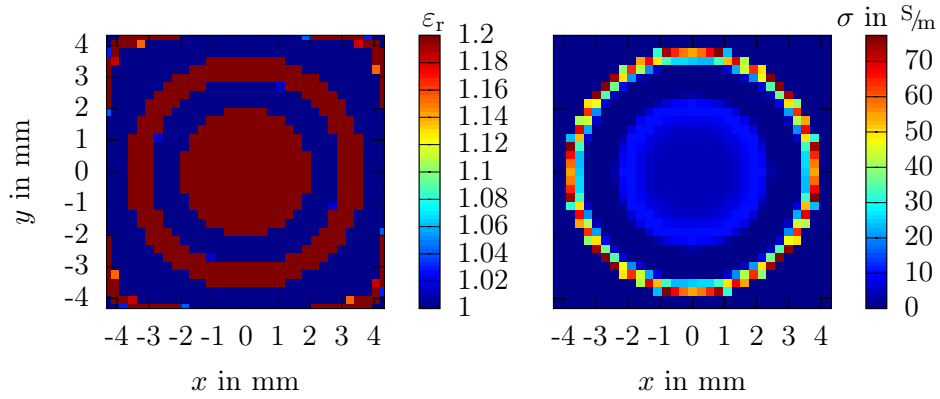


Fig. 4.16: The relative permittivity (left) and the conductivity (right) reconstructed with 1000 iterations (21 receivers, 12 emitters, 75 GHz, discretization with $0.27 \text{ mm} \approx \lambda_{0,\min}/10$). Scattered fields of the cylinder, $D = 8 \text{ mm}$, have been measured in a distance of 300 mm.

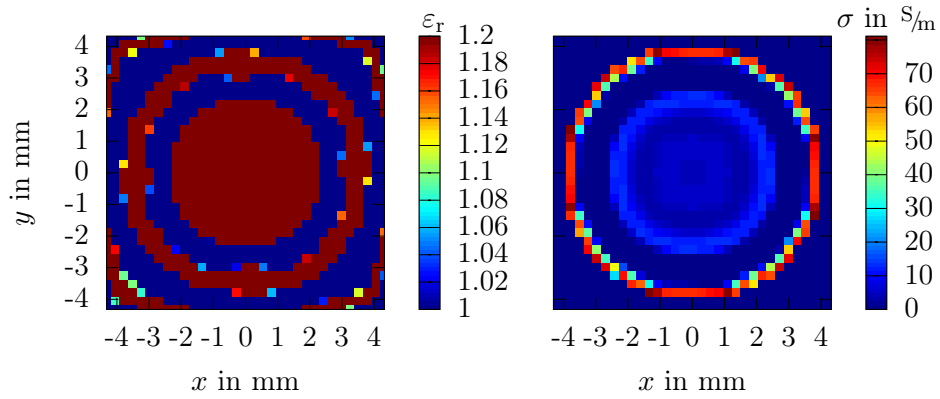


Fig. 4.17: The relative permittivity (left) and the conductivity (right) reconstructed with 1000 iterations (21 receivers, 12 emitters, 92.5 GHz, discretization with $0.27 \text{ mm} \approx \lambda_{0,\min}/10$). Scattered fields of the cylinder, $D = 8 \text{ mm}$, have been measured in a distance of 300 mm.

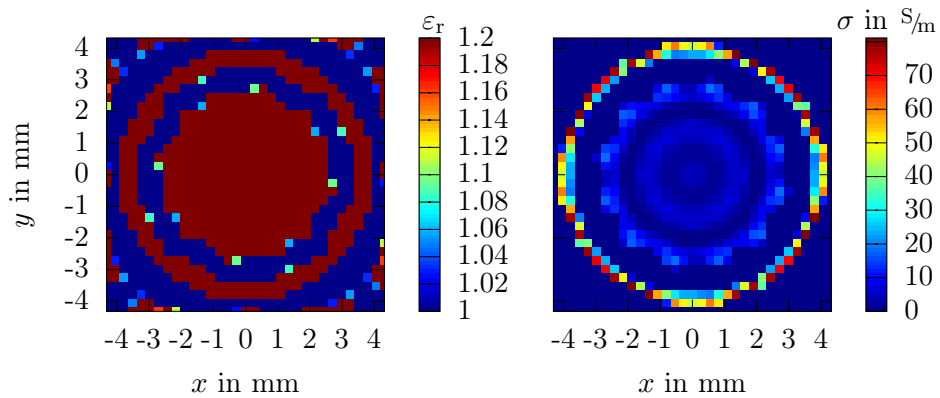


Fig. 4.18: The relative permittivity (left) and the conductivity (right) reconstructed with 1000 iterations (21 receivers, 12 emitters, 110 GHz, discretization with $0.27 \text{ mm} \approx \lambda_{0,\min}/10$). Scattered fields of the cylinder, $D = 8 \text{ mm}$, have been measured in a distance of 300 mm.

Interesting is, that the values of sigma (the maxima are 77.37 S/m , 81.12 S/m and 81.08 S/m for 75 GHz, 92.5 GHz and 110 GHz) have now a scaling factor of 8 compared to the low frequency results at 10 GHz [19] that matches the frequency scaling factor. Together with the increase of sigma a better contrast between the cylinder contour and the rest of the domain is obtained.

4.3 Conclusion

In a first step, the contour of all three targets has been precisely reconstructed with a fast back-propagation scheme. In a second step, this results have been used to estimate the area for simulations with an inverse problem algorithm. The increase of the reconstructed values of sigma with higher frequencies points out the advantage of the short wavelength. The conjugate gradient algorithm presented here, and applied to measured scattered data has shown its effectiveness in the reconstruction of metallic objects. This method can be applied to any kind of lossy dielectric objects. Further investigations are going to be the reconstruction based on extracted scattered fields of the measured acrylic cylinder in future.

FMCW-Radar Measurements

5.1 Introduction of Application

The so far presented investigations have been done in a laboratory environment: the targets of interest have been isolated. Therefore, it has been possible to measure the scattered field with a set of receivers surrounding the TUT. Additionally, the studied objects have been embedded in an homogeneous background. The targets have been successfully localized and qualitatively and quantitatively retrieved. For practical applications the number of receivers is drastically limited. Additionally, the objects of interest can be found in an inhomogeneous environment. Millimeter-wave systems are already used for the detection and localization of small objects due to the high resolution provided by the small wave-length. These systems are pushed to identification nowadays that means the extension to imaging. In the following, the motivation of the chosen application, the detection of FOD, is introduced. Furthermore, the limitations of detection capabilities should be investigated with a mm-wave system assembled with two transmitters to set a first basis to estimate possibilities for quantitative imaging in future in the W-band.

The detection of FOD on airports becomes more and more important. It has been estimated that FOD damage costs the aerospace industry over \$4 billion (US) per year, mostly in the costs associated with engine damage and loss of use of the aircraft. At its worst, FOD can lead to loss of life as seen in the Concorde accident of July 2000. Air France Flight 4590 crashed after departing from Charles de Gaulle International Airport near Paris, France. The aircraft had run over a piece of titanium debris on the runway.

Since over 5 years, several companies have developed, proposed and tested automated FOD detection systems. Different approaches have been investigated: the TARSIER by QINETIQ [97] is based on mm-wave radar modules operating around 94.5 GHz and has been recently completed by a camera for identification purposes. Two large radar modules are necessary for covering one runway. On the other hand, optical-based systems have also been proposed: they are based on CCD camera, LIDAR or LADAR equipments [98,99]. The latter are the most performing regarding identification capabilities but performances are greatly decreased under bad weather conditions. Another approach also uses millimeter-wave radar but within the 77 GHz band [100,101]. Although it is less favorable than the 94 GHz one for propagation, it benefits from the low-cost MMICs developed for the automotive cruise control application. In addition to that, the possibility to work with a

bandwidth of 5 GHz improves the range resolution [116,118]. TREX ENTERPRISE'S FODFINDER, that uses infrared cameras and mm-wave radar mounted on the roof of a vehicle, provides FOD detection also on taxiways, apron areas etc. due to its mobility [102]. The LAOTSE PROJECT investigates up to 220 GHz. The system comprises an infrared camera, optical 2D and 3D cameras, and networked radar sensors [103]. Some of the above mentioned approaches [97,98,101,102] have been already evaluated by the Federal Aviation Administration (FAA) in order to develop performance standards for FOD detection systems [104].

The chosen system configuration for our study is shown in Fig. 5.1 [8] [121]. The FOD detection system consists of several small low power and low cost sensors, developed within the work presented in [69,105], placed near the runway, each of them covering a given part of it.

Up to now, the two-dimensional back scattering map of the runway surface has been obtained by mechanically scanning the sensor. The following approach, presented in Section 2.3.2, is different: it has been shown that imaging is possible by performing separate measurements from two different positions using wide-beamwidth antennas [2,68,106] for 24 GHz at least in the close range. This approach is investigated in the following in the W-band firstly with a vector measurement equipment and secondly with a mm-wave radar system.

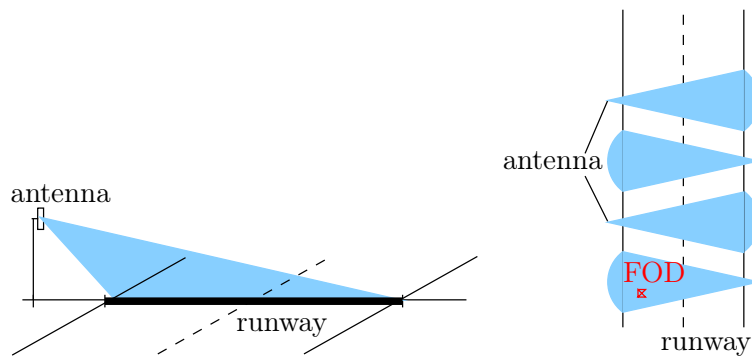


Fig. 5.1: Runway surveillance system consisting of mm-wave sensors located at both sides of the runway.

5.2 Theoretical Results - Simulation

Before going into measurements, investigations have been done in simulation. Therefore, the targets already presented in Tab. 3.2 have been chosen as targets of interest and are indicated in the following as shown in Tab. 5.1. They have been located as shown in Fig. 5.2. This is close to the configuration presented in [2] where a center frequency of 24 GHz with a bandwidth of 1 and 11 GHz respectively has been studied. The scene has been illuminated with one line source located at $(0.75|0.0)$ named as port 1 in Fig. 5.2 and the scattered fields have been simulated at port 1, which is proportional to S_{11} , and at port 2, which corresponds to S_{12} . Afterwards port 2 has been used as illuminator. The so simulated scattered fields have been back-propagated with (2.58).

Target 1	metal cylinder	diameter	D	$20 (\sim 5 - 7.5\lambda_0)$	mm
Target 2	metal cylinder	diameter	D	$8 (\sim 2 - 3\lambda_0)$	mm
Target 3	dielectric cylinder	diameter	D	$15 (\sim 3.75 - 5.5\lambda_0)$	mm

Tab. 5.1: Chosen targets for simulation with their dimensions. The diameters in brackets are given for the lowest and highest frequencies in the W-band.

On one hand, the whole W-band from 75 to 110 GHz has been investigated in order to show possibilities which are given in a laboratory environment with a vector network analyzer. On the other hand, a limited bandwidth of 5 GHz with a center frequency of 77.5 GHz, the one used by our radar system, has been simulated. Simulations have been carried out with ESCALE. The coupling scattering effects between the various targets is not taken into account. In both cases 3201 frequencies have been taken. This is a good trade-off in having an acceptable time of computation by the simulation and of acquisition by the measurement. The scattered fields have been used as input for the back-propagation (2.58). Results are shown in Fig. 5.3. The amplitude of the radar image $S(x, y)$ is normalized with respect to the maximum of the whole image. The arrangement of the targets can be clearly recognized due to the circular and elliptical locus curves. For increasing distance, the response is widened as the angles between the two circles and the ellipse become increasingly smaller (see Fig. 2.13 for comparison). To show properly this effect the normalized magnitude in the 2D representation (see Fig. 5.3 (left)) has been limited to 0.01. Due to the presence of strong scatterers, here the two metallic cylinders, the dielectric cylinder is less visible. This problem could be overcome by dividing the investigated areas in zones or by cutting-out already detected and identified targets. One could for example exclude an area of $0.5 \times 0.5 \text{ m}^2$ for the strongest scatterer and then for the second strongest scatterer and so on. Ground staff at the airport would see if there is another FOD in this area when picking-up the detected target. Doing so, other FOD, like the dielectric cylinder here, would be directly much more visible then.

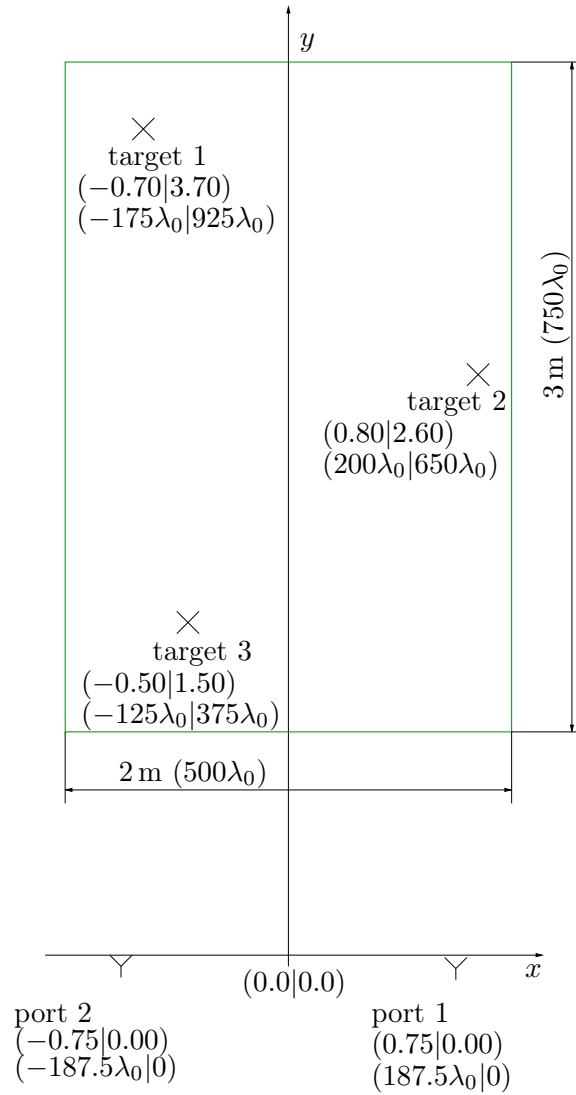


Fig. 5.2: Geometrical arrangement of two metal and one dielectric cylinders. Coordinates are given in meters and in terms of λ_0 for 75 GHz. The area inside the green rectangle $2 \times 3\text{ m}^2$ is used for further reconstructions.

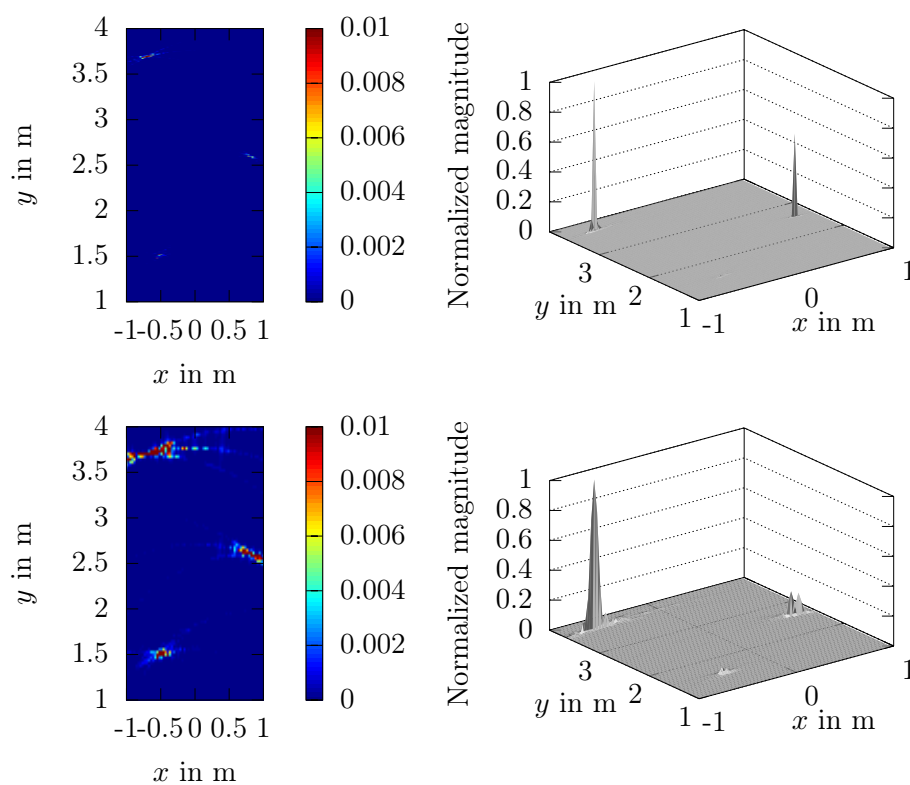


Fig. 5.3: Radar images of a three cylinders arrangement. Scattered fields have been simulated with ESCALE (3201 frequencies) for a bandwidth of 35 GHz (top) and 5 GHz (bottom).

5.3 Ideal Setup with Network Analyzer

In a first step, the simulated configuration with the both metallic and the dielectric cylinders has been investigated in measurements with a network analyzer. In a second step, real FOD are measured and results presented hereinafter.

5.3.1 Scene with Vertical Cylinders

Measurements have been done in a class room. In order to reduce reflections from tables and walls to a minimum they have been covered by absorber material as shown in Fig. 5.4 (bottom). The setup with the network analyzer in combination with mm-wave heads is presented in Fig. 5.4 (top). The measurements have been done with AGILENT'S PNA-X microwave network analyzer in combination with mm-wave modules [83, 84]. As shown in Fig. 5.4 (top) a stand alone vector network analyzer has been used as the so far presented equipment of the anechoic chamber, presented in Chapter 3, remains there as it is used permanently for antenna measurements.

Open ended waveguides have been used as antennas in order to have a wide illumination of the area of interest.

First, a measurement without the targets of interest has been done to measure the incident field $(A_z^{(i)}, \Phi^{(i)})$ in amplitude and in phase. Then, the cylinders have been installed and the total field has been measured $(A_z^{(t)}, \Phi^{(t)})$. Again with a vectorial subtraction the scattered fields of the targets of interest $(A_z^{(s)}, \Phi^{(s)})$ have been extracted. For the free space measurements the supports have already been taken into account. Results have shown, at least for the dielectric cylinder, that scattered fields from the target support have been dominant compared to the ones of the target of interest itself. The obtained radar images are shown in Fig. 5.5 and Fig. 5.6. The results are in excellent accordance with the simulations for a bandwidth of 35 as well as of 5 GHz.

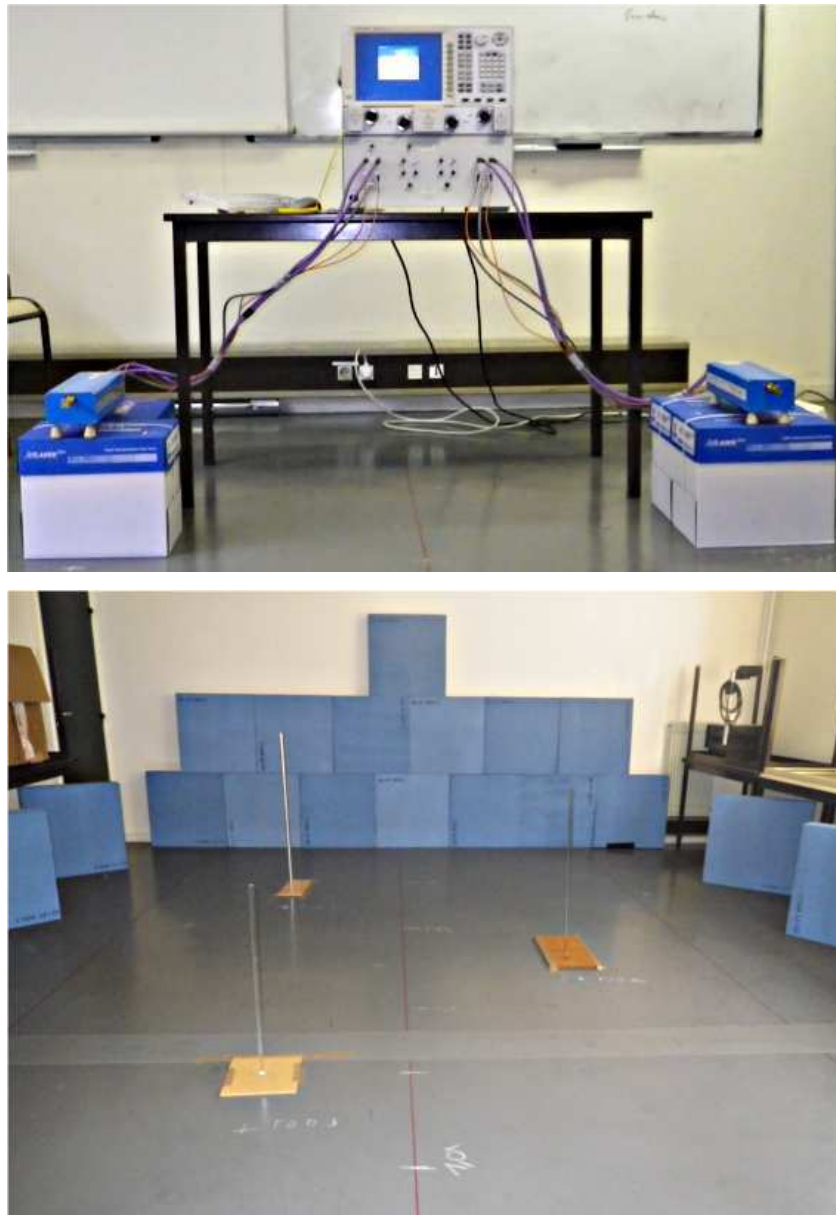


Fig. 5.4: Photograph of a three cylinders arrangement inside. Setup of the analyzer with two open ended waveguides as antennas (top). Scene of the three cylinders (bottom).

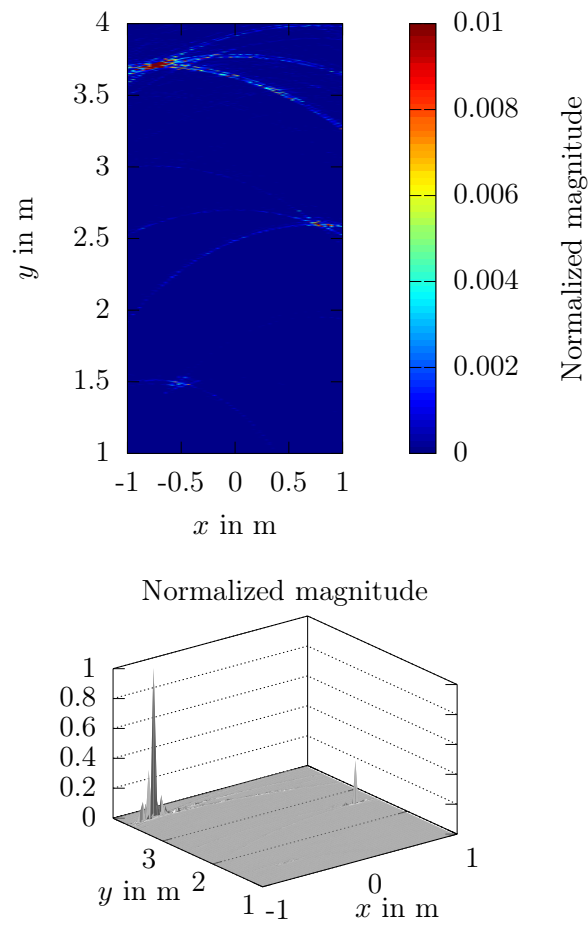


Fig. 5.5: Radar images of a three cylinders arrangement. Measurements have been done with the network analyzer (3201 frequencies) for a bandwidth of 35 GHz.

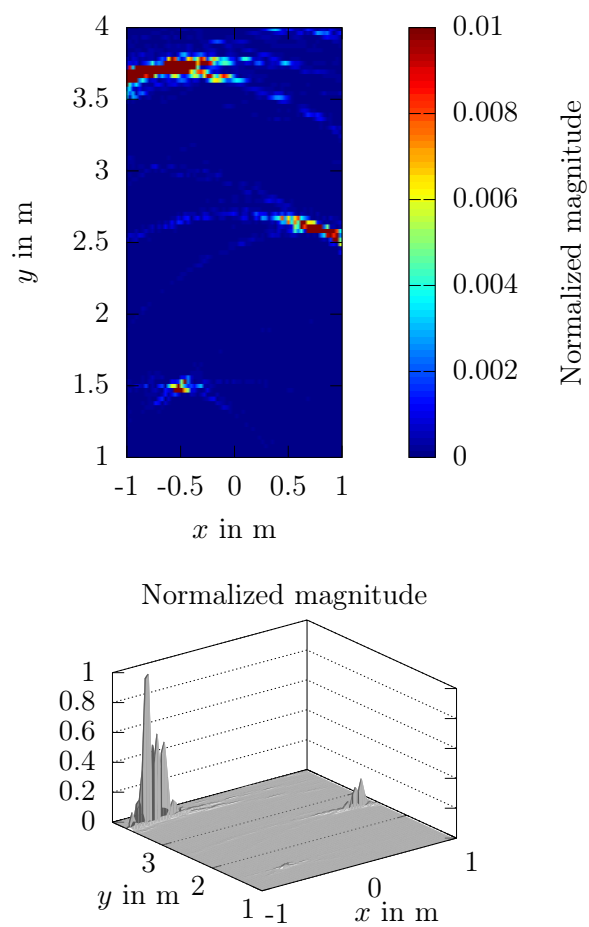


Fig. 5.6: Radar images of a three cylinders arrangement. Measurements have been done with the network analyzer (3201 frequencies) for a bandwidth of 5 GHz.

5.3.2 Detection of Foreign Object Debris

After this preliminary investigations in simulation and measurement with regular targets, “real” FOD have been considered. These objects have been found on runways at Charles de Gaulle airport in Paris, France. The TUT are summarized in Tab. 5.2. A photo of the scene and of the FOD in detail is shown in Fig. 5.7. Radar images are

	Description	Position ($x y$) in meter
FOD 1	piece of plane	($-0.70 3.40$)
FOD 2	piece of plane brake	($-0.80 2.30$)
FOD 3	plane tank cap	($-0.50 1.20$)

Tab. 5.2: Description and position of investigated FOD. Positions are referenced to the center point (0.0|0.0) between the two antennas (see Fig. 5.2).

shown in Fig. 5.8 and in Fig. 5.9. The arrangement of all three FOD can be clearly recognized. Even the small pieces of a plane brake have been perfectly retrieved with a bandwidth of 5 GHz. All these results have been evaluated without special windowing. As explained in Section 2.3.2 the resolution raises with increasing bandwidth. Therefore, the maxima become larger for potential targets in the image for a smaller bandwidth. That’s why the targets can be more easily recognized by the eye for the measurements done with $\Delta f = 5$ GHz.

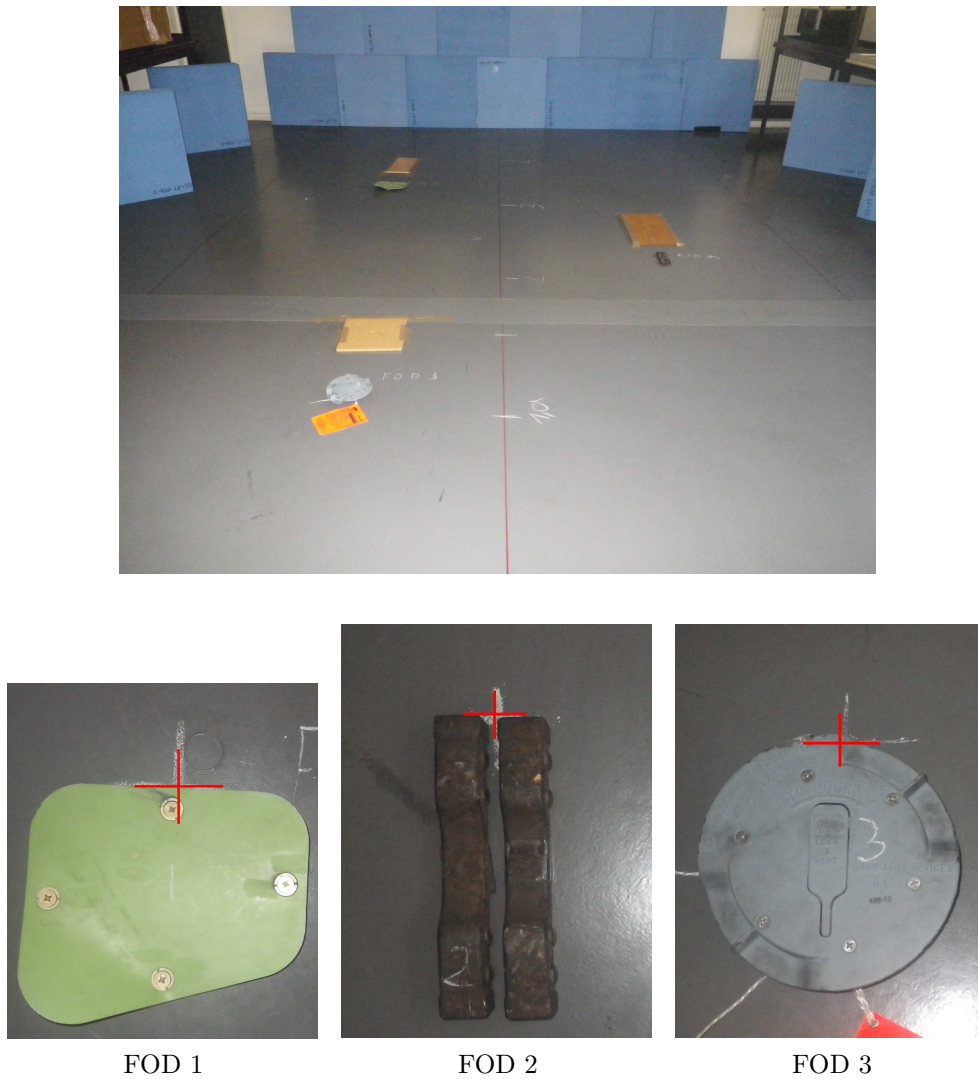


Fig. 5.7: Photograph of an arrangement inside with three FOD. Scene with the position of the FOD (top). The three FOD in detail (bottom). The red markers correspond to the point used as reference where the targets are located in the coordinate system.

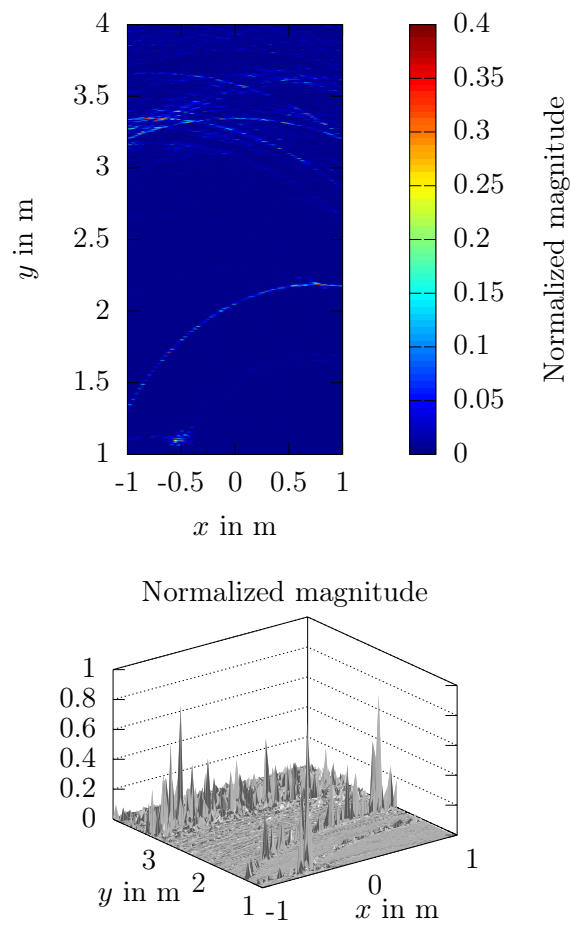


Fig. 5.8: Radar images of a three FOD arrangement. Measurements have been done with the network analyzer for a bandwidth of 35 GHz.

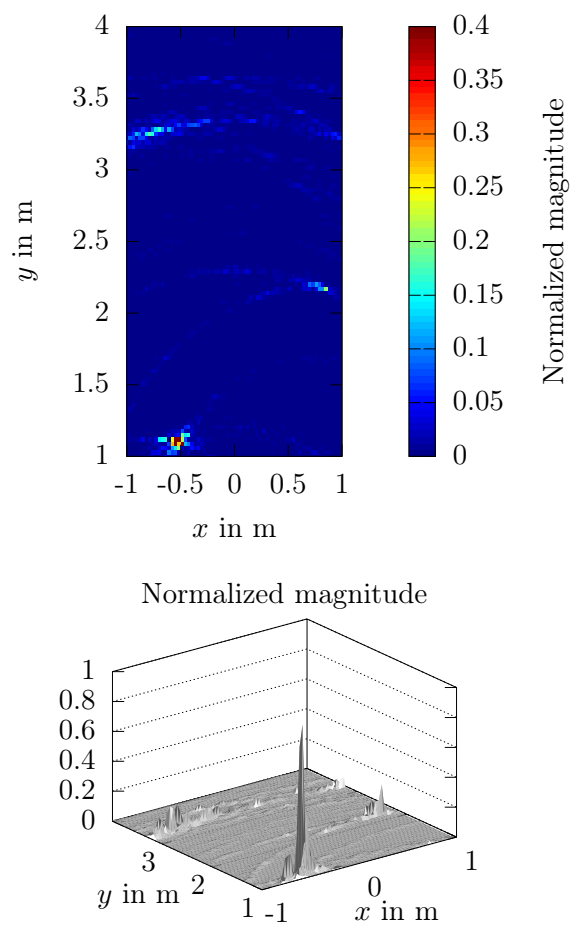


Fig. 5.9: Radar images of a three FOD arrangement. Measurements have been done with the network analyzer for a bandwidth of 5 GHz.

5.4 FMCW-Radar System

5.4.1 Sensor Overview and Signal Processing

The same FMCW radar sensor as in the previous work [121] has been used for measurements. It comprises a Phase Locked Loop (PLL) and operates at frequencies from 73 GHz to 80 GHz. A block diagram of the sensor is shown in Fig. 5.10. The mm-wave circuit of the sensor contains a Voltage-Controlled Oscillator (VCO)

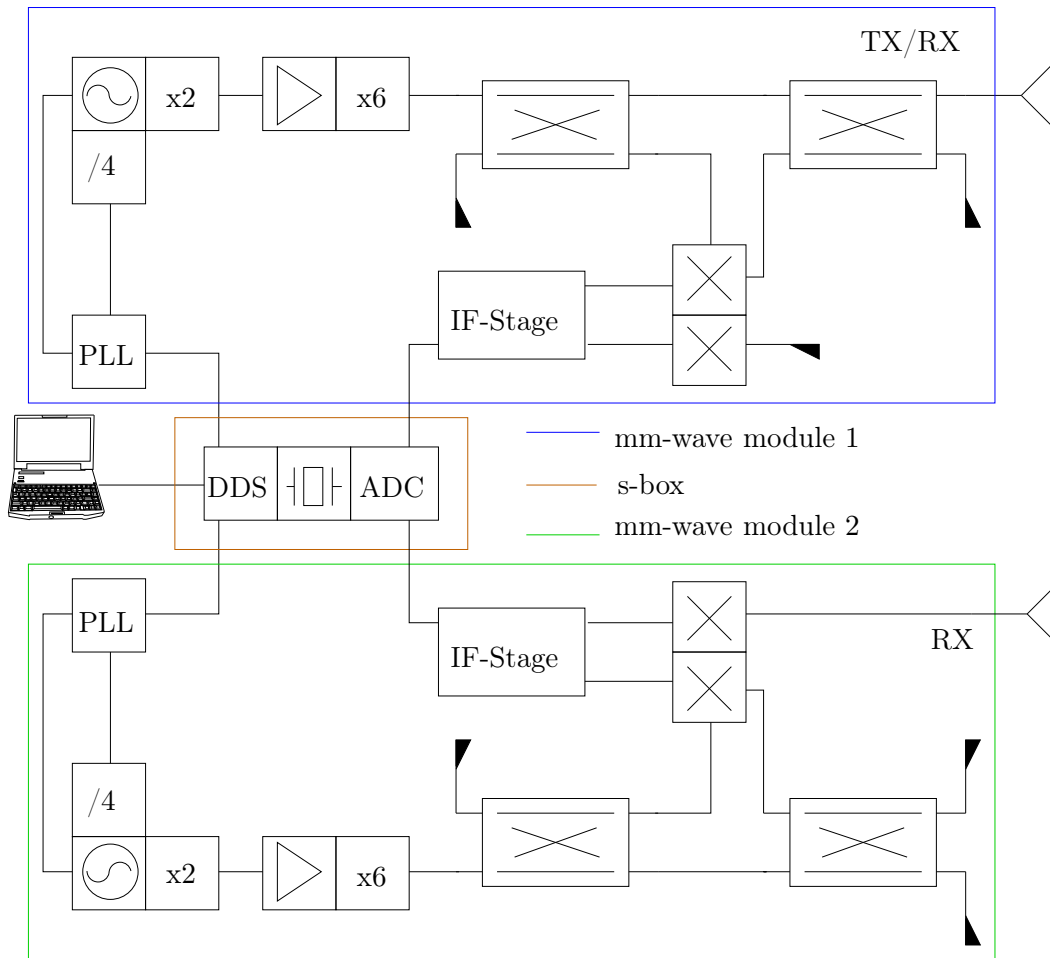


Fig. 5.10: Block diagram of the FMCW sensors used for measurements.

operating at approximately 6.4 GHz. A built-in frequency doubler and an external active multiplier generate the transmitted signal in the desired frequency range. The first coupler splits the signal to the transmit path and the Local Oscillator (LO) port of the dual channel mixer. The second coupler acts as transmit- / receive duplexer which connects the transmit path to the antenna and the receive path to the input port of the mixer. The second receiver path has not been used and therefore matched with a waveguide load. This configuration has been used for the first module, see on the left side in Fig. 5.11, to get the mono-static response.



Fig. 5.11: Photograph of the setup with the radar system with a standard gain horn as antenna.

To obtain the bi-static response with the second module, see on the right side in Fig. 5.11, the receiver path has been connected with the antenna and the transmit path has been matched with a wave-guide load.

The core of the FMCW sensor is a synthesizer based on a PLL and Direct Digital Synthesis (DDS). The linear frequency modulated base band signal is digitally generated at frequencies lower than 25 MHz. This signal serves as reference signal of the PLL which controls the VCO. An important feature of the sensor is that the clock for the DDS and the Analogue Digital Conversion unit (ADC) are both derived from the same crystal oscillator. Therefore, not only the frequency synthesis but also the data acquisition are phase-locked to a very stable reference. This offers the possibility to coherently sum up subsequent radar measurements and in consequence improve the SNR. The setup in Fig. 5.11 shows the two mm-wave modules. Both have been driven by two synchronized DDS in one s-box (see Fig. 5.10). The second s-box is only used as power supply for the second mm-wave module. In order to provide a configuration similar to the one presented in Section 5.3 with the network analyzer the following steps have been done: the first mm-wave module, used in TX/RX configuration, has been mounted on the position, where the port 1 was. With it the mono-static radar response for this position has been retrieved. The second mm-wave module, located at the position where the port 2 was, has been used to obtain the bi-static radar response. Afterwards, the position of the modules has been manually changed to get the mono-static response from port 2 and the bi-static one from port 1.

Before presenting the measurement process a short description of retrieved values with the FMCW radar system should be given hereinafter. The received signal (RX) is an attenuated copy of the transmitted signal (TX), delayed by one round trip delay $\tau = 2R/c_0$ between sensor and the target as shown in Fig. 5.12. The slope of the linear frequency modulation can be defined as:

$$S = \frac{\Delta f}{T}. \quad (5.1)$$

Knowing this, the intermediate frequency can be written as:

$$f_{IF} = S\Delta T. \quad (5.2)$$

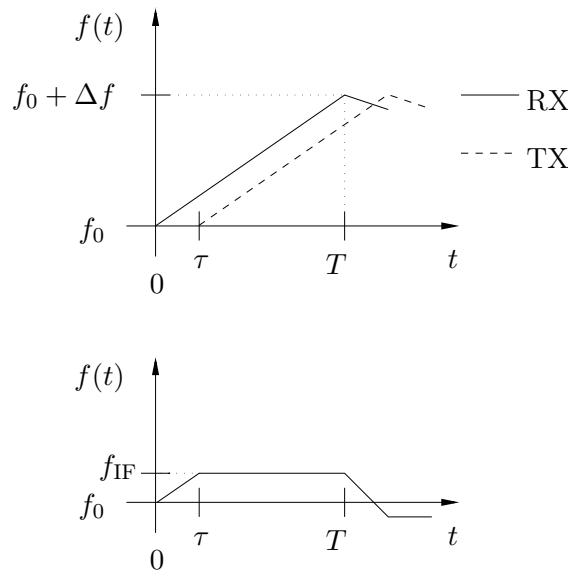


Fig. 5.12: Instantaneous frequencies of transmitted (TX), received (RX) and intermediate frequency (IF) signal.

For FMCW radars the IF-time domain samples directly provide the RF-frequency domain representation of the channel response. In the following, the IF signal in the frequency domain is directly taken. In the used FMCW radar no I/Q receiver is used. So only the real part of the complex frequency response is measured. As the pulse response of the radar channel is a causal and real valued signal, the imaginary part can be calculated using the Hilbert transform [70,105]. Following, the already presented back-propagation algorithm is applied.

5.4.2 Measurement Results

Measurements have been done from 75 GHz to 80 GHz. There the output power of the sensors varies from 5 dBm to 9 dBm. This is less than the output power of the vector network analyzer equipment. For this reason, standard gain horns have had to be used as antennas. Their radiation patterns reduce drastically the area of interest for measurements as shown in Fig. 5.13. In order to detect the TUT with both sensors the targets have been located in a distance larger than 4.3 m. Measurements have been done for 3201 frequencies as with the network analyzer. This results in a ramp duration of $T = 512 \mu\text{s}$ with the fixed sampling frequency of the ADC of 6.25 MHz. To improve the signal to noise ratio 16 measurements have been integrated. The overall coherency of the system makes it possible to calibrate the measurements by acquiring an empty scene measurement and subtracting these data from the actual measurements as done with the network analyzer. Processing of the IF signals has been done in a manner which is typical for FMCW sensors: the sampled data have been weighted using a Chebyshev window with a side lobe suppression of 60 dB [107], resulting in a much better visibility of the targets in

the radar image.

The scene of interest is shown in Fig. 5.14. The investigated targets are summarized in Tab. 5.3.

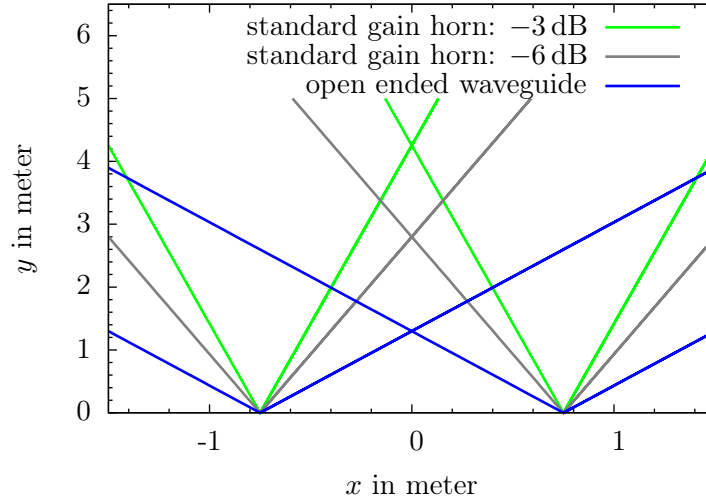


Fig. 5.13: Zone covered by the antennas. The angles for the 3 dB- and 6 dB-beam-width have been plotted as function of x and y .

	Description	Diameter D	Position ($x y$) in meter
Cylinder 1	metallic cylinder	70 mm	(-0.8 11.6)
Cylinder 2	metallic cylinder	20 mm	(0.5 9.7)
Cylinder 3	dielectric cylinder	70 mm	(0.0 5.8)

Tab. 5.3: Description and the approximate position of the investigated cylinders. The positions are referenced to the center point (0.0|0.0) between the two antennas.

Unfortunately, no meaningful bi-static response could be measured with the presented setup. This might be due to different propagation delays in the cables used to connect the sensor modules with the s-box. The cables between the s-box and the modules did not have the same length. Additionally, the two DDS might not work totally synchronize. For this reason, only images obtained with the monostatic radar response are presented in the following. All three cylinders have been detected as shown in Fig. 5.15. Furthermore, the advantage of having a short ramp duration should be shown. It has been demonstrated in [109], that fast modulation ramps have the benefit to increase the delta between two IF signals and comes with a lower sensitivity to phase noise. For comparison, 30000 frequencies have been used for the same $\Delta f = 5$ GHz. This leads to a ramp duration of $T = 4.8$ ms. The obtained radar image is shown in Fig. 5.16. The image is much more noisy which



Fig. 5.14: Photograph of a three cylinders arrangement inside. Setup of the radar system with a standard gain horn as antenna (left). Scene of the three cylinders (right).

makes it nearly impossible to identify the targets without a-priori information.

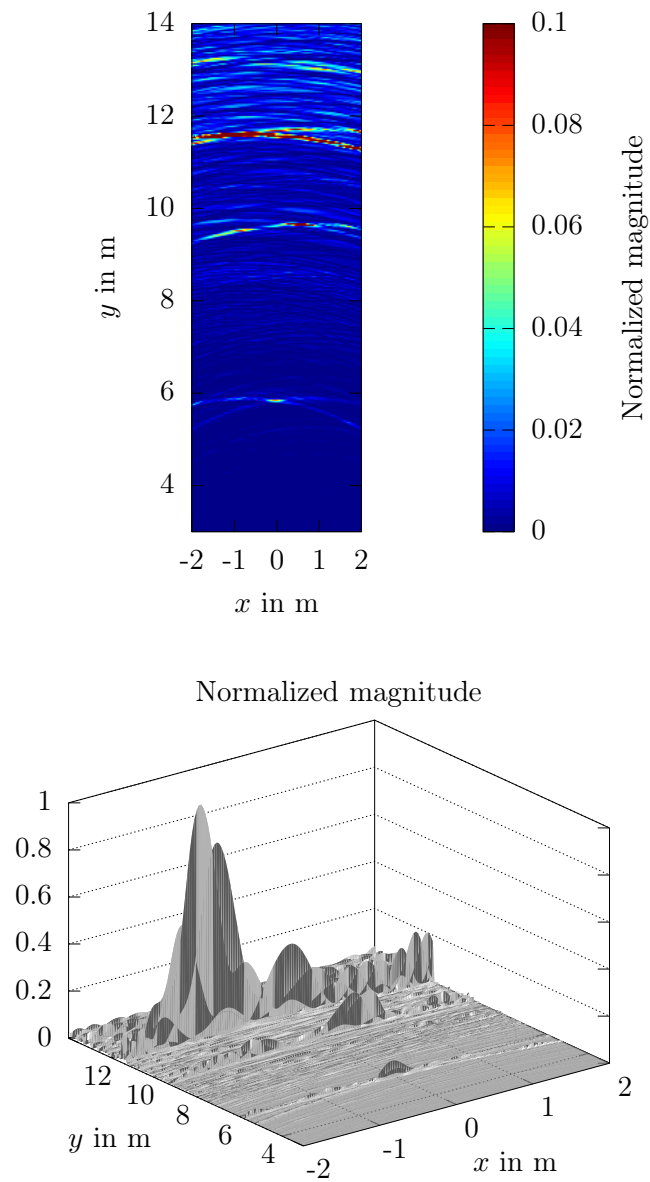


Fig. 5.15: Radar images of a three cylinders arrangement. Measurements have been done with the radar system for a bandwidth of 5 GHz with 3201 frequencies.

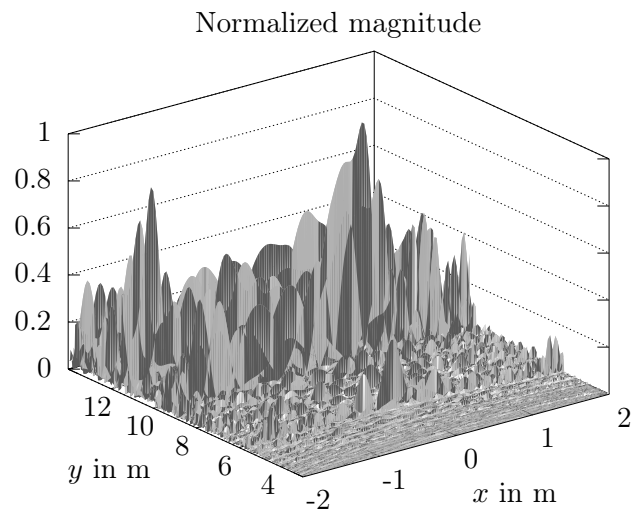
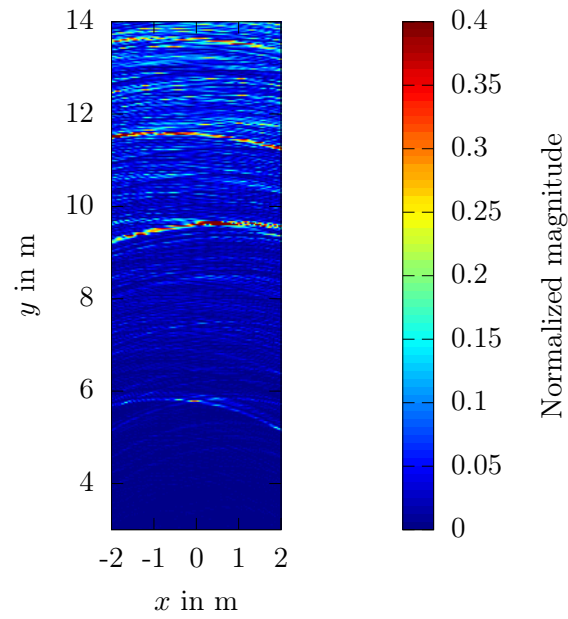


Fig. 5.16: Radar images of a three cylinders arrangement. Measurements have been done with the radar system for a bandwidth of 5 GHz and 30000 frequency points.

5.5 Conclusion

The results have shown that the proposed approach with fixed antennas could be an interesting candidate for FOD detection without the need for mechanical scanning. Measurements have been done with a laboratory equipment as well as with a radar system. With the later the need for a short ramp duration have been pointed out. Further investigations have to be done with more adequate antennas, like antennas directive in elevation and with a large beam-width in azimuth, in order to improve detection capabilities. Reflect array antennas could be good candidates for that particular case. Additionally, studies are foreseen to obtain the bi-static response with the presented setup of the radar system as shown with the network analyzer.

Conclusion and Outlook

6.1 Conclusion

In this work a valuable measurement system of 2D circular targets for imaging purposes in the W-band has been presented. It has been tested on two metallic cylinders of 20 mm and 8 mm diameters, respectively, and on a dielectric cylinder of 15 mm. For this purpose, advantage has been taken of the short wavelength value to build a small size system ($0.7\text{ m} \times 0.6\text{ m}$). A post-processing scheme has been proposed to correct misalignment errors as well as to reduce the noise. Hence, an original filtering has been developed that does not require a-priori knowledge of the target. This is a key point in the perspective of the inversion of scattered fields from unknown objects. It has been successfully applied to the measured data of the two metallic and the dielectric cylinders and validated in simulations on irregular objects under AWGN. Finally, the large metallic cylinder has been used as reference target for deriving the calibration coefficients and the smaller cylinders have been used as test objects. Averaged values of the signal to noise ratio over W-band are 15.4 dB and 10 dB for the large and the small metallic cylinders, respectively, and 5.7 dB for the dielectric one.

The measurement results have been used for the first time in the W-band for quantitative imaging purpose. The small metallic cylinder has been properly retrieved with a high sigma value. This could be related to the benefit of using mm-waves, that enhances the absolute resolution. Finally, the system sets the first basis for a more complex system capable to handle irregular objects.

A first measurement project in field has been started during this thesis to obtain results for close range imaging based on a setup with two fixed antennas. Results have been pointed out that the presented approach could be a good candidate for the detection of FOD with the already developed radar system in the W-band.

6.2 Outlook

A discussion on possible future work is given in the following.

- Based on the presented results the laboratory can establish a more complex measurement system which is needed to provide the multi-incidence and multi-view case to measure asymmetric objects. The calibration procedure developed here can still be applied while using a metallic cylinder as the reference target.

- Further investigations are going to be done in the inversion of the data measured for the larger metallic cylinder and the dielectric cylinder. Due to the good agreement of the measured scattered fields of these targets with the analytic solution this should be possible with a marginal longer computation time. The retrieved reconstructions obtained with the back-propagation set the basis to estimate precisely the domain which has to be used for the quantitative imaging. So far, no regularization scheme has been investigated. In the future, a multiplicative regularization is going to be implemented in an additional module in FLEXIMOM.
- Additional studies in order to simulate any polarization have been already proceeded. Therefore, a module in FLEXIMOM is under investigation to simulate also the 2D-TE case.
- In general, the developed software FLEXIMOM, due to its modular architecture, is going to be used as starting point to elaborate future direct and inverse electromagnetic scattering problems.
- To create a database of “in-field” measurements for benchmarking algorithms, more adequate antennas have to be used. The standard gain horns should be replaced by an antenna having a directive radiation pattern in elevation and an omni-directional radiation pattern in azimuth. For this purpose, a reflect array antenna could be a good candidate due to the experience in their development and realization of the laboratory.

Resume in German and French

Due to the co-tutelle convention between the University of Nice - Sophia Antipolis and the University of Ulm it is supposed to provide a resume in German and English, which can be found in the following.

7.1 Zusammenfassung und Ausblick auf Deutsch

In der vorgestellten Arbeit wurde ein leistungsfähiges Messsystem für zweidimensionale kreisförmige Objekte mit dem Ziel der Rekonstruktion im W-Band präsentiert. Dieses wurde an zwei metallischen Zylindern mit Durchmessern von jeweils 20 mm und 8 mm getestet sowie an einem dielektrischen Zylinder mit einem Durchmesser von 15 mm. Aufgrund der kurzen Wellenlänge konnte ein kompaktes System ($0.7\text{ m} \times 0.6\text{ m}$) entwickelt werden. Ein Signalverarbeitungsprozess wurde vorgestellt, um Justierungsfehler zu korrigieren und Rauschen zu reduzieren. Dabei wurde eine neue Filtermethode entwickelt, welche keine Kenntnisse über das Objekt voraussetzt. Dieser kommt eine Schlüsselrolle zu, da zukünftig eine Rekonstruktion durchgeführt werden soll mit Streufeldern von unbekanntem Objekten. Die Methode wurde erfolgreich auf die Messdaten der zwei metallischen und des dielektrischen Zylinders angewandt. Auch wurde sie in Simulationen von unsymmetrischen Objekten unter AWGN validiert. Schließlich wurde der große metallische Zylinder als Referenzobjekt verwendet, um die Kalibrationskoeffizienten zu ermitteln. Die zwei kleineren Zylinder dienten als Testobjekte. Durchschnittswerte des Signal-Rausch-Verhältnis über das W-Band sind 15.4 dB für den großen metallischen Zylinder und 10 dB für den kleinen metallischen Zylinder sowie 5.7 dB für den dielektrischen Zylinder. Die Messergebnisse wurden erstmals im W-Band zur quantitativen Rekonstruktion verwendet. Der kleine metallische Zylinder wurde erfolgreich mit einem hohen Konduktivitätswert rekonstruiert. Dies könnte im Zusammenhang mit dem Nutzen vom mm-Wellen stehen, welche eine hohe absolute Auflösung bereitstellen. Das vorgestellte System setzt die Basis für die zukünftige Entwicklung eines komplexeren Messaufbaus, welcher genutzt werden soll, um unsymmetrische Objekte zu vermessen. Zusätzlich wurde eine erste Messkampagne im Feld gestartet, um Abbildungen im Nahbereich mit einem FMCW Radarsystem und zwei festen Empfängerpositionen zu erzielen. Die Ergebnisse zeigten, dass der vorgestellte Ansatz geeignet ist für die Detektierung von FOD im W-Band.

Im Folgenden wird ein Ausblick auf zukünftige Schwerpunkte gegeben. Basierend auf den präsentierten Ergebnissen kann das LEAT nun ein komplexeres Mess-

system projektieren, welches benötigt wird, um unterschiedliche Empfängerpositionen mit unterschiedlichen Sendepositionen zu kombinieren. Dies ist notwendig, um unsymmetrische Objekte zu vermessen. Die entwickelte Kalibrationsmethode mit einem metallischen Zylinder als Referenzobjekt kann auch für diesen Fall angewendet werden. Es werden Bestrebungen stattfinden, um die Messergebnisse von dem großen metallischen Zylinder und dem dielektrischen Zylinder zur quantitativen Rekonstruktion zu verwenden. Durch die sehr gute Übereinstimmung der gemessenen Streufelder mit der analytischen Lösung sollte die Rekonstruktion mit nur unwesentlich längeren Berechnungszeiten möglich sein. Die Ergebnisse der qualitativen Rekonstruktion setzen hierfür die Basis, um präzise den Bereich abzuschätzen, welcher für die quantitative Rekonstruktion verwendet werden wird. Bisher wurden noch keine Regularisierungsalgorithmen eingesetzt. Zukünftig wird eine multiplikative Regularisierung in einem zusätzlichen Modul von FLEXIMOM implementiert und untersucht werden. Zusätzliche Untersuchungen sind schon jetzt im Gange, um jede beliebige Polarisierung zu simulieren. Momentan wird die Implementierung eines zusätzlichen Moduls in FLEXIMOM vorangetrieben, um den 2D-TE Fall zu berechnen. Generell wird FLEXIMOM, dank des modularen Aufbaus, als Plattform für zukünftige direkte und inverse elektromagnetische Streufeldberechnungen dienen. Des weiteren soll eine Datenbank aufgebaut werden, welche Daten aus Feldmessungen mit dem FMCW Radarsystem enthält. Diese soll für die Validierung von Algorithmen herangezogen werden. Zusätzliche Messungen sollten mit Antennen durchgeführt werden, welche über ein direktives Strahlungsdiagramm in der Elevation und ein omni-direktionales Strahlungsdiagramm im Azimuth verfügen. Für diesen Zweck könnten Reflectarray-Antennen untersucht werden. In deren Entwicklung und Herstellung verfügt das MWT und das LEAT über langjährige Erfahrungen.

7.2 Résumé en français

Durant la dernière décennie, les radars millimétriques en bande W (75 – 110 GHz) pour les applications civiles se sont largement développés, en partie grâce aux progrès des circuits intégrés et à la possibilité de fabriquer des systèmes compacts à haute résolution. Les domaines d'applications sont nombreux et variés : secteur automobile (radar d'aide à la conduite à 77 GHz), aide au pilotage d'hélicoptères ou encore détection d'objets sur pistes d'aéroports (radars FOD à 77 GHz ou 94 GHz). Dans un premier temps ces systèmes ont été utilisés à des fins de détection. Cependant, leur maturité ainsi que les exigences accrues en termes d'application, orientent actuellement les recherches vers l'insertion de fonctions permettant l'identification.

Ainsi, des systèmes d'imagerie radar ont été développés, notamment à l'aide d'imagerie SAR. Les premiers résultats obtenus avec cette imagerie qualitative sont très prometteurs car ils permettent de retrouver précisément la forme des objets. Afin de reconstruire les propriétés électromagnétiques des objets, il est à présent nécessaire de travailler de manière quantitative. De nombreux travaux ont été conduits en ondes centimétriques dans ce domaine, cependant aucun système d'imagerie quantitative n'existe, à notre connaissance, en gamme millimétrique.

L'objectif du travail présenté dans ce manuscrit est à la fois de poser les bases d'un système d'imagerie quantitative en gamme millimétrique mais aussi de le comparer à l'imagerie radar de systèmes développés en collaboration avec le «Institut für Mikrowellentechnik» de l'Université d'Ulm (Allemagne). Compte-tenu du peu de travaux dans le domaine de l'imagerie quantitative en bande millimétrique, la première étape consiste en la validation du processus de reconstruction sur des cibles canoniques. Nous avons choisi deux cylindres métalliques et un cylindre diélectrique. Ce manuscrit décrit l'ensemble du processus au travers de six chapitres organisés comme suit.

Après un bref chapitre introductif, le chapitre 2 décrit les fondements théoriques des modèles utilisés à la fois pour le calcul du problème direct et du problème inverse. En gamme millimétrique de nombreux objets peuvent être vus en deux dimensions (2D), par exemple les lignes à haute tension particulièrement dangereuses pour les hélicoptères. Ainsi la modélisation du champ diffracté est développée pour le cas 2D-TM (Transverse Magnétique) et repose sur l'utilisation d'une Méthode des Moments (MoM). Le logiciel ainsi développé est appelé FLEXIMOM. C'est ce que nous appellerons modélisation du problème direct. Pour le cas particulier des cylindres il existe de plus une solution analytique qui a été implémentée dans un logiciel développé au laboratoire, appelé ESCALE. Ce dernier est dédié au calcul du champ diffracté pour les cas où une solution analytique existe. Les comparaisons entre la solution analytique et FLEXIMOM valident la modélisation du problème direct. Le problème inverse est implémenté avec une méthode de gradient conjugué.

Le troisième chapitre décrit le système de mesure. La difficulté de travailler en gamme millimétrique est double. D'une part la faible valeur de la longueur d'onde demande une meilleure précision mécanique. D'autre part, les performances des appareils de mesure, plancher de bruit et dynamique notamment, sont moindres qu'aux basses fréquences. Une spécificité supplémentaire est liée à l'activité principale de la chambre anéchoïde du LEAT qui est la mesure d'antennes. Ainsi le système de mesure doit être compatible avec la mesure d'antennes, c'est à dire facile à installer et démonter.

Le système proposé tient compte de toutes ces contraintes et tire également partie des faibles valeurs de la longueur d'onde qui permet de concevoir un système dans un volume réduit. Ainsi, l'émetteur est placé à 400 mm du système cible-récepteur. Afin que l'erreur d'alignement récepteur-cible soit constante et donc n'influence que la dynamique de mesure, la cible et le récepteur sont solidaires et placés, par l'intermédiaire d'un mât, sur la tour de mesure. Le système ainsi conçu permet l'acquisition du champ diffracté en mono-incidence/multivues sur un cercle, ce qui correspond bien au cas modélisé 2D-TM. Cependant, la présence physique de l'émetteur empêche une mesure sur 360° , la zone couverte est de 300° ($\phi = 30^\circ - 330^\circ$). La symétrie des cibles permet ensuite de passer facilement au cas multi-incidences/multivues par duplication fictive des émetteurs. Les trois fréquences de mesure sont les fréquences limites de la bande W (75 GHz et 110 GHz) et la fréquence centrale (92.5 GHz). La comparaison des mesures brutes avec la solution exacte (ESCALE) met en évidence trois problèmes :

- un mauvais alignement entre l'émetteur et la cible qui se traduit par une phase dissymétrique,
- la présence de bruit,
- la nécessité de normaliser correctement les mesures et les simulations afin de prendre en compte la différence de puissance incidente dans les deux cas.

Le chapitre décrit ensuite l'ensemble des corrections apportées aux mesures et l'estimation des performances du système. La première étape est la correction du dés-alignement qui est dû au dé-centrage du mât par rapport au centre de rotation de la tour. Elle est obtenue par optimisation à partir du grand cylindre métallique qui devient notre objet de calibrage. Le bruit de mesure est supprimé par filtrage. Ce bruit a une double cause. Il est lié d'une part à l'imprécision du positionnement lors de deux rotations de la tour. Comme le champ diffracté est issu de la soustraction entre le champ sans cible (champ incident) et le champ avec cible (champ total), cette imprécision va générer du bruit. On montre en estimant son influence en simulations grâce à ESCALE, que ce dernier apparaît aux hautes «fréquences» du spectre issu de la transformation du champ $E(\phi)$. Il peut donc être supprimé par un filtre passe-bas. La seconde cause du bruit est liée aux appareils de

mesure. Le bruit est d'autant plus important que les valeurs des champs incident et total sont proches. C'est pourquoi, pour nos cibles particulières testées, il apparaît surtout dans les premiers lobes. Une technique de filtrage originale qui ne nécessite pas de connaissance préalable des cibles sous test et fondée sur la détection de pente, permet de supprimer les interférences du bruit avec le signal. Ce filtrage est aussi de type passe-bas. Finalement on montre que tout le bruit peut être éliminé par un filtre passe-bas dont la fréquence de coupure est déterminée par la détection de pente des spectres.

Enfin, la normalisation déjà utilisée au laboratoire à plus basse fréquence, et qui repose sur la corrélation des champs mesurés et simulés est appliquée. Les résultats ainsi corrigés présentent un SNR de 15.4 dB pour le grand cylindre (ce qui constituera aussi notre limite haute du système), de 10 dB pour le plus petit cylindre métallique et de 5.7 dB pour le cylindre diélectrique.

Le chapitre 4 est consacré à l'imagerie réalisée à partir de ces mesures. Dans un premier temps, une imagerie qualitative, qui repose sur un algorithme de rétro-propagation est testée et donne d'excellents résultats puisque tous les contours des cylindres sont reconstruits avec une précision d'une demi-longueur d'onde pour un seuillage à 3 dB.

Dans un second temps, le petit cylindre est utilisé pour l'inversion. Son contour est lui aussi parfaitement reconstruit. Les caractéristiques diélectriques donnent une permittivité relative proche de 1 et un sigma compris entre 77.37 S/m et 81.12 S/m . La dispersion des valeurs de sigma est liée au nombre de récepteurs utilisé pour l'inversion. Ces valeurs de la permittivité complexe sont caractéristiques d'un métal. Cependant, bien que quantitatif, l'algorithme d'inversion utilisé ne permet pas de retrouver des valeurs de sigma réelles du métal (plusieurs MS/m). En d'autres termes, nous pouvons identifier le métal mais nous ne sommes pas en mesure de dire de quel métal il s'agit. Cependant, cette dernière limitation n'est pas un frein pour les applications citées plus haut.

Enfin, des mesures sont initiées au chapitre 5 avec un système radar FM-CW bistatique développé en collaboration avec l'Université d'Ulm. Il est utilisé dans un cadre d'imagerie qualitative et repose sur l'utilisation de trois paramètres S de la mesure (S_{11} , S_{12} ou S_{21} et S_{22}). Dans un premier temps, les mesures sont conduites avec un analyseur de réseau vectoriel pour valider le concept. Différents FOD ont été détectés avec succès avec toute la bande passante de la bande W, puis avec une bande passante réduite de 5 GHz, qui correspond à la bande passante maximale de notre radar. Les mesures radar montrent les paramètres S_{11} et S_{22} sont exploitables et que les FOD peuvent être trouvés à condition que l'objet soit dans la zone d'intersection des champs de vision des deux antennes du radar. L'exploitation du paramètre S_{21} et/ou S_{12} reste problématique et les recherches doivent être poursuivies dans ce domaine.

L'ensemble des résultats obtenus valident le processus développé pour d'imagerie quantitative en gamme millimétrique. Les recherches doivent être poursuivies aussi bien en mesure qu'en modélisation. D'une part le système de mesure doit évoluer vers un vrai système multi-incidences/multivues. Grâce aux résultats obtenus avec notre système simplifié, ce dernier a pu être dimensionné et nous espérons des fonds pour pouvoir l'installer. D'autre part, le cas 2D-TE doit être implémenté afin de pouvoir traiter un objet 2D quelconque dans n'importe quelle polarisation. Enfin, les mesures à partir de systèmes radar réels doivent être poursuivies, en particulier pour rendre exploitables les mesures des coefficients de transmission. Ces dernières sont indispensable si l'on veut un jour appliquer les algorithmes d'inversion à des mesures issues de systèmes radar.

Approach of the Integration of the Green's Function

The following equation has to be calculated:

$$\begin{aligned} G_{mn} &= \int_{C_n} G(\mathbf{r}_m - \mathbf{r}') d\mathbf{r}' \\ &= -\frac{j}{4} \int_{C_n} H_0^{(2)}(k_1 |\mathbf{r}_m - \mathbf{r}'|) d\mathbf{r}' \end{aligned} \quad (\text{A.1})$$

$$I = \iint_{R_d} \frac{j}{4} H_0^{(2)}(k_1 |\mathbf{r}_m - \mathbf{r}'|) d\mathbf{r}' \approx \iint_{C_a} \frac{j}{4} H_0^{(2)}(k_1 |\mathbf{r}_m - \mathbf{r}'|) d\mathbf{r}' \quad (\text{A.2})$$

The variables are changed as following (Fig. A.1):

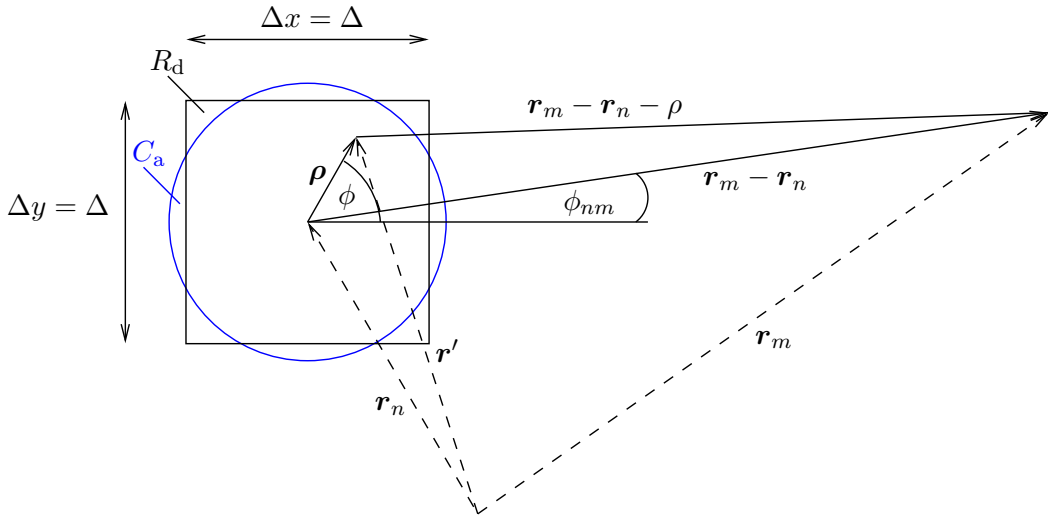


Fig. A.1: Approximation for the integration of the Green's function.

$$\begin{aligned} \boldsymbol{\rho} &= \mathbf{r}' - \mathbf{r}_n \\ \boldsymbol{\rho} &= \rho e^{j\phi} \\ \mathbf{r}_m - \mathbf{r}_n &= |\mathbf{r}_m - \mathbf{r}_n| e^{j\phi_{nm}} \\ \boldsymbol{\rho} &= \rho d\rho d\phi. \end{aligned}$$

$$I = \iint_{C_a} \frac{j}{4} H_0^{(2)}(k_1 |\mathbf{r}_m - \mathbf{r}_n - \boldsymbol{\rho}|) d\boldsymbol{\rho} \quad (\text{A.3})$$

A.1 Self Element Case, $n = m$, Diagonal Matrix Elements

$$\begin{aligned}
 I &= \iint_{C_a} \frac{j}{4} H_0^{(2)}(k_1 \rho) d\rho \\
 &= \int_0^{2\pi} \int_0^R \frac{j}{4} H_0^{(2)}(k_1 \rho) \rho d\rho d\phi \\
 &= \frac{j\pi}{2} \int_0^R H_0^{(2)}(k_1 \rho) \rho d\rho \\
 &= \frac{j\pi}{2} \frac{1}{k_1} \int_0^R H_0^{(2)}(k_1 \rho) k_1 \rho d\rho
 \end{aligned} \tag{A.4}$$

Integration by substitution

$$\begin{aligned}
 t = k_1 \rho &\Rightarrow \frac{dt}{d\rho} = k_1 \Rightarrow d\rho = \frac{dt}{k_1} \\
 &= \frac{j\pi}{2} \frac{1}{k_1} \int_{t=0}^{t=k_1 R} H_0^{(2)}(t) t \frac{dt}{k_1} \\
 &= \frac{j\pi}{2} \frac{1}{k_1^2} \left[H_1^{(2)}(t) t \right]_{t=0}^{t=k_1 R} \\
 &= \frac{j\pi}{2} \frac{1}{k_1^2} \left(H_1^{(2)}(k_1 R) k_1 R - H_1^{(2)}(t) t |_{t \rightarrow 0} \right)
 \end{aligned}$$

One has to calculate: $H_1^{(2)}(t) t |_{t \rightarrow 0}$

$$t H_1^{(2)}(t) |_{t \rightarrow 0} = t [J_1(t) - j Y_1(t)] |_{t \rightarrow 0}$$

After [110]:

$$\begin{aligned}
 Y_n(z) &= - \frac{\left(\frac{1}{2}z\right)^{-n}}{\pi} \sum_{k=0}^{n-1} \frac{(n-k-1)!}{k!} \left(\frac{1}{4}z^2\right)^k \\
 &\quad + \frac{2}{\pi} \ln\left(\frac{1}{2}z\right) J_n(z) \\
 &\quad - \frac{\left(\frac{1}{2}z\right)^n}{\pi} \sum_{k=0}^{\infty} [\psi(k+1) + \psi(n+k+1)] \frac{\left(-\frac{1}{4}z^2\right)^k}{k!(n+k)!}
 \end{aligned}$$

$$\psi(1) = -\gamma$$

$$\psi(n) = -\gamma + \sum_{k=1}^{n-1} k^{-1} \quad (n \leq 2)$$

$$\begin{aligned}
 Y_1(z) &= -\frac{\left(\frac{1}{2}z\right)^{-1}}{\pi} \sum_{k=0}^{1-1} \frac{(1-k-1)!}{k!} \left(\frac{1}{4}z^2\right)^k \\
 &\quad + \frac{2}{\pi} \ln\left(\frac{1}{2}z\right) J_1(z) \\
 &\quad - \frac{\left(\frac{1}{2}z\right)^1}{\pi} \sum_{k=0}^{\infty} [\psi(k+1) + \psi(1+k+1)] \frac{\left(-\frac{1}{4}z^2\right)^k}{k!(1+k)!} \\
 Y_1(z) &= -\frac{\left(\frac{1}{2}z\right)^{-1}}{\pi} \sum_{k=0}^{1-1} \frac{(1-k-1)!}{k!} \left(\frac{1}{4}z^2\right)^k \\
 &\quad + \frac{2}{\pi} \ln\left(\frac{1}{2}z\right) J_1(z) \\
 &\quad - \frac{\left(\frac{1}{2}z\right)^1}{\pi} \sum_{k=0}^{\infty} \left[\left(-\gamma + \sum_{n=1}^{(k+1)-1} n^{-1} \right) \right. \\
 &\quad \quad \left. + \left(-\gamma + \sum_{n=1}^{(1+k+1)-1} n^{-1} \right) \right] \frac{\left(-\frac{1}{4}z^2\right)^k}{k!(1+k)!} \\
 Y_1(z) &= -\frac{2}{z\pi} \frac{0!}{0!} \left(\frac{1}{4}z^2\right)^0 \\
 &\quad + \frac{2}{\pi} \left[\ln\left(\frac{1}{2}\right) + \ln(z) \right] J_1(z) \\
 &\quad - \frac{z}{2\pi} \sum_{k=0}^{\infty} \left[\left(-\gamma + \sum_{n=1}^k n^{-1} \right) + \left(-\gamma + \sum_{n=1}^{1+k} n^{-1} \right) \right] \frac{\left(-\frac{1}{4}z^2\right)^k}{k!(1+k)!} \\
 Y_1(z) &\approx -\frac{2}{z\pi} \\
 &\quad + \frac{2}{\pi} \left[\ln\left(\frac{1}{2}\right) + \ln(z) \right] J_1(z) \\
 &\quad \underbrace{-z}_{1} (Cz^2)
 \end{aligned}$$

$$\begin{aligned}
 tH_1^{(2)}(t)|_{t \rightarrow 0} &= t [J_1(t) - j Y_1(t)] |_{t \rightarrow 0} \\
 &= t J_1(t)|_{t \rightarrow 0} - t j Y_1(t)|_{t \rightarrow 0} \\
 &\approx 0 - j t \left(-\frac{2}{t\pi} + \frac{2}{\pi} \left[\ln\left(\frac{1}{2}\right) + \ln(t) \right] J_1(t) - t (Ct^2) \right) |_{t \rightarrow 0} \\
 &= j \frac{2}{\pi}
 \end{aligned}$$

$$\boxed{I = \frac{j\pi}{2} \frac{1}{k_1^2} \left(H_1^{(2)}(k_1 R) k_1 R - \left(j \frac{2}{\pi} \right) \right)} \quad (\text{A.5})$$

¹This gives a first approximation of first order to calculate the equations (2.47) and (2.48).

A.2 General Case, $n \neq m$, Non-diagonal Matrix Elements

With the addition theorem [111] one can write:

$$H_0^{(2)}(k_1 |\mathbf{r}_m - \mathbf{r}_n - \boldsymbol{\rho}|) = \sum_{q=-\infty}^{\infty} H_q^{(2)}(k_1 |\mathbf{r}_m - \mathbf{r}_n|) J_q(k_1 \rho) e^{jq(\phi - \phi_{nm})} \quad (\text{A.6})$$

since $\rho < |\mathbf{r}_m - \mathbf{r}_n|$

The integral becomes:

$$I \approx \frac{j}{4} \sum_{q=-\infty}^{\infty} H_q^{(2)}(k_1 |\mathbf{r}_m - \mathbf{r}_n|) \int_0^R J_q(k_1 \rho) \rho d\rho \int_0^{2\pi} e^{jq(\phi - \phi_{nm})} d\phi \quad (\text{A.7})$$

The last term in the sum gets:

$$\int_0^{2\pi} e^{jq(\phi - \phi_{nm})} d\phi = \begin{cases} 0, & \text{if } q \neq 0 \\ 2\pi, & \text{if } q = 0 \end{cases}$$

Only the term $q = 0$ is conserved.

$$\int x^{\lambda+1} Z_\lambda(z) dx = z^{\lambda+1} Z_{\lambda+1}(x)$$

In the following, one has to solve:

$$\int_0^R J_0(k_1 \rho) \rho d\rho \quad (\text{A.8})$$

$$\int_0^R J_0(k_1 \rho) \rho d\rho = \frac{1}{k_1} \int_0^R J_0(k_1 \rho) k_1 \rho d\rho$$

Using integration by substitution

$$\begin{aligned} t = k_1 \rho \Rightarrow \frac{dt}{d\rho} = k_1 \Rightarrow d\rho &= \frac{dt}{k_1} \\ &= \frac{1}{k_1} \int_{t=0}^{t=k_1 R} J_0(t) t \frac{dt}{k_1} \\ &= \frac{1}{k_1^2} \int_{t=0}^{t=k_1 R} J_0(t) t dt \\ &= \frac{1}{k_1^2} [J_1(t) t]_{t=0}^{t=k_1 R} \\ &= \frac{1}{k_1^2} (k_1 R J_1(k_1 R) - t J_1(t)|_{t \rightarrow 0}) \end{aligned}$$

with $J_1(x)|_{x \rightarrow 0} = 0$

$$= \frac{R}{k_1} J_1(k_1 R)$$

$$\begin{aligned} I &= \iint_{C_a} \frac{j}{4} H_0^{(2)}(k_1 |\mathbf{r}_m - \mathbf{r}_n - \boldsymbol{\rho}|) d\boldsymbol{\rho} \\ &= \frac{j}{4} 2\pi \frac{R}{k_1} J_1(Rk_1) H_0^{(2)}(k_1 |\mathbf{r}_m - \mathbf{r}_n|) \end{aligned}$$

$$\boxed{I = \frac{j \pi R}{2k_1} H_0^{(2)}(k_1 |\mathbf{r}_m - \mathbf{r}_n|) J_1(Rk_1)} \quad (\text{A.9})$$

Approach for the Integration over a Squared Disc with an Optimal Circular Disc

B.1 Demonstration

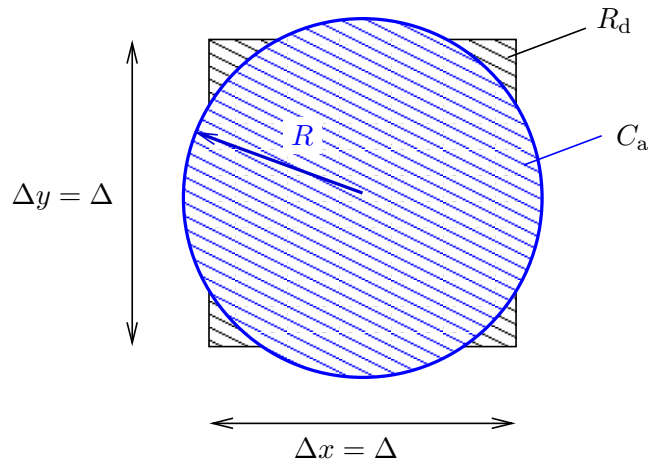


Fig. B.1: Approximate integration over a squared cell over an optimal circular disc.

One can show that each polynomial $P(x, y)$ of order three ¹:

$$P(x, y) = c_0 + c_1x + c_2y + c_3x^2 + c_4xy + c_5y^2 + c_6x^3 + c_7x^2y + c_8xy^2 + c_9y^3$$

fulfills

$$\iint_{R_d} P(x, y) dx dy = \frac{3}{\pi} \iint_{C_a} P(x, y) dx dy \quad (\text{B.1})$$

assumed that the rectangle is square and its side length and the radius of the circle R are related by

$$R = \frac{\Delta}{\sqrt{3}}. \quad (\text{B.2})$$

¹Second approximation of order 3 to calculate the equations (2.47) and (2.48)

$$\iint_{R_d} P(x, y) dx dy = \int_{-\frac{\Delta}{2}}^{\frac{\Delta}{2}} \int_{-\frac{\Delta}{2}}^{\frac{\Delta}{2}} c_0 + c_1 x + c_2 y + c_3 x^2 + c_4 xy + c_5 y^2 + c_6 x^3 + c_7 x^2 y + c_8 xy^2 + c_9 y^3 dx dy \quad (B.3)$$

$$\iint_{C_a} P(x, y) dx dy = \int_0^{2\pi} \int_0^R c_0 + c_1 x + c_2 y + c_3 x^2 + c_4 xy + c_5 y^2 + c_6 x^3 + c_7 x^2 y + c_8 xy^2 + c_9 y^3 r dr d\phi \quad (B.4)$$

$$\begin{aligned} \int_{-\frac{\Delta}{2}}^{\frac{\Delta}{2}} \int_{-\frac{\Delta}{2}}^{\frac{\Delta}{2}} P(x, y) dx dy &= c_0 \Delta^2 + c_3 \frac{\Delta^4}{12} + c_5 \frac{\Delta^4}{12} \\ \int_0^{2\pi} \int_0^R P(x, y) r dr d\phi &= c_0 \pi R^2 + c_3 \frac{1}{4} R^4 \pi + c_5 \frac{1}{4} R^4 \pi \end{aligned}$$

$$\begin{aligned} \int_{-\frac{\Delta}{2}}^{\frac{\Delta}{2}} \int_{-\frac{\Delta}{2}}^{\frac{\Delta}{2}} P(x, y) dx dy &= C \int_0^{2\pi} \int_0^R P(x, y) r dr d\phi \\ &\Rightarrow C = \frac{\Delta^2}{\pi R^2} \text{ et } R = \frac{\Delta}{\sqrt{3}} \\ &\Rightarrow C = \frac{3}{\pi} \end{aligned}$$

One has to show that the algebraical expression to integrate equation (A.8) and equation (A.4) are polynomials of order three to apply the following approximation.

$$\begin{aligned} \int_{(x_i - \frac{\Delta}{2})}^{(x_i + \frac{\Delta}{2})} \int_{(x_i - \frac{\Delta}{2})}^{(x_i + \frac{\Delta}{2})} \underbrace{J_0(k_1 \rho)}_{P_1(x, y)} dx' dy' &= C \int_0^R \int_0^{2\pi} J_0(k_1 \rho) \rho d\rho d\phi \\ \int_{(x_i - \frac{\Delta}{2})}^{(x_i + \frac{\Delta}{2})} \int_{(x_i - \frac{\Delta}{2})}^{(x_i + \frac{\Delta}{2})} \underbrace{H_0^{(2)}(k_1 \rho)}_{P_2(x, y)} dx' dy' &= C \int_0^R \int_0^{2\pi} H_0^{(2)}(k_1 \rho) \rho d\rho d\phi \end{aligned} \quad (B.5)$$

$$\begin{aligned} \text{with } R &= \frac{\Delta}{\sqrt{3}} \\ C &= \frac{3}{\pi} \\ \rho &= \sqrt{x'^2 + y'^2} \end{aligned}$$

with the substitutions:

$$\begin{aligned} x' &= \rho \cos(\phi) \\ y' &= \rho \sin(\phi) \\ dx' dy' &= \rho d\rho d\phi \end{aligned}$$

$$\begin{aligned}
P_1(x, y) &= J_0(k_1\rho) \\
P_2(x, y) &= H_0^{(2)}(k_1\rho) \\
H_0^{(2)}(\rho) &= J_0(\rho) - j Y_0(\rho)
\end{aligned}$$

With [111]

$$J_0(\rho) = 1 - \frac{\frac{1}{4}\rho^2}{(1!)^2} + \frac{(\frac{1}{4}\rho^2)^2}{(2!)^2} - \frac{(\frac{1}{4}\rho^2)^3}{(3!)^2} + \dots \quad (\text{B.6})$$

$$\begin{aligned}
Y_0(\rho) &= \frac{2}{\pi} \left\{ \ln\left(\frac{1}{2}\rho\right) + \gamma \right\} J_0(\rho) \\
&+ \frac{2}{\pi} \left\{ \frac{\frac{1}{4}\rho^2}{(1!)^2} - \left(1 + \frac{1}{2}\right) \frac{(\frac{1}{4}\rho^2)^2}{(2!)^2} + \left(1 + \frac{1}{2} + \frac{1}{3}\right) \frac{(\frac{1}{4}\rho^2)^3}{(3!)^2} - \dots \right\} \quad (\text{B.7})
\end{aligned}$$

One has to show that $J_0(\rho)$ is a polynomial of third order.

$$\rho = \sqrt{x'^2 + y'^2}$$

$$J_0(x', y') = 1 - \frac{\frac{1}{4}(x'^2 + y'^2)}{(1!)^2} + \frac{(\frac{1}{4}(x'^2 + y'^2))^2}{(2!)^2} - \frac{(\frac{1}{4}(x'^2 + y'^2))^3}{(3!)^2} + \dots \quad (\text{B.8})$$

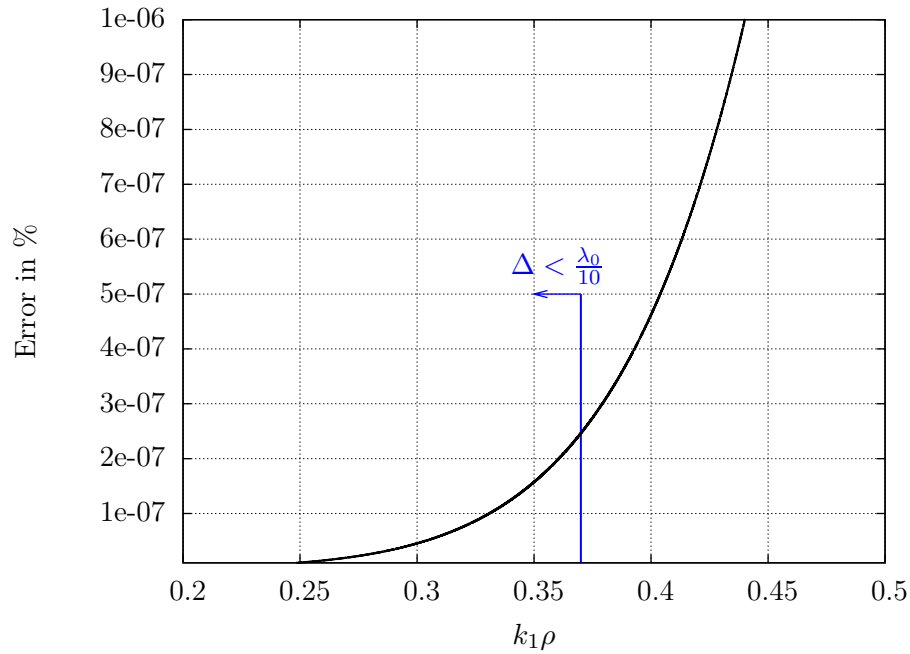


Fig. B.2: Error between the function $J_0(k_1\rho)$ approximated with a polynomial of third order (B.6) and the implemented function in Fortran.

B.2 Numerical Integration

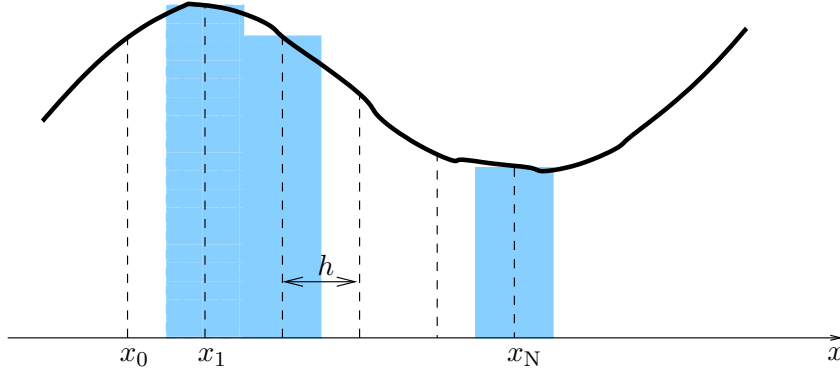


Fig. B.3: Numerical integration.

B.2.1 Approximate Integration

Let $f(x)$ a function with known points $x_i = x_0 + ih$. We define $f_i = f(x_i)$. The integral over f can be approximated [50,112]:

$$I_1 = \int_{x_1}^{x_N} f(x) dx \approx h \sum_{i=1}^N (s_N)_i f_i = h \mathbf{s}_N^T \mathbf{f}, \quad (\text{B.9})$$

where

$$\mathbf{f} = (f_1 \quad f_2 \quad \dots \quad f_N)^T,$$

and, depending on the order of approximation, the integration points are given:

$$\mathbf{s}_N = \left(\begin{array}{cccc} \frac{1}{2} & 1 & \dots & 1 \\ & & & \underbrace{\hspace{1cm}}_{N-1} \\ & & & \underbrace{\frac{1}{2}}_N \end{array} \right)^T \quad \text{second order,} \quad (\text{B.10})$$

$$\mathbf{s}_N = \left(\begin{array}{ccccccc} \frac{5}{12} & \frac{13}{12} & 1 & \dots & 1 & \frac{13}{12} & \frac{5}{12} \\ & & & & \underbrace{\hspace{1cm}}_{N-2} & \underbrace{\hspace{1cm}}_{N-1} & \underbrace{\hspace{1cm}}_N \end{array} \right)^T \quad \text{third order,} \quad (\text{B.11})$$

$$\mathbf{s}_N = \left(\begin{array}{cccccccc} \frac{3}{8} & \frac{7}{6} & \frac{23}{24} & 1 & \dots & 1 & \frac{23}{24} & \frac{7}{6} & \frac{3}{8} \\ & & & & & \underbrace{\hspace{1cm}}_{N-3} & \underbrace{\hspace{1cm}}_{N-2} & \underbrace{\hspace{1cm}}_{N-1} & \underbrace{\hspace{1cm}}_N \end{array} \right)^T \quad \text{fourth order.} \quad (\text{B.12})$$

B.2.2 Approximate Double Integration

Let $f(x, y)$ a function with known points (x_i, y_i) where $x_i = x_0 + ih_x$ and $y_j = y_0 + jh_y$. We define $f_{ij} = f(x_i, y_j)$. The double integral over f can be approximated:

$$\begin{aligned}
 I_2 &= \iint_{(x_1, y_1)}^{(x_N, y_M)} f(x, y) dx dy = \int_{y_1}^{y_M} \left(\int_{x_1}^{x_N} f(x, y) dx \right) dy \\
 &\approx \int_{y_1}^{y_M} \left(h_x \sum_{i=1}^N (s_N)_i f_{ij} \right) dy \\
 &\approx h_x h_y \sum_{i=1}^N \sum_{j=1}^M (s_N)_i (s_M)_j f_{ij} = h_x h_y \mathbf{s}_N^T \mathbf{F} \mathbf{s}_M \quad (\text{B.13})
 \end{aligned}$$

where the elements of the matrix \mathbf{F} , which has the dimension $N \times M$, are the values of f_{ij} . The integral I_2 can also be written as:

$$I_2 \approx h_x h_y \sum_{i=1}^N \sum_{j=1}^M (d_{NM})_{ij} f_{ij} \quad (\text{B.14})$$

where the weights $(d_{NM})_{ij} = (s_N)_i (s_M)_j$ are the elements of the matrix \mathbf{D}_{NM} , which has the dimension $N \times M$, given by:

$$\mathbf{D}_{NM} = \mathbf{s}_N \mathbf{s}_M^T. \quad (\text{B.15})$$

B.3 Comparison between Chosen Approach and Numerical Integration

The equations (2.47) and (2.48) have been implemented in FLEXIMOM. Also the numerical integration presented in (2.41) and (2.43) is choice-able. In order to calculate the integral for the case $n = m$, N and M have to be even-numbers. If this is not the case one would be in a singularity of $H(0)$.

B.3.1 Wavelength in the Order of Meters

The difference between the results obtained for a cell size of $\lambda_0/10$ and $\lambda_0/20$ can be explained as following: smaller the cell is closer are the results for the approximation and for the numerical integration to the exact solution. That's why also the difference between both is smaller.

Appendix B. Approach for the Integration over a Squared Disc with an
148 Optimal Circular Disc

Parameter	First case	Second case	Unit
Frequency	$f = 1$		GHz
Area	$x = -1.5 \cdots 1.5$		m
	$y = -1.5 \cdots 1.5$		m
Δx	$0.03 = \frac{\lambda_0}{10}$	$0.015 = \frac{\lambda_0}{20}$	m
Δy	$0.03 = \frac{\lambda_0}{10}$	$0.015 = \frac{\lambda_0}{20}$	m

Tab. B.1: Chosen parameters to compare numerical integration with chosen approach.

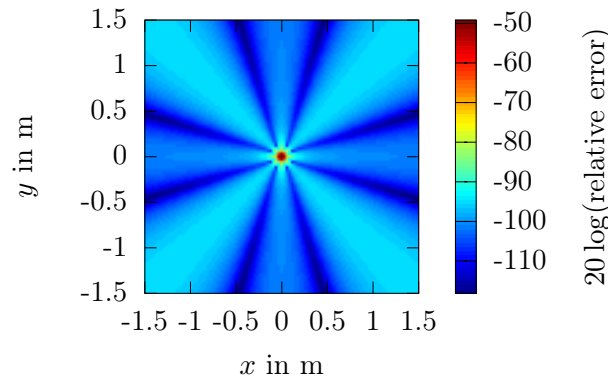


Fig. B.4: Error between approach and numerical integration for $N=10$ and $\Delta = \frac{\lambda_0}{10}$.

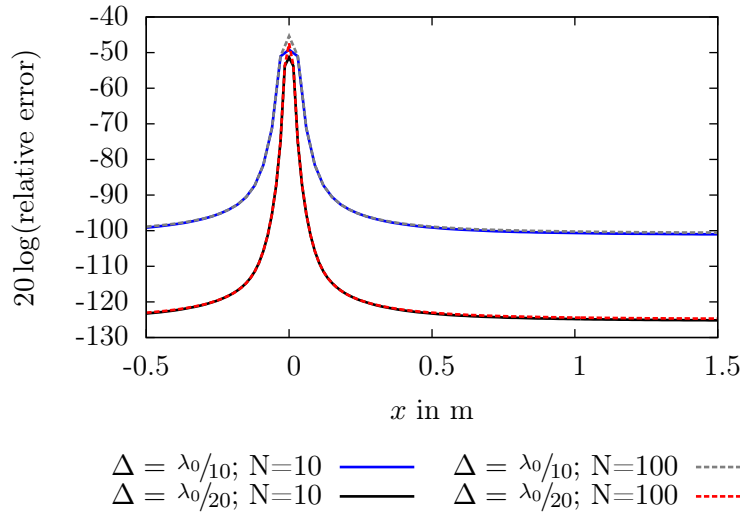


Fig. B.5: Error as function of N .

	Time in CPU seconds	
	$\frac{\lambda_0}{10}$	$\frac{\lambda_0}{20}$
Approximation	0.012001	0.040002
$N = 10$	1.8841	7.5845
$N = 100$	88.210	359.91

Tab. B.2: Differences in computation time between the approach and the numerical integration.

B.3.2 Wavelength in the Order of Millimeters

Parameter	First case	Second case	Unit
Frequency	$f = 100$		GHz
Area	$x = -0.015 \dots 0.015$		m
	$y = -0.015 \dots 0.015$		m
Δx	$0.0003 = \frac{\lambda_0}{10}$	$0.00015 = \frac{\lambda_0}{20}$	m
Δy	$0.0003 = \frac{\lambda_0}{10}$	$0.00015 = \frac{\lambda_0}{20}$	m

Tab. B.3: Chosen parameters to compare numerical integration with chosen approach.

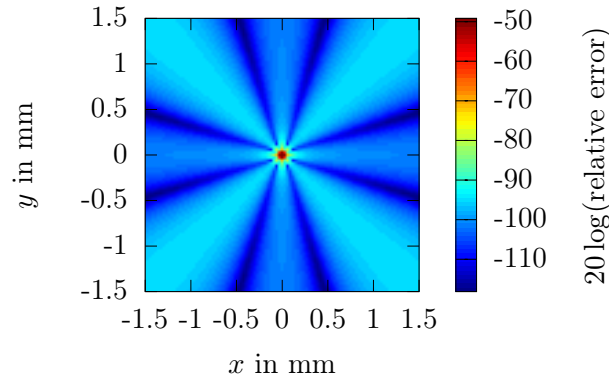


Fig. B.6: Error between approach and numerical integration for $N=10$ and $\Delta = \frac{\lambda_0}{10}$.

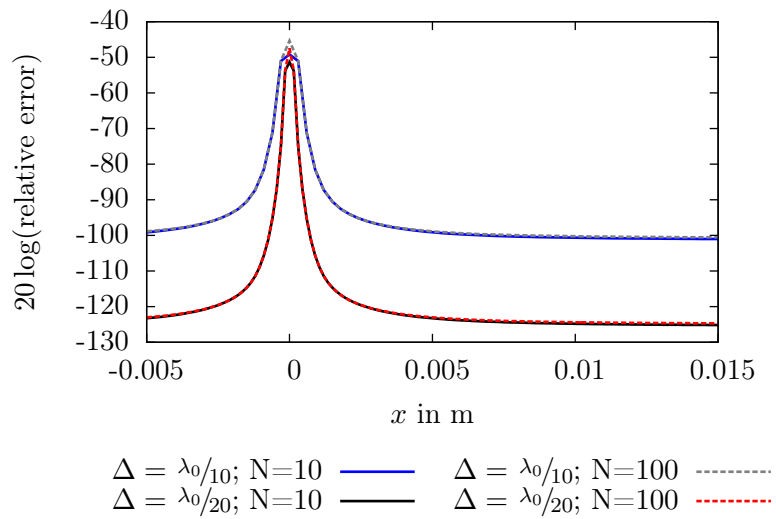


Fig. B.7: Error as function of N.

Additional Scattered Field Measurements

In the main body of the manuscript only measurements have been shown for the center frequency of 92.5 GHz. In the following, results are presented for 75 GHz and 110 GHz. The results have been obtained by using the open-ended waveguide as emitting antenna and the standard gain horn as receiver.

Firstly, the results are plotted for 75 GHz: the measured incident field (Fig. C.1), the measured total field for the metallic cylinders with $D = 20$ mm (Fig. C.2) and $D = 8$ mm (Fig. C.4), respectively, as well as for the dielectric cylinder (Fig. C.6). Out of these results the scattered fields are extracted (see Fig. C.3, Fig. C.5 and Fig. C.7) and compared with the analytic solution. Therefore, the amplitude of the measured and simulated scattered fields have been normalized with respect to their maxima. In simulation with ESCALE a diameter of 15.4 mm, an $\varepsilon_r = 2.49$ and a $\sigma = 0.1243$ S/m have been taken to characterize the dielectric cylinder.

Additionally, measured fields for 110 GHz are visualized: the measured incident field (C.8), the measured total field for the metallic cylinders with $D = 20$ mm (Fig. C.9) and $D = 8$ mm (Fig. C.11), respectively, and for the dielectric cylinder (Fig. C.13). The extracted scattered fields from measurements are compared with simulations in Fig. C.10, Fig. C.12 and Fig. C.14.

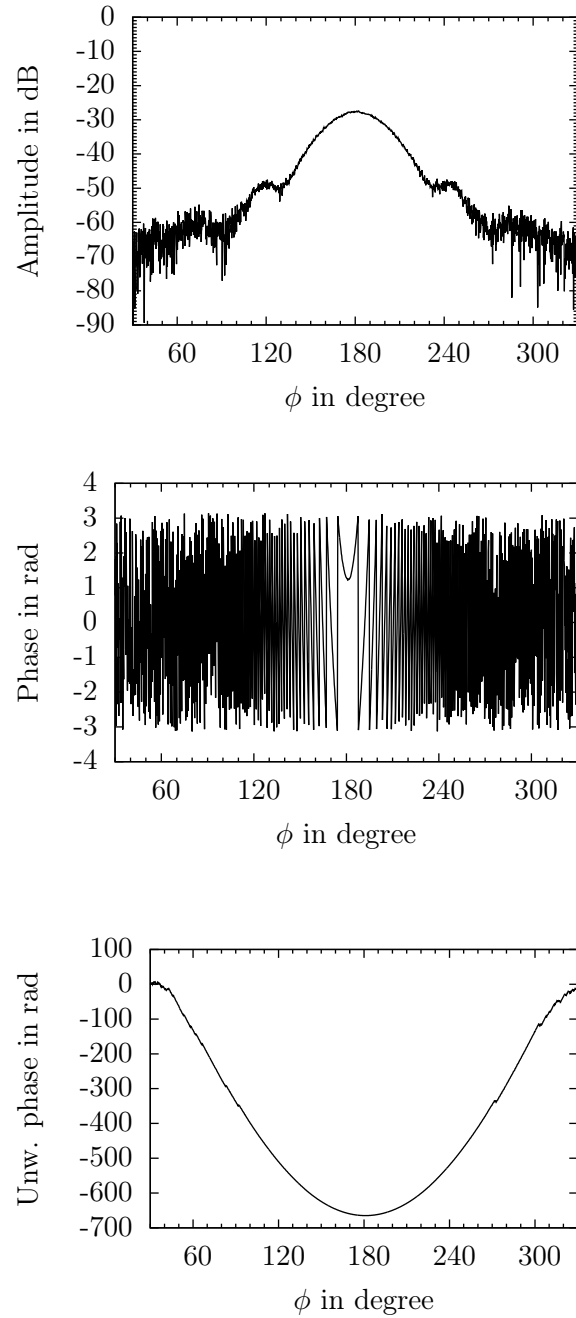


Fig. C.1: Measured incident field for $f = 75$ GHz in amplitude (top), phase (middle) and unwrapped phase (bottom).

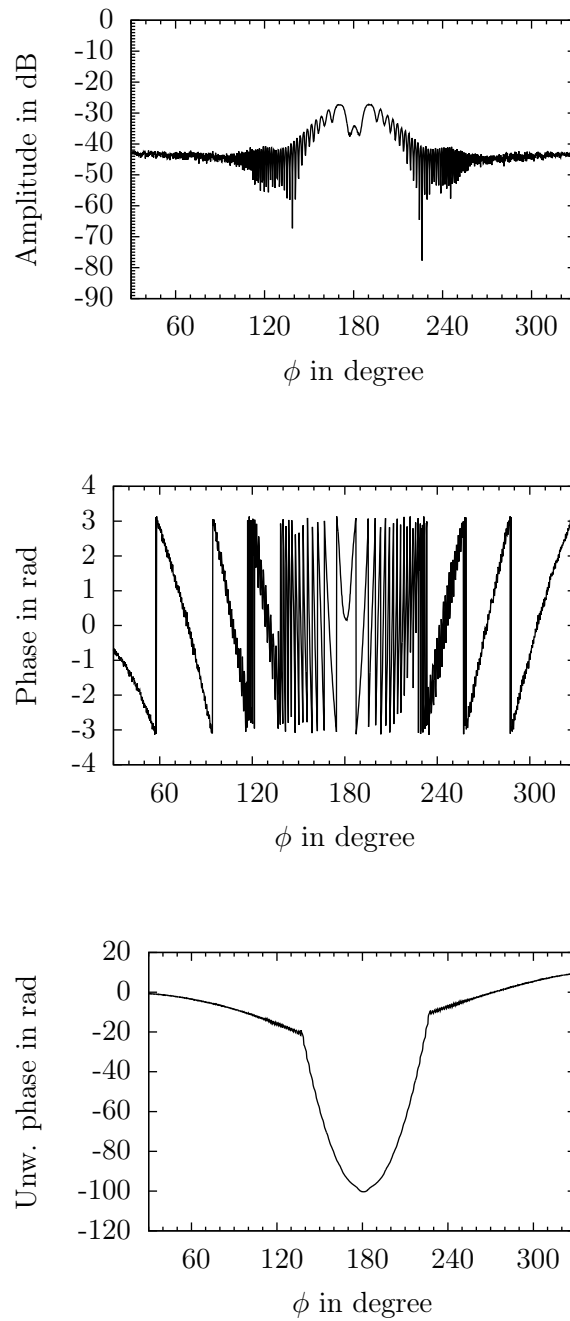


Fig. C.2: Measured total field with metallic cylinder, $D = 20$ mm, for $f = 75$ GHz in amplitude (top), phase (middle) and unwrapped phase (bottom).

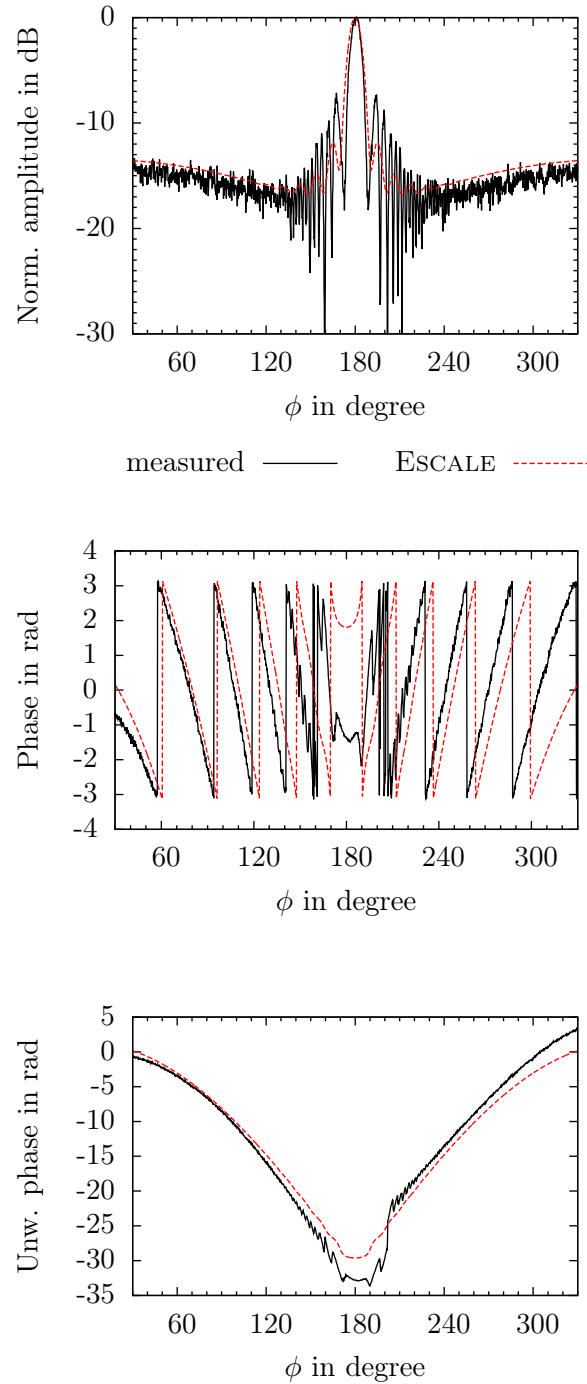


Fig. C.3: Extracted scattered field with metallic cylinder, $D = 20$ mm, for $f = 75$ GHz in normalized amplitude (top), phase (middle) and unwrapped phase (bottom).

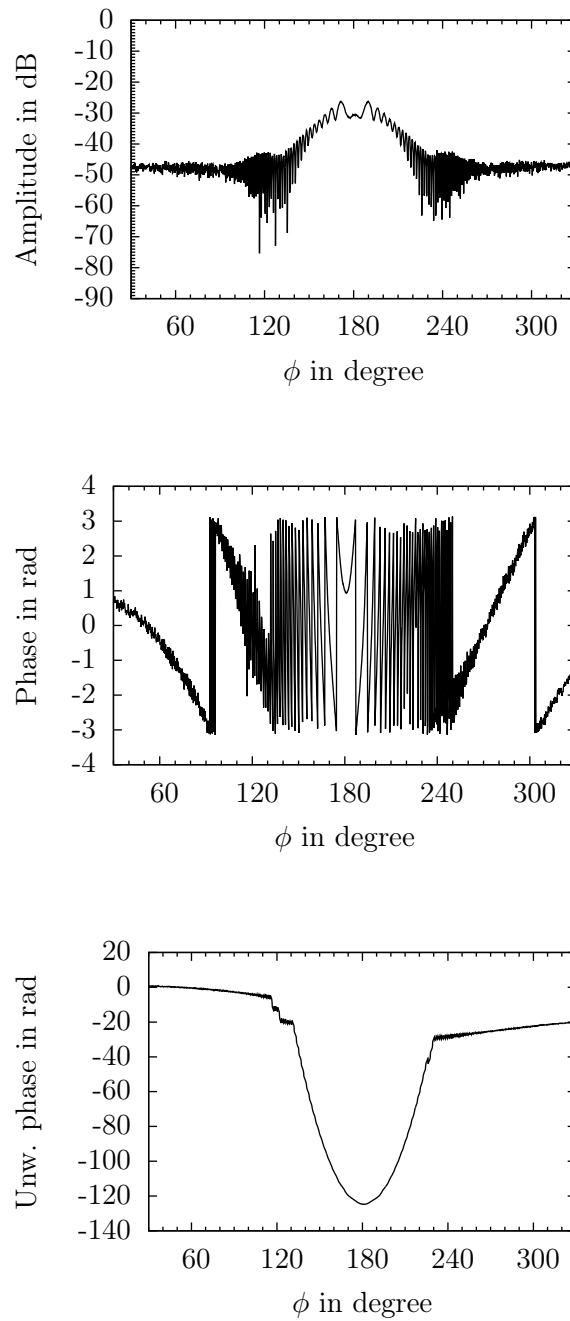


Fig. C.4: Measured total field with metallic cylinder, $D = 8$ mm, for $f = 75$ GHz in amplitude (top), phase (middle) and unwrapped phase (bottom).

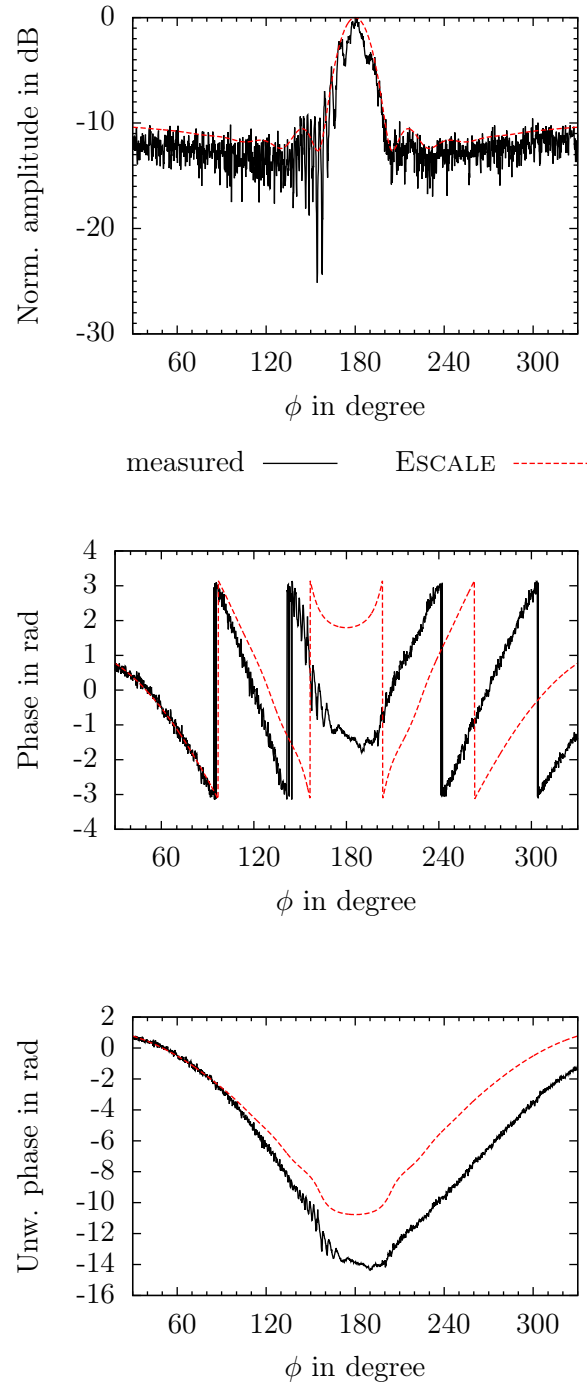


Fig. C.5: Extracted scattered field with metallic cylinder, $D = 8$ mm, for $f = 75$ GHz in normalized amplitude (top), phase (middle) and unwrapped phase (bottom).

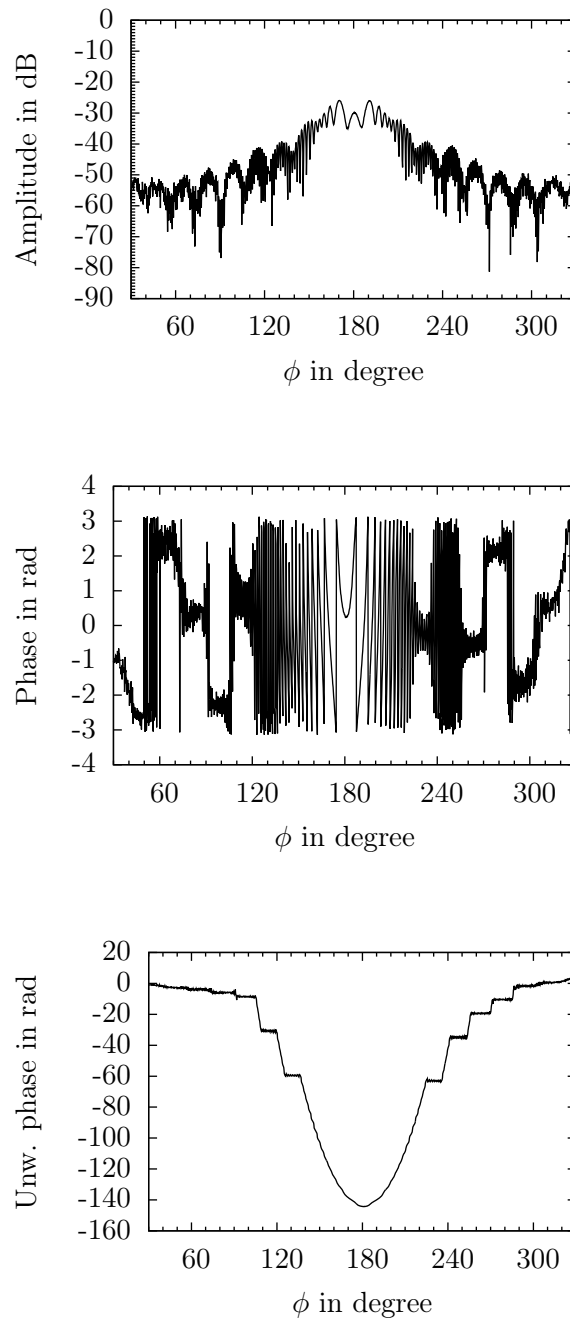


Fig. C.6: Measured total field with dielectric cylinder for $f = 75$ GHz in amplitude (top), phase (middle) and unwrapped phase (bottom).

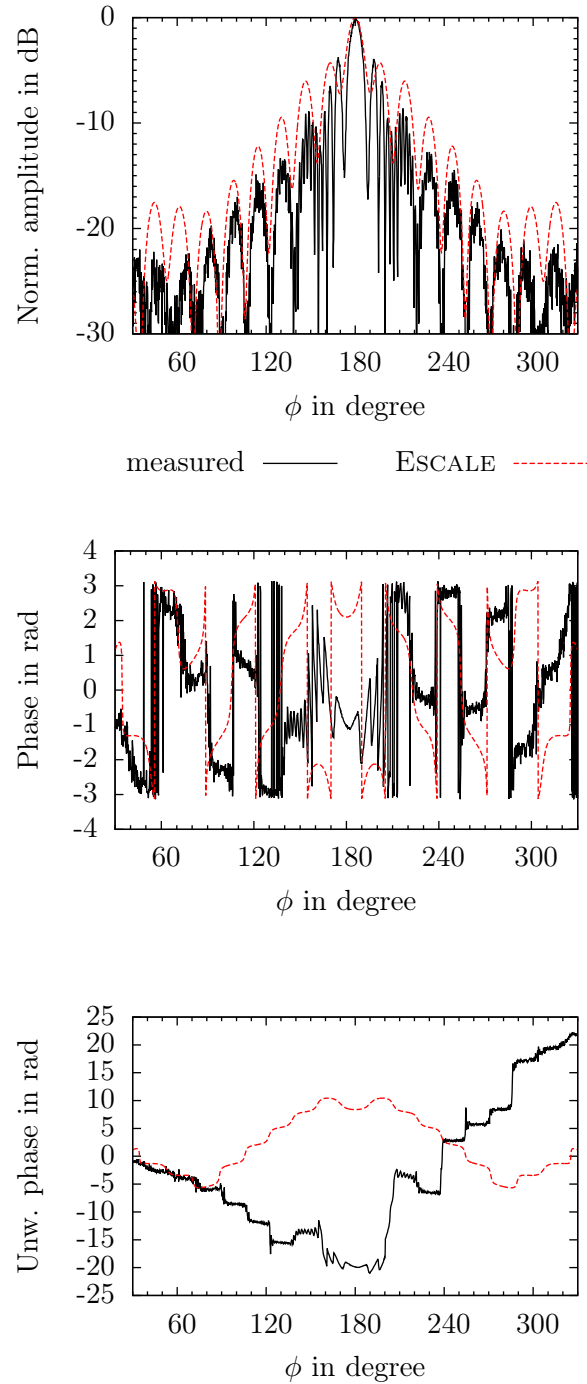


Fig. C.7: Extracted scattered field with dielectric cylinder for $f = 75$ GHz in normalized amplitude (top), phase (middle) and unwrapped phase (bottom).

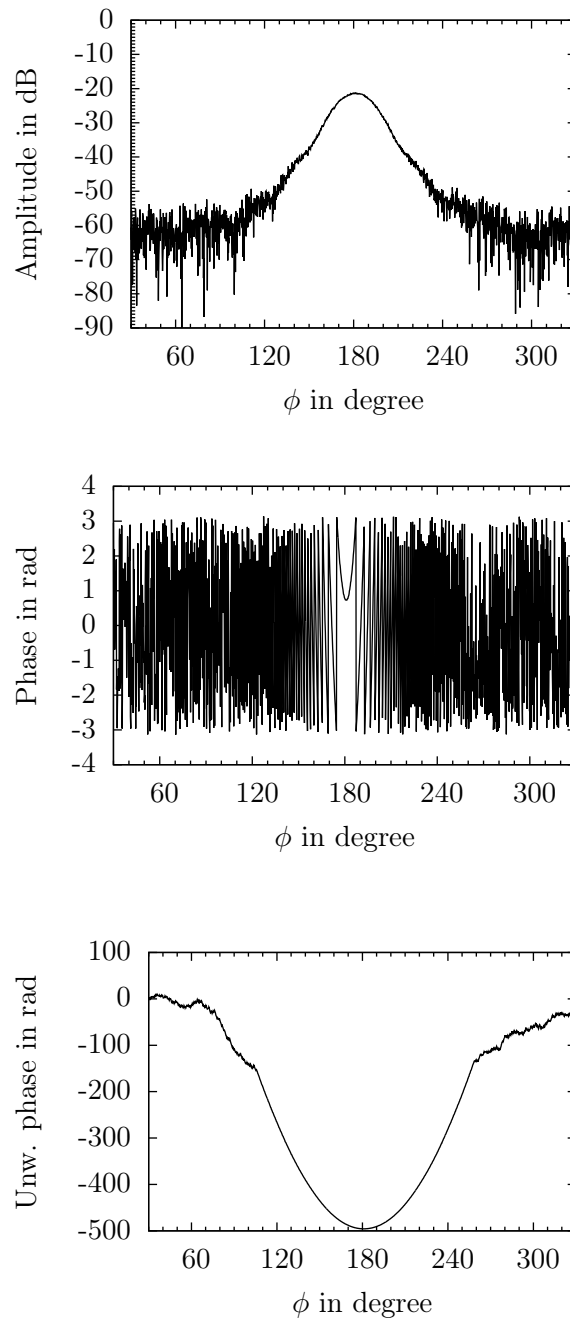


Fig. C.8: Measured incident field for $f = 110$ GHz in amplitude (top), phase (middle) and unwrapped phase (bottom).

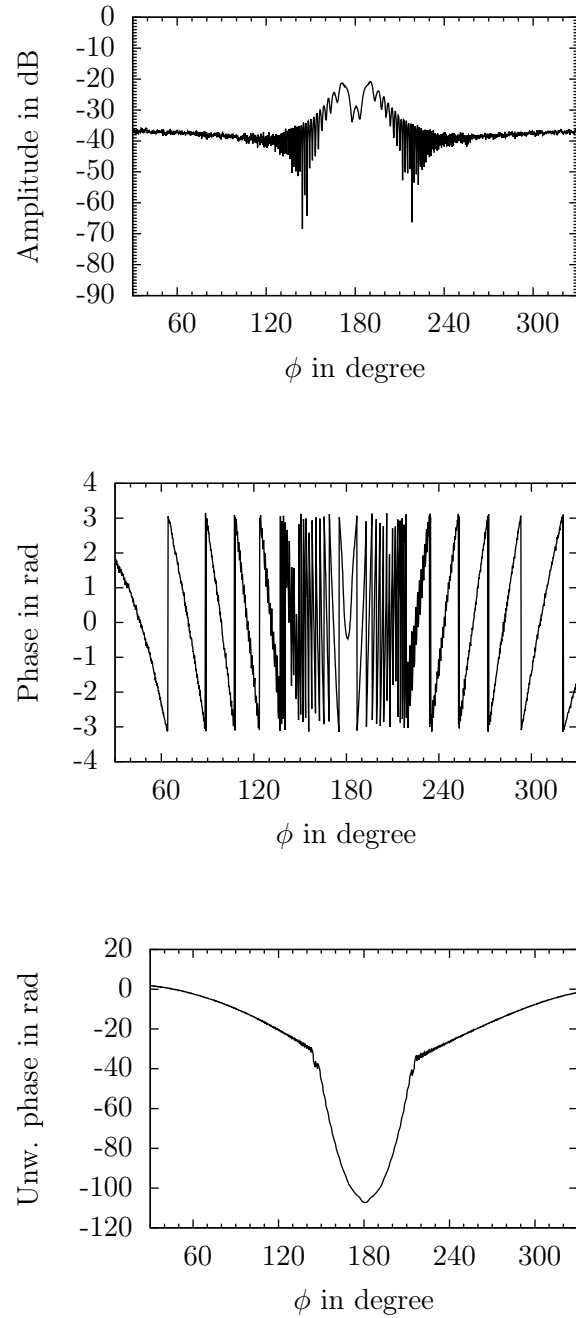


Fig. C.9: Measured total field with metallic cylinder, $D = 20$ mm, for $f = 110$ GHz in amplitude (top), phase (middle) and unwrapped phase (bottom).

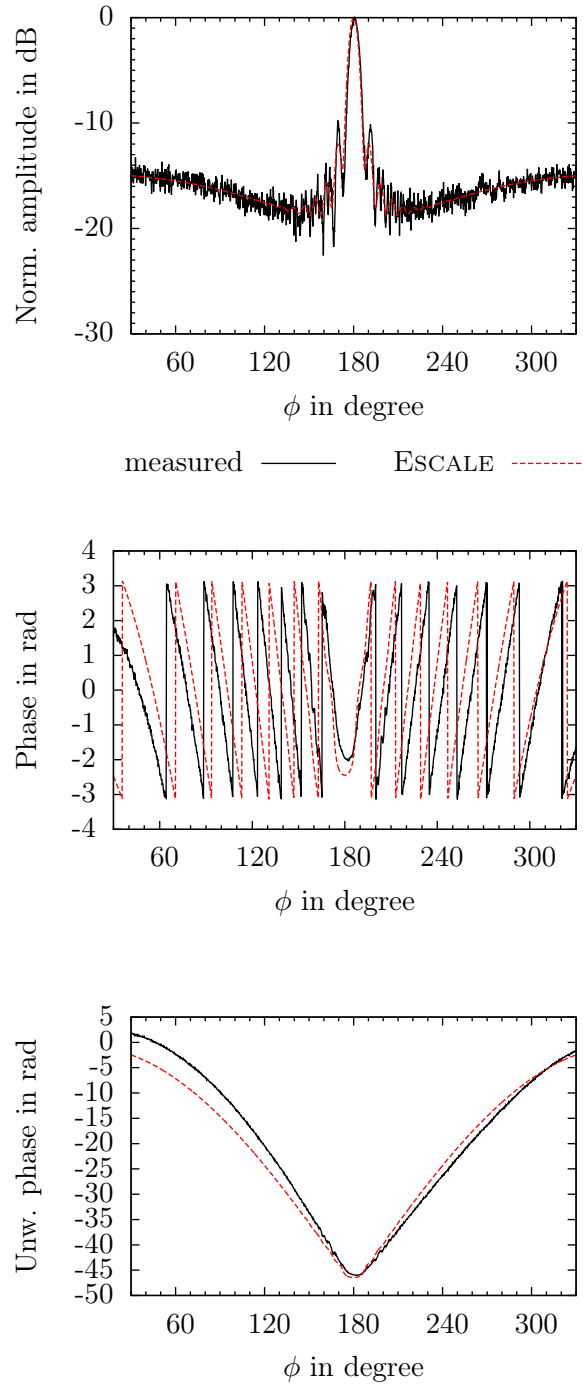


Fig. C.10: Extracted scattered field with metallic cylinder, $D = 20$ mm, for $f = 110$ GHz in normalized amplitude (top), phase (middle) and unwrapped phase (bottom).

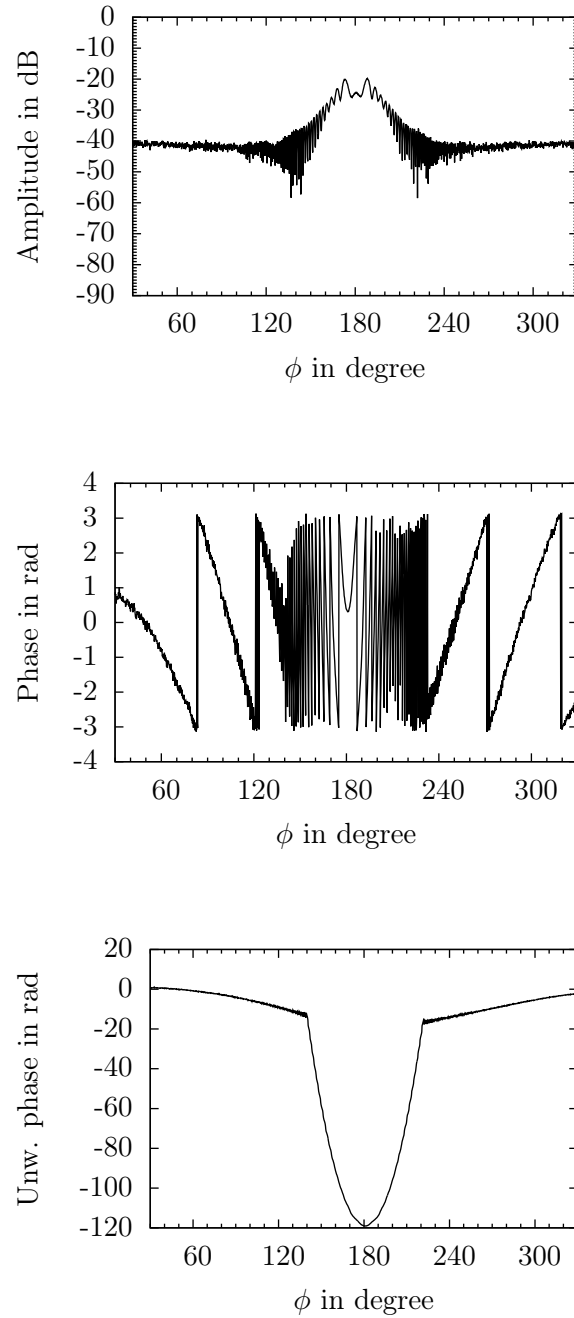


Fig. C.11: Measured total field with metallic cylinder, $D = 8$ mm, for $f = 110$ GHz in amplitude (top), phase (middle) and unwrapped phase (bottom).

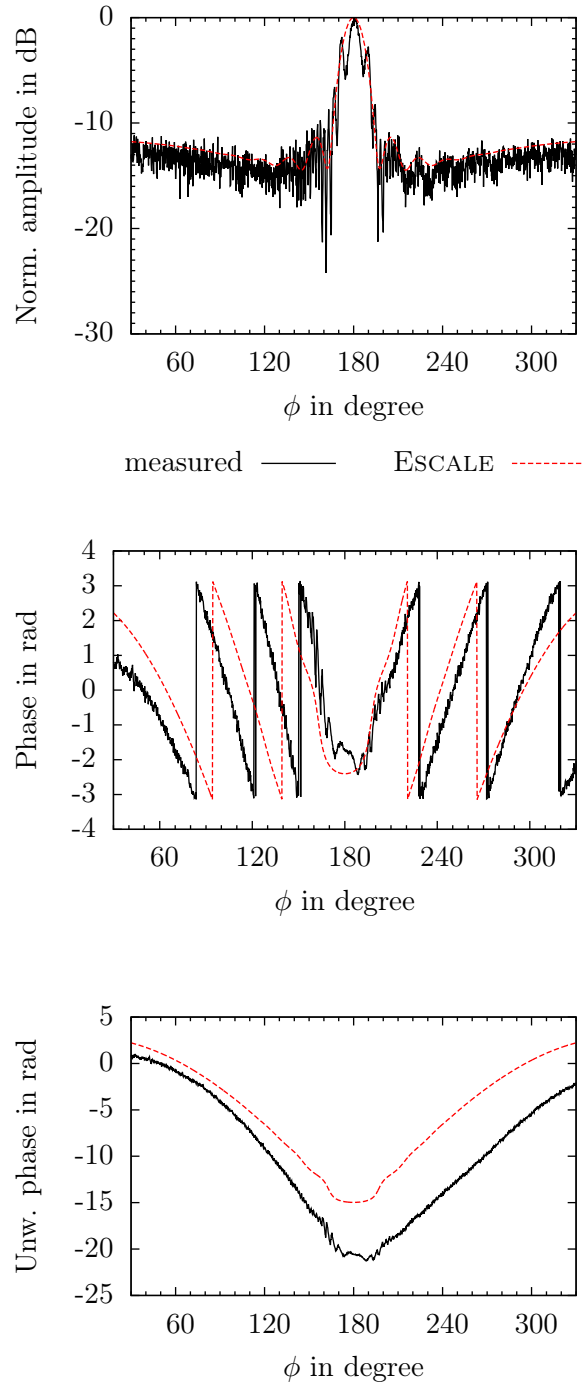


Fig. C.12: Extracted scattered field with metallic cylinder, $D = 8$ mm, for $f = 110$ GHz in normalized amplitude (top), phase (middle) and unwrapped phase (bottom).

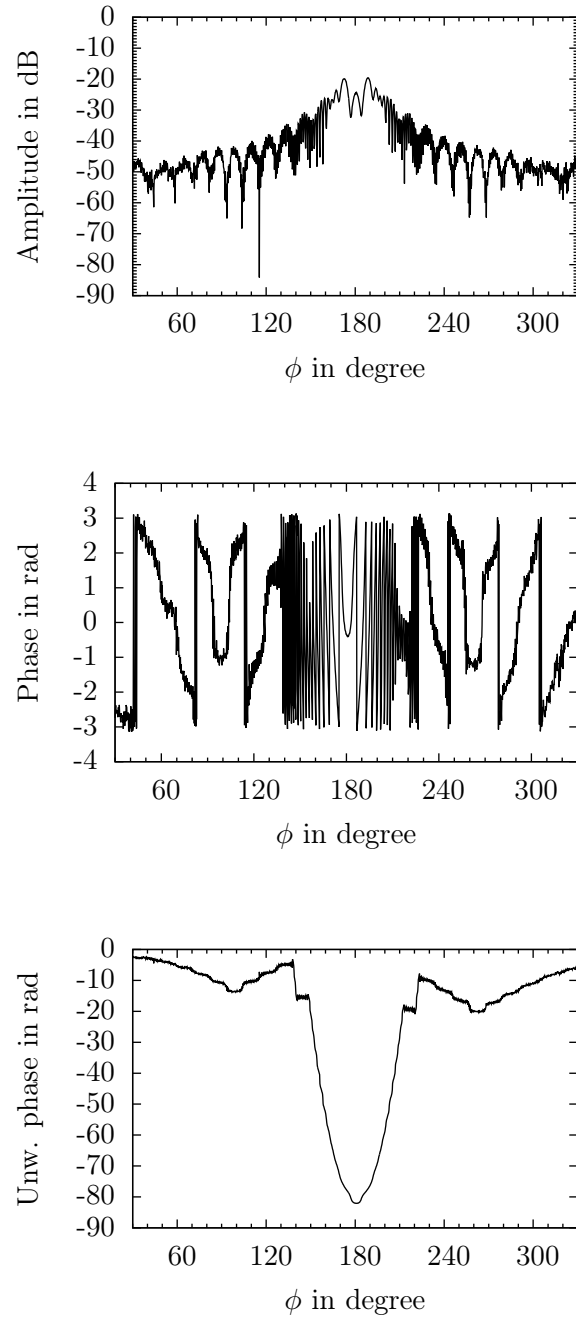


Fig. C.13: Measured total field with dielectric cylinder for $f = 110$ GHz in amplitude (top), phase (middle) and unwrapped phase (bottom).

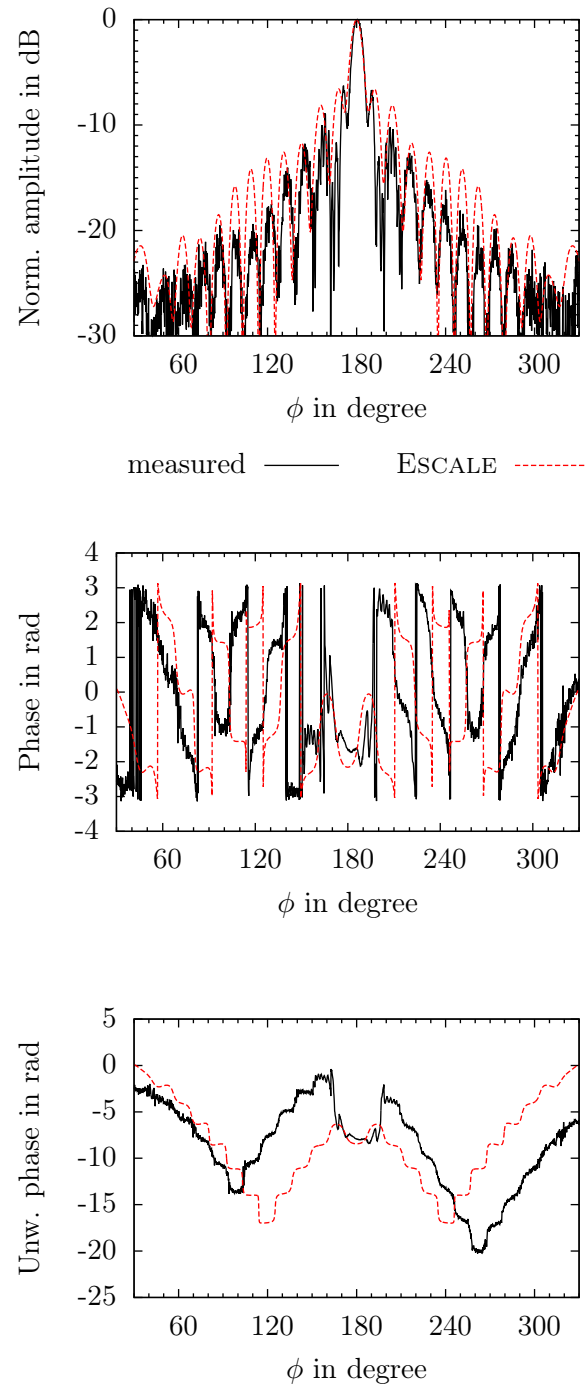


Fig. C.14: Extracted scattered field with dielectric cylinder for $f = 110$ GHz in normalized amplitude (top), phase (middle) and unwrapped phase (bottom).

Bibliography

- [1] W. Mayer, A. Gronau, W. Menzel, and H. Leier, “A Compact 24 GHz Sensor for Beam-Forming and Imaging,” in *9th International Conference on Control, Automation, Robotics and Vision (ICARCV 2006)*. IEEE, Dec. 2006, pp. 1–6.
Referenced on page: 1, 1
- [2] B. Michael, W. Menzel, and A. Gronau, “A real-time close-range imaging system with fixed antennas,” *IEEE Transactions on Microwave Theory and Techniques*, vol. 48, no. 12, pp. 2736–2741, Dec. 2000.
Referenced on page: 1, 1, 28, 108, 109
- [3] M. Andres, P. Feil, and W. Menzel, “3D-scattering center detection of automotive targets using 77 GHz UWB radar sensors,” in *6th European Conference on Antennas and Propagation (EUCAP 2012)*. IEEE, Mar. 2012, pp. 3690–3693.
Referenced on page: 1
- [4] C. Migliaccio, B. D. Nguyen, C. Pichot, N. Yonemoto, K. Yamamoto, K. Yamada, H. Nasui, W. Mayer, A. Gronau, and W. Menzel, “Millimeter-Wave Radar for Rescue Helicopters,” in *9th International Conference on Control, Automation, Robotics and Vision (ICARCV 2006)*. IEEE, Dec. 2006, pp. 1–6.
Referenced on page: 1, 1
- [5] H. Essen, S. Boehmsdorff, G. Biegel, and A. Wahlen, “On the scattering mechanism of power lines at millimeter-waves,” *IEEE Transactions on Geoscience and Remote Sensing*, vol. 40, no. 9, pp. 1895–1903, Sep. 2002.
Referenced on page: 1, 1
- [6] K. Sarabandi and M. Park, “Extraction of power line maps from millimeter-wave polarimetric SAR images,” *IEEE Transactions on Antennas and Propagation*, vol. 48, no. 12, pp. 1802–1809, Dec. 2000.
Referenced on page: 1, 1
- [7] —, “A radar cross-section model for power lines at millimeter-wave frequencies,” *IEEE Transactions on Antennas and Propagation*, vol. 51, no. 9, pp. 2353–2360, Sep. 2003.
Referenced on page: 1, 1
- [8] P. Feil, W. Menzel, T. P. Nguyen, C. Pichot, and C. Migliaccio, “Foreign objects debris detection (FOD) on airport runways using a broadband 78 GHz sensor,” in *European Radar Conference (EURAD 2008)*. IEEE, Oct. 2008, pp. 451–454.
Referenced on page: 1, 1, 1, 108

- [9] M. R. Hajihashemi and M. El-Shenawee, "The Level Set Shape Reconstruction Algorithm Applied to 2D PEC Targets Hidden Behind a Wall," *Progress In Electromagnetics Research B*, vol. 25, pp. 131–154, 2010.
Referenced on page: 1
- [10] A. Cresp, I. Aliferis, M. J. Yedlin, C. Pichot, and J.-Y. Dauvignac, "Investigation of time-reversal processing for surface-penetrating radar detection in a multiple-target configuration," in *European Radar Conference (EURAD 2008)*. IEEE, Oct. 2008, pp. 144–147.
Referenced on page: 1, 2
- [11] M. Yedlin, A. Cresp, C. Pichot, I. Aliferis, J.-Y. Dauvignac, S. Gaffet, and G. Sénéchal, "Ultra-wideband microwave imaging of heterogeneities," *Journal of Applied Geophysics*, vol. 68, no. 1, pp. 17–25, May 2009.
Referenced on page: 1, 2
- [12] M. Leib, E. Schmitt, A. Gronau, J. Dederer, B. Schleicher, H. Schumacher, and W. Menzel, "A Compact Ultra-wideband Radar for Medical Applications," *Frequenz*, vol. 63, no. 1-2, pp. 2–8, Feb. 2009.
Referenced on page: 1
- [13] D. L. McMakin, D. M. Sheen, J. W. Griffin, N. B. Valentine, and W. M. Lechelt, "Personnel and mail screening with millimeter waves," in *Defense and Security Symposium 2005*, vol. 5778, no. 1. The International Society for Optical Engineering., Aug. 2005, pp. 160–168.
Referenced on page: 1
- [14] O. M. Bucci, L. Crocco, T. Isernia, and V. Pascazio, "Inverse scattering problems with multifrequency data: reconstruction capabilities and solution strategies," *IEEE Transactions on Geoscience and Remote Sensing*, vol. 38, no. 4, pp. 1749–1756, Jul. 2000.
Referenced on page: 1
- [15] M. R. Hajihashemi and M. El-Shenawee, "Shape Reconstruction Using the Level Set Method for Microwave Applications," *Antennas and Wireless Propagation Letters, IEEE*, vol. 7, pp. 92–96, 2008.
Referenced on page: 1
- [16] M. El-Shenawee, O. Dorn, and M. Moscoso, "An Adjoint-Field Technique for Shape Reconstruction of 3-D Penetrable Object Immersed in Lossy Medium," *IEEE Transactions on Antennas and Propagation*, vol. 57, no. 2, pp. 520–534, Feb. 2009.
Referenced on page: 1
- [17] K. Belkebir, J. M. Elissalt, J. M. Geffrin, and C. Pichot, "Newton-Kantorovich and Modified Gradient - Inversion Algorithms Applied to Ipswich Data," *Antennas and Propagation Magazine*, vol. 38, no. 3, pp. 41–44, Jun. 1996.
Referenced on page: 1, 1, 35

- [18] D. A. Woten, M. R. Hajishemi, A. M. Hassan, and M. El-Shenawee, "Experimental Microwave Validation of Level Set Reconstruction Algorithm," *IEEE Transactions on Antennas and Propagation*, vol. 58, no. 1, pp. 230–233, Jan. 2010.
Referenced on page: 1
- [19] P. Lobel, R. E. Kleinman, C. Pichot, L. Blanc-Féraud, and M. Barlaud, "Conjugate-Gradient Method for Solving Inverse Scattering with Experimental Data," *Antennas and Propagation Magazine*, vol. 38, no. 3, pp. 48–51, Jun. 1996.
Referenced on page: 1, 1, 25, 30, 35, 66, 98, 101, 104, 106
- [20] P. M. van den Berg, M. G. Cote, and R. E. Kleinman, "'Blind' shape reconstruction from experimental data," *IEEE Transactions on Antennas and Propagation*, vol. 43, no. 12, pp. 1389–1396, Dec. 1995.
Referenced on page: 1, 35
- [21] B. Gustafson, "Microwave analog to light scattering measurements: A modern implementation of a proven method to achieve precise control," *Journal of Quantitative Spectroscopy and Radiative Transfer*, vol. 55, no. 5, pp. 663–672, May 1996.
Referenced on page: 1, 36
- [22] Y. Xu, "A generalized multiparticle Mie-solution: further experimental verification," *Journal of Quantitative Spectroscopy and Radiative Transfer*, vol. 70, no. 4-6, pp. 395–419, Aug. 2001.
Referenced on page: 1
- [23] J. M. Geffrin and P. Sabouroux, "Continuing with the Fresnel database: experimental setup and improvements in 3D scattering measurements," *Inverse Problems*, vol. 25, no. 2, Feb. 2009.
Referenced on page: 1, 36
- [24] J.-M. Geffrin, P. Sabouroux, and C. Eyraud, "Free space experimental scattering database continuation: experimental set-up and measurement precision," *Inverse Problems*, vol. 21, no. 6, pp. S117–S130, Dec. 2005.
Referenced on page: 1, 36, 36
- [25] M. G. Cote, "Automated swept-angle bistatic scattering measurements using continuous wave radar," *IEEE Transactions on Instrumentation and Measurement*, vol. 41, no. 2, pp. 185–192, Apr. 1992.
Referenced on page: 1, 35
- [26] A. Tamminen, J. Ala-Laurinaho, and A. V. Raisanen, "Indirect holographic imaging at 310 GHz," in *European Radar Conference (EURAD 2008)*. IEEE, Oct. 2008, pp. 168–171.
Referenced on page: 1, 2

- [27] H. T. Chen, R. Kersting, and G. C. Cho, "Terahertz imaging with nanometer resolution," *Applied Physics Letters*, vol. 83, no. 15, pp. 3009–3011, 2003.
Referenced on page: 1
- [28] D. M. Sheen, D. L. McMakin, and T. E. Hall, "Three-dimensional millimeter-wave imaging for concealed weapon detection," *IEEE Transactions on Microwave Theory and Techniques*, vol. 49, no. 9, pp. 1581–1592, Sep. 2001.
Referenced on page: 1
- [29] A. Schiessl and S. S. Ahmed, "W-band imaging of explosive substances," in *European Radar Conference (EURAD 2009)*. IEEE, 2009, pp. 617–620.
Referenced on page: 1, 2
- [30] M. Hiebel, "Differential Measurements Extended to the W-Band 75 GHz - 110 GHz," in *German Microwave Conference (GEMIC 2008)*. VDE, Mar. 2008, pp. 1–4.
Referenced on page: 1
- [31] S. S. Ahmed, A. Schiessl, and L. P. Schmidt, "Multistatic mm-Wave Imaging with Planar 2D-Arrays," in *German Microwave Conference (GEMIC 2009)*. IEEE, Mar. 2009, pp. 1–4.
Referenced on page: 1, 2
- [32] M. Multari, J. Lanteri, J. L. Le Sonn, L. Brochier, C. Pichot, C. Migliaccio, J. L. Desvilles, and P. Feil, "77 GHz Stepped Lens With Sectorial Radiation Pattern as Primary Feed of a Lens Based CATR," *IEEE Transactions on Antennas and Propagation*, vol. 58, no. 1, pp. 207–211, Jan. 2010.
Referenced on page: 1
- [33] A. Bréard, K. Mazouni, J. Lanteri, C. Migliaccio, A. Yatsou, D. Oriot, and T. Meynard, "INFRADAR : Fusion de capteur infrarouge et Radar pour l'aide au pilotage d'hélicoptères," in *GDR Ondes*, Nice, France, Oct. 2011.
Referenced on page: 1, 95
- [34] C. Pichot, P. Lobel, L. Blanc-Féraud, M. Barlaud, K. Belkebir, J. M. Elissalt, and J. M. Geffrin, "Gradient and Newton-Kantorovich Methods for Microwave Tomography," in *Inverse Problems in Medical Imaging and Nondestructive Testing*, H. W. Engl, A. K. Louis, and W. Rundell, Eds. Wien, New York: Springer-Verlag, 1997, pp. 168–187.
Referenced on page: 1, 98
- [35] P. Lobel, C. Pichot, L. Blanc-Féraud, and M. Barlaud, "Microwave imaging: Reconstructions from experimental data using conjugate gradient and enhancement by edge-preserving regularization," *Int. J. Imaging Syst. Technol.*, vol. 8, no. 4, pp. 337–342, 1997.
Referenced on page: 1, 66, 98

- [36] *Bayesian Approach to Inverse Problems (ISTE)*, 1st ed. Wiley-ISTE, Jun. 2008.
Referenced on page: 5
- [37] P. C. Hansen, *Discrete Inverse Problems: Insight and Algorithms (Fundamentals of Algorithms)*. SIAM-Society for Industrial and Applied Mathematics, Feb. 2010.
Referenced on page: 5
- [38] A. F. Peterson, S. L. Ray, and R. Mittra, *Computational Methods for Electromagnetics (IEEE Press Series on Electromagnetic Wave Theory)*, 1st ed. Wiley-IEEE Press, Dec. 1997.
Referenced on page: 5
- [39] Y. Zheng, S. Wang, J. Feng, Z. Ouyang, and X. Li, “Measurement of the complex permittivity of dry rocks and minerals: application of polythene dilution method and Lichtenecker’s mixture formulae,” *Geophysical Journal International*, vol. 163, no. 4, pp. 1195–1202, 2005.
Referenced on page: 7
- [40] I. Aliferis, “Ondes Electromagnétiques,” lecture notes, University of Nice-Sophia Antipolis, Polytech Nice Sophia, Sep. 2010.
Referenced on page: 7
- [41] *Free Space Materials Measurement Seminar*, Agilent Technologies, Jun. 2005.
Referenced on page: 7
- [42] C. Pichot, “personal notes,” University of Nice-Sophia Antipolis, Electronics, Antennas and Telecommunications Laboratory (LEAT), Nov. 2011.
Referenced on page: 8, 99
- [43] —, “Introduction to Microwave Imaging,” lecture notes, University of Nice-Sophia Antipolis, Electronics, Antennas and Telecommunications Laboratory (LEAT), Jan. 2012.
Referenced on page: 8, 25
- [44] —, “Méthodes Numériques en Electromagnétisme,” lecture notes, University of Nice-Sophia Antipolis, Electronics, Antennas and Telecommunications Laboratory (LEAT), Jan. 2012.
Referenced on page: 9
- [45] —, “Électromagnétisme,” in *Editions des Techniques de l’Ingénieur, Electronics Series*, Oct. 1986.
Referenced on page: 9
- [46] P. Lobel, “Problèmes de diffraction inverse : reconstruction d’image et optimisation avec régularisation par préservation des discontinuités - Application à

- l'imagerie microonde," Ph.D. dissertation, University of Nice-Sophia Antipolis, Electronics, Antennas and Telecommunications Laboratory (LEAT), Sep. 1996.
Referenced on page: 9, 98
- [47] E. Le Brusq, "Imagerie microonde : influence de la polarimétrie du champ diffracté," Ph.D. dissertation, University of Nice-Sophia Antipolis, Electronics, Antennas and Telecommunications Laboratory (LEAT), Oct. 2003.
Referenced on page: 9
- [48] R. Ferrayé, "Développement d'un algorithme de diffraction inverse par déformations eulériennes de courbes de niveaux pour la reconstruction d'images microondes application à l'imagerie radar," Ph.D. dissertation, University of Nice-Sophia Antipolis, Electronics, Antennas and Telecommunications Laboratory (LEAT), Mar. 2002.
Referenced on page: 9
- [49] C. Dourthe, "Tomographie microonde d'objets enterrés. Application à l'auscultation radar," Ph.D. dissertation, Ecole Nationale des Ponts et Chaussées ParisTech, Sep. 1997.
Referenced on page: 9
- [50] I. Aliferis, "Imagerie microonde d'objets enterrés : modélisations numériques bidimensionnelles et étude de l'extension tridimensionnelle," Ph.D. dissertation, University of Nice-Sophia Antipolis, Electronics, Antennas and Telecommunications Laboratory (LEAT) and National Technical University of Athens, Dec. 2002.
Referenced on page: 9, 146
- [51] L. B. Felsen and N. Marcuvitz, *Radiation and Scattering of Waves (IEEE Press Series on Electromagnetic Wave Theory)*. Wiley-IEEE Press, Jan. 1994.
Referenced on page: 10
- [52] C. Pichot, "Méthode des Moments," lecture notes, University of Nice-Sophia Antipolis, Electronics, Antennas and Telecommunications Laboratory (LEAT), Jan. 2012.
Referenced on page: 11
- [53] W. C. Gibson, *The Method of Moments in Electromagnetics*, 1st ed. Chapman and Hall/CRC, Nov. 2007.
Referenced on page: 11
- [54] R. F. Harrington, *Field Computation by Moment Methods (IEEE Press Series on Electromagnetic Wave Theory)*. Wiley-IEEE Press, Apr. 1993.
Referenced on page: 11
- [55] J. Richmond, "Scattering by a dielectric cylinder of arbitrary cross section shape," *IEEE Transactions on Antennas and Propagation*, vol. 13, no. 3, pp.

- 334–341, May 1965.
Referenced on page: 13, 14, 21
- [56] —, “TE-wave scattering by a dielectric cylinder of arbitrary cross-section shape,” *IEEE Transactions on Antennas and Propagation*, vol. 14, no. 4, pp. 460–464, Jul. 1966.
Referenced on page: 14
- [57] A. Francois, “Application de la technique du recuit simulé à l’imagerie microonde,” Master’s thesis, Université de Paris-XI, Jun. 1989.
Referenced on page: 14
- [58] —, “Contribution à la tomographie microonde : algorithmes de reconstruction quantitative et vérifications expérimentales,” Ph.D. dissertation, Université de Paris-XI, Jun. 1993.
Referenced on page: 14
- [59] Semendjajew, *Taschenbuch der Mathematik*, 7th ed. Deutsch Harri GmbH, Jul. 2008.
Referenced on page: 15
- [60] C. A. Balanis, *Advanced Engineering Electromagnetics*. Wiley, May 1989.
Referenced on page: 17, 17
- [61] S. Chapman, *Fortran 95/2003 for Scientists & Engineers*, 3rd ed. McGraw-Hill Science/Engineering/Math, Apr. 2007.
Referenced on page: 17
- [62] Understand, Source Code Analysis & Metrics. Scitools. [Online]. Available: <http://www.scitools.com/>
Referenced on page: 17
- [63] The Lattix Architecture Management System. [Online]. Available: <http://www.lattix.com>
Referenced on page: 17
- [64] *LAPACK - Linear Algebra PACKage*. [Online]. Available: <http://www.netlib.org/lapack/>
Referenced on page: 19
- [65] *PLplot, The ultimate in cross-platform plotting*. [Online]. Available: <http://plplot.sourceforge.net/>
Referenced on page: 19
- [66] J. W. Eaton, *GNU Octave*. [Online]. Available: <http://www.gnu.org/software/octave/>
Referenced on page: 20

- [67] R. E. Ziemer and W. H. Tranter, *Principles of Communication: Systems, Modulation and Noise*, 5th ed. Wiley, Jul. 2001.
Referenced on page: 23, 69
- [68] B. Michael and W. Menzel, “A novel close-range imaging system,” in *26th European Microwave Conference (EuMC 1996)*. IEEE, Oct. 1996, pp. 130–134.
Referenced on page: 28, 108
- [69] W. Mayer, “Abbildender Radarsensor mit sendeseitig geschalteter Gruppenantenne,” Ph.D. dissertation, Ulm University, Institute of Microwave Techniques, Feb. 2008.
Referenced on page: 28, 108
- [70] N. Maaref, “Étude d’un concept de radar de détection de personnes à travers les murs et les obstacles,” Ph.D. dissertation, University of Nice-Sophia Antipolis, Electronics, Antennas and Telecommunications Laboratory (LEAT), 2009.
Referenced on page: 28, 122
- [71] J. Hadamard, *Lectures on Cauchy’s Problem in Linear Partial Differential Equations (Dover Phoenix Editions)*. Dover Publications, Dec. 2003.
Referenced on page: 30
- [72] C. Eyraud, “Caractérisation et optimisation, dans le domaine des hyperfréquences, des mesures de champs diffractés. Applications aux problèmes directs et inverses tridimensionnels,” Ph.D. dissertation, Université de Provence, Aix-Marseille 1, Institut Fresnel, Dec. 2006.
Referenced on page: 35, 75
- [73] R. V. McGahan and R. E. Kleinman, “Second annual special session on image reconstruction using real data,” *IEEE Antennas and Propagation Magazine*, vol. 39, no. 2, pp. 7–9, Apr. 1997.
Referenced on page: 35
- [74] L. Gürel, H. Bağcı, J. C. Castelli, A. Cheraly, and F. Tardivel, “Validation through comparison: Measurement and calculation of the bistatic radar cross section of a stealth target,” *Radio Science*, vol. 38, no. 3, pp. 12–1–12–10, Jun. 2003.
Referenced on page: 36
- [75] J. Garat, P. Naud, and J. P. Prulhière, “Moyens de mesure de la surface équivalente radar,” *Chocs - la revue scientifique et technique de la Direction des applications militaires (DAM)*, pp. 65–74, Sep. 1993.
Referenced on page: 36
- [76] J.-M. Geffrin, C. Eyraud, and A. Litman, “3D Inversion of lossy targets from free space scattering measurements,” in *6th European Conference on Antennas*

- and Propagation (EUCAP 2012)*. IEEE, Mar. 2012, pp. 3699–3702.
Referenced on page: 36
- [77] A. J. Sieber, “The European Microwave Signature Laboratory,” in *International Geoscience and Remote Sensing Symposium (IGARSS 1992)*. IEEE, 1992, pp. 1195–1200.
Referenced on page: 37
- [78] B. Hauck, F. Ulaby, and R. DeRoo, “Polarimetric bistatic-measurement facility for point and distributed targets,” *IEEE Antennas and Propagation Magazine*, vol. 40, no. 1, pp. 31–41, Feb. 1998.
Referenced on page: 37
- [79] J. Fordham, T. Schwartz, G. Cawthon, Y. Netzov, S. McBride, M. Awadalla, and D. Wayne, “Achieved accuracy of a spherical near-field arch positioning system,” in *6th European Conference on Antennas and Propagation (EUCAP 2012)*. IEEE, Mar. 2012, pp. 3195–3199.
Referenced on page: 37
- [80] A. Munoz-Acevedo, L. Rolo, M. Sierra-Castaner, and M. Paquay, “Influence of atmospheric conditions on mmWave CATR facilities: Formulation and compensation scheme,” in *6th European Conference on Antennas and Propagation (EUCAP 2012)*. IEEE, Mar. 2012, pp. 3681–3685.
Referenced on page: 37
- [81] *Agilent Technologies 85325A R/Q/U/V/W Millimeter Subsystem, Agilent Technologies 85326A Millimeter-Wave Interface Kit*, Nov. 1999. [Online]. Available: <http://www.home.agilent.com>
Referenced on page: 38, 42
- [82] B. T. DeWitt and W. D. Burnside, “Electromagnetic scattering by pyramidal and wedge absorber,” *IEEE Transactions on Antennas and Propagation*, vol. 36, no. 7, pp. 971–984, Jul. 1988.
Referenced on page: 38
- [83] *Agilent, 2-Port and 4-Port, PNA-X Network Analyzer*, Jun. 2010. [Online]. Available: <http://www.home.agilent.com>
Referenced on page: 39, 112
- [84] *Agilent Technologies N5261A and N5262A, User’s and Service Guide, Millimeter Head Controller*, Mar. 2009. [Online]. Available: <http://www.home.agilent.com>
Referenced on page: 39, 112
- [85] A. Papió-Toda, S. Amaya, L. Jofre, and F. De Flaviis, “Lens Antenna Probe for Near-Field W-Band Imaging,” in *IEEE International Symposium on Antennas and Propagation (IEEE APS 2011)*, Jul. 2011.
Referenced on page: 44

- [86] V. H. Rumsey, "Reaction Concept in Electromagnetic Theory," *Physical Review*, vol. 94, no. 6, pp. 1483–1491, Jun. 1954.
Referenced on page: 44
- [87] S. Ishigami, H. Iida, and T. Iwasaki, "Measurements of complex antenna factor by the near-field 3-antenna method," *IEEE Transactions on Electromagnetic Compatibility*, vol. 38, no. 3, pp. 424–432, Aug. 1996.
Referenced on page: 45
- [88] C. A. Balanis, *Antenna Theory: Analysis and Design*, 3rd ed. Wiley-Interscience, Apr. 2005.
Referenced on page: 45
- [89] *Microwave Products*, Microwave Flann, 2010. [Online]. Available: <http://www.flann.com/>
Referenced on page: 50
- [90] B. Gustafson, "Scaled analogue experiments in electromagnetic scattering," in *Light Scattering Reviews 4*, ser. Springer Praxis Books, A. A. Kokhanovsky, Ed. Berlin, Heidelberg: Springer Berlin Heidelberg, 2009, ch. 1, pp. 3–30.
Referenced on page: 58
- [91] S. Dieter, J. Li, S. Keyrouz, J. Ren, and W. Menzel, "Investigations of advanced folded reflectarray antennas," in *International Conference on Electromagnetics in Advanced Applications (ICEAA 2010)*. IEEE, 2010, pp. 89–92.
Referenced on page: 59
- [92] J. A. Nelder and R. Mead, "A Simplex Method for Function Minimization," *The Computer Journal*, vol. 7, no. 4, pp. 308–313, Jan. 1965.
Referenced on page: 64
- [93] L. Bellomo, "Study and Realization of an UWB Microwave RADAR based on Phase Conjugation," Ph.D. dissertation, Université du Sud Toulon Var, Laboratoire de Sondages Electromagnétiques de l'Environnement Terrestre (LSEET), Nov. 2011.
Referenced on page: 67
- [94] L. Desrumaux, "Contribution à la conception de sources de rayonnement Ultra Large Bande appliquées à l'imagerie Radar et aux rayonnements forte puissance," Ph.D. dissertation, University of Limoges, XLIM, Sep. 2011.
Referenced on page: 94
- [95] C. Pichot, "Introduction à l'imagerie microonde," lecture notes, University of Nice-Sophia Antipolis, Electronics, Antennas and Telecommunications Laboratory (LEAT), Jan. 2012.
Referenced on page: 97

- [96] O. M. Bucci and T. Isernia, "Electromagnetic inverse scattering: Retrievable information and measurement strategies," *Radio Science*, vol. 32, no. 6, pp. 2123–2137.
Referenced on page: 99, 99, 100, 104
- [97] P. D. L. Beasley, G. Binns, R. D. Hodges, and R. J. Badley, "Tarsier, a millimetre wave radar for airport runway debris detection," in *First European Radar Conference (EURAD 2004)*. IEEE, Oct. 2004, pp. 261–264.
Referenced on page: 107, 108
- [98] Stratech Systems Limited: iFerret, Intelligent Airfield/Runway Surveillance and FOD (Foreign Object & Debris) Detection System. [Online]. Available: http://www.stratechsystems.com/iv_iferret.asp
Referenced on page: 107, 108
- [99] Laseroptronix: Applications at airports for electro optical systems. [Online]. Available: <http://www.laseroptronix.se/airpor/airport.html>
Referenced on page: 107
- [100] Navtech Radar LTD: Airport Surface Movement - Runway Surveillance. [Online]. Available: <http://www.navtechradar.com/Runway%20Surveillance.htm>
Referenced on page: 107
- [101] Xsight - Advanced radar and optic sensors for FOD detection and homeland security. [Online]. Available: <http://www.xsightsys.com/>
Referenced on page: 107, 108
- [102] Trex Enterprises Corporation: FOD Finder. [Online]. Available: <http://www.trexenterprises.com/fodfinderSite/pages/fodfinder.html>
Referenced on page: 108, 108
- [103] Fraunhofer: Making runways safer - Flying safely with the LaotSe project. [Online]. Available: <http://www.mikroelektronik.fraunhofer.de/en/press-media.html>
Referenced on page: 108
- [104] Federal Aviation Administration - FAA Airport Technology Research & Development Branch. [Online]. Available: <http://www.airporttech.tc.faa.gov/>
Referenced on page: 108
- [105] P. Feil, "Broadband mm-Wave Sensors for Industrial and Security Applications," Ph.D. dissertation, Ulm University, Institute of Microwave Techniques, Feb. 2012.
Referenced on page: 108, 122
- [106] B. Michael and W. Menzel, "A realtime close-range imaging system with fixed antennas," in *Microwave Symposium Digest. 2000 IEEE MTT-S International*,

- vol. 3. IEEE, 2000, pp. 1411–1414 vol.3.
Referenced on page: 108
- [107] F. J. Harris, “On the use of windows for harmonic analysis with the discrete Fourier transform,” *Proceedings of the IEEE*, vol. 66, no. 1, pp. 51–83, Jan. 1978.
Referenced on page: 122
- [108] V. K. Ingle and J. G. Proakis, *Digital Signal Processing Using MATLAB (Bookware Companion)*, 2nd ed. CL-Engineering, Aug. 2006.
Referenced on page: 122
- [109] S. Trotta, M. Wintermantel, J. Dixon, U. Moeller, R. Jammers, T. Hauck, A. Samulak, B. Dehlink, K. Shun-Meen, H. Li, A. Ghazinour, Y. Yin, S. Pacheco, R. Reuter, S. Majied, D. Moline, T. Aaron, V. P. Trivedi, D. J. Morgan, and J. John, “An RCP Packaged Transceiver Chipset for Automotive LRR and SRR Systems in SiGe BiCMOS Technology,” *IEEE Transactions on Microwave Theory and Techniques*, vol. 60, no. 3, pp. 778–794, Mar. 2012.
Referenced on page: 123
- [110] M. Abramowitz and I. A. Stegun, *Handbook of Mathematical Functions: with Formulas, Graphs, and Mathematical Tables*, 1st ed., ser. Dover books on mathematics. Dover Publications, Jun. 1965.
Referenced on page: 138
- [111] G. Petiau, *La théorie des fonctions de Bessel exposée en vue de ses applications à la Physique Mathématique*. Centre National De La Recherche Scientifique, 1955.
Referenced on page: 140, 145
- [112] W. H. Press, S. A. Teukolsky, W. T. Vetterling, and B. P. Flannery, *Numerical Recipes: The Art of Scientific Computing*, 1st ed. Cambridge University Press, Jan. 1986.
Referenced on page: 146

Publications of the Author

- [113] J. Lanteri, A. Zeitler, J.-Y. Dauvignac, C. Pichot, C. Migliaccio, P. Feil, and W. Menzel, “Investigation of Wideband Millimetre-Wave Reflectarrays for Radar Applications Operating in the W Band,” in *3rd European Conference on Antennas and Propagation (EUCAP 2009)*, Mar. 2009, pp. 826–830.
Referenced on page: 1
- [114] A. Bréard, A. Zeitler, J. Lanteri, K. Mazouni, and C. Migliaccio, “Reconstruction de la matrice de phase d’un reflectarray à l’aide d’un algorithme d’optimisation de type essaim particulière PSO combiné à une modélisation basée sur les polynômes de Tchebychev (Reconstruction of the Phase Matrix for Reflectarrays, Using a Particle Swarm Optimization (PSO) and a Modeling Based on the Tchebychev Polynomials),” in *17èmes Journées Nationales Microondes*, Brest, France, May 2011.
Referenced on page: 1
- [115] C. Migliaccio, J. Lanteri, B. D. Nguyen, T. P. Nguyen, K. Mazouni, A. Zeitler, and C. Pichot, “Réflecteurs imprimés en bande millimétrique (Printed reflectarrays in the W-band),” in *GDR Ondes*, Paris, France, Nov. 2009.
Referenced on page: 1
- [116] A. Zeitler, T. P. Nguyen, P. Feil, C. Migliaccio, C. Pichot, and W. Menzel, “Antenne réseaux réflecteurs en cosécante carrée pour application FOD dans la bande 76-81 GHz (Cosecan Squared Reflectarrays for FOD Applications in the 76-81 GHz Band),” in *GDR Ondes*, Paris, France, Nov. 2009.
Referenced on page: 1, 108, 112
- [117] C. Migliaccio, K. Mazouni, A. Breard, A. Zeitler, J. Lanteri, J.-Y. Dauvignac, C. Pichot, N. Yonemoto, A. Kohmura, and S. Futatsumori, “Reflectarrays for mm-Wave radar applications,” in *IEEE International Symposium on Antennas and Propagation (IEEE APS 2011)*. IEEE, Jul. 2011, pp. 105–108.
Referenced on page: 1
- [118] A. Zeitler, J. Lanteri, C. Pichot, C. Migliaccio, P. Feil, and W. Menzel, “Folded Reflectarrays With Shaped Beam Pattern for Foreign Object Debris Detection on Runways,” *IEEE Transactions on Antennas and Propagation*, vol. 58, no. 9, pp. 3065–3068, Sep. 2010.
Referenced on page: 1, 108, 112
- [119] K. Mazouni, A. Zeitler, J. Lanteri, C. Pichot, J.-Y. Dauvignac, C. Migliaccio, N. Yonemoto, A. Kohmura, and S. Futatsumori, “76.5 GHz millimeter-wave radar for foreign objects debris detection on airport runways,” *International Journal of Microwave and Wireless Technologies*, vol. 4, no. Special Issue 03,

pp. 317–326, 2012.

Referenced on page: 1

- [120] ———, “76.5 GHz millimeter-wave radar for Foreign Object Debris detection on airport runways,” in *European Radar Conference (EURAD 2011)*, Oct. 2011, pp. 222–225.
- [121] P. Feil, A. Zeitler, T. P. Nguyen, C. Pichot, C. Migliaccio, and W. Menzel, “Foreign object debris detection using a 78 GHz sensor with cosec antenna,” in *European Radar Conference (EURAD 2010)*, Oct. 2010, pp. 33–36.
Referenced on page: 1, 108, 120, 112, 125
- [122] A. Zeitler, C. Migliaccio, A. Moynot, I. Aliferis, L. Brochier, J.-Y. Dauvignac, and C. Pichot, “W-band imaging with complex scattered field measurements of a dielectric cylinder,” in *6th European Conference on Antennas and Propagation (EUCAP 2012)*. IEEE, Mar. 2012, pp. 3686–3689.
Referenced on page: 59, 62
- [123] A. Moynot, A. Zeitler, I. Aliferis, C. Migliaccio, J.-Y. Dauvignac, and C. Pichot, “Millimeter-wave imaging: Quantitative reconstructions from experimental data in the W-band,” in *IEEE International Conference on Wireless Information Technology and Systems*, Nov. 2012.
Referenced on page: 102, 105
- [124] A. Zeitler, C. Migliaccio, A. Moynot, I. Aliferis, J.-Y. Dauvignac, and C. Pichot, “Mesure du champ diffracté par un cylindre métallique en bande W (Measurements of scattered fields of a metallic cylinder in the W-band),” in *GDR Ondes*, Nice, France, Oct. 2011.
- [125] C. Kossiavas, A. Zeitler, G. Clementi, C. Migliaccio, R. Staraj, and G. Kossiavas, “X-band circularly polarized antenna gain enhancement with metamaterials,” *Microw. Opt. Technol. Lett.*, vol. 53, no. 8, pp. 1911–1915, 2011.
- [126] A. Zeitler, C. Migliaccio, A. Moynot, I. Aliferis, L. Brochier, J.-Y. Dauvignac, and C. Pichot, “Amplitude and Phase Measurements of Scattered Fields for Quantitative Imaging in the W-band,” *IEEE Transactions on Antennas and Propagation*, 2013, accepted for publication, to appear.

Curriculum Vitae

Armin Zeitler

SCHOOLING

1989/09 – 1995/07	Primary school, Grund- und Hauptschule, Offingen, Germany
1995/09 – 1999/07	Secondary school, Markgrafen-Realschule, Burgau, Germany
1999/10 – 2002/06	Technical high school, Robert-Bosch-Schule, Ulm, Germany

UNIVERSITY STUDIES

2003/10 – 2008/10	Studies of Electrical Engineering, University of Ulm, Ulm, Germany
2009/01	Diploma degree in Electrical Engineering, specialization in communications/systems technology, University of Ulm, Ulm, Germany

PROFESSIONAL CAREER

2009/01 – 2009/09	Research engineer with fixed term contract, Electronics, Antennas and Telecommunications Laboratory (LEAT), University of Nice-Sophia Antipolis, Valbonne, France
2009/10 – 2012/09	Ph.D. student, Electronics, Antennas and Telecommunications Laboratory (LEAT), University of Nice-Sophia Antipolis, Valbonne, France and Institute of Microwave Techniques, University of Ulm, Ulm, Germany. French state scholarship of the Doctoral School of Information and Communication Sciences (École Doctorale STIC)
Since 2012/11	Algorithm development engineer radar, Division Chassis & Safety, Continental, Ottobrunn, Germany

Munich, April 7, 2013

